Identification of Acoustic Emission sources in machinery; application to injection/combustion processes in Diesel engines

Wael Saber Soliman Abdou

A dissertation submitted for the degree of Doctor of Philosophy on completion of research in the School of Engineering and Physical Sciences
Heriot-Watt University

May 2015

Abstract

The high temporal resolution of Acoustic Emission offers great promise in the on-line monitoring of complex machines such as diesel engines. The fuel injection process is one of the most important processes in the diesel engine and its timing and fuel delivery control are critical in combustion efficiency. In this work, the phenomena leading to the generation of acoustic emission during injection are investigated by simulation of the injection process in a specially designed rig and through test in running engines on a test-bed. Signal processing approaches are devised to produce diagnostic indicators for the quality of the injection process. The novelty of the research lies in; 1) obtaining a coherent set of data which allows the separation of the part of the signal associated with injection in a given cylinder from other sources adjacent in time and space, and 2) in developing a signal processing approach which allows this separation to be achieved on line using an array of sensors. As such, the research is generic to multi-source multi-sensor analysis in machines.

A series of experiments were performed on an experimental injector rig, and two-stroke and four-stroke diesel engines under different operating conditions. The injector rig experiments provided useful information on the characteristic signatures of the injection events, finding which could be implemented to the more complex signal from the running engines. A number of sensor arrays (sets of two and three sensors) were used on two types of four-stroke engine at different running speeds to investigate the source identification of the injection events, the essential strategy being to add complexity to the information in the AE record by using engines of varying degrees of mechanical sophistication.

It has been concluded that the AE signals are generated by the mechanical movements of the components in the pump and injector as well as aspects of the fuel flow through the injector and the piping. Also, it is found that the temporal structure of the AE is highly sensitive to sensor position, and that transmission path differences to a sensor array are generally large enough to allow source separation. Applying a purpose-designed thresholding technique, followed by canonical correlation allows the separate identification of parts of the AE signal in the short crank angle widow where sources involved in injection, inlet valve opening and combustion are operating.

Dedication

To my beloved Parents

To my lovely wife Noha

To my sweetest kids Ahmed, Nour and Malak

Acknowledgements

It has been a long journey of learning and discovery throughout my PhD in which I have put my full trust in the almighty Allah who gave me the strength to be able to complete my journey. After Allah (SWT) I owe my success to my family; my beloved father and mother (the greatest parents that anyone can ever have), my wife (the love of my life) and my children Ahmed, Nour and Malak as their presense in my life made all the difference.

I can’t say enough to thank my supervisor Prof Bob Reuben as his guidance and wisdom made this journey worth doing. I would like to thank all the staff and technicians in the department for their support and help especially Dr Peter Cumber, Mr Richard Kinsella and Mrs Iren Fox.

I would like to thank my friends and colleagues who inspired, supported and encouraged me during all these years especially Hesham, Zannar, Khalid, Angus, Faisal, Steve, Mansour, Elshaib.

ACADEMIC REGISTRY

Research Thesis Submission

Name*:*	Wael Saber Soliman Abdou		
School/PGI:	Engineering and Physical Sciences		
Version: *(i.e. First, Resubmission, Final)*	Final	Degree Sought (Award **and** Subject area)	Ph.D. in Mechanical Engineering

Declaration

In accordance with the appropriate regulations I hereby submit my thesis and I declare that:

1) the thesis embodies the results of my own work and has been composed by myself
2) where appropriate, I have made acknowledgement of the work of others and have made reference to work carried out in collaboration with other persons
3) the thesis is the correct version of the thesis for submission and is the same version as any electronic versions submitted*.
4) my thesis for the award referred to, deposited in the Heriot-Watt University Library, should be made available for loan or photocopying and be available via the Institutional Repository, subject to such conditions as the Librarian may require
5) I understand that as a student of the University I am required to abide by the Regulations of the University and to conform to its discipline.

* *Please note that it is the responsibility of the candidate to ensure that the correct version of the thesis is submitted.*

Signature of Candidate*:*		Date:	

Submission

Submitted By *(name in capitals):*	WAEL SABER SOLIMAN ABDOU
Signature of Individual Submitting:	
Date Submitted:	

For Completion in the Student Service Centre (SSC)

Received in the SSC by *(name in capitals):*			
Method of Submission *(Handed in to SSC; posted through internal/external mail):*			
E-thesis Submitted (**mandatory for final theses**)			
Signature:		Date:	

Table of Contents

Lists of Tables

Lists of Figures

List of Symbols

$\dot{m}_f$	Fuel mass flow rate (kg/s)
λ_{opt}	Optimum wave length for jet disruption (m)
η	Viscosity of fuel (m/s)
h^*	Half sheet thickness at break up
v_j	Jet velocity (m/s)
A_n	Nozzle flow area per hole (m^2)
B	Decay constant (greater than 0)
C	Constant in the range of 3-4.5
C_d	Discharge coefficient
C_l	Velocity of longitudinal waves (m/s)
C_R	Velocity of Rayleigh waves (m/s)
C_S	Velocity of shear waves (m/s)
d	Droplet diameter (m)
D	Mean droplet diameter (m)
d_j	Jet diameter (m)
d_l	Ligament diameter (m)
d_n	The nozzle hole diameter (m)
E	Energy (kg m^2/s^3)
E	Young's modulus of elasticity for the material (N/m^2)
n	Number of nozzle holes
Q_e	Volumetric flow rate (m^3/s)
S	The spray penetration distance (m)
t	Time (s)
$t_{breakup}$	The break up time of the fuel jet (s)
t_i	Time after the start of injection (s)
V	Output voltage of sensor
V_o	Initial signal amplitude
α	Empirical constant equals 15.7
γ	Liquid fuel surface tension (N/m)
Δp	The pressure drop across the nozzle (kg/s^2 m)
ρ	Density of the material (kg/m^3)
ρ_f	Fuel density (kg/m^3)

ρ_g	Gas density (kg/m^3)
υ	Poisson's ratio for the material
ω	Angular frequency

List of Abbreviations

AE	Acoustic Emission
AES(n)	Acoustic Emission Sensor number (n)
AET	Acoustic Emission Testing
ATDC	After Top Dead Centre
BDC	Bottom Dead Centre
BSI	British Standards Institute
BSS	Blind Source Separation
BTDC	Before Top Dead Centre
CBM	Condition Based Maintenance
CE	Combustion Engine
CH(n)	Cylinder Head number (n)
CI	Compression Ignition
CM	Condition Monitoring
CR	Common Rail
CWT	Continuous Wavelet Transform
DAQ	Data Acquisition Card
DE	Diesel Engine
DI	Direct Injection
ECU	Engine Control Unit
EDC	Electronic Diesel Control
EV(n)	Exhaust Valve (n)
EVC	Exhaust Valve Closure
EVO	Exhaust Valve Opening
FB	Start of Delivery [Förderbeginn]
FE	End of Delivery [Förderenden]
FFT	Fast Fourier Transform
HSDI	High Speed Direct Injection
IC	Internal Combustion
ICA	Independent Component Analysis
ICAV	Instantaneous Crankshaft Angular Velocity
ID	Indirect Injection
INJ(n)	Injector (n)
IV(n)	Inlet Valve (n)

IVC	Inlet Valve Closure
IVO	Inlet Valve Opening
NDT	Non Destructive Testing
NI	National Instruments
PAC	Physical Acoustic Corporation
PCA	Principle Component Analysis
PLI	Pump Line Injector
PS	Power Spectra
PSD	Power Spectral Density
RBF	Radial Basis Function
RMS	Root Mean Square
RPM	Revolution Per Minute
SB	Start of Injection (spray) [Spritzbeginn]
SCU	Signal Conditioning Unit
SE	End of Injection (spray) [Spritzenden]
SICCA	Source Identification using Canonical Correlation Analysis
SNR	Signal to Noise Ratio
SPWVD	Smoothed Pseudo-Wigner-Ville Distribution
STFT	Short Time Fourier Transform
SV	Injection Lag [Spritz Verzögerung]
TDC	Top Dead Centre
UIS	Unit Injector System
VB	Start of Ignition (combustion) [Verbrennungsbeginn]
VE	Distributer Injection Pump [Verteilereinspritzpumpe]
VE	End of Ignition (combustion) [Verbrennungenden]
WT	Wavelet Transform
WVD	Wigner-Ville Distribution
ZV	Ignition Lag [Zündung Verzögerung]

List of Publications by the Candidate

Abdou, W., Hunter, C., Shehadeh, M. F. , Steel, J. A. and Reuben, R. L. Monitoring of Diesel Fuel Injection using Acoustic Emission (AE), Proceedings of the 5th International Conference on Condition Monitoring and Machinery Failure Prevention Technologies, Edinburgh, UK, 15-18 July 2008, pp 1-11.

Shehadeh, M. F., **Abdou, W.**, Steel, J. A. and Reuben, R. L. Aspects of Acoustic Emission (AE) attenuation in steel pipes subject to different internal and external environments, *Proceedings of the Institution of Mechanical Engineers, Journal of Process Mechanical Engineering*, 222(1), pp. 41-54, 2008.

Ossi, Z., **Abdou, W.**, Reuben, R. L. and Ibbetson, R. J. In-vitro monitoring the primary stability of dental implants using acoustic emission, East European Congress of Dental Implantation, Lviv, Ukraine, 12-14 March 2009.

Ossi, Z., **Abdou, W.**, Reuben, R. L. and Ibbetson, R. J. Monitoring the primary stability of dental implants using Acoustic Emission (AE)-A preliminary study, British Society for Dental Research (BSDR) Scientific Meeting, Glasgow, UK, 1-4 September 2009.

Reuben, R. L., **Abdou, W.**, Cunningham, S., Droubi, M. G., Nashed, M. S. and Thakkar, N. A. Processing techniques for dealing with pulsatile AE signals, Proceedings of World Conference on Acoustic Emission, Beijing, China, 24-26 August 2011, pp 85-89.

Ossi, Z., **Abdou, W.**, Reuben, R. L. and Ibbetson, R. J. In-vitro assessment of bone/implant interface using Acoustic Emission Test, *Proceedings of the Institution of Mechanical Engineers, Part H: Journal of Engineering in Medicine*, 226(1), pp. 63-69, 2011.

Abdou, W., Balodimos, N. and Reuben, R. L. Acoustic emission in diesel engines – a time series model for the injection process, Proceedings of 30th European Conference on Acoustic Emission testing and 7th International Conference on Acoustic Emission, Granada, Spain, September 2012, pp394-406.

Ossi, Z., **Abdou, W.**, Reuben, R. L. and Ibbetson, R. J. Transmission of acoustic emission (AE) in bones, implants and dental materials, Proceedings of the Institute of Mechanical Engineers, Part H: Journal of Engineering Medicine, 227(11), pp. 1237-1245, 2013.

Abdou, W. and Reuben, R. L. Monitoring of the Direct Fuel Injection System in Diesel Engines using Acoustic Emission (AE), International Journal of Engine Research, July 2014 (submitted).

Abdou, W. and Reuben, R L. Monitoring of Diesel Engines using Canonical Correlation of Acoustic Emission (AE) Signals, Proceedings of 31st European Conference on Acoustic Emission testing, Dresden, Germany, September 2014.

Abdou, W. and Reuben, R. L. Identification of diesel engine events using Acoustic Emission (AE) and Canonical Correlation Analysis (manuscript in preparation for Journal of Mechanical Systems and Signal Processing)

Abdou, W. and Reuben, R. L. Real-Time Multi-Source Multi-Sensor Condition Monitoring of Diesel Engines using Acoustic Emission (AE) and Canonical Correlation Analysis (manuscript in preparation for Journal of Mechanical Systems and Signal Processing)

Chapter 1

Introduction

1.1 Research Overview

Condition monitoring (CM) is a key element in maintenance management and process control, and can be regarded as a holistic multidisciplinary discipline [1]. Condition monitoring has been implemented in machines to detect faults and identify the corresponding causes. Technical advances in CM techniques have led to the development of condition based maintenance (CBM) in machinery for both diagnostic and prognostic aspects in order to provide an effective predictive maintenance strategy [2]. Improvements in operating efficiency, reliability and risk management with the resulting reduced maintenance costs are the main benefits of machine condition monitoring [3]. Vibration analysis is the most common non-intrusive technique used for condition monitoring of machinery applications [4, 5], but the vibration signatures of internal combustion engines are non-stationary and this, coupled with the potential for significant vibration noise make the use of vibration analysis challenging [6]. This thesis seeks to amplify some of the benefits of a CM technique, which superficially resembles vibration monitoring, but offers reduced noise and greater specificity in fault identification, namely acoustic emission (AE) monitoring.

Fuel injection is central to the efficient operation of diesel engines, and developments in the control of air and fuel delivery are essential to meet increasingly stringent requirements on emissions, noise and fuel efficiency [7]. This, coupled with a seemingly relentless demand for higher performance has driven developments in fuel injection systems for diesel engines [8]. In addition, the potential for diesel engines to use alternative fuels to standard diesel requires more effective and flexible monitoring of fuel injection. The hydraulic behaviour of the injector pump, tubing and injectors is quite complex, involving pressure waves which travel at the speed of sound between the pump and the injector [9], and whose interaction with the injectors constitutes a dynamical system which influences the duration, timing and pressure of the injection process. The pressure waves may be reflected at the nozzle in a form which depends upon whether it is open or closed, further complicating the process [10]. Many modern engines have electronic management of the injectors to introduce active control and

dynamic models already exist for the analysis and vibration monitoring of the injection process [11, 12].

The fuel injection system must ensure that the correct fuel droplet size, fuel distribution and mixture is formed in the combustion chamber for the best combustion efficiency [7]. In diesel engines the air-fuel mixture is relatively heterogeneous, fuel being unevenly distributed through the cylinder and combustion chamber. Injected fuel spray needs to penetrate the compressed and heated air mass where and be broken into very small droplets [10].

One of the main problems in monitoring engines is the multiplicity of sources, a problem partly alleviated in very large engines where the cylinders are physically separated from each other. Another significant problem is that the structure of a given source (as in combustion) may itself be quite complex, necessitating a sub-analysis of windowed-out parts of the time series.

Acoustic emission has shown promise for the condition monitoring of engines due to its sensitivity to a wide range of mechanical and fluid-mechanical phenomena [13], [6]. It has been found that individual events and processes (such as engine speed [14], event timing [15, 16], injection [17-21] and combustion processes [22]) can be examined and detected successfully using AE techniques due to their high spatial and temporal resolution. Both the monitoring of diesel engine performance [81, 106] and diagnosis of faults (such as exhaust valve leakage [23], cylinder head gasket leakage [24] and liner scuffing [25, 26]) have been demonstrated. Spatial source location of the multiple sources using an array of sensors is possible [27], although the propagation of AE waves in such structures as an engine block, is complicated by refraction, reflection, mode conversion and attenuation [28, 29].

This study is aimed at investigating the use of acoustic emission technology in monitoring the diesel engines, more specifically in separating sources which are adjacent both temporally and spatially. As a typical such challenge, the study is focused on the injection process and the associated pulsatile flow particularly the extent to which injection and combustion can be separated in the crankshaft angle window from 10°BTDC to 30°ATDC approximately on the firing stroke. The research is therefore

largely an experimental study of the monitoring of the injection process in internal combustion engines. The phenomena leading to the generation of acoustic emission during injection are investigated by simulation of the injection process in a specially designed rig and *in situ* in engines on a test-bed. Different types of engines have been used in this study to provide a generic identification of the diesel engine events using a common approach in interpreting the AE signal. Particular emphasis is placed on signal processing techniques which can separate signals in the time domain using information on the propagation of AE in the relevant structures obtained by careful calibration using simulated sources.

1.2 Research aims and objectives

This research aims to develop an automatable processing approach for machinery monitoring in which there are a number of sources which are separated in space and time, and where their sequences and locations are known from the mechanical features of the machine. To make the task manageable, the work is focussed onto the injection-combustion processes in small diesel engines.

To meet this aim, the following specific research objectives were devised:

- Carry out a series of calibrations on all of the machinery to be monitored to establish propagation parameters (time delays and attenuation) for possible sources to arrays of sensors.
- Carry out a series of tests on injectors removed from an engine to establish the characteristic AE signatures of the injection process and the associated fuel supply processes for a range of simulated crankshaft speeds.
- Carry out a series of tests on small two- and four-stroke engines of increasing complexity to gather data on the injection-combustion window under a variety of running conditions.
- Develop a means of isolating the injection-combustion window in a way that can be automated.
- Identify a way of processing the injection-combustion AE data obtained at a number of sensors which isolates sources and measures their AE features on-line.
- Establish how the AE features of the injection-combustion sources vary with engine operating conditions.

1.3 Research methodology

In order to achieve the research objectives, three main stages of work were required; experimental set up and calibration, systematic experiments on injector rig and test engines, and signal processing and analysis. In the first stage, a range of engines of increasing levels of complexity was chosen for inclusion in the experimental protocol and an experimental rig to simulate the injection system in one of these engines was designed and commissioned. A range of different sensor array settings were examined to determine the most suitable matrix for monitoring the engine events and a set of measurements carried out with simulated sources to characterise potential source-sensor propagation processes. In the second stage, experiments were carried over a range of engine and injector pump operating conditions, aimed at assessing how the injector AE characteristics change with these conditions in an isolated pump-injector configuration and in running engines. The third stage involved analysing the acquired signals using a wide range of signal processing approaches, each of which needed to be coded separately in order to extract the necessary features in a way that was non-subjective, i.e. did not require the intervention of an operator.

1.4 Thesis layout

This thesis is presented in six chapters which can be summarised as:

Chapter1: Introduction

This chapter gives a brief introduction to the context of the study and outlines the main objectives of the research. Also, it describes the research methods used and indicates the novelty of the work.

Chapter 2: Technology review

This chapter describes the most important/relevant technological developments underlying the work, namely developments of diesel engines, injection systems and acoustic emission technology.

Chapter 3: Literature review

This chapter critically reviews the previous work by other researchers in the field of condition monitoring of diesel engines and injection systems. Relevant signal processing methods are also reviewed. The chapter culminates in a statement of the detailed research topic to be purse in the current work.

Chapter 4: Experimental set up and procedures

This chapter describes the experimental apparatus, including measurement systems and test rigs. The calibration procedures for sensors and test rigs are also described and analysed, and the experimental protocol and procedures are described and justified. Finally, methods of signal processing are described in detail, concentrating on the application of canonical correlation analysis to pairs of time series.

Chapter 5: Analytical discussion of the results of injector rig two stroke engine experiments

This chapter considers the experiments on the injector rig and the two stroke engine, which are the two simplest of the test objects considered in the work. First, the results from injector rig experiments are discussed with a view to isolating the AE characteristics of diesel injection, isolated from the closely related valve and combustions events. Next, the two stroke engine is considered using both conventional time and frequency domain techniques and also to introduce the canonical correlation algorithm to study the injection/combustion events.

Chapter 6: Analytical discussion of the results of four stroke engine experiments

This chapter considers the four-stroke, four cylinder engines, which potentially have several sources even within one stroke of the engine cycle. It builds on the analysis carried out in Chapter 5 on the injector rig and on the simple two-stroke engine and develops the multi-source, multi-sensor approach using canonical correlation.

Chapter 7: Conclusions and recommendations

This chapter summarises the most significant findings of this research study. It identifies the extent to which the original aims have been met and indicates the areas that require further investigation and have the potential for extended research work.

1.5 Research novelty

The online non-intrusive monitoring diesel engines is a very challenging task, particularly if the various sources are to be separated for detailed diagnosis. Traditionally, sound and vibration measurements have been used, but each of these requires intensive processing, especially if information is to be recovered from the not inconsiderable noise. Acoustic emission is well-known to be relatively free of ambient noise, although its sensitivity to a number of potential sources renders it susceptible to signal overlap and ambiguity of interpretation.

This work has two dimensions of novelty:

- The first of these is the acquisition and analysis of a set of AE data aimed at identifying the sources of AE in diesel engine injectors, as distinct from the resulting combustion events which accompany injection. This has involved the calibration of the test objects for AE propagation, coupled with the acquisition of test data to an array of sensors. This process itself is novel in that it provides a methodology for preparing any machine for quantitative AE monitoring, as well as setting the limits of temporal and spatial discrimination of sources.

- The second is the development of a technique which can be used on-line to separate individual signatures for sources from a different time or place in an AE record. Besides the adaptation of a number of signal processing methods routinely applied to AE, the method of canonical correlation is applied to pairs of signals to allow a sliding time-window approach to separate sources automatically. As far as the author is aware, the use of canonical correlation for AE source location in diesel engines has not been attempted previously.

Chapter 2

Technological review

This chapter provides a comprehensive summary of recent developments in diesel engine and acoustic emission technology. Although it contains little research per se, mostly consisting of established knowledge, it provides the essential background theories of the machinery and monitoring techniques used in this study.

First, the diesel engine fundamentals will be described, including the theory of their operation, focusing on a discussion of developments in the science and technology of diesel injection systems. The second part of this chapter will describe the acoustic emission (AE) technique, highlighting its use in monitoring the engine performance. In addition, the features of a typical AE signal and its interpretation will be presented.

2.1 Diesel engine fundamentals

The diesel engine is a compression ignition (CI) engine where the rise in temperature and pressure is sufficient to cause self ignition of the fuel. It operates with a heterogeneous charge of previously compressed air to which a spray of liquid fuel is added and self-ignites to cause the combustion of the mixture [8]. The great advantage that CI engines have is their excellent fuel efficiency which exceeds 40% to 50% [30]. In addition, CI engines are recognised for their low specific fuel consumption and carbon dioxide emissions over spark ignition (SI) engines. As has been highlighted recently, this last advantage can be compromised by increased soot and smoke emission in high performance engines, hence the need for continuous improvement in injection behaviour.

2.1.1 Basic diesel engine types

Diesel engines can be classified into high, medium and low speed and into size groups; small, medium and large. However, the main distinction is between four-stroke and two-stroke engines.

In the case of a four-stroke engine, there are two strokes of the piston for each crankshaft revolution; i.e. there are two crank revolutions for every complete cycle. The four-stroke cycle can be described with reference to Figure 2.1:

i) The intake stroke, where the piston travels downward starting from top dead centre (TDC) while drawing in the charge of air as the intake valve is open.

ii) The compression stroke which begins at bottom dead centre (BDC) and in which the piston compresses the air while it moves upward with both intake and exhaust valves closed. The fuel is injected near TDC and ignition occurs around the end of the compression stroke.

iii) The power stroke, where both the temperature and pressure rise as the combustion propagates and the piston is forced to move down. Both valves remain closed to maintain the forces on the piston.

iv) The exhaust stroke which commences near the end of the power stroke when the exhaust valve is opened. As the piston moves upward the exhaust gases are expelled in what is called blow-down [9].

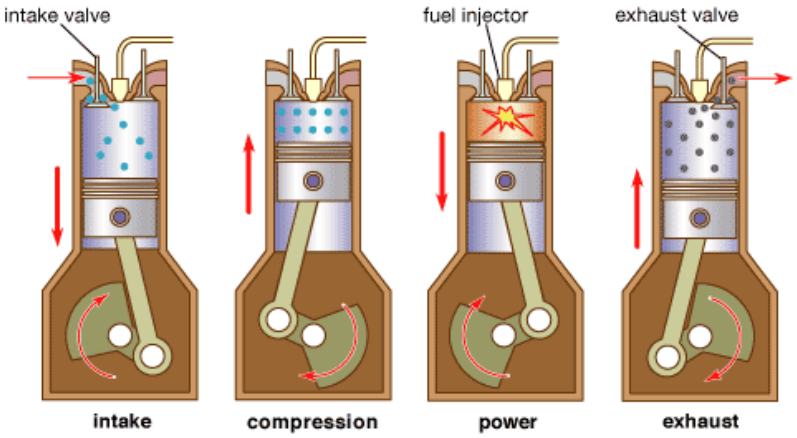

Figure 2.1: Four-stroke diesel engine. (from 2007 Encyclopaedia Britannica)

This complete engine cycle (720^o crank angle and 360^o cam angle) can be represented in crank angle domain as an event map (Figure 2.2), in which the events associated with each stroke at their corresponding angles.

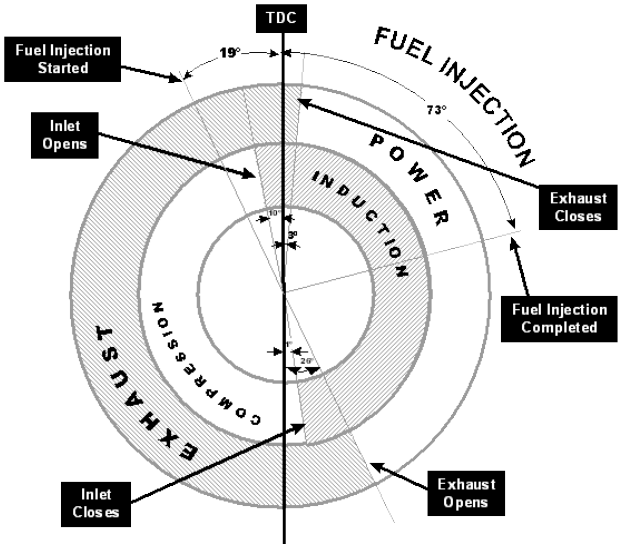

Figure 2.2: Example of an event map for a four stroke diesel engine. [31]

In two-stroke engines, combustion occurs in the region of TDC for every crankshaft revolution; i.e. one complete cycle occurs for each revolution of the crankshaft. Since the two-stroke engine must go through the same four events as the four-stroke engine it is necessary for several events to occur in each stroke. The operation can be described with reference to Figure 2.3:

i) The compression stroke where the piston moves upward to the TDC and covers the intake ports while compressing the trapped air. The fuel is injected close to the end of the compression stroke and combustion will start before top dead centre.

ii) The power stroke commences at the end of the compression stroke when the products of combustion raise the temperature and pressure in the cylinder, and force the piston to move down. While the piston is moving towards BDC the exhaust port is uncovered and blow down occurs [9].

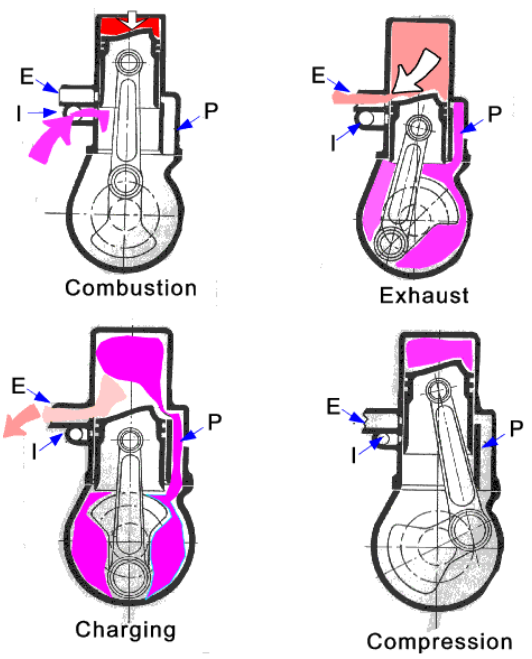

Figure 2.3: Two-stroke diesel engine. [32]

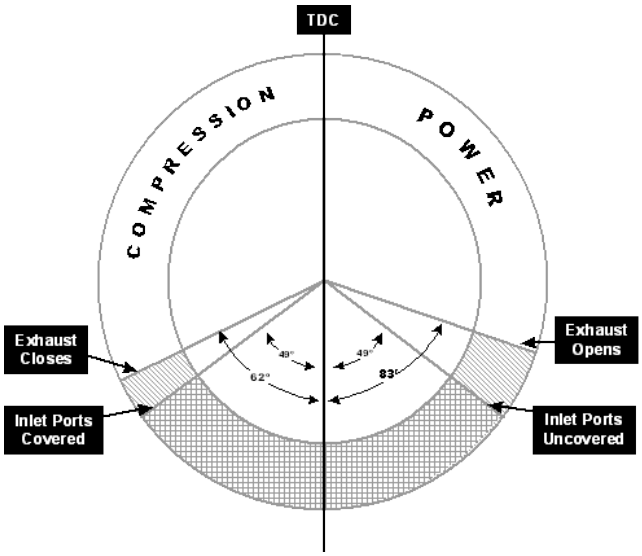

Figure 2.4: Example of event map for a two stroke diesel engine. [33]

The air-fuel mixing process is crucial to the operation of diesel engines and, as such, has received more attention, reflected in the variety of available combustion systems. There are two classes of combustion chamber: those with direct injection (DI) into the main chamber, and those with indirect injection (ID) into some form of divided chamber [8].

2.1.2 Types of injection

There are two basic types of injection, direct and indirect, and these are described briefly in the following two sections.

2.1.2.1 Direct injection (DI)

In DI engines, the fuel is injected directly into a combustion chamber above the piston where the compression ratio is often between 12:1 and 16:1. The fuel injector is usually close to the centreline of the combustion chamber and can be either normal or angled to the cylinder head. Figure 2.5(a) shows a typical large cylinder in a medium speed engine where mixing can be done even in relatively quiescent air by using multi-hole injector with up to twelve jets. This type of chamber requires high injection pressure, 1000-1500 bar or more, in order that the high velocity of the fuel droplets entrains air into the jet and the amount of swirl can be reduced. The number of holes is reduced, usually to four, in small sized engines with wide speed ranges and CRs of between 13:1 and 15:1, as shown in Figure 2.5(b). In such engines, the injection pressure is reduced to the range of 700-1000 bar but the air is given a high degree of swirl [8].

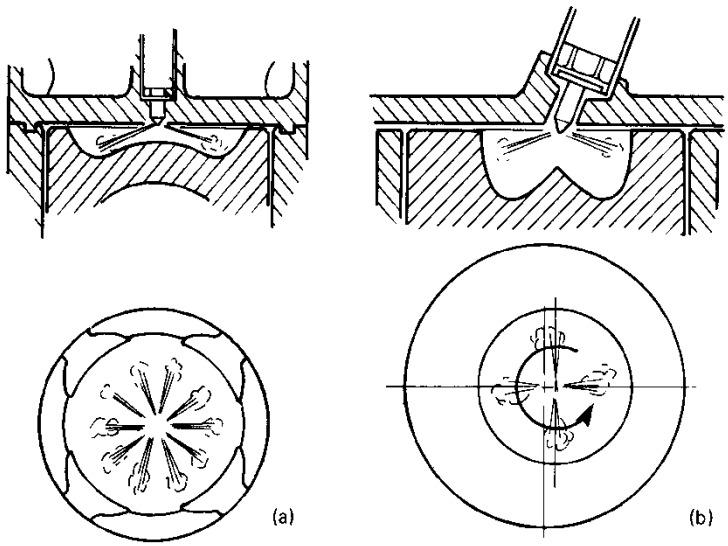

Figure 2.5: Different types of direct injection combustion chambers: (a) Direct injection quiescent chamber; (b) Direct injection bowl chamber with swirl. [8]

2.1.2.2 Indirect injection (ID)

Indirect injection systems have a divided combustion chamber, with some form of pre-chamber, into which the fuel is injected, and a main chamber with piston and valves. The main function of a divided combustion chamber is to speed up the combustion

process, in order to increase the engine output by increasing the engine speed. There are two principal types of ID system; pre-chamber and swirl chamber. Figure 2.6 (a) shows a typical swirl chamber in which a strong air vortex is generated during the compression stoke, and the fuel is injected into this swirling air. When the combustion starts, the burning air-fuel mixture is forced into the cylinder through the throat area and mixed with the residual combustion air [7]. Pre-chambers rely on turbulence to increase the combustion speed, as shown in Figure 2.6 (b). During the compression stroke, air enters the chamber and the fuel is sprayed into the chamber to initiate the ignition. The burning air-fuel mixture enters the main combustion chambers through a number of passages to mix with the remaining air to complete the combustion. Injection requirements for indirect injection engines are less demanding and so single-hole injectors with pressures of about 300 bar can normally be used [9].

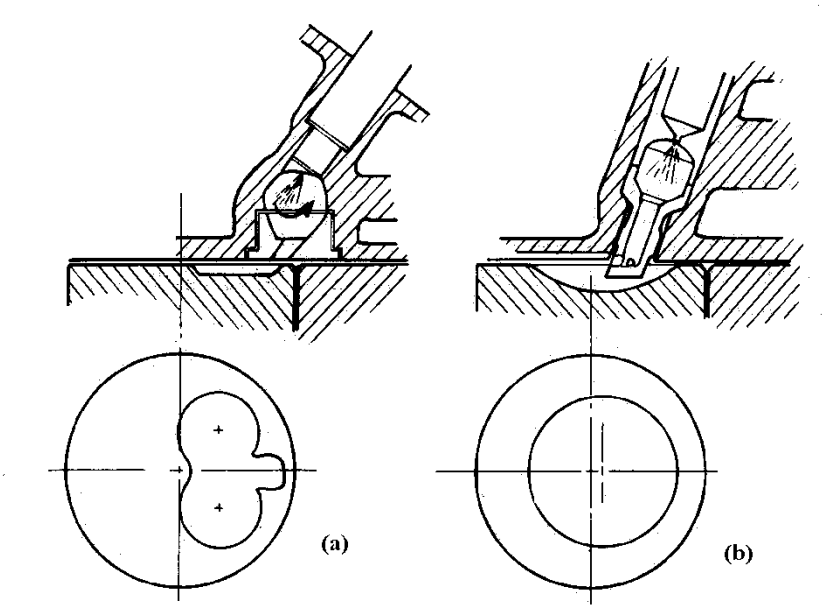

Figure 2.6: Different types of indirect injection combustion chamber: (a) Swirl combustion chamber; (b) Pre-combustion chamber. [8]

2.2 Fuel injection in diesel engines

The function of the fuel injection system is to supply the engine with the exact amount of fuel accurately timed to accomplish complete combustion. Each injector receives fuel at very high pressure in order to produce rapid injection coupled with a high velocity spray. The fuel spray entrains air and breaks up into droplets; this provides rapid mixing which is essential if the combustion is to occur sufficiently fast. In multi-cylinder

engines the delivery quantity, the timing and period of injection must be accurately matched to maintain the balance of power in the cylinders.

2.2.1 Diesel Fuel injection systems

Figure 2.7 outlines the four main types of injection system, (a) unit injector system, (b) distributor (c) fuel injection pump and (d) accumulator injection system.

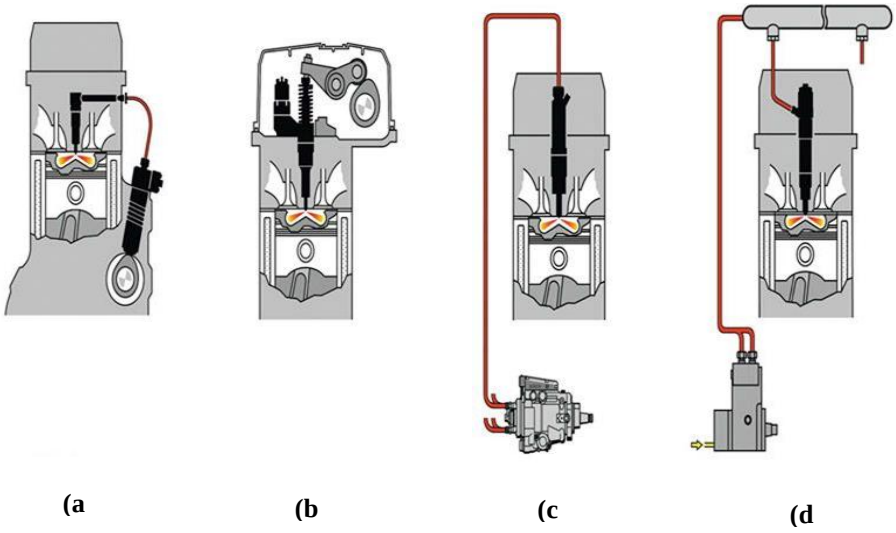

Figure 2.7: Diesel fuel injection systems. [7]

A traditional pump-line-injector (PLI) system, also called in-line injection pump, is the most common arrangement for fuel injection in diesel engines. However, higher fuel injection pressures have led to an increase use of unit injectors and common rail fuel injection systems. Figure 2.8 shows a traditional PLI system in which the injection pump is directly coupled to the engine (at half the engine speed for a four-stroke engine). The function of the fuel pump is to control the quantity and timing of the fuel injection and the amount of injected fuel per cycle will vary according to the engine load. Under certain circumstances, the injection timing depends on the engine speed and load. The timing should be advanced as the engine speed increases to adjust the ignition delay. As the load increases, either the ignition timing is reduced for fixed injection timing or the fuel is injected earlier for the same ignition delay.

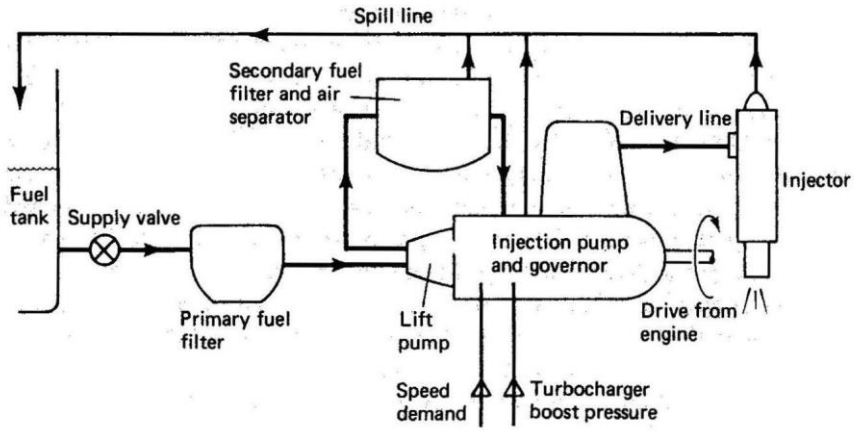

Figure 2.8: Pump-line-injector system. [9]

Both the pumping element and injector are packed together to form a unit injector system (UIS) as shown in Figure 2.9. Each UIS is installed in the cylinder head of the engine, and driven directly by a tappet or indirectly from a camshaft in the cylinder head. This eliminates the high-pressure fuel line which enables the system to operate at higher injection pressure (up to 2050 bar) [7].

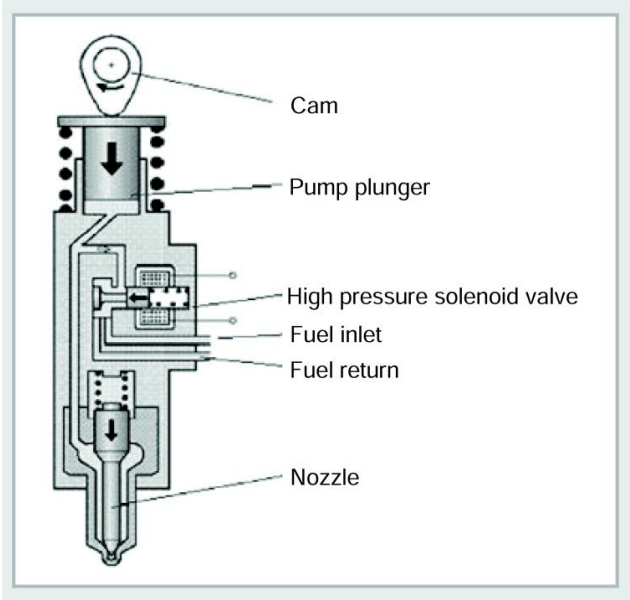

Figure 2.9: Unit injector system. [34]

The distributer fuel injection system, normally called VE pump (Figure 2.10), combines a fuel supply pump, a high pressure pump, a governor, and a timing device into a single compact unit. It has only one fuel metering plunger which delivers the required amount of fuel at the desired pressure to each outlet port. This allows the VE pump to deliver accurate metering and timing in addition to the main function of pressurizing the fuel.

Also, it has a control function, through the governor (either mechanical or electronic), to control the engine speed.

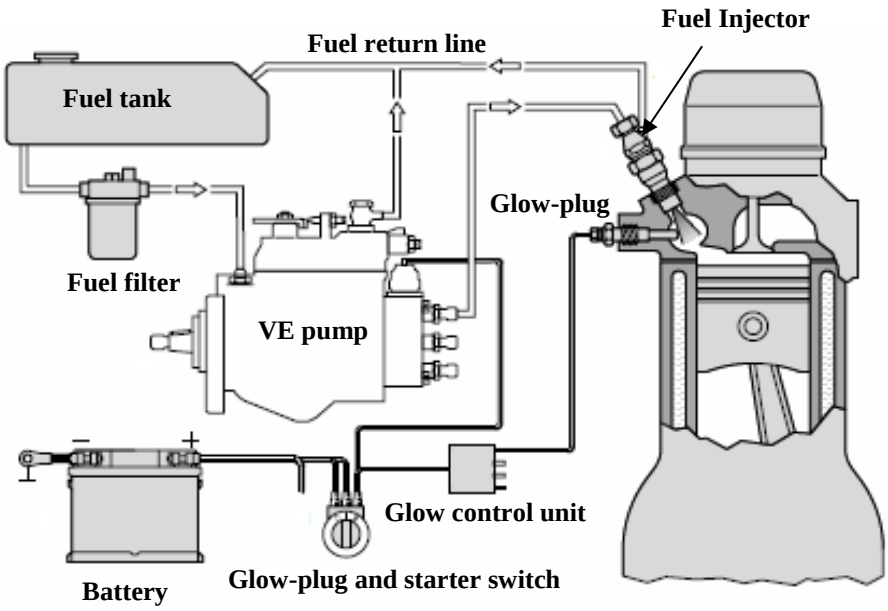

Figure 2.10: Distributor fuel injection system.[7]

The common rail fuel injection system (CR) has a high-pressure fuel pump which produces a controlled and steady pressure (Figure 2.11). The injection pressure is generated independent of engine speed and the quantity of fuel injected and stored in the rail. Both the injection timing and fuel quantity are controlled by the electronic control unit (ECU) and implemented at each cylinder through a triggered solenoid valve.

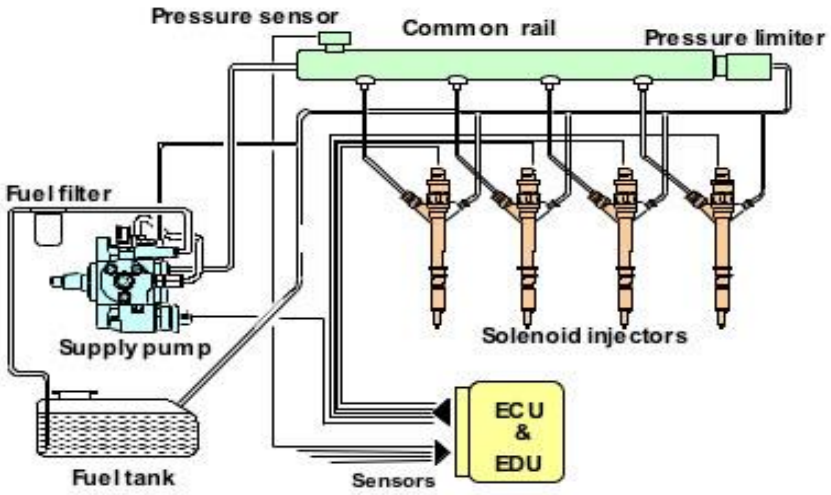

Figure 2.11: Common rail injection system. (DENSO 2002)

2.2.2 Fuel Injectors

The most important part of the injector is the nozzle, hence there is a high degree of international standardization for these. Figure 2.12 shows the structure of single and dual stage injectors. Closed nozzles are used much more than open nozzles as the latter type tends to dribble which results in the formation of combustion deposits on the injector and may lead to hole blockage. In closed nozzles both the opening and closing pressure of the needle can be determined by the force of the spring and the projected area of the needle, as shown in Figure 2.13. The differential pressures are controlled by the diameters of needle and seat, where a high needle-closing pressure is recommended for better sealing in order to prevent blockage of the nozzle holes caused by decomposition of leaked fuel. There are two main categories of injector nozzle, those for direct injection engines and those for indirect injection.

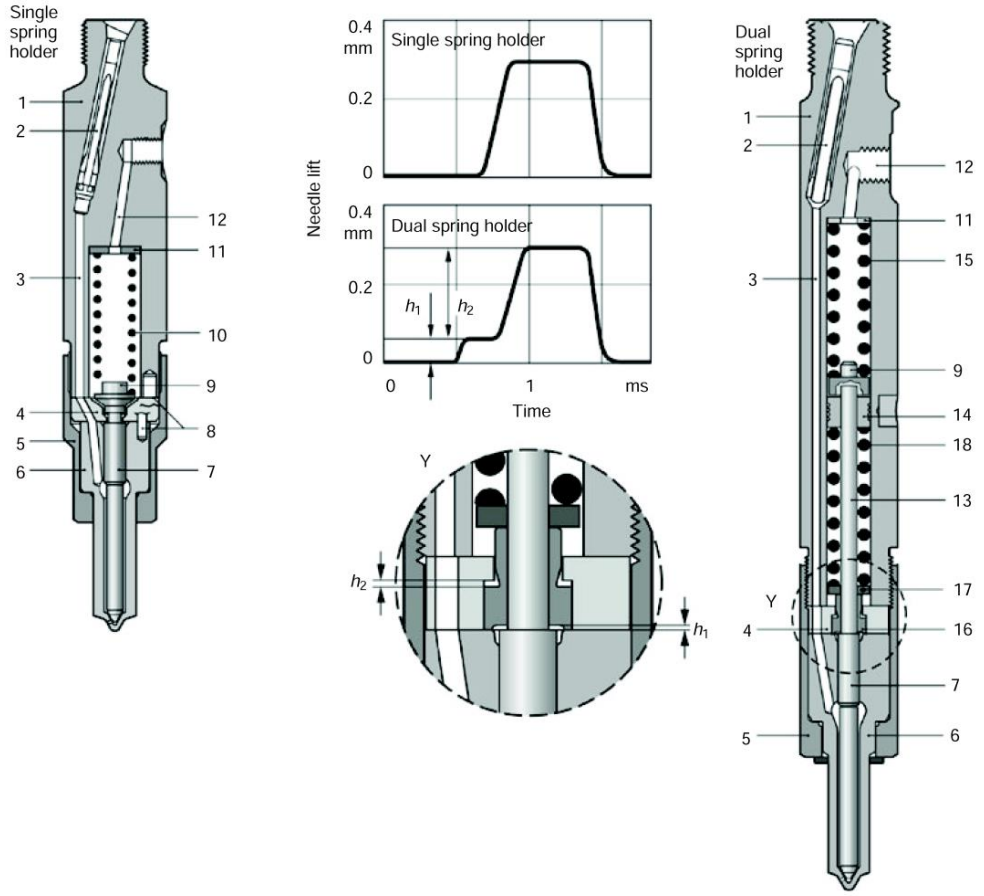

Figure 2.12: Nozzle holder assembly. 1 Injector body; 2 Edge filter; 3 High pressure inlet; 4 Intermediate disk; 5 Nozzle retaining nut; 6 Nozzle body; 7 Nozzle needle; 8 Locating pin; 9 Push rod; 10 Compression spring; 11 Shim; 12 Fuel return; 13 Pressure pin; 14 Guide disk, 15 Compression spring 1; 16 Stroke adjustment sleeve; 17 Spring shim; 18 Compression spring 2. [34]

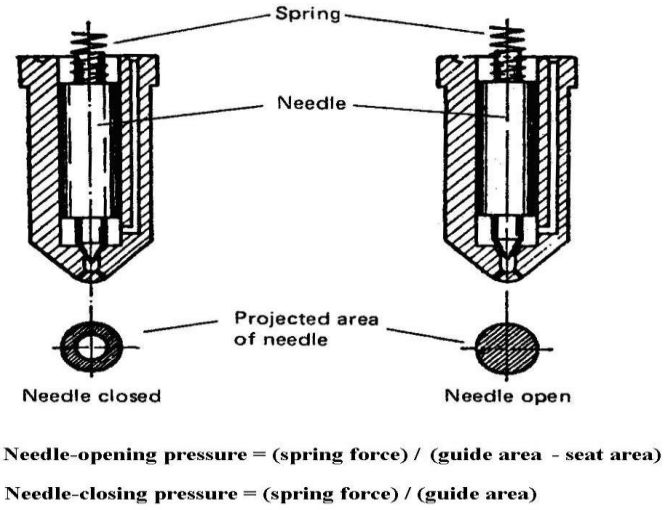

Figure 2.13: Differential action of the injector needle. [9]

The development of fuel injectors is crucial to enhance the combustion and the performance of diesel engines [35, 36].

2.2.3 Fuel spray formation

The injection of liquid fuel into combustion chambers through nozzles facilitates the disintegration of the liquid into a spray of droplets lying within a specified size range [37]. Spray characteristics depend upon the pressure and viscosity of the fuel. Generally, spray penetration increases as the injection pressure increases but, above a certain pressure, the spray becomes finely atomised and does not have sufficient momentum to penetrate very far. The nozzle dimensions, such as the aspect ratio (ratio of length to diameter), also affect the spray characteristics. The mass flow rate of the fuel through the injector can be described by [9]:

$$\dot{m}_f = C_d A_n \sqrt{2\rho_f \Delta p} \qquad \textbf{2-1}$$

where $\dot{m}_f$ is the fuel mass flow rate (kg.s^{-1}), C_d is the discharge coefficient, A_n is the nozzle flow area per hole (m^2), Δp is the pressure drop across the nozzle (N.m^{-2}) and ρ_f is the fuel density (kg.m^{-3}).

Thus, the fuel flow rate in a nozzle hole can be represented as:

$$Q = C_d A_n \sqrt{\frac{2\Delta p}{\rho_f}} \qquad \textbf{2-2}$$

where Q is the fuel flow rate ($m^3 .s^{-1}$).

Nozzle hole diameters (d_n) are typically in the range of 0.15-1 mm with aspect ratios from 2 to 8. A fuel jet with high penetration and less diversion can be obtained by increasing the aspect ratio of the nozzle. The differential pressure, which is typically greater than 300 bar, produces a high velocity jet (typically faster than 250 $m.s^{-1}$) which becomes turbulent. The jet spreads out as a result of entraining air, and breaks up into droplets and, as the jet diverges, the spray velocity decreases [9]. Increasing the density of the fuel increases penetration while increasing the density of the air reduces jet penetration. Also, denser fuels are more viscous which leads to jet divergence and less atomization.

The most effective way of utilizing energy imparted to the fuel is to arrange that the fuel mass has a large specific surface before it commences to break down into drops [37]. Thus, the primary function of the nozzle is to transpose bulk liquid fuel into thin liquid fuel sheets. Less than 0.5% of the applied energy is utilised in breaking up fuel into small drops and so practically the whole amount is imparted to the fuel as kinetic energy [37]. The rate of work required for supply through a pressurised nozzle is given by

$$\dot{E} = 1.331 \times 10^3 Q_e \Delta p \qquad \textbf{2-3}$$

where $\dot{E}$ is the rate of work required ($J .s^{-1}$), Q_e is the volumetric flow rate ($m^3 .s^{-1}$) and Δp is the pressure drop across the nozzle ($N.m^{-2}$).

The basic principle of the disintegration of a liquid fuel jet relies on increasing its surface area until it becomes unstable and disintegrates. The basic mechanism of drop formation consists essentially of the breaking down of unstable threads of fuel into rows of drops conforming to the classical mechanism postulated by Lord Rayleigh. The theory states that a free column of liquid is unstable if its length is greater than its circumference and that, for a non-viscous liquid, the wavelength of the disturbance

which will grow most rapidly in amplitude is 4.5 times the diameter. Weber has shown that, for viscous liquids, the optimum wavelength for jet disruption is

$$\lambda_{opt} = \sqrt{2\pi\, d_j \left[1 + 3\eta\left(\rho_f \gamma d_j\right)^{1/2}\right]^{1/2}} \qquad \textbf{2-4}$$

where λ_{opt} is optimum wave length for jet disruption (m), d_j is jet diameter (m), η is viscosity of fuel (m/s) and γ is liquid fuel surface tension (N/m).

A uniform thread will break down into a series of drops of uniform diameter, each separated by one or more satellite drops. Because of the irregular character of the atomisation process, non-uniform threads are produced, which results in a wide range of drop size. A homogeneous spray can be produced only when the formation and disintegration of threads are controlled.

The complex process of drop formation from a sheet subject to aero dynamic waves has been modelled by Dombrowski, Figure 2.14 [38]. This shows that the waves on the sheet continue to grow until the crests are blown out. The sheet is thus broken up into half wavelengths which rapidly contract into ligaments which in turn break up into drops. The volume of liquid per unit width in a half wavelength of sheet is [38]

$$\lambda_{opt} h^* = \frac{\pi d_l^2}{4} \qquad \textbf{2-5}$$

where d_l is ligament diameter (m) and h^* is half sheet thickness at break up.

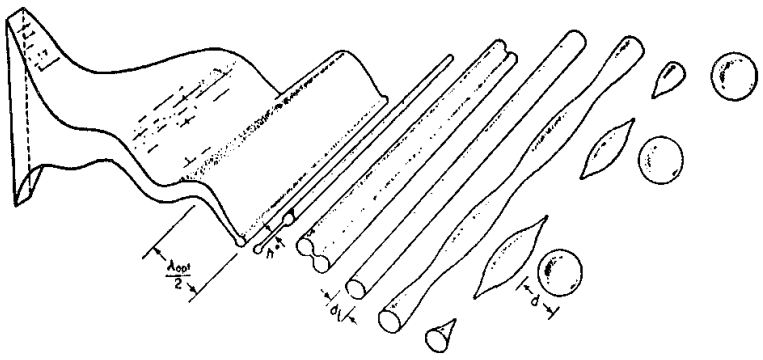

Figure 2.14: Idealised process of drop formation from a liquid sheet. [37]

The initial average drop diameter, d, is proportional to the wavelength of the most unstable surface waves [9].

2.2.4 Fuel injection in diesel engines

Figure 2.15 shows the sequence of the injection process in the diesel engine cycle. FB represents the start of fuel delivery in the injection pump after which the inlet port of the pump has been closed and the required pressure has been reached. The injection process itself will not start until the pressure builds up and reaches the nozzle-opening pressure, which occurs at point SB near a few degrees before TDC. The opening of the needle in the injector has been caused by a propagating pressure wave through the high pressure line. The speed of the pressure waves can be calculated as [8]

$$C^2 = K/\rho_f \qquad \textbf{2-6}$$

where C is the velocity of the wave (ms^{-1}), K is the bulk modulus of the fuel (Pa) and ρ_f is the fuel density ($m^3.kg^{-1}$)

The time required for the pressure wave to travel through the pipe is determined by its speed (speed of sound in diesel fuel, approx. 1,500 m/s) and the length of the high pressure pipe, irrespective of the speed of the engine [39]. This period is commonly known as the injection lag (SV) and includes the period between the start of delivery (FB) and the start of injection (SB). While the piston travels upward toward TDC the compression of the fuel air mixture increases and the ignition starts at VB. The start of injection can be identified using a needle-lift sensor, but the identification of the start of ignition is far more complex. Cylinder pressure measurement is often used to determine the heat release rate of which a change in slope can be used to identify the start of ignition [40]. It is usually in the range of 0.2-2ms ATDC and can be calculated for steady state conditions using Arrhenius type equations [30]:

$$\tau_{id} = C_1 \cdot p_g^{-C_2} \cdot e^{\left(\frac{E_a}{R_{mol} T_g}\right)} \qquad \textbf{2-7}$$

where τ_{id} is the ignition delay time (ms), C_1 and C_2 are constants depending on the fuel and the injection characteristics, p_g is the integrated mean gas pressure during the ignition delay, E_a is the apparent activation energy for the fuel auto-ignition process, R_{mol} is the universal gas constant and T_g is the integrated mean gas temperature during the ignition delay.

For transient conditions this can be written as [41]

$$\tau_{id} = C_1 \cdot p_g^{-C_2} \cdot \Phi^{-C_3} \cdot e^{\left(\frac{E_a}{R_{mol} T_g}\right)} \qquad \textbf{2-8}$$

where Φ is the fuel–air equivalence ratio, which accounts for discrepancies during transients compared with steady-state operation.

The injection process reaches its end (SE) when the nozzle needle closes due to the fall in pressure from the injection pump and combustion will cease (VE). The duration of the injection process, usually around 20^o of crankshaft angle, is generally less than the period required for combustion which is about 40^o-50^o of crankshaft angle [42]. When increasing the engine speed, both the injection lag (SV) and the ignition lag (ZV) will remain constant which requires a timing device to advance the start of fuel delivery in response to the engine's crankshaft speed [7]. A generic representation of the characteristic curves of these three processes (fuel delivery, fuel injection, combustion) is shown in Figure 2.16.

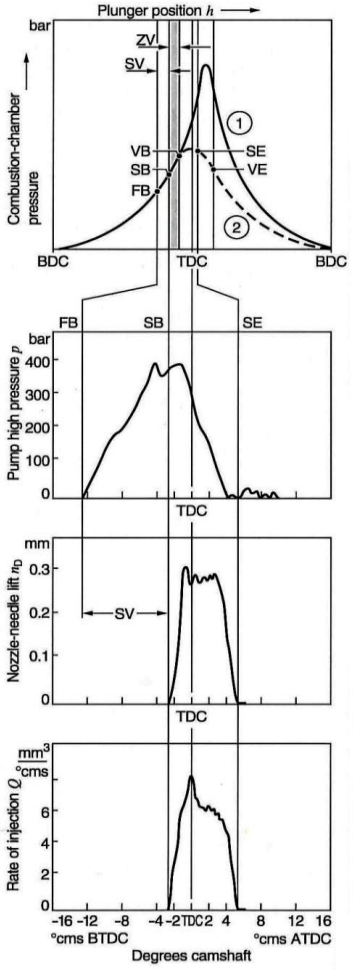

Figure 2.15: Typical injection/combustion in VE pump [7].

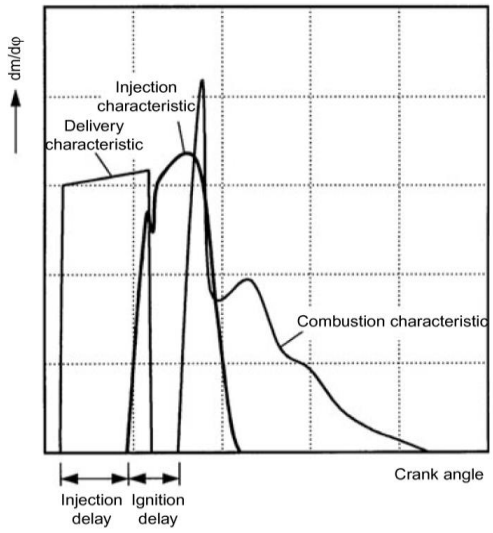

Figure 2.16: Fuel delivery curve, injection and combustion characteristics.[34]

Correct installation of the injection pump and its interconnection with the injectors is very important to ensure good engine performance. The combination of pump and injector must be designed to eliminate dribble at the nozzle and the formation of carbon during the combustion process.

The pressure-flow characteristics in an injection system will vary with the diameter and length of the pipe and the number and diameter of the nozzle holes. From equation 2-2 the flow through the nozzle hole can be written as [8]

$$Q_n = C_n A_n \sqrt{\frac{2(P_1 - P_e)}{\rho_f}} \qquad \textbf{2-9}$$

where Q_n is the fuel flow rate through the nozzle ($m^3.s^{-1}$), A_n is the nozzle flow area per hole (m^2), ρ_f is the fuel density ($m^3.kg^{-1}$) and P_1 and P_e are the nozzle sac and engine back pressures, respectively, (Pa).

As the injection pump starts to deliver the fuel to each injector the pressure P_p builds up as the sudden flow Q_p starts at the pump end, and can be expressed as [8]

$$P_p = \frac{Q_p}{A_p}\sqrt{K.\rho_f} \qquad \textbf{2-10}$$

where P_p is the pipe pressure (Pa), Q_p is the fuel flow rate at the outlet port of the pump ($m^3.s^{-1}$), A_p is the pipe cross-section area (m^2), K is the bulk modulus of the fuel (Pa) and ρ_f is the fuel density ($m^3.kg^{-1}$).

Both equations (**2-9** and **2-10**) can be simplified by substituting 0.7 for the nozzle orifice coefficient, 1482MPa and 825 kg.m^{-3} for the bulk modulus and density of the fuel, respectively, where the flow through nozzle and the flow in the high pressure pipe can can be written as [8] (where Q in mm^3.s^{-1}, A in mm^2 and P in bar)

$$Q_n = 10.899\, A_n \sqrt{(P_1 - P_e)} \qquad \textbf{2-11}$$

$$Q_p = 90.4\, A_p P_p \qquad \textbf{2-12}$$

The conditions for matching the pipe-nozzle area, assuming there is no reflection of the pressure wave at the nozzle, can be described by [8]:

$$Q_p = Q_n \quad \& \quad P_p - P_r = P_1 \qquad \textbf{2-13}$$

where P_r is the residual pressure in the pipes (bar).

The pattern of the complete injection system is modified by compressibility effects in the fuel, and the size and length of the interconnection pipes. Pressure (compression or rarefaction) waves are set up between the pump and the injector, which travel at the speed of sound. The pressure variations caused by these waves can influence the injection pressure, period of injection and even cause secondary injection. Figure 2.17 shows a fuel-line pressure diagram in which there is a pressure wave after the main injection period that is sufficient to open the injector [9]. Another phenomenon, called after-dribble, is the result of pressure waves impeding injector closing leading the injector not to close completely, and some fuel entering the nozzle at very low pressure to form a spray.

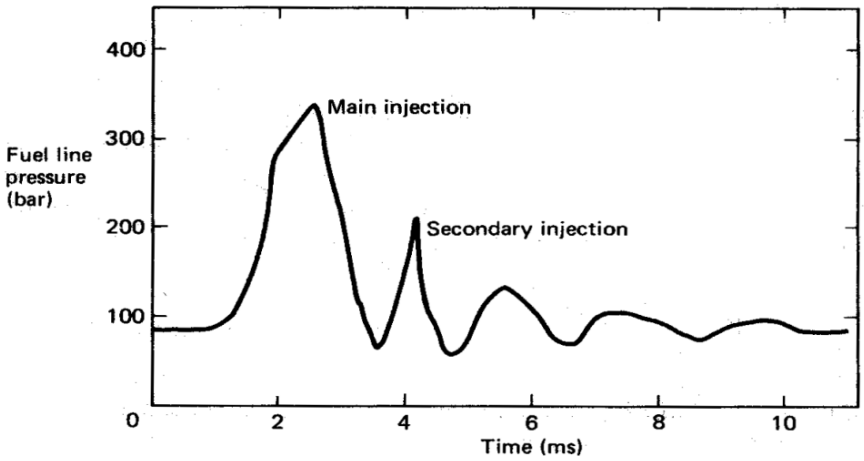

Figure 2.17: Pressure waves in the fuel line from the pump to the injector [9].

The operating conditions of diesel engines need to be described as transients in three different cases:

I. Load change at constant governor setting
II. Throttle position change
III. Cold or hot start

For example, Figure 2.18 shows the change in engine behaviour during the transient period resulting from a change in load [30].

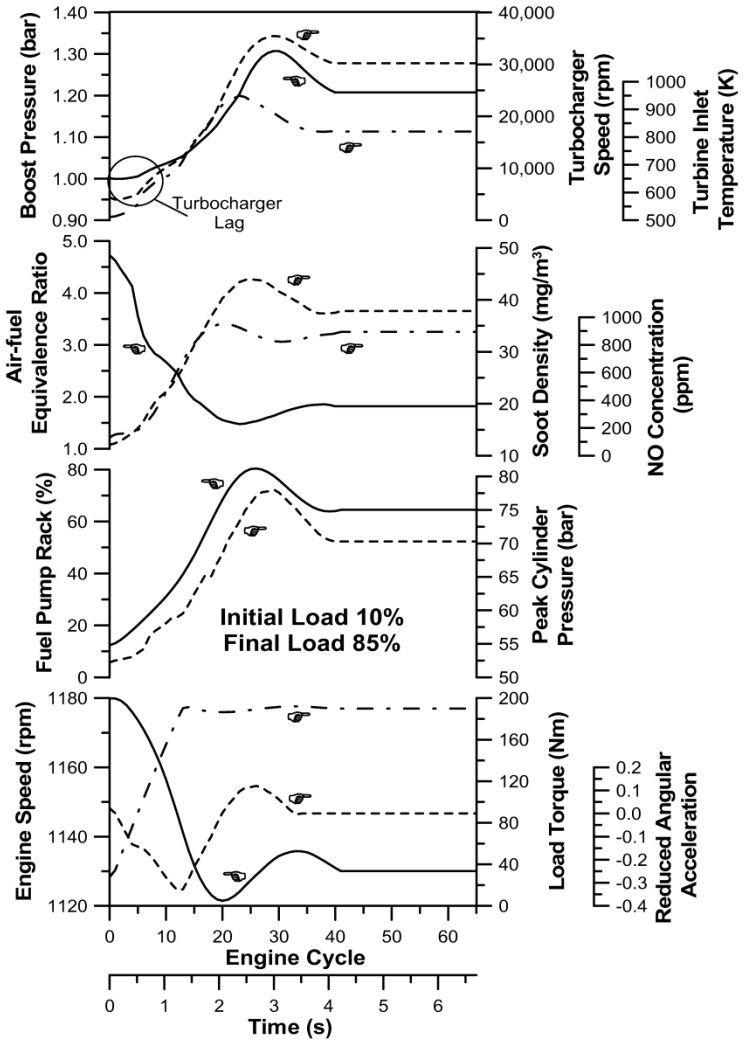

Figure 2.18: Behaviour of a four stroke, turbocharged engine during a load increase transient event.[30]

Transient conditions cause a continuous change of the engine/pump speed due to the transient fluid mechanics of the injection pump and the dynamic response of mechanical components in the injection system. This will affect a number of injection parameters such as rate of injection, line pressure, timing and duration of injection [30]. The dynamic injection timing changes in a linear way with the amount of fuel injected during the fuelling transient period, as shown in Figure 2.19. Also, there is a significant change in the shape of the fuel injection rate during the transient period, in terms of throttling period and start of injection, as shown in Figure 2.20 [43].

Figure 2.21 shows the effect of a throttle change for a VE pump at a speed of 1000 rpm (2000 rpm engine speed). The required fuel quantity is reached within four injection cycles for this pump speed although more cycles would be needed for higher speeds.

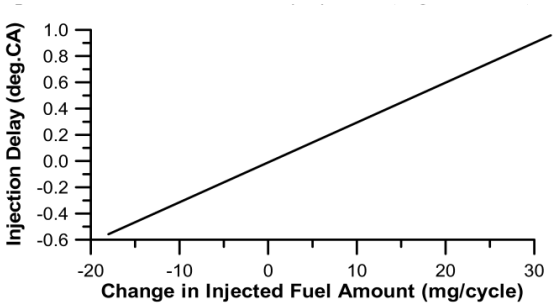

Figure 2.19: Change in the dynamic fuel injection timing due to the deformation of the injection pump driving system, resulting from changes in the amount of injected fuel. [43]

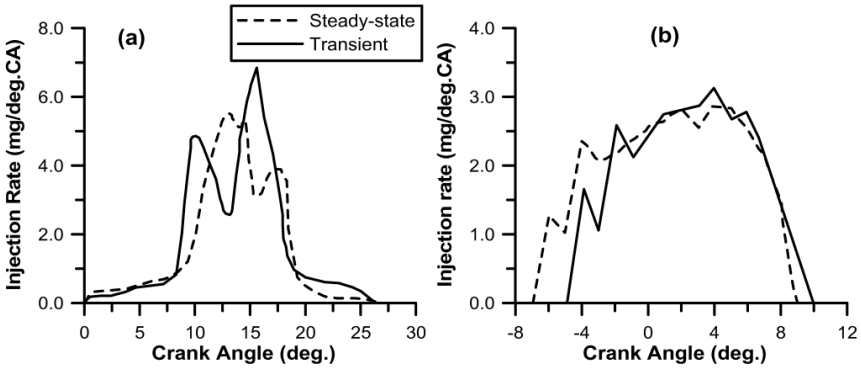

Figure 2.20: Change in the fuel injection rate during an early cycle of a transient event due to throttling compared with the respective steady-state operation, a) naturally aspirated engine, b) turbocharged engine. [43]

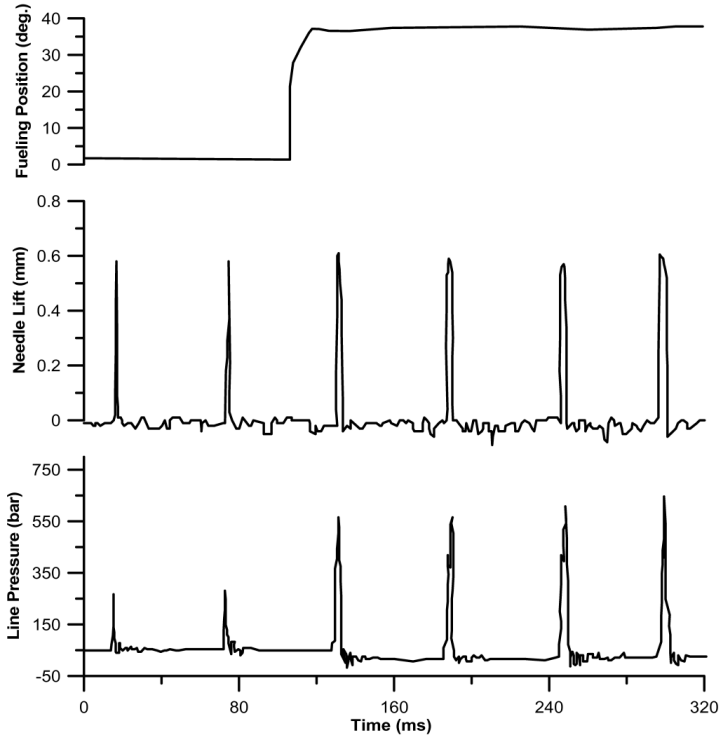

Figure 2.21: Response of speed control position, needle lift and line pressure for a transient fuelling test of a VE injection pump at 1000 rpm. [30]

2.2.5 Cavitation in injectors

Cavitation occurs when the fuel vapour pressure is higher than the local static pressure, which results in the formation of a cloud of vapour bubbles. The temperature of the nozzle tip will be very high, and inside the nozzle holes there will be a region of recirculation in the *vena contracta*, as shown in Figure 2.22. The highly compressed contents of the bubbles will generate instantaneous high pressure which will produce cavitation noise. The generated acoustic pressure can be represented as [44]

$$p_a = \frac{\rho L}{4\pi R}\frac{d^2V}{dt^2} \qquad \textbf{2-14}$$

where p_a is the radiated acoustic pressure, ρ is fuel density, L is the linear distance, R the distance from the cavity center to the point of measurement, V is the volume and t is the time.

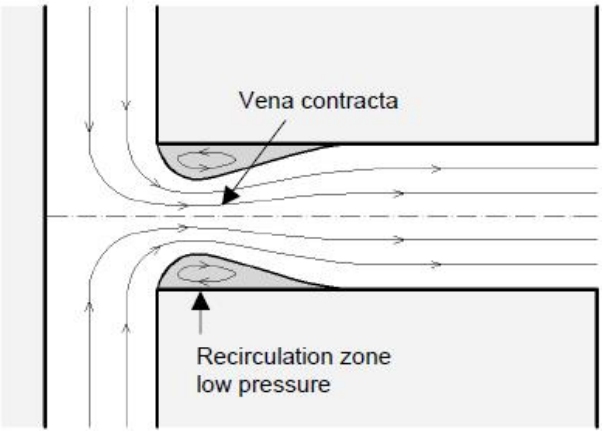

Figure 2.22: Cavitating flow in a nozzle. [45]

The sound level can be represented as the root mean square pressure over the frequency range (f) using the spectral density function $\mathcal{G}(f)$, which allows the acoustic pressure (p_s) to be written as [44]

$$p_s^2 = \overline{p_a^2} = \int_0^\infty \mathcal{G}(f)df \qquad \textbf{2-15}$$

Figure 2.23 shows the spectra of cavitation noise in an orifice for a range cavitation number, σ.

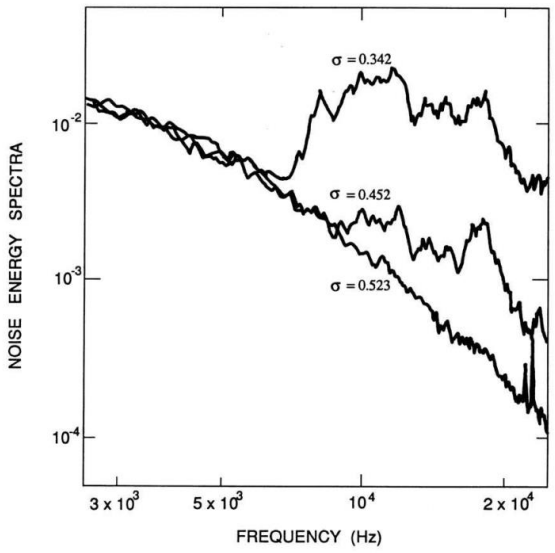

Figure 2.23: Acoustic power spectra from a model spool valve operating under noncavitating (σ = 0.523) and cavitating (σ = 0.452 and 0.342) conditions. [46]

2.3 Pulsatile flow

Flow with periodic variations is commonly known as pulsatile flow, the heart being the best known example of such type of flow. Due to the importance of this organ and its function, there has been much study of pulsatile flow including accurate ways of monitoring its behavior [47-50]. Injectors are nothing like as complex as the heart-vascular system, but nevertheless there are challenges there as well.

The analysis of fluid flow requires knowledge of the characteristics of the fluid (such as compressibility) and the behavior of its motion (such as steady or unsteady flow). For flow of a given fluid in a constrained volume (e.g. a pipe), conservation of mass is a common starting point, which means considering the continuity equation. Also, the momentum of the fluid element has to be considered by using the Navier-Stokes equations.[51]

For a fluid with no variation in the density from point to point (incompressible fluid flow), the continuity equation can be represented as [52] (according to the notation in Figure 2.24)

$$\frac{\partial u}{\partial x} + \frac{\partial v}{\partial r} + \frac{v}{r} + \frac{1}{r}\frac{\partial w}{\partial \theta} = 0 \qquad \textbf{2-16}$$

and the Navier-Stokes equations as [52]

$$\rho\left(\frac{\partial u}{\partial t} + u\,\frac{\partial u}{\partial x} + v\,\frac{\partial u}{\partial r} + \frac{w}{r}\frac{\partial u}{\partial \theta}\right) + \frac{\partial p}{\partial x} = \mu\left(\frac{\partial^2 u}{\partial x^2} + \frac{\partial^2 u}{\partial r^2} + \frac{1}{r}\frac{\partial u}{\partial r} + \frac{1}{r^2}\frac{\partial^2 u}{\partial \theta^2}\right) \qquad \textbf{2-17}$$

$$\rho\left(\frac{\partial v}{\partial t} + u\,\frac{\partial v}{\partial x} + v\,\frac{\partial v}{\partial r} + \frac{w}{r}\frac{\partial v}{\partial \theta} - \frac{w^2}{r}\right) + \frac{\partial p}{\partial r} = \mu\left(\frac{\partial^2 v}{\partial x^2} + \frac{\partial^2 v}{\partial r^2} + \frac{1}{r}\frac{\partial v}{\partial r} - \frac{v}{r^2} + \frac{1}{r^2}\frac{\partial^2 v}{\partial \theta^2} - \frac{2}{r^2}\frac{\partial w}{\partial \theta}\right) \qquad \textbf{2-18}$$

$$\rho\left(\frac{\partial w}{\partial t} + u\,\frac{\partial w}{\partial x} + v\,\frac{\partial w}{\partial r} + \frac{w}{r}\frac{\partial w}{\partial \theta} + \frac{vw}{r}\right) + \frac{1}{r}\frac{\partial p}{\partial \theta} = \mu\left(\frac{\partial^2 w}{\partial x^2} + \frac{\partial^2 w}{\partial r^2} + \frac{1}{r}\frac{\partial w}{\partial r} - \frac{w}{r^2} + \frac{1}{r^2}\frac{\partial^2 w}{\partial \theta^2} + \frac{2}{r^2}\frac{\partial v}{\partial \theta}\right) \qquad \textbf{2-19}$$

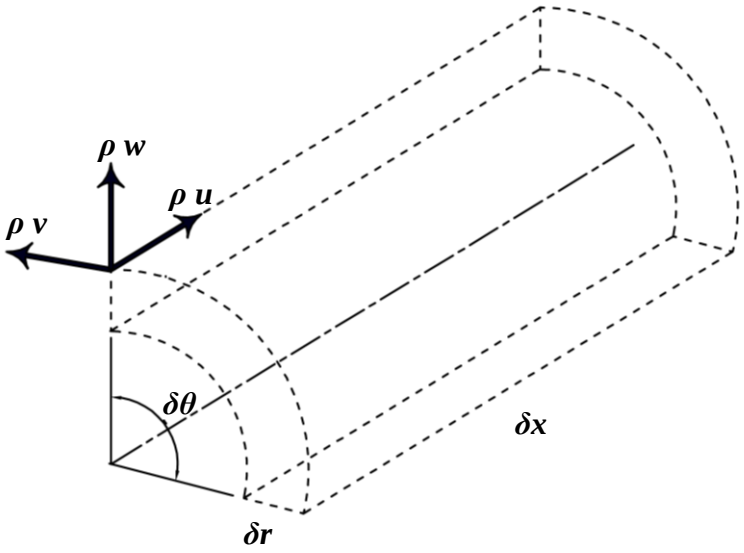

Figure 2.24: Control volume of fluid flow in pipe. [52]

For a straight pipe of circular cross section with no external forces, the continuity and Navier-Stokes equations can be simplified to take advantage of the symmetry about the longitudinal axis of the pipe. Restricting consideration to the fully developed region the governing equation of the fluid flow can be written as [52]

$$\rho \frac{\partial u}{\partial t} + \frac{1}{\rho}\frac{\partial p}{\partial x} = \mu\left(\frac{\partial^2 u}{\partial r^2} + \frac{1}{r}\frac{\partial u}{\partial r}\right) \qquad \textbf{2-20}$$

During the pumping action, the pulsatile flow can be described in terms of two components, steady and oscillatory. Figure 2.25 illustrates the pressure gradient in pulsatile flow, in which $k(t)$ represents the total pressure gradient and k_s and k_φ represent the steady and oscillatory parts, respectively.

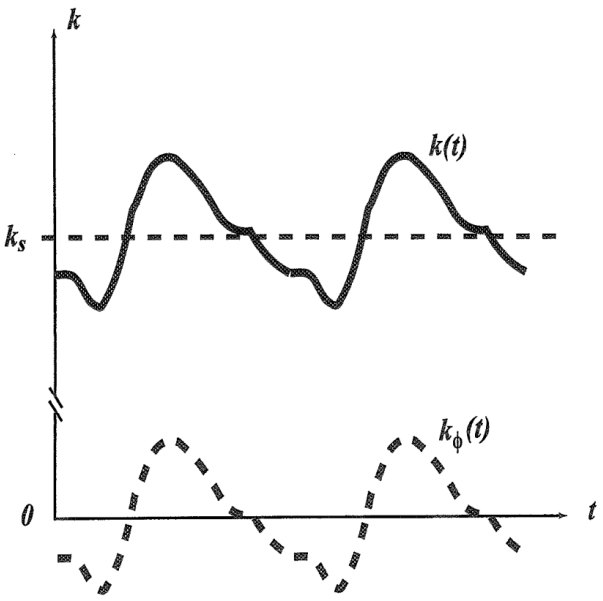

Figure 2.25: Pulsatile pressure gradient. [52]

The steady component can be described as

$$\frac{dp_s}{dx} = \mu\left(\frac{d^2u_s}{dr^2} + \frac{1}{r}\frac{\partial u_s}{\partial r}\right) \qquad \textbf{2-21}$$

while the oscillatory component can be represented as

$$\rho\frac{\partial u_\phi}{\partial t} + \frac{\partial p_\phi}{\partial x} = \mu\left(\frac{\partial^2 u_\phi}{\partial r^2} + \frac{1}{r}\frac{\partial u_\phi}{\partial r}\right) \qquad \textbf{2-22}$$

The fluid (water) hammer is one of the most common phenomena of sound wave propagation in pipelines which occurs due to the sudden closure of valves and also pulsating pumps [53]. There is the possibility that injector lines might display some elements of fluid hammer.

2.4 Acoustic emission testing

Acoustic emission testing (AET) is non destructive testing (NDT) method which is used widely in condition monitoring (CM) and condition based maintenance (CBM). In many applications, the main focus is in counting and locating isolated events, for example due to crack extensions in a structure, for which a “hit-based” system is normally used, with a trigger set to record for a fixed period of time (usually short) when a threshold is exceeded. In the current work, the AE record is continuous with a

number of events which occur in an expected sequence so the types of processing involved are different.

2.4.1 Acoustic emission concepts and characteristics

Acoustic Emission (AE) is the generation and propagation of transient elastic waves due to the rapid release of energy from localised sources within or on the surface of a material [54]. The amount of energy released by an AE and the amplitude of the waveform are related to the magnitude and velocity of the source event. Acoustic emission (AE) testing is based on the detecting and converting these elastic waves into electric signals. AE is a passive condition monitoring technique, in which the energy that is detected is released within the material and can be inspected by using remote sensors.

The frequency range most commonly used for acoustic emission testing is 100 kHz to 300 kHz, since higher frequency waves attenuate faster and lower frequencies are subject to interference from background noise [55]. A short, transient AE signal is produced by a very fast release of elastic energy which propagates in all directions in an approximately spherical shape around the source and is detected by one or more sensors [56] (Figure 2.26). AE sensors can convert the very small surface displacements into electrical signals that can be amplified and processed.

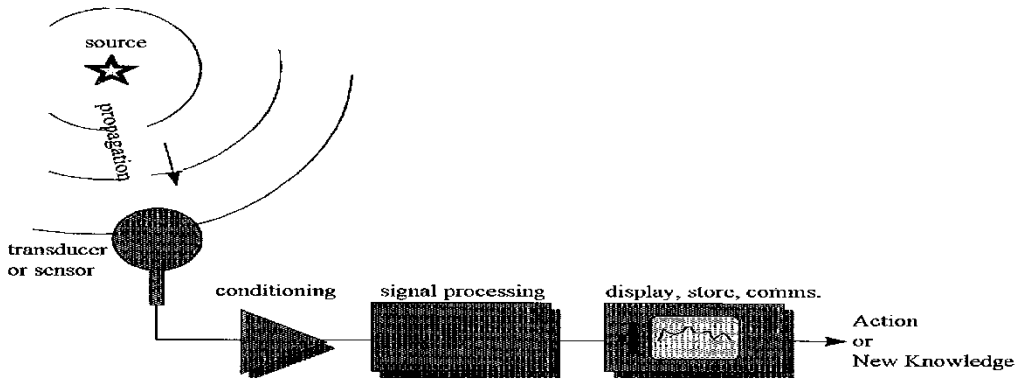

Figure 2.26: The basic principles of AE. [57]

2.4.2 Acoustic emission equipment

The main common components of AE systems are sensors, preamplifiers, filters and amplifiers. Figure 2.27 shows a block diagram of a generic four channel acoustic

emission system. A typical AE system consists of a sensor, amplifier (along with preamplifier), filter, data measurement and storage and display equipment. The generated AE event is captured by the sensor which converts the mechanical activity into an electrical voltage signal. A preamplifier is normally placed close (or integrated) with the sensor in order to boost the voltage and overcome the resistance of the cable. Sensors and preamplifiers are designed to filter the signal from most of the background noise and electromagnetic interference. However, a band-pass filter is used to eliminate further unwanted signals at both low and high frequencies. The generated signals will be interrupted by a measurement circuit in the form of digital pules. Finally, the digital data will be collated using a data acquisition system which is stored and displayed for further analysis.

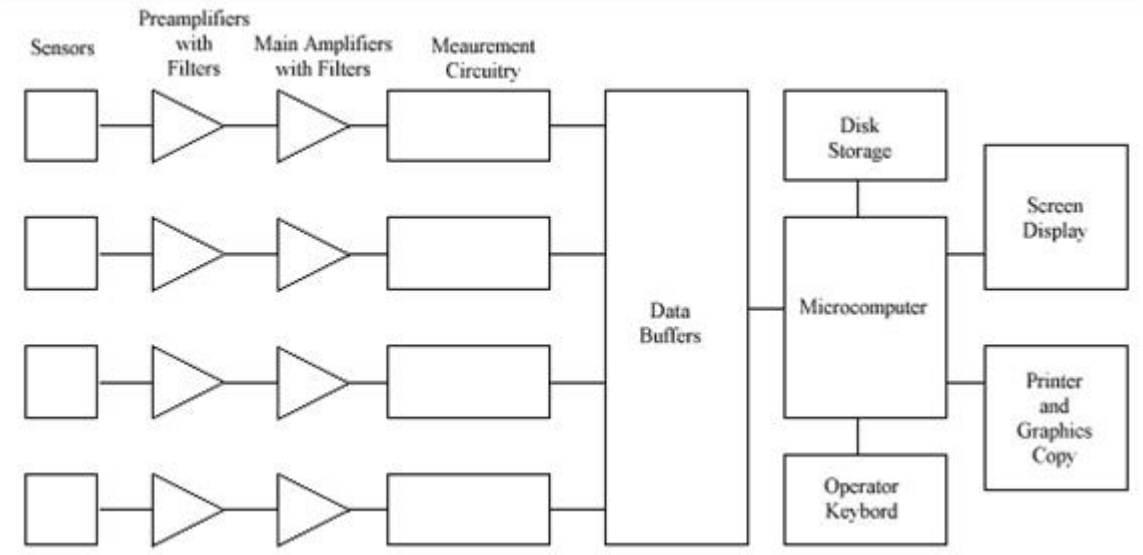

Figure 2.27: Schematic diagram of a basic four channel acoustic emission testing system.[54]

2.4.2.1 Acoustic emission sensors

AE sensors are of critical importance in any experiment, and both wide band and resonant sensors are available. AE sensors generally use a small disc of piezoelectric material as a sensing element, lead zirconium titanate (PZT) being the most commonly used material (Figure 2.28). The main considerations for the selection of sensors are operating frequency, sensitivity, and environmental and physical characteristics. A good acoustic contact between the sensor and the surface is very important in terms of good representation of the AE signal, usually achieved using a coupling agent (such as high vacuum grease).

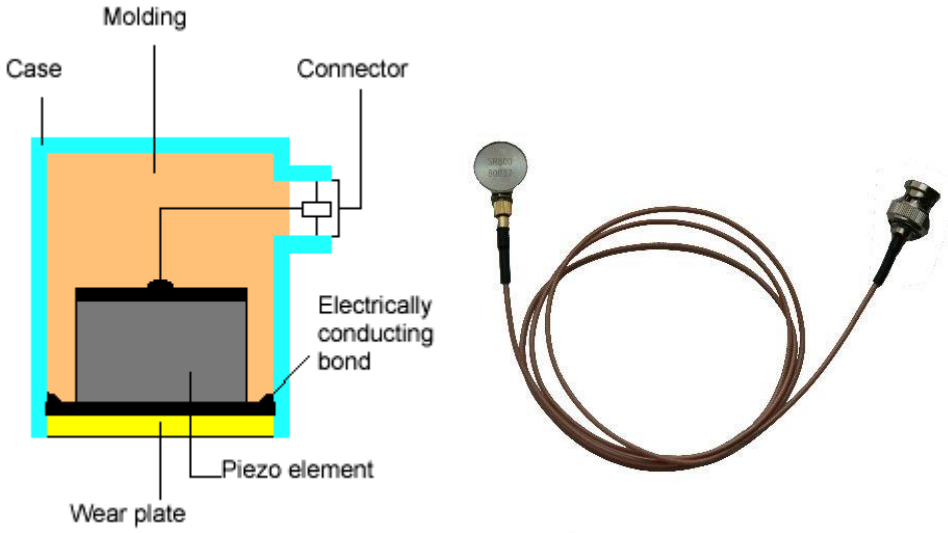

Figure 2.28: AE sensor. [56]

2.4.2.2 Acoustic emission amplifiers

Under most circumstances it is necessary to amplify the sensor signal as the signal from piezoelectric materials are very feeble at high frequency, thus the sensing element itself cannot drive the signals over a long distance of cable. A preamplifier must be placed close to the sensor; also it is very often that it is integrated into the sensor housing. The preamplifier provides required gain, cable drive capability and filtering by which the monitoring frequency for AE can be defined.

2.4.3 Acoustic emission signals

High frequency dynamic signals contain too much information to be interpreted by inspection in real time and some type of signal processing is needed to extract the required information from the gathered signals and minimise the influence of unwanted effects on the signal. The signal waveform is affected by many factors such as; characteristics of the source, the path taken from the source to the sensor, sensor characteristics, and the measuring system [54]. AE signals can be categorised into three main forms; burst activity, continuous activity, and mixed mode activity. Figure 2.29a shows the burst type where the signal has the form of discrete transients which can be presented as an exponentially decaying sinusoid. In continuous activity the signal has a random oscillatory shape normally resulting from the overlapping of multiple indistinguishable bursts, and is often regarded as background noise for hit-based systems (Figure 2.29b). Leaks, flow and many fabrication processes produce non-discrete pulses of acoustic energy, giving a continuous signal that resembles noise [58]. The combination of these two signal types will form the mixed mode signal as shown in

Figure 2.29c. As the acoustic emission burst signal is usually associated with continuous background noise, a threshold detection level is set above the background level. The signals acquired from engines, however, do not necessarily have a fixed background level and have a continuous and a transient component. In this case, special processing techniques are required to ensure that data are not lost by thresholding.

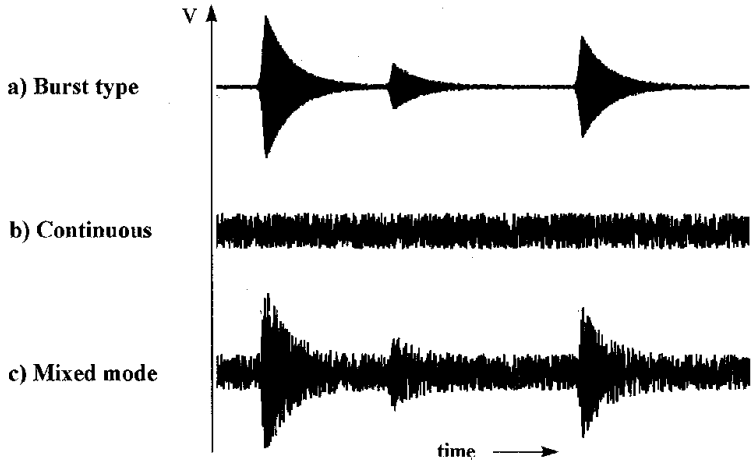

Figure 2.29: Different AE signal types. [57]

For hit-based systems, the AE signal is traditionally characterised by the parameters shown in Figure 2.30; number of events, counts, event energy, signal amplitude, signal duration, and signal rise time. Cumulation of these parameters in such features as total events, amplitude distribution, and accumulated energy can be defined as a function of time or test parameter, as a measure of performance or structural integrity [54].

An idealised AE burst can be represented by:

$$V = V_o\, e^{(-Bt)}\, \sin(\omega t) \qquad \textbf{2-23}$$

where V is the output voltage of the sensor, V_o is the initial signal amplitude, B is the decay constant, t is the time and ω is the angular frequency.

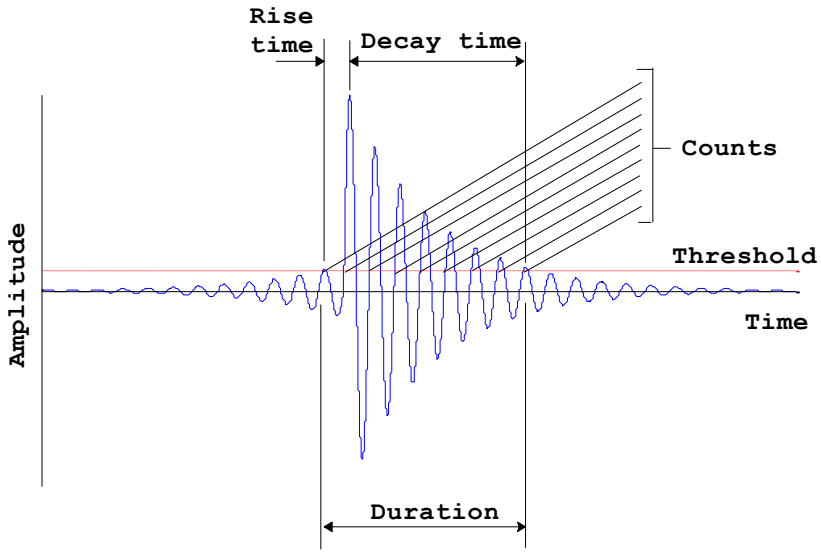

Figure 2.30: AE signal.

For an impulsive event, the peak signal amplitude is related to the AE source intensity and will depend on the attenuation between source and sensor. The burst rise time refers to the time interval between the first threshold crossing and the maximum amplitude of the burst, the duration represents the time interval between the first and last time of the crossing, and these times can be useful in determining the AE energy associated with an event. AE event energy is directly proportional to the area under the acoustic emission waveform, and can be calculated as [54]

$$E = \int_0^{t_{lim}} V^2(t)dt \qquad \textbf{2-24}$$

where E is the acoustic emission energy in V^2.s, $V(t)$ is the amplitude of the AE signal in volts as a function of time t and t_{lim} is the length of the time period of interest in seconds.

The term attenuation is used to describe the reduction in the amplitude of a wave due to natural processes. As an AE wave spreads from its point of origin the most significant initial reduction in amplitude is due to geometrical expansion of the wave front [57], although a number of other attenuation mechanisms are active in complex objects.

2.4.3.1 Wave propagation

The generated AE waves can travel in a number of modes, where wave mode is the term used to describe the propagation of waves which depends on the oscillatory behaviour of the particles and the geometry of the structure.

Sound waves, including AE waves, can propagate in fluids as a secession of compressions and rarefactions of the molecules, known as compressive or longitudinal waves. Longitudinal acoustic waves travel through a single phase fluid with a velocity that depends on the fluid density and compressibility [59]. Also, sound waves can propagate in solids as four main types; longitudinal, surface (Rayleigh), shear (transverse), and plate waves.

Longitudinal waves travel as a succession of compressions and rarefactions in the direction of the wave propagation where their particle density fluctuates as they move, as shown in Figure 2.31. The velocity of longitudinal waves (C_l) does not depend on the frequency and can be calculated by

$$C_l = \sqrt{\frac{E(1-\nu)}{\rho(1+\nu)(1-2\nu)}} \qquad \textbf{2-25}$$

where ν is the Poisson's ratio for the material, ρ is the density of the material (kg/m^3) and E is Young's modulus of elasticity for the material (N/m^2).

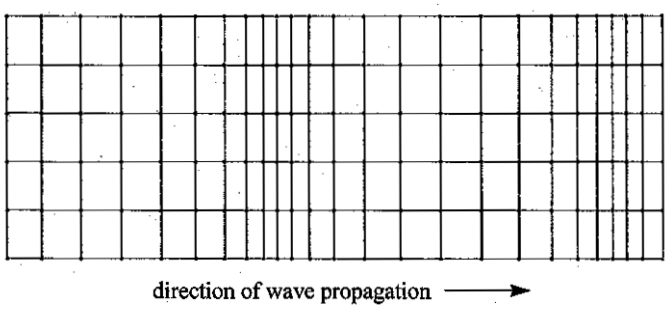

Figure 2.31: Longitudinal wave. [57]

Transverse waves travel as an oscillatory shearing motion between successive planes at a right angle or transverse to the direction of propagation (Figure 2.32). The velocity of shear waves (C_S) is also independent of frequency and given by

$$C_s = \sqrt{\frac{E}{2\rho(1+\nu)}} \qquad \textbf{2-26}$$

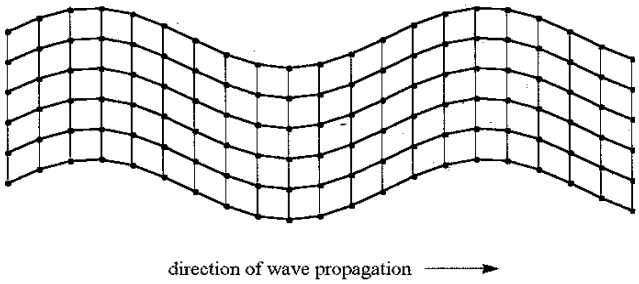

Figure 2.32: Transverse wave. [57]

Elastic waves can also travel along the surface of solid materials as a successive displacement of surface above and below the equilibrium surface position, known as Rayleigh (surface) waves (Figure 2.33). This type of wave has an independent velocity (C_R) which is approximately given by

$$C_R \cong 0.9\, C_s \qquad \textbf{2-27}$$

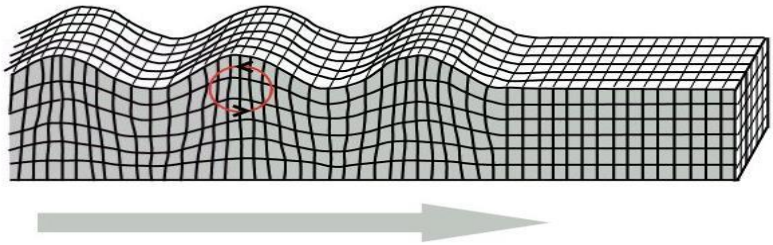

Figure 2.33: Rayleigh wave. [57]

Plate waves can propagate only in very thin materials, and propagation can occur in a series of anti-symmetric modes (where both surfaces simultaneously deflect in the same position), and symmetric modes (where both surfaces simultaneously pinch together). Lamb waves are the most common representation of plate waves that have been used in acoustic emission testing (Figure 2.34). The propagation of Lamb waves depends on the density and elastic material properties of the component and their velocities are very dependent upon both frequency and plate thickness.

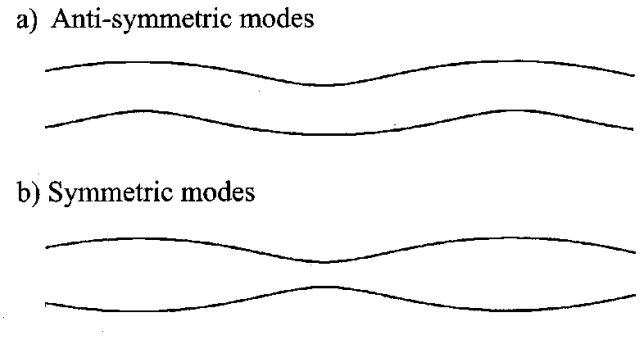

Figure 2.34: Plate waves. [57]

However, waveforms in practical structures are more complicated and any sensor record will probably be a combination of different wave modes, which can make interpretation in objects such as machines rather difficult.

2.4.3.2 Source location techniques

Most of the acoustic emission signals acquired in practice contain unwanted information which can not readily be separated from wanted information on a frequency basis. Thus, signal separation is often achieved on a spatial rather a frequency basis, the signal being identified by its place of origin by using the spatial filtering [60]. Source location techniques assume that AE waves travel at a constant velocity in a material [61]. However, various effects can alter the expected velocity of the AE waves (e.g. reflections and multiple wave modes) and can affect the accuracy of this technique. Therefore, the geometry of the structure being tested and the operating frequency of the AE system must be considered when determining whether a particular source location technique is feasible [61]. The most common source location techniques are linear location, point location, zone isolation, and the order of arrival technique.

In the linear location technique, the distance of the source from the midpoint between two sensors can be calculated by multiplying both the velocity and the arrival time of the wave. This applies to any event where the source is between the sensors, whether the location lies to the right or left of the midpoint and is determined by whichever sensor first records the hit (Figure 2.35).

$$x = \frac{1}{2}[L - c \cdot (t_2 - t_1)] = \frac{1}{2}[L - c \cdot \Delta t] \qquad \textbf{2-28}$$

where x is the distance between first sensor and the AE source, c is the wave speed, L is the distance between the two sensors, t_1 and t_2 are the times of signal arrival at the first and second sensor, respectively, and Δt is the arrival time difference between the two sensors.

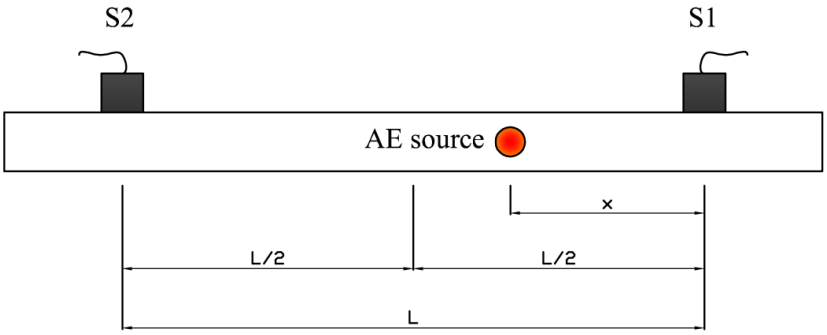

Figure 2.35: Linear location technique.

In the point location technique, the position of the source can be calculated by placing sensors on the structure and determining the sequence from the various sensors and signal time of arrival. The wave fronts from the source can be shown as concentric circles centred on the sensors with intersecting defining hyperbolae [60], as shown in Figure 2.36. The signals must be detected in a minimum number of sensors: two for linear, three for planar, four for volumetric.

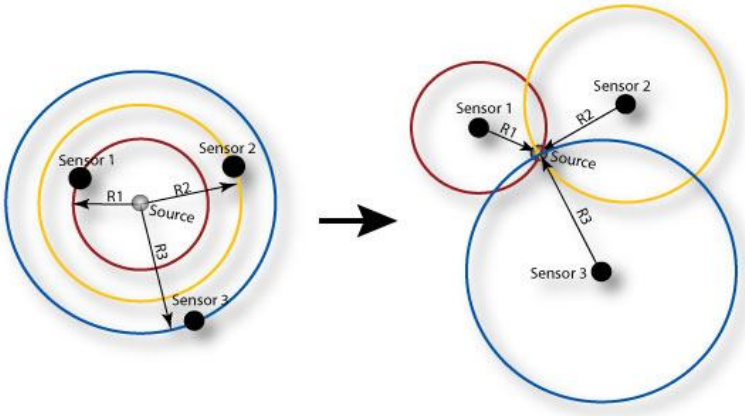

Figure 2.36: Point location technique. [61]

The zone isolation technique is widely used when AE is likely to come from certain well defined regions and aims to trace the waves to a specific zone or region around a sensor (Figure 2.37). Zones are presented as lengths, areas or volumes depending on the

dimensions of the arrangement. This method is used in anisotropic materials or in other structures where sensors are spaced relatively far apart or when high material attenuation affects the quality of signals at multiple sensors [61].

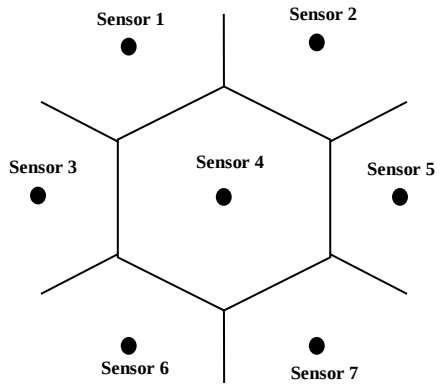

Figure 2.37: Planer zone isolation technique. [61]

The order of arrival of signals is one of the most powerful source location techniques. Figure 2.38 shows the most commonly used array for this technique, a triangular array. The area within the array can be divided into six zones based on orders of arrival; if each zone can be used to encompass a hole then there is no need to make further calculations [60].

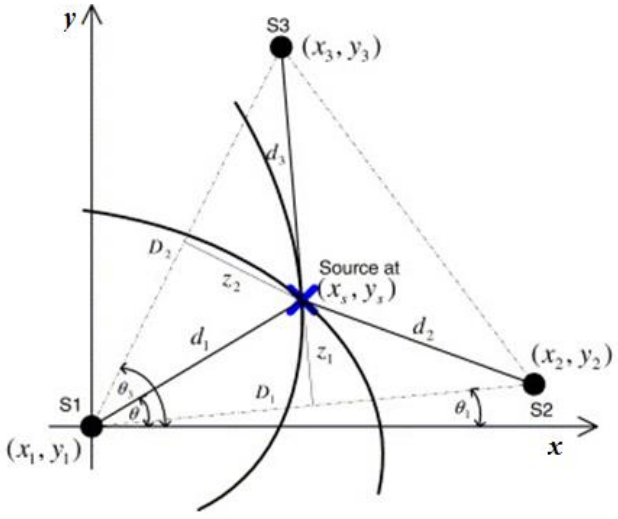

Figure 2.38: Order of arrival technique [62].

Delta T source location has been introduced to identify the AE sources in geometrically complex structures more accurately [63]. Information about source timing and sensor

location are not required in this method, but it relies on constructing an independent user-predefined grid (as shown in Figure 2.39).

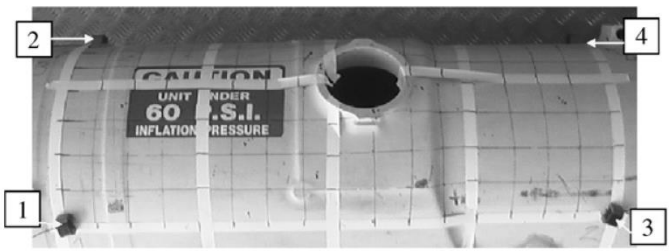

Figure 2.39: Example of the selected grid of an aircraft component [63].

Chapter 3

Literature Review

As mentioned in Chapter 1, the main contributions in this work are in the AE monitoring of diesel engines, specifically in isolating the AE associated with the injection process using a new application of canonical correlation analysis. Accordingly, this review is divided into four parts. First, there is a brief discussion of the science of diesel fuel injection as essential background to the phenomena which may give rise to AE. Next, the various studies on AE monitoring of diesel engines are critically reviewed, followed by a summary of the techniques that have been used to monitor diesel injection, assessing the potential role of AE. Finally, a critical analysis of the various signal processing techniques is carried out to highlight the potential of canonical correlation to solve multi-source, multi-sensor monitoring problems.

3.1 Investigation of diesel engine and injection behaviour

Continuing regulatory pressure on exhaust and noise emission, and the demand for higher performance and lower fuel consumption rates has maintained scientific and technological interest in fuel injection systems and the combustion process in diesel engines [2]. The study of combustion in diesel engines continues to be a very active research topic in which computer simulation and modelling play a vital role, not least in diesel fuel injection using CFD and other modelling approaches [64] (Figure 3.1).

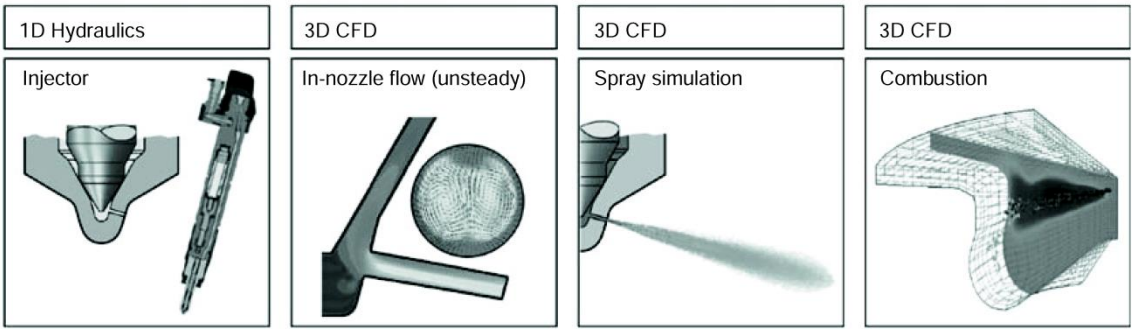

Figure 3.1: Simulation process chain [34].

Many empirical correlations and modelling codes have been developed to simulate the combustion process in diesel engines in order to give better prediction of the engine performance over a wide range of operating conditions [65, 66]. Three main approaches

have been taken to the modelling of combustion in diesel engines. The first method is zero-dimensional simulation (thermodynamic) in which empirical correlation of the combustion process is based on the heat release equations [67, 68]. The phenomenological multi-zone model is the second method, in which the cylinder is divided into two or more zones to study the spatial distribution of the temperature and chemical composition [69-74]. The third method includes the multidimensional computational fluid dynamics (CFD) models which use the conservation equations to simulate the chemical reaction mechanism and fluid flow behaviour for diesel engines [75-77]. As a detailed example, Weißenborn *et al.* [78] developed a simulation-based cylinder pressure approach to monitor diesel engine performance, which focuses on the extension of an empirical, zero-dimensional cylinder pressure model using the engine speed signal in order to detect cylinder-wise variations in combustion. They compared different methods for the model-based reconstruction of the combustion pressure, including nonlinear Kalman filtering and found that the incorporation of an engine speed signal enhanced the accuracy of the empirical cylinder pressure model. In order to minimize system costs and avoid the need for additional sensors, the standard sensor configuration of a series- production vehicle was utilised for engine speed measurement. Elsewhere [79], radial basis function (RBF) networks have been used to develop models of such nonlinear processes as combustion in diesel engines.

Many combustion models include the injection process and spray break up as part of the combustion simulation. However, a large number of models have been formulated to describe the injection process itself, focusing on the identification of its parameters and the associated output performance. For example, Nissan Research Centre have developed a numerical code to simulate, with high accuracy, the fuel injection system in IDI diesel engines [80]. The characteristics of fuel injection rate (as shown in Figure 3.2) were predicted successfully using a lumped parameter model to describe the injection pipe system. Currently, the implementation of simulation models is limited by the computational time required for detailed inputs, such as precise component geometry and the injection system specifications. A number of approaches have therefore been taken to reduce the computational time and minimise amount of input data specifically to reduce the development cost and time in the automotive industry [81]. Partridge and Greeves [82] have reported a computer model for diesel fuel spray formation in which both fuel evaporation and two phase flow were considered, the fuel spray being divided into liquid and gas regions. The liquid jet was assumed to have a

uniform flow with a reduced cross sectional area due to the fuel evaporation. Both the evaporating fuel and the relative shear between the liquid and gaseous phases caused a transfer of momentum from the liquid to the gas phase. The momentum exchange has a direct effect on the flow velocity for both liquid and gas phases, the gas phase accelerating while the liquid phase is decelerated. The model was validated using fuel spray measurements in an engine with optical access and was used to explain the effect of the engine operating conditions and fuel injection parameters on combustion.

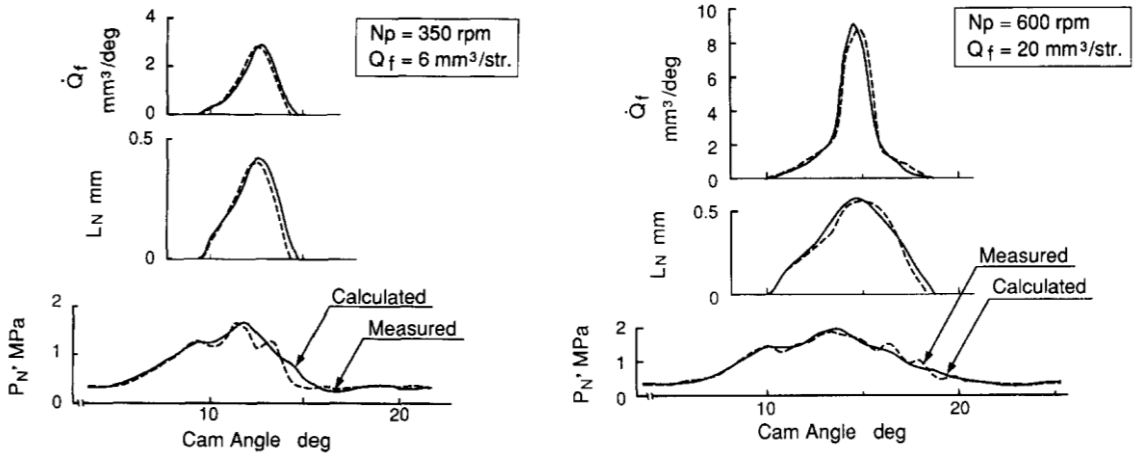

Figure 3.2: Experimental and simulated results of injection parameters from IDI diesel engine (a) idling and (b) at a speed of 600rpm. [80]

Timoney [83] estimated the fuel spray trajectory during the injection period in an attempt to put the design process for DI engines on a more rational basis. The estimation of the fuel spray within the swirling air flow was carried out by using the laws of motion and semi-empirical correlations describing the drag forces on the spray. The relative velocity between the fuel spray and the swirling air was calculated in the tangential direction at the moment that the tip of the spray impinges on the piston bowl. It was shown that the magnitude of the tangential relative velocity can be correlated with the specific fuel consumption and smoke emissions.

There has been extensive work done on the measurement of spray patterns in order to study their effect on engine combustion and performance [84-87]. One example is spray force analysis which provides accurate information on such spray characteristics as efficiency, symmetry, spray breakup and structure [34]. A multi-point pressure sensor is

typically used mounted at different distances from the nozzle where the corresponding detected signals reflect the spray structure (as shown in Figure 3.3).

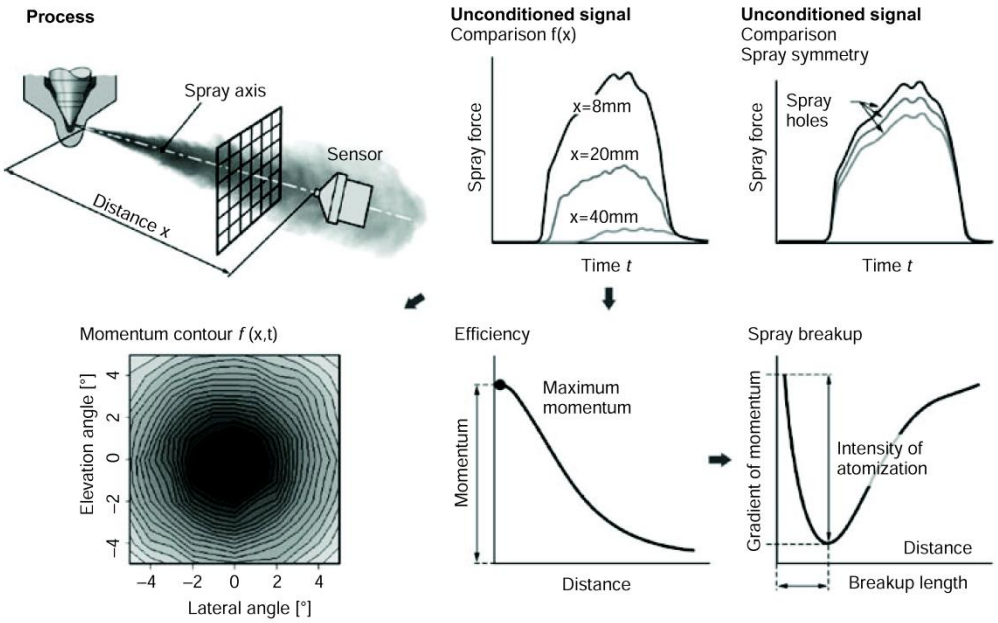

Figure 3.3: Spray force analysis. [34]

3.2 Acoustic emission and diesel engines

Acoustic emission has been widely advocated for the condition monitoring of engines due to its sensitivity to a wide range of mechanical and fluid-mechanical phenomena, often complementary to the sensitivity of vibration measurement [13]. It has been observed that many individual events and processes (such as valve movements, sliding contact and injection and combustion processes) can be detected using AE due to its high spatial and temporal resolution [88], and the additional capability of AE to provide source location information has distinct advantages in separating near-simultaneous events and in providing comparisons between individual cylinders [62]. It has been shown that individual events and processes (such as engine speed, event timing and injection and combustion processes) can be examined and detected successfully using AE. For example, the AE arising from cylinder-liner interactions and from bearings can be distinguished relatively easily from other engine sources by judicial positioning of sensors because, even in small engines, AE is quite poorly transmitted between the cylinder head and the block. The use of AE sensors is non-intrusive and therefore there is no interference with the engine performance or its operating parameters. The AE analysis is a dynamic technique where more sophisticated applications can be operated

on-line while the data analysis can be carried out live for more efficient representation and processing. The complex geometry of the diesel engine blocks and components make it very difficult to interpret the AE signals, however a number of models has been implemented in order to identify the corresponding AE signatures [26, 89, 90].

To get the most out of AE monitoring of engines, it is important to estimate the attenuation and propagation paths from various potential sources to a sensor placed on the surface of the engine. Nivesrangsan *et al.* [91] have used a technique that they call "spatial reconstitution" to reconstruct the time series due to sources at a set of given locations from the synchronous record of AE at a sensor array. Such an approach is useful in solving the multi-source, multi-sensor problem in a complex geometry such as a diesel engine block. They first calibrated the cylinder head of a small four-stroke fuel injection diesel engine using simulated sources at various points on the cylinder head recording the arrival time and relative energy of the same source at each point a nine-sensor array. They then carried out engine running tests focusing the analysis on reconstitution of injector and exhaust valve opening events. They found the attenuation factors for injector events to be similar to those measured from the simulated sources, but those for exhaust valve-opening showed a relatively poor correlation. They attributed this difference to variation in the actual source position during valve opening and also variable transmission though the multiple, moving interfaces in the cam, push rods and rockers.

Even for simple impulsive sources, the propagation of AE in complex structures is not possible to solve analytically. One approach is to simulate the propagation using numerical analysis, but this can become challenging for something like an engine with multiple interfaces and different possible paths. A technique pioneered by Lim *et al.* [92] uses a ray firing procedure to model the transmission of rays both across the surface and through the interior of a complex solid. The approach considers the attenuation to be related to the AE path length and uses a virtual sensor to collect all rays arriving within a given extinction time, cumulating the energy arriving from each ray, modified according to its path length and number of reflections. The results of the computational simulation gave good agreement with measurements made on a cylinder block and various other simple cast iron objects.

Robertson *et al*. have demonstrated ways of identifying sources of AE in the liners of large (10MW) diesel engine cylinder liners [93] . They carried out a set of experiments using simulated sources on a cylinder liner of around 600mm bore to characterise the signal propagation to chosen locations on the liner surface. Figure 3.4 shows the results of this study and confirms the expected result that sensitivity to circumferential position is greater when the source to sensor axial distance is shorter. It also illustrates that larger circumferential displacements result in smaller arrival time differences in an axial array. A technique for source identification on the cylinder liner based on wave arrival time was developed and applied to running engines also using knowledge about the timing and duration of the mechanical events which occur during normal running. To enable subsequent identification of events without knowledge of the Top Dead Centre (TDC) location, a consistent event within the cycle needs to be identified. For this application (large engines) such events are most likely to arise from direct mechanical cylinder-liner interactions such as the piston rings passing the scavenging ports, as other major events such as injection and the opening and closing of exhaust valves could be independently controlled on some engines and are not therefore reliable indicators of engine crank angle position. In this way, AE events associated with an oil groove and scavenging port (Figure 3.5) were identified automatically on an in-service power generation engine.

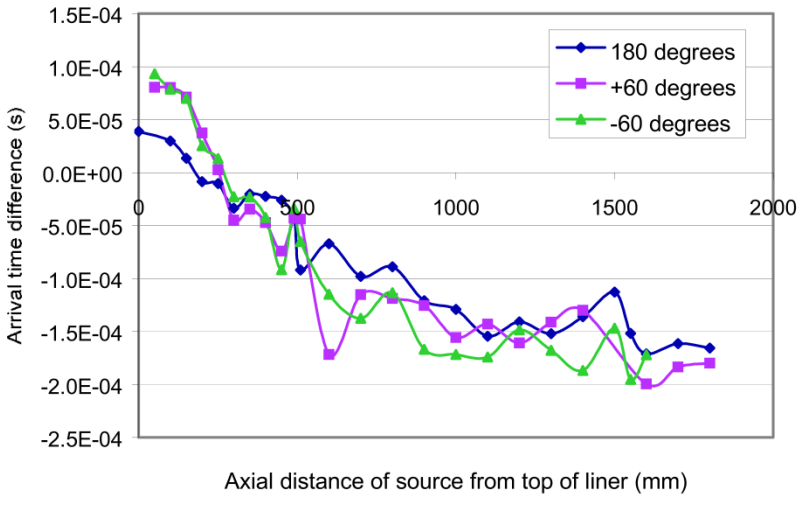

Figure 3.4: Effect of circumferential and axial position on arrival time of a simulated source on a large bore cylinder liner (from Robertson *et al.* [93])

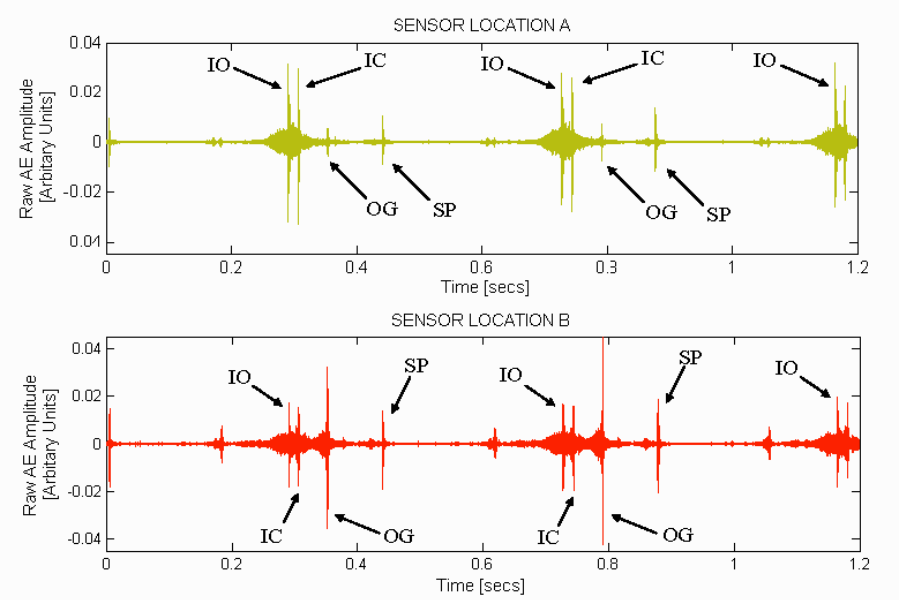

Figure 3.5: Raw AE signals from the running engine at two sensor locations A and B showing the main events. (from Robertson et al. [93])

Gill *et al*. [22] have demonstrated that AE can be used to detect the diesel engine faults in two different four stroke, high speed diesel engines. Data were acquired with the engine running in a reference condition with a single sensor at various positions. It was demonstrated that misfire and irregularities in fuel supply could be detected using a single sensor provided that the attenuation was well known for the reference conditions.

Pontoppidan and Douglas [15] have taken the identification of events in diesel engines a stage further using a signal processing technique called "warping". In this approach, knowledge of engine events is used to reconfigure data acquired under one operational condition into a format resembling another known operating condition. They claimed that the approach enables condition monitoring across known condition changes and thus enables non-stationary condition monitoring. Using data from a large electronically controlled 2-stroke marine diesel engine running under simulated marine conditions (different load settings on the propeller curve) they were able to align acoustic emission signals observed under different load settings. Using the method on data from the fuel injection period (where the largest deviations in timing occurred) they were able to use an already-developed component analysis framework for non-stationary monitoring of condition changes [94]. They also pointed out that the warp framework could also be used for alignment across cylinders and engines. As well as event analysis, AE has proven useful for assessing faults in the flow across valves (valve leakage) in a number of industrial areas, including in diesel engines [95-97].

El Amin *et al.* [98] have systematically investigated the suitability of AE for the condition monitoring of diesel engine valve faults. The clearance on one exhaust valve was varied between normal and excessive (fault) in a Ford FSD 425 four-cylinder, four-stroke, in-line OHV, direct injection diesel engine was successfully detected and diagnosed from the recorded AE signals. In the course of this work El Amin *et al.* expressed the opinion that valve events (exhaust valve opening), mechanical impacts, and gas flow over the valve face are the main sources of AE in diesel engines.

El-Ghamry *et al.* [24] have presented a generic technique for on-line automatic monitoring of reciprocating machines using AE. Cyclic data from three types of reciprocating machines, ranging from a small diesel engine to a large in-service hyper-compressor, under normal operation and with various fault conditions were used for the study. An algorithm was developed to isolate automatically those parts of the signal related to specific mechanical events, identified where the RMS AE was locally elevated. The signals were then subdivided to quantify and identify the events, giving a particular feature vector, which could then be compared with a predefined class of normal and fault features.

In an intensively practical study, Frances *et al*. [99] have studied the variability of the AE signals from a set of medium sized marine diesel engines in service in ferry boats. The AE signals were acquired from four separate engines, working in pairs on each boat, during a variety of operating conditions from different positions on the individual cylinder heads, cylinder blocks and sumps while a high resolution shaft encoder was used throughout testing. The sensor position on the cylinder head exhaust port during the combustion and exhaust windows was selected for particular quantitative study. With reference to the maintenance records for the engines, it was shown that AE signals can be correlated to distinguish between engine conditions in the face of different operating conditions and between different engines.

Gu *et al.* have carried out a intensive study of the capacity of acoustic (i.e. sound) measurements in condition monitoring of diesel engines [11, 12]. First, they modelled the sound generation of a diesel engine based upon the combustion process, and used time-frequency analysis to reveal the expected underlying characteristics of the sound waves. For example, the frequency bandwidth of the sound was significantly widened around the TDC positions, with the energy concentrated predominantly at the firing

frequency and its harmonics and their model predicted an increase in sound level with increasing engine load and speed. To cope with the contamination of real acoustic data from a test bay, they used a smoothed pseudo-Wigner-Ville distribution and continuous wavelet transform (CWT). After a series of conditioning procedures on the noise contaminated signals, they demonstrated that a number of real faults, could be identified and distinguished from the shape of the contours in the CWT.

3.3 Condition monitoring of diesel injection

The monitoring of injectors poses particular problems because it is difficult to isolate experimentally the mechanisms which generate the AE. On the one hand, there are complex fluid-mechanical events occurring during the injection of fuel into the engine, including turbulent flow and cavitation [100], both of which phenomena are known to generate AE [101, 102]. On the other hand, the opening of the injectors involves an interaction between the injector pump (or rail) and the various mechanical parts of the needle lift mechanism, leading to some temporal structure on a millisecond timescale. Added to this, the injectors are, in many cases, driven by the engine and so there is a coupling between engine running and injection, not to mention the fact that timing and volume of injection also affect the combustion process.

As an example of the coupling between injection and combustion, El Ghamry *et al.* [89] have developed a method of reconstructing cylinder pressure using AE measurements alone. Guided by synchronous measurements of AE, injector needle lift and in-cylinder pressure, they developed an algorithm based on separating the pressure rise and fall parts of the curve utilising the complex cepstrum of the AE. The refined method was found to transfer well to a large two-stroke marine diesel in the absence of needle lift measurements. It should be emphasised that, whilst effective, this method did not attempt to diagnose the source of the AE and was not, in this sense, a fault-monitoring technique. Gu *et al.* [103] have carried out a similar study, this time using instantaneous crankshaft angular velocity, recorded synchronously with pressure, to develop a radial basis function network to reconstruct the pressures in each of the cylinders of a small diesel truck engine. They claimed some success in detecting a slight fault in one of the cylinders using this technique. Barelli *et al.* [104] have also proposed a methodology for obtaining internal indicated mean effective pressure in internal combustion engines

using external acoustic and vibration measurements, Vibration and acoustic indexes were introduced to estimate the combustion quality, against reference values.

Both intrusive and non intrusive methods have been developed to monitor fuel injection parameters in diesel engines. Marcic [105, 106] has assessed fuel injection rate by measuring the electric charge generated in the injection nozzle due to fuel friction in the nozzle (Figure 3.6) arising from fuel droplets passing the electrode at velocities of 100–300 m/s. Marcic has also devised a method of measuring the injection rate from each hole in multi hole injectors [107] to address one the common problem of irregular thermal load distribution in combustion chamber due to variations in injection rate from each hole. The method relies on measuring the deformation of a membrane at which the fuel jet is directed and obviously can only be deployed as a quality control method with the injector dismounted from the engine.

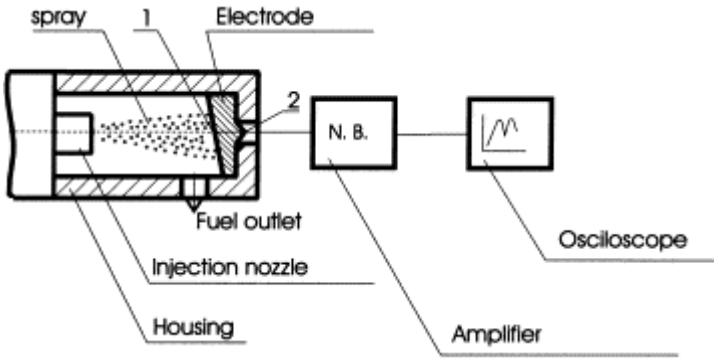

Figure 3.6: Sensor of charge measuring method. [105]

Carlucci *et al.* have investigated the relationship between injection parameters (timing, fuel quantity and mean injection pressure) and cylinder block vibration [108]. They placed two accelerometers in two different zones of the engine block, defining a characteristic ‘‘signature’’ for each parameter. A complete three factor experimental plan, varying the injection parameters was carried out and signatures were derived using conventional Fourier analysis and time–frequency analysis, significant frequency bands of vibration and pressure being correlated with the parameters. They found that injection pressure and injected quantity affected the vibration signals in a specific way; injection timing affected the engine block vibration in a less evident way, but a characteristic signature was also defined for this factor. They also were able to recognise piston slap using time frequency analysis of the vibration.

Gu and Ball [109] developed a dynamic model for the needle motion of a common hole-type, single stage diesel fuel injector. A two-mass dynamic model was used, including the contact stiffness and material and fluid damping. The model was verified by estimating the opening and closing needle impacts, which successfully correlated with the corresponding injection parameters, including injection pressure, fuelling rate and timing. They also predicted that that the opening needle impact would have higher frequency and lower amplitude than for the closing impact, while the amplitude for both opening and closing impacts would increase with an increase in the fuelling rate. In a later paper, the same authors compared the model predictions with vibration data recorded on an injector [110]. They found that the vibration signals corresponded to the flow of high pressure fuel inside the injector and the needle hitting its backstop and seat (Figure 3.7) and that there is a linear relationship between the fuel supply line pressure and the corresponding injector vibration amplitude. On this basis, they suggested that the vibration based approach could provide a powerful alternative to the conventional technique based on measuring the fuel line pressure and the needle lift (as shown in Figure 3.8).

Albarbar *et al.* [18] used airborne acoustic analysis to monitor the injection process, using a Wigner-Ville transform to generate features. Using Independent Component Analysis, they were able to recover the injector signal from the noise associated with combustion and mechanical excitation.

Elamin *et al.* [111] have investigated the use of AE to identify a series of seeded injector faults in a 72kW four-stroke HSDI engine, concluding that both time- and frequency-domain features were required. They also suggested that, for their particular engine and sensor positions, the strongest AE signals were generated by the opening of the inlet valves and that injector faults were reflected in the inlet valve transient.

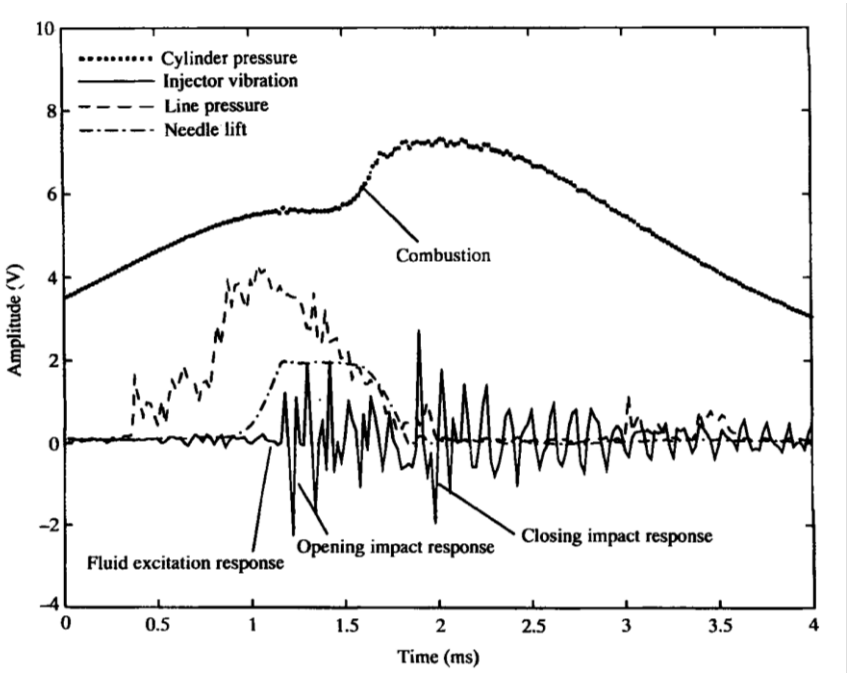

Figure 3.7: Injector vibration versus cylinder pressure, line pressure and needle lift. [110]

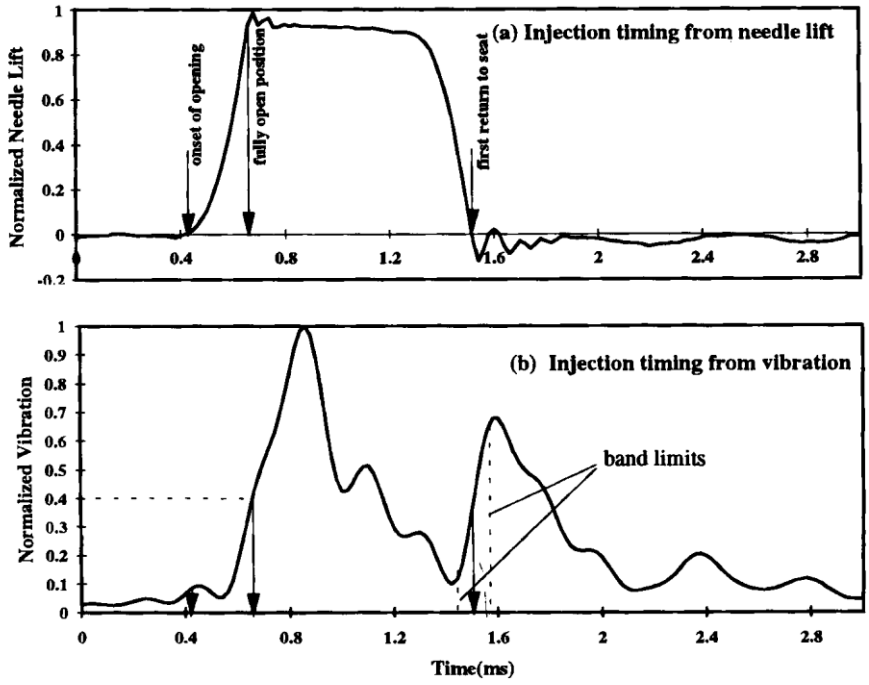

Figure 3.8: Fuel injection timing as revealed by needle lift and fuel line pressure [110]

Brown *et al.* [112] have studied the benefit of using AE piezopolymer sensor with a fast temporal response for a diesel fuel injector. It has been shown that the use of this sensor can reveal more detailed structures within the time signal and also can identify multiple acoustic emission events which correlate with mechanical movements and other sources. The spectra for two different fluid mechanical conditions were compared where

those from the piezopolymer sensor contained a wider range of features that could be used to identify the source of the AE.

AE can potentially provide a better representation of the signal generated from the injection process than some of the other methods described above due to its higher frequency response than for vibration measurement making it less prone to unwanted signal from whole-body vibrations. More fundamentally, there is the potential that AE can detect the actual flow of fuel through the injector as opposed to the result (after combustion) as is more likely with sound or vibration monitoring. Also, the structural transmission paths for AE are more selective and, probably, more reliable in terms of propagation speed offering better noise rejection than airborne sound and the ability to use source location techniques with multiple sensors to further enhance sensitivity. Amongst the first attempts to use AE to monitor diesel injection was by Gill *et al.* [20]. They carried out a series of tests with varying injector settings on a high speed, four-cylinder direct injection diesel engine (HSDI) recording AE and vibration during the injection and combustion processes. They found that the injector discharge pressure can be effectively described by using AE and, by correlating with a needle lift sensor, that both the point of increase in fuel pressure and the opening of injector nozzle could be detected. Generally, they also found that AE offered a better representation of the injection process than did vibration measurement, because the high frequency response of the AE sensor eliminates the problems associated with engine resonances and low frequency vibration caused by background noise.

Douglas *et al.* [21] have investigated the AE signal generated during the injection process of two different types of diesel engine. They studied the AE signature from large marine diesel engine with a two-stage spring type injector and a small high speed direct injection diesel engine with a one-stage injector. They found the AE signal to be sensitive to the mechanical movements of the components of the injectors as well as the fuel flow, including pressure build-up before needle opening, the full opening of the needle, fuel delivery, needle closing impact, and fuel excitation after closing the needle. Figure 3.9 shows the RMS AE signal during the injection process from the two-stage injector in the large engine. The event labelled A corresponds to the pressure build-up in the injector, while events B and C are associated with needle opening and closing impacts, respectively. The event D was assumed to be the result of back pressure fluctuation in the fuel line after needle closing. A change in the engine load, as shown in

Figure 3.10, was found to affect the location of event C significantly. Figure 3.11 shows the raw AE signal as an angle-frequency plot during the injection period from the single-stage injector, again with a number of events labelled. As for the two-stage injector, the first event represents the build-up of pressure before needle opening, while both the second and third events are related to the opening and closing impacts, respectively. Again, it was thought that the fourth event could be the back pressure fluctuation in the fuel line after needle closing. There is a clear mix of low and high frequency (with distinct band switch) associated with the four events. Also, the contour plot in Figure 3.11 shows the distribution of the frequency spectral content, in which it can be seen that high frequency spectral content is associated with the lead-up to events 1 to 4 tentatively identified as fluid flow and low frequency spectral content was associated with impact type events.

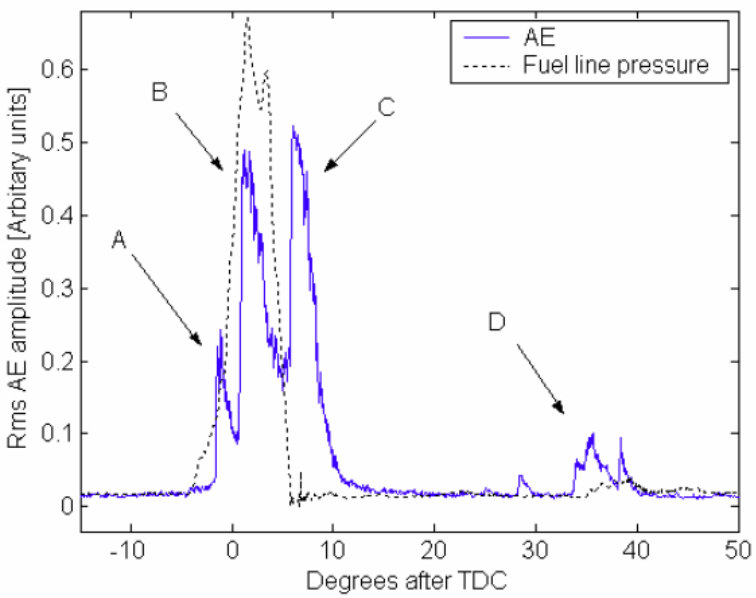

Figure 3.9: Plot of RMS AE signal and fuel line pressure versus crank angle at 25% of full load from 6MW diesel engine. [21]

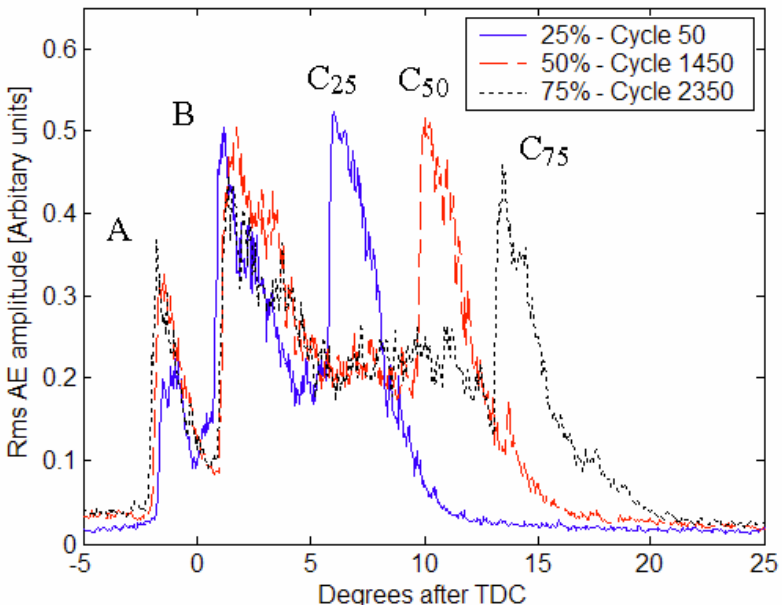

Figure 3.10: Plot of RMS AE signal for injector events at different engine loads.[21]

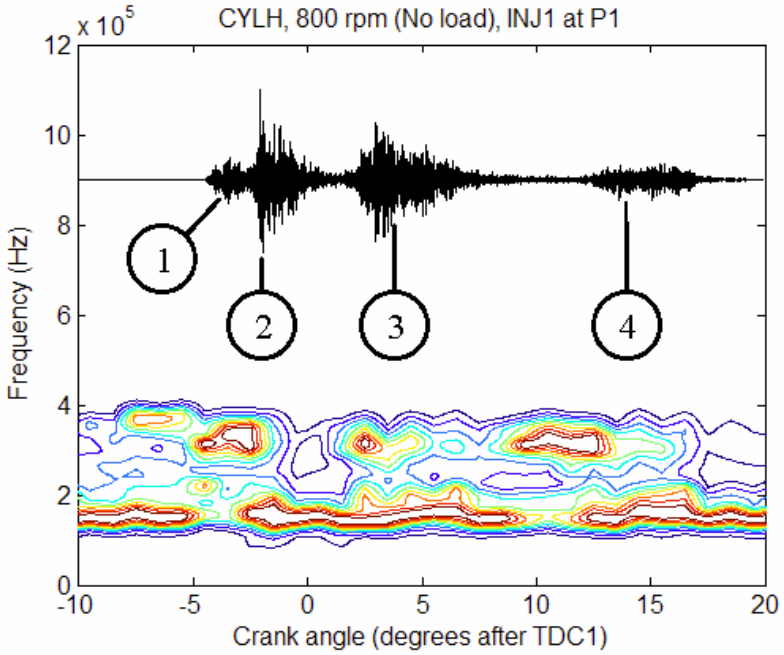

Figure 3.11: Contour plot of crank angle against measured raw AE signal and frequency.[21]

3.4 Signal processing algorithms in condition monitoring

As mentioned in the foregoing sections, it is almost inevitable that some type of signal processing needs to be done when converting a sensor signal to a monitoring indicator. In the simplest case, the measurement is more-or-less direct, such as is the case for in-cylinder pressure measurement, which has historically been used for off-line

combustion diagnosis, although online application for real-time combustion control has become of great interest. Diesel engine combustion can be examined by analysing the instantaneous variation of the chamber pressure, directly obtained using a conventional piezoelectric sensor [113]. Such methods are based on the detection of sudden changes in the chamber pressure (caused thermodynamic phenomena within the cylinder) which can be amplified by differentiating the pressure time series. Conventional signal analysis tools both in time and in time-frequency domains can be used for detecting the start of combustion, the end of combustion and the heat release peak. In less direct measurements (such as acceleration or AE monitoring) some kind of correlation is required between the measured and the monitoring target.

Independent component analysis (ICA) and principal component analysis (PCA) are both widely used in machinery condition monitoring [114-116], ICA to separate individual sources in multi-sensor signals and PCA to stratify the main sources of variation in a given signal. Pontopiddan and Larssen have presented a new method for unsupervised change detection in large diesel engines, which combines independent component modelling and probabilistic outlier detection [117] The method was successfully applied to condition change detection in a large marine diesel engines using the AE signal and compared favourably to more conventional techniques based on PCA and Gaussian mixture models. Pontoppidan *et al.* [118] also used ICA with automated grouping to pick up the increased friction between piston and liner associated with different operating conditions in the same large diesel engine.

A slightly different, and novel, application of ICA in monitoring combustion in a common rail diesel engine is offered by by Bizon *et al.* [119] applied to 2D images of combustion-related luminosity. The images were acquired from an optically accessible diesel engine and the raw data, from a sequence of crank-angle resolved images, were treated by ICA in order to identify leading independent structures. Two main independent components (IC) were extracted from sets of luminosity images, and their coefficients used to study the transient during a single cycle, and for the assessment of cycle variability. Data on dynamic in-cylinder pressure, rate of heat release and integral luminosity were used to aid the analysis. Within a cycle, the two independent components were found to be related to combustion events near the fuel jets and near the bowl walls, respectively. The analysis over a number of cycles allowed a separation of the mean combustion luminosity field from the random, erratic flame structures

which are responsible for cyclic variability. The statistics of the two independent components indicated lower variability of the jet flames and higher variability of combustion near the chamber walls, in agreement with the idea that impingement of fuel sprays onto the piston bowl walls in HSDI engines is responsible for an increase in unburned hydrocarbons and smoke emissions.

Badawi *et al.* [120] have applied ICA to the record of a single accelerometer mounted on the surface of a single cylinder diesel engine. They recognised that forces contributing to engine vibration arise from: exhaust valve closure, inlet valve closure, fuel injection, combustion, piston slap, exhaust valve opening and inlet valve opening and simulated the expected vibration time series in a cycle. The simulated and measured vibration series were separated by ICA using time-frequency analysis and filtering of segmented parts of the original signal. The events mentioned above could all be identified from the measured signal as well as from the simulated one, indicating that the engine was behaving as expected by the model and by the specification.

Zheng and Leung [121] developed an analysis procedure for processing the sound signals from internal combustion engines using the time frequency distribution. The sound source for a diesel fuel injector was identified and abnormal conditions were detected in the time-frequency distribution of the sound signal. The beginning and ending times of the injection were also successfully determined from the time-frequency distribution of the sound signal, which was found to be capable of identifying even very weak events by localising the signal analysis.

Another way of focusing on relevant parts of a signal is by adaptive filtering, as advocated by Albarbar *et al.* [19]. These authors recorded the sound emitted from a diesel injector operating with a range of injector pressures using a condenser microphone. The bandpass filtered microphone signal was subjected to time-frequency analysis (using a Wigner-Ville transform) and the relevant frequency bands for needle opening and closing impacts identified. Filtering of the relevant windows of the time series was found to give a much clearer indication of injector pressure than could be determined from the unfiltered signals. A similar approach was advocated by Pruvost *et al.* [122] for separating the sound associated with combustion from more general mechanical noise in diesel engines, the motivation being to isolate the combustion noise. They found that, because the sources are correlated and overlap in both the time

and frequency domains, the best way to separate them was to use only the random part of the signal, on the basis that the mechanical noise is associated with engine and other cyclic sources whereas diesel combustion in particular can be quite irregular. They therefore developed a spectrofilter to remove the periodic parts of the signal allowing the analysis to be concentrated on the remaining (random) part.

Wavelet analysis has been shown to be a powerful tool in signal decomposition and component analysis [123] and a number of authors have applied it to acoustic emission signals for medical and structural applications, either to segment components of the signal [124] or to separate propagations modes in large structures [125, 126]. Peng and Chu [127] have produced a comprehensive review on the use of the wavelet transform in machinery condition monitoring. Ranachowski and Bejger have used the wavelet transform to analyse acceleration signals recorded from a six-cylinder diesel engine with sensors placed on each of the injector and pump outlet ports [128]. They found, among other things, that wavelet decomposition provided very good separation of the combustion and injection events. Wu and Chen [129] carried out a more ambitious study in which they monitored sound and acceleration signals from an IC engine and its associated cooling fan. They used a continuous wavelet transform to overcome such diagnostic problems as "smearing" due to variable engine speed and fault signals buried in background noise. They demonstrated the approach on two sets of experimental fault data, one associated with the engine's fan and the other covering such engine faults as misfiring and a leaky inlet manifold. Barelli *et al.* [130] claimed to have developed an innovative diagnostic system of the combustion process specifically for cogenerative reciprocating engines. The target was to evaluate the energy content of the vibration signal acquired on the cylinder head and they found that correlating maintenance and performance records with a decomposition using the Discrete Wavelet Transform allowed them to distinguish between good and bad conditions of the combustion chambers. Finally, Wang *et al.* [131] have introduced a novel de-noising technique using adaptive wavelet packets, which they have applied to vibration signals from diesel engines. They introduced further de-noising techniques, including a modified ensemble mode decomposition to avoid mode mixing. They demonstrated the effectiveness of the techniques in separating impact signals from generator vibration signals, even when the impact signatures were buried within unrelated vibration.

The complexity of the relationship between sensor signals and potential diagnostic outcomes has led many researchers to apply higher level signal processing techniques, such as neural networks and expert systems, often using modifications some of the above methods to generate features or indicators. In an early application [132], diesel engine faults have been detected by using a single sensor for each of the cylinder pressure and vibration, and two sets of artificial neural networks were shown to identify the faults with success level of 90%. For example Wu and Liu [133], when attempting on-line fault diagnosis for engines based on sound signals, used the discrete wavelet transform to generate features for neural network input, choosing the DWT over the CWT [129] because of its speed of computation in on-line monitoring. Later, the same authors [134] used a wavelet packet transform combined with a neural network to develop a kind of diagnostic expert system.

Canonical correlation analysis (CCA) is a kind of blind source separation [135] and has recently attracted interest in the field of condition monitoring especially where there is significant high temporal and spatial variations as in monitoring the water quality [136]. In the only application to IC engines, so far, [137] canonical variety analysis (a form of multivariate statistics) has been used to identify misfire events in a 6-cylinder engine using the first six harmonics of the torsional vibration. No application of CCA to IC engines has yet been published and the idea is further developed in Chapter 4.

3.5 Summary and identification of thesis topic

Current developments in the area of condition monitoring in internal combustion engines moved along three main research themes; developing new measurement devices, developing new signal processing algorithms and developing simulation models. The current work aims to contribute in the first two of these, being about new processing algorithms for a relatively new sensor type for this application. The current state of the art, whilst using sophisticated signal processing algorithms, is not optimised or configured for the fact that multiple sources will produce records in a sensor array where the order of source signal arrival varies in a way that can be pre-calibrated on the object being monitored.

The current work aims to improve the resolution of AE in small diesel engines, using careful calibration of sensors and attenuation paths, to exploit to the full the advantages

of AE measurements in time resolution and source location. To give a manageable, but challenging, case-study, the work is focused on the time- and crankshaft angle windows covering injection, inlet valve opening and combustion in an attempt to identify more clearly what contribution to the AE is made from the various mechanical and fluid mechanical sources. The method is, however, generic to machinery applications where multiple AE sources are operating in close temporal and/or spatial proximity.

Chapter 4

Experimental set-up and procedures

This chapter describes the apparatus, monitoring equipment and experimental procedures that have been used in this thesis. First, the diesel engines and experimental injector rig used in the research are presented followed by a description of the AE system which was used as the monitoring tool. Next the various calibration tests for the sensors and propagation paths on the engines and injector rig are described and analysed. The procedures used for the main body of data collection on the engines and the injector rig are then described and justified, and, finally, the methods of processing and analysing the experimental data are detailed.

4.1 Test engines

Three different diesel engines were used in this study in order to investigate a broad range of operating parameters and to have a range of detailed mechanical configurations in the interest of generality of findings. The engines comprised of two four-stroke, four-cylinder engines and one two-stroke, two-cylinder engine as shown in Table 4.1.

Specifications	**Stuart Turner (Engine A)**	**Perkins A4.270 (Engine B)**	**Perkins T1004 (Engine C)**
Operating mode	Running	Running	Running
Control system	Mechanical	Mechanical	Mechanical
Fuel	Light Diesel oil/ Biodiesel	Diesel oil	Diesel
Power	6.6 kW (9hp at 700 rpm)	46 kW (62 hp at 2000 rpm)	99 kW (135 hp at 2500 rpm)
No of cylinders	2	4	4
Cycle	Two stroke	Four stroke	Four stroke
Induction system	Pump scavenged	Normally aspirated	Turbocharged
Nominal bore	69.85mm (2.75in)	108mm (4.25in)	100mm (3.94in)
Stroke	101.6mm (4in)	120.5mm (4.75in)	127mm (5in)
Compression ratio	16.5:1	16:1	17.25:1
Cubic Capacity	0.779 litre	4.42 litres	4 litres
Firing order	1, 2	1, 3, 4, 2	1, 3, 4, 2
Max. governed speed	1500 rpm	2000 rpm	2500 rpm
Cylinder liner	Wet	Wet	Dry, transition fit, flanged, with flame ring
Type of injection	Direct injection	Direct injection	Direct injection

Table 4.1: Specifications of test engines.

In addition, a specially-designed injector rig was used to acquire data on the AE associated with the injectors only, without the noise of other mechanical aspects of the engine. The engines and the injector rig are described in the following sections.

4.1.1 Engine A (Stuart Turner Engine)

Engine A (shown in Figure 4.1) was a 6.6 kW, 0.779 litre, two-stroke, two-cylinder, pump-scavenged diesel engine made by Stuart Turner for propelling small boats. It was equipped with a flange-mounted type C.A.V. fuel injection pump, which is a cam-operated spring return plunger pump of constant stroke. The engine used direct injection which starts 25^{o} BTDC with an injection pressure of 170 bar in open chamber.

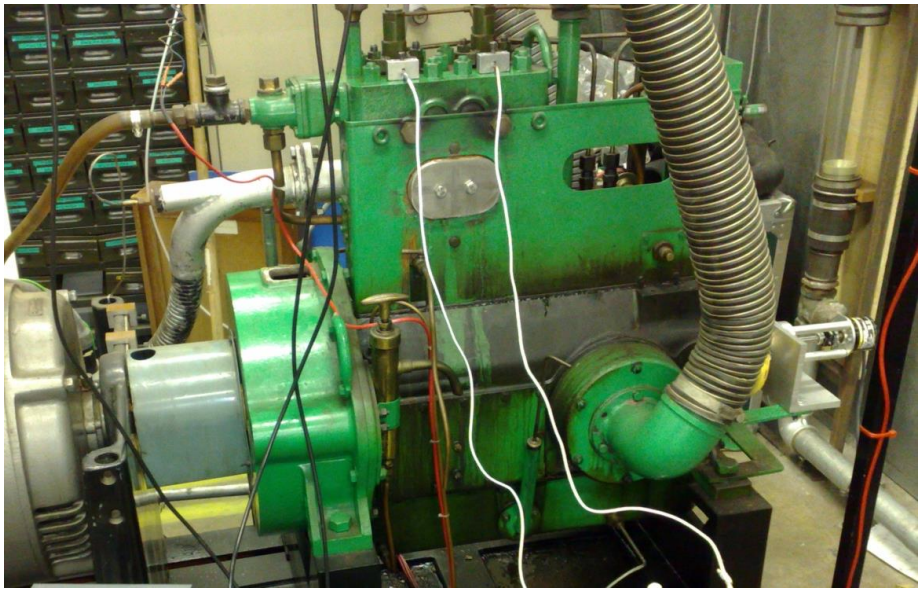

Figure 4.1: Stuart Turner diesel engine (Engine A).

4.1.2 Engine B (Perkins A4.270)

The second engine used in this study was a Perkins A4.270, 46 kW, 4.42 litre, four-cylinder, naturally aspirated, wet-lined diesel engine which has been shown in Figure 4.2. A distributor, a flange mounted fuel injection pump and a mechanical governor were fitted on this engine and direct injection was delivered via four multi-hole injectors with conical spray into a toroidal chamber. The injection pressure was 170 bar and the static injection starts at 16^{o} BTDC. Naturally aspirated diesel engines have better transient combustion response than their counterpart turbocharged diesel engines [30].

Figure 4.2: Perkins A4.270 diesel engine (Engine B).

4.1.3 Engine C (Perkins T1004)

Engine C (shown in Figure 4.3) was a 76 kW, 4-litres, four-stroke, four-cylinder, turbocharged, high speed direct injection (HSDI) Perkins T1004 diesel engine. This engine used direct injection delivered by a Bosch VE diesel injection pump and four multi hole, long stem, single spring Lucas injectors, with an injection pressure of 240 bar. The use of turbochargers in diesel engines improves specific brake power and fuel consumption and reduces carbon dioxide emissions. However, this type of diesel engine also suffers from what is called “turbocharger lag” which, under severe acceleration, results in poor transient combustion efficiency and heavy exhaust emissions [30].

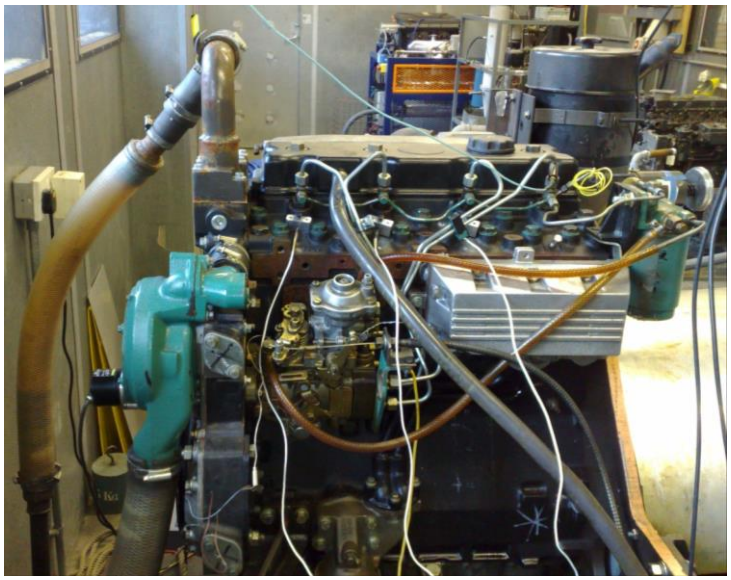

Figure 4.3: Perkins T1004 diesel engine (Engine C).

4.1.4 Experimental injector rig

An experimental rig (Figure 4.4) was designed to mimic the injection process, in order to isolate the AE associated with injection process from other sources of both signal and noise that can found in a running engine. Similar experimental rigs have been used to study the injection spray by others [138-142].

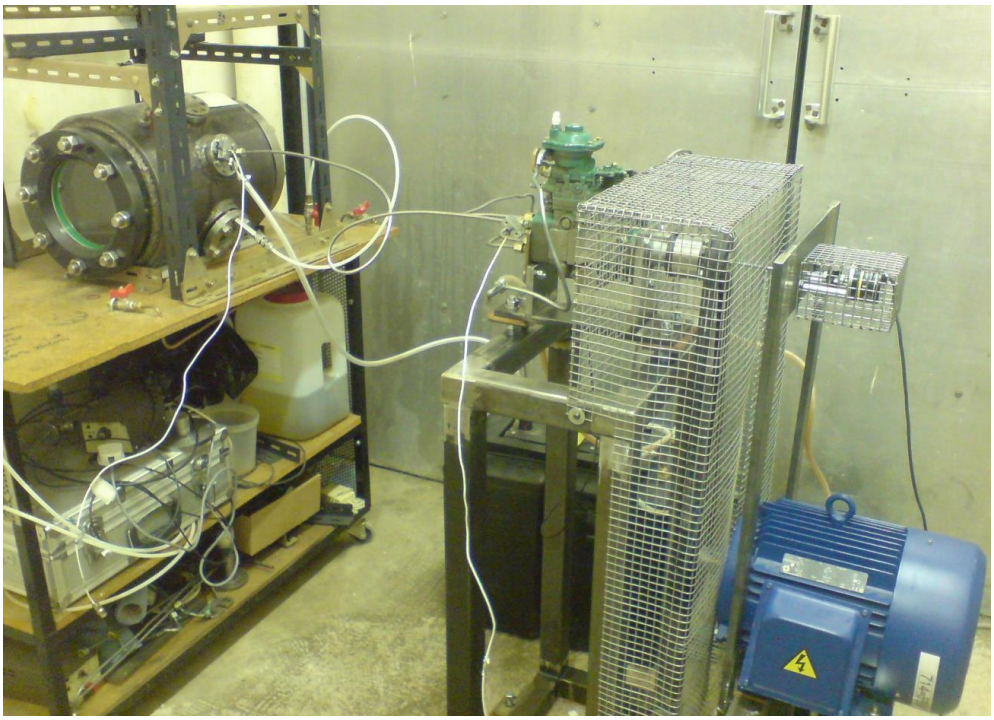

Figure 4.4: Diesel injector rig set up.

Figure 4.5 illustrates the diesel injector rig in schematic form. A Bosch VE (4/12 1250RV 137931) diesel injection pump, which is similar to the VE pump in engine C, was used in the rig to deliver the diesel fuel to the injectors at a pressure of 240 bar (Figure 4.6). The pump was driven by an electric motor with a variable speed controller to replace the normal driving motion from the crankshaft of the diesel engine (Figure 4.7). A multi hole long stem LUCAS (LJCX 69113) injector (Figure 4.8) was mounted into an injection chamber. The other outlets from the injector pump were connected to three similar injectors which were vented to a return fuel tank (Figure **4.9**). The injection chamber is a pressure vessel designed to withstand an internal pressure of up to 16 bar (Figure 4.10) but during all the experiments, the chamber was used under atmospheric pressure because this study focused on the identification of the injection event rather than being an in depth study of the spray formation and the behaviour of

the combustion which require accurate simulation of the injection/combustion conditions.

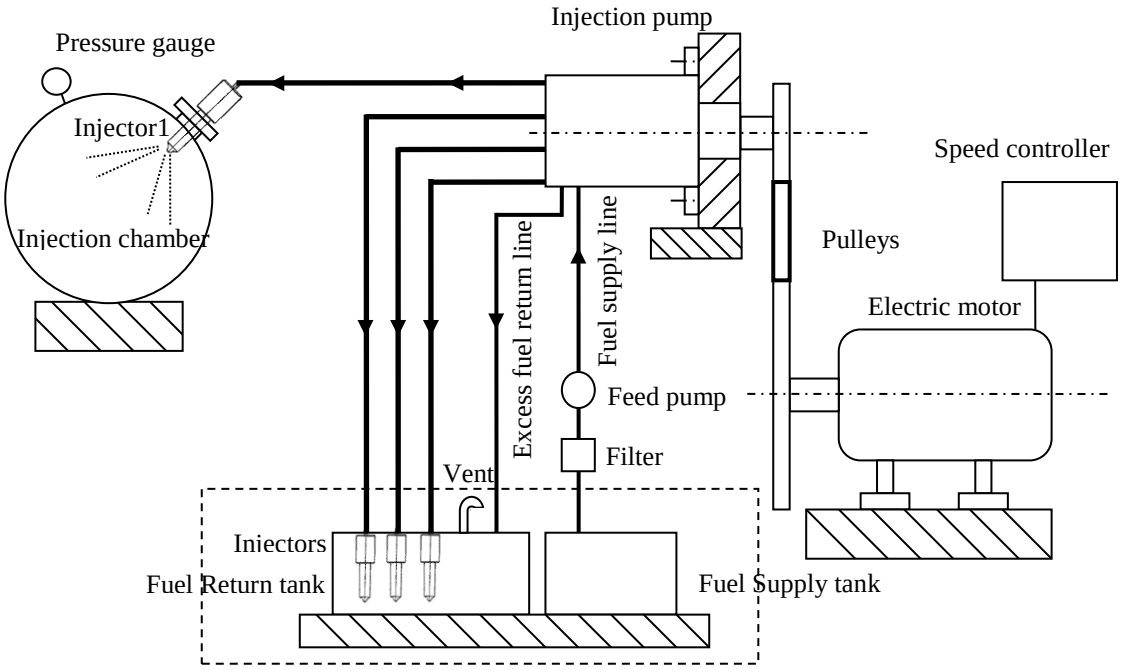

Figure 4.5: Schematic diagram of the injector rig set up.

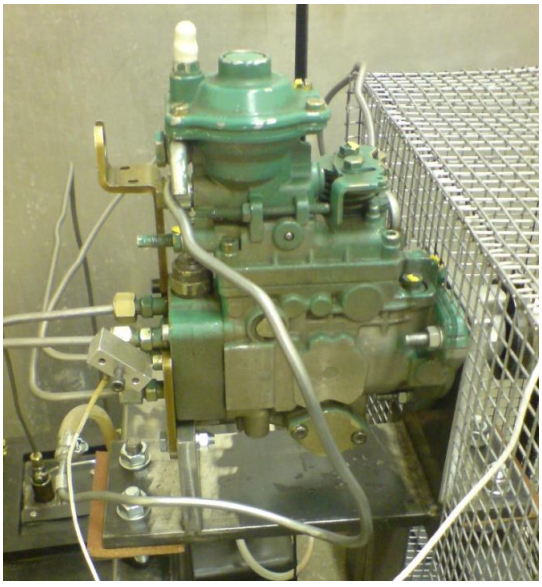

Figure 4.6: Bosch VE injection pump.

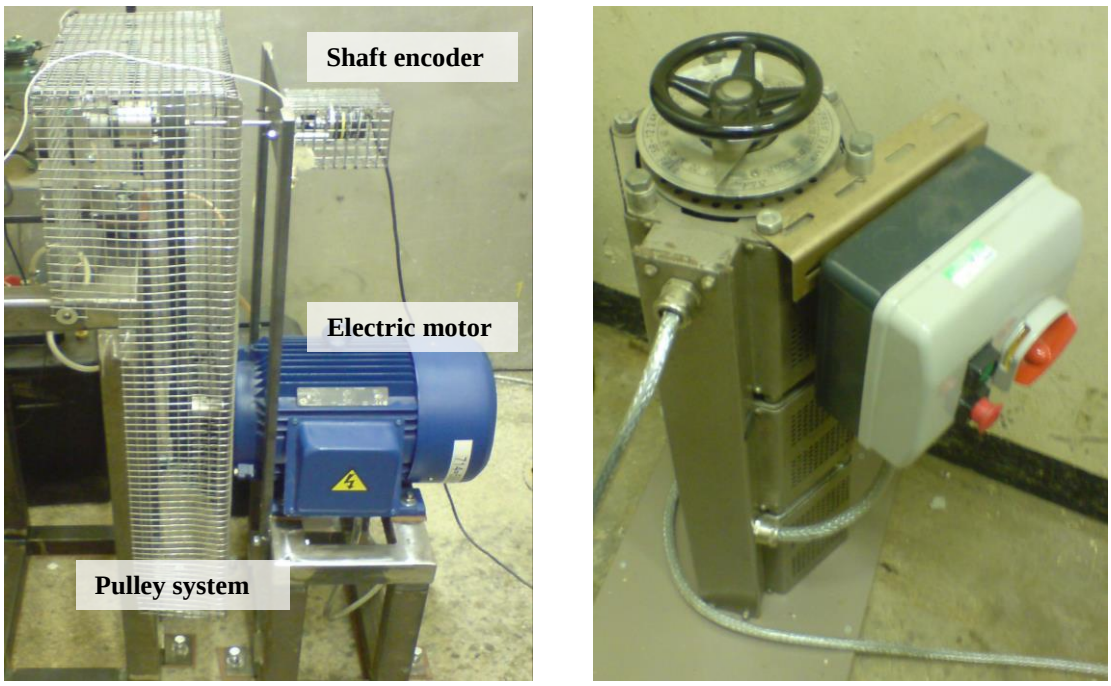

(a) **(b)**

Figure 4.7: Power transmission system including electric motor and pulleys (a) and variable speed controller (b).

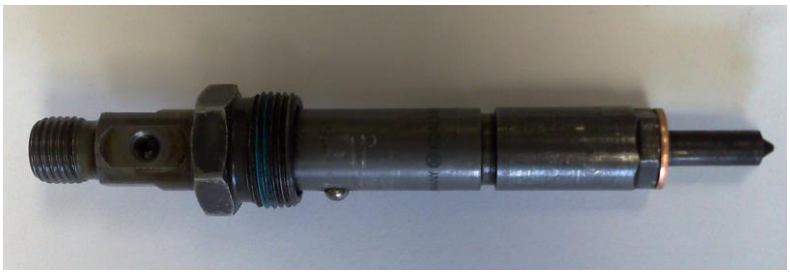

Figure 4.8: LUCAS LJCX 69113 injector.

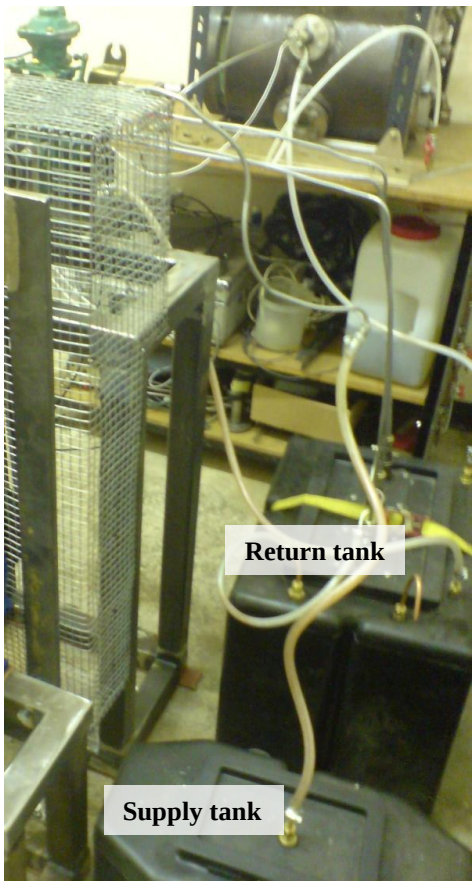

Figure 4.9: Fuel tank arrangement.

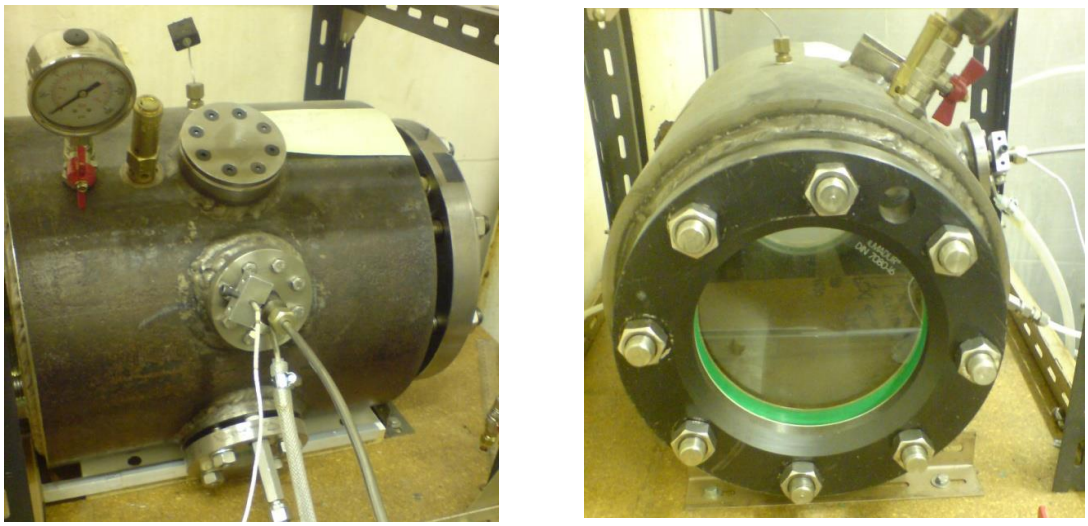

Figure 4.10: Injection (compression) chamber.

4.2 Acoustic Emission condition monitoring equipment

A custom-built AE system (shown in Figure 4.11) was used in this research, in which an AE sensor array (up to three sensors) was polled using high-speed data capture to enable raw acoustic emission to be acquired at full bandwidth for later processing.

Figure 4.11: AE system.

4.2.1 Acoustic emission sensors

The AE sensors used in this study were broadband Physical Acoustics Corporation (PAC) Micro-80D transducers with operating frequency range of 0.175-1MHz and main resonances at 325 kHz and 650 kHz. These sensors are 10 mm in diameter and 12 mm in height and are enclosed in a cylindrical stainless steel case to provide electromagnetic interface shielding. The sensor element is made of lead zirconate titanate (PZT) piezoceramic, with an operating temperature range of -65^{o}C to 177^{o}C, suitable for use on the engine cylinder head outer surface, where the temperature will not exceed 100^{o}C. A calibration was performed to check the sensitivity of each AE sensor against the calibration certificate (Appendix A) prior to every engine experiment.

4.2.2 Acoustic emission preamplifiers

The electrical signal produced by the AE sensor is normally weak and requires to be amplified to be transmitted any distance. Each sensor was connected to a PAC-1120A preamplifier (shown in Figure 4.12) with a band pass filter in the range 0.1-1 MHz. The preamplifier was 2/4/6 type which indicates the three selectable gain settings of 20/40/60 dB. This preamplifier has a wide dynamic range and low noise level (less than 2 μV) with a large output signal (20Vpp into 50 ohms). The power supply of 28V and the signal output were provided through a single BNC connector.

Figure 4.12: PAC preamplifier

4.2.3 Signal conditioning unit

A 4 channel AE signal conditioning unit (SCU) was custom-designed to provide the power supply to the preamplifier (28V) as well as further signal amplification or attenuation, as required. Four gain settings were provided for this purpose: +6, 0, -6, -12 dB using a selectable switch. An analogue RMS output was integrated into this unit, with selectable RMS averaging settings, although measurements in this work used the raw signal output.

4.2.4 Connectors and coupling

High vacuum grease couplant, from Dow Corning, was used to ensure good contact between the sensor and the surface. The couplant enhances the transmission of the acoustic waves through the surface of the transducer. This high vacuum grease has good heat stability over the range -40^{o}C to 200^{o}C.

A number of different holders (shown in Figure 4.13) were used to hold the sensors in contact with the surface of the cylinder head or injector, including magnetic and screw-down holders.

A number of custom PAC cables with BNC connectors were used to transfer the amplified AE signals. All were coaxial cables with shielding against external EMI noise.

A NI-BNC-2120 shielded connector block with BNC connectors was used to carry the outputs from the SCU and route them to the data acquisition card.

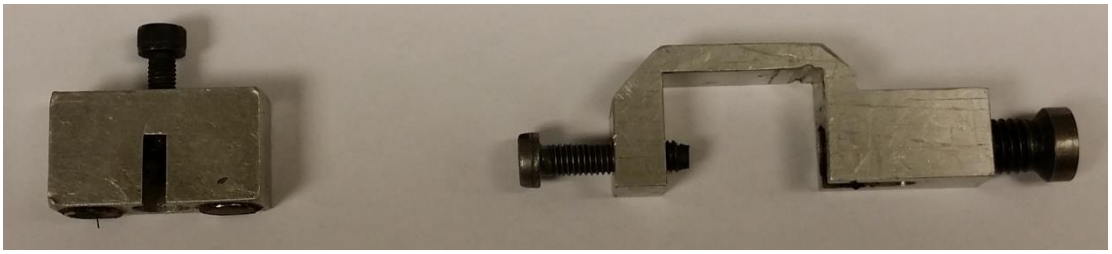

Figure 4.13: Sensor holders.

4.2.5 Data acquisition and processing units

The input data was acquired by using 4 high speed input channel, 10 MS/s per channel, two 12-Bit output Simultaneous-Sampling Multifunction DAQ card (NI PCI-6115). AE signals were managed using a LABVIEW program, while several MATLAB codes have been produced to analyse the AE signals (discussed in detail later).

4.2.6 Shaft encoder

An Omron shaft encoder model E5C2-CWZ6C, delivering 360 pulses per revolution was coupled to the fuel injection pump in order to record the angular position and determine the in-cycle and between cycle rotational speed. The shaft encoder was connected directly to the shaft of the injection pump using a flexible coupling (Figure 4.14). A TDC marker was used to identify the position of TDC point so that it could be displayed as a double height pulse as shown in Figure 4.15.

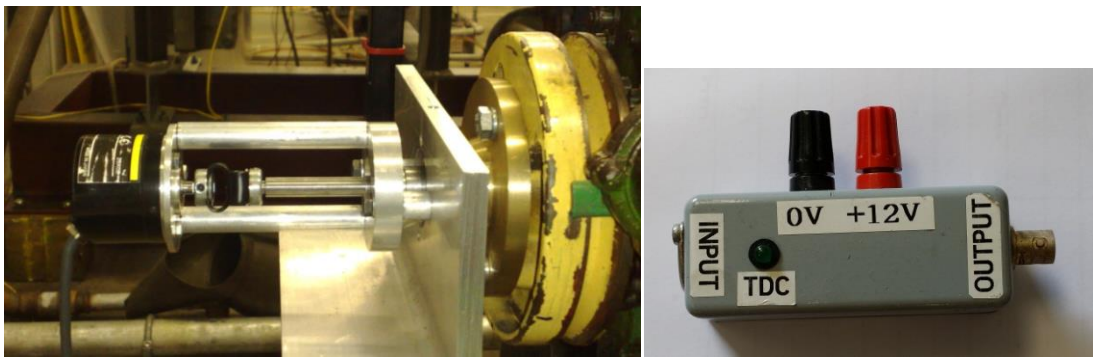

Figure 4.14: Shaft encoder (left) and TDC signal can be identified by the TDC marker (right).

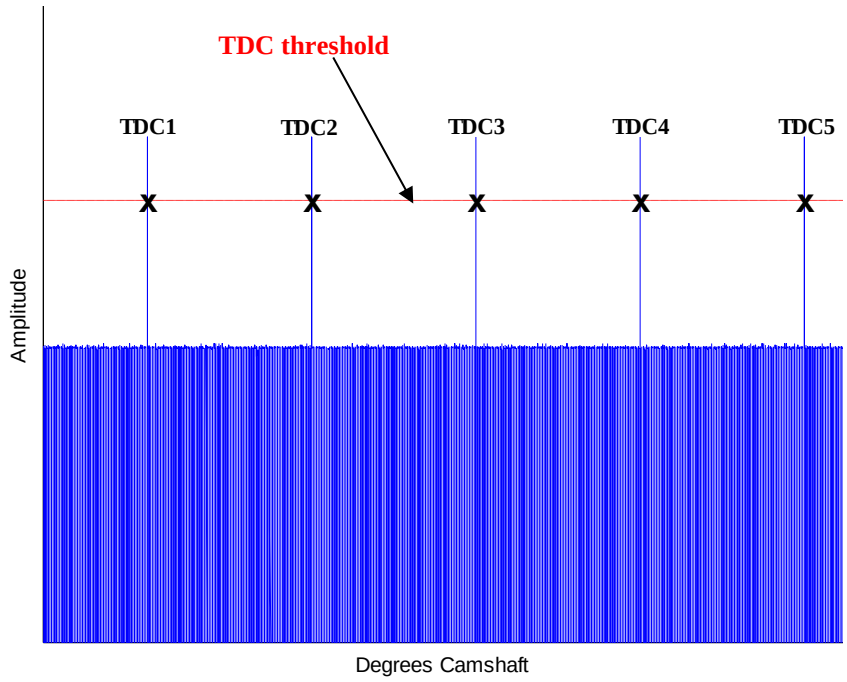

Figure 4.15: Typical signal from the shaft encoder where TDC signal can be identified by threshold crossing of the signal peaks identified by the TDC marker.

4.3 Calibration

Because the analysis of the results relies on the time series obtained from multiple sources to an array of sensors, it is important to calibrate the sensors, the transmission paths and also any uncontrolled variables, such as sensor placement. To this end, a series of calibration tests were carried out on a simple steel block and also on each of the engines and the injection rig. The calibration tests, as well their results, are described in the following sections.

Three AE sensors were consistently used throughout the work, and their calibration certificates (which describe their frequency response) are shown in Appendix A. All of the calibrations used a pencil lead break (Hsu-Nielsen source [143]), as shown in Figure 4.16, as a reasonably reproducible step unload source which can be applied easily at a precise location on the steel block, engine or rig.

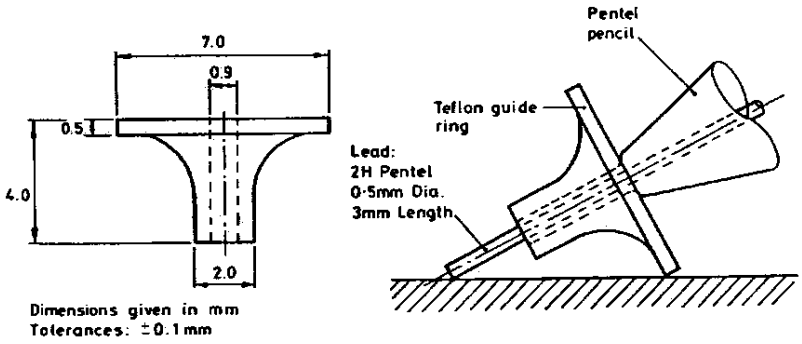

Figure 4.16: Hsu-Nielsen source test [143].

4.3.1 Calibration of AE sensors on steel block and plate

Two sets of calibration were carried out on the solid steel cylinder shown schematically in Figure 4.17. The calibration consisted of breaking pencil leads in the centre of the top face with the three sensors arranged at the same radial position R_S. In the first calibration, the three sensors (AES1, AES2 and AES3) were arranged at positions P1, P2 and P3, respectively on a pitch circle radius of 70mm. The sensors were removed and replaced five times, and 20 records of pencil lead breaks were acquired for each placement. Analysis of these records allows an assessment of the reproducibility of the sensor placement (coupling) and of the pencil lead breaks themselves, as well as giving an inter-sensor sensitivity calibration. In the second calibration, the sensors were moved to different positions on a pitch circle radius of 100mm, making three arrays; [AES1/P1, AES2/P2, AES3/P3]; [AES1/P2, AES2/P3, AES3/P1] and [AES1/P3, AES2/P1, AES3/P2]. For each array, 10 pencil lead records were acquired for each sensor, the sensors removed and replaced and a further 10 pencil lead records acquired for each sensor. This second calibration was used to distinguish between the effects of the sensor sensitivity and any systematic variations between the positions on the block. Each pencil lead record was acquired at a sampling rate of 5 MHz for 0.1 second using a fixed gain (28dB) with the same amplifier and channel for each sensor (Table B.1 in Appendix B).

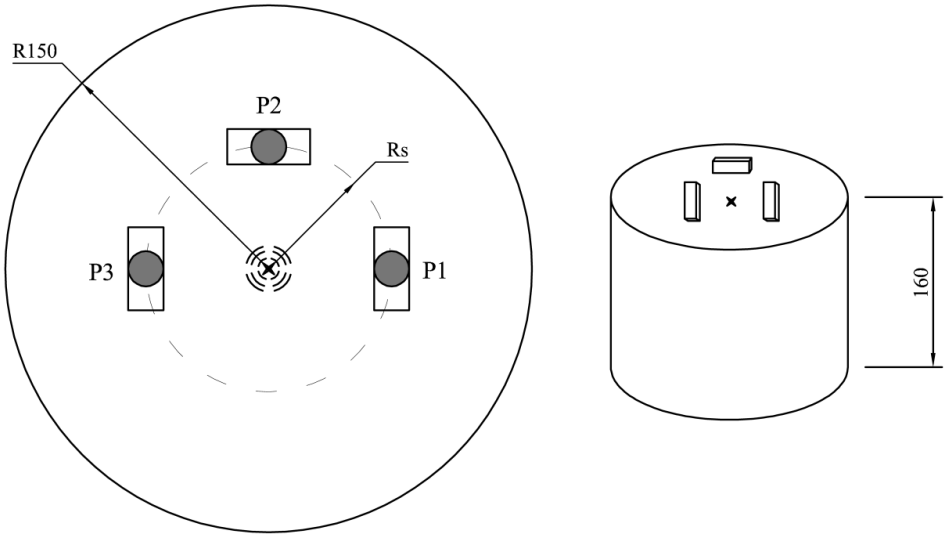

Figure 4.17: AE sensor calibration set-up, showing pencil lead source (X) and sensor positions (P1, P2 and P3). (All dimensions in mm.)

Figure 4.18 shows a typical 0.1 second record from the sensor calibration tests, with a zoom in on the first two hundred or so microseconds. As can be seen, the signal decays quite slowly but there are clear returns at around 40μs and around 100μs, corresponding to reflection of a surface wave from the cylinder edge and a bulk wave from the bottom surface. Thus, the whole record contains multiple reflections and modes of propagation, but the first few tens of microseconds contain the essential information about the source. Figure 4.19 shows the mean and the standard deviation of the energy of the whole record for each of the re-mounts for each of the sensors when their positions are kept the same. It appears that the energy from a pencil lead break can vary by around ±30% for any sensor without it being removed, and that removal and replacement can result in a variation in energy of about ±10%. It is also evident that AES1 records energies a factor of about 3 times higher than AES2 and AES3 seems to lie between the two. Figure 4.20 shows the same data as Figure 4.19, but plotted against signal arrival time relative to AES1 which is used as the acquisition trigger. It is clear that there is a difference in the signal arrival time which is correlated quite well (given the variability of pencil lead breaks and re-mounts) with energy using a relationship as suggested by Equation 2-24. It might be noted in passing that the time difference between AES2 and AES1 corresponds to around 5mm for a Rayleigh wave travelling at $3000ms^{-1}$ and also that there may be coincidental differences in sensor sensitivity which enhance the variations in energy. Figure 4.21 shows the results of the second calibration test, where the sensors were moved between the positions. It is clear that there is a shift in mean

energy between positions for any given sensor, and that position 2 gives consistently higher energies than the other two positions. Coupled with the findings shown in Figure 4.20, this would suggest that the shift in mean between positions is partly due to the accuracy of placement of the sensors and partly due to different reflection conditions at the bottom surface (mounting blocks under positions 1 and 3). Overall, it can be said that there is a variability of about ±10% in what might be recorded by a given sensor with a given source strength in a nominally identical experiment, this being due to inaccuracy in the placement of the sensor and also in variations in its coupling to the surface. Figure 4.21 suggests that AES3 is about twice as sensitive as AES2 with AES1 being intermediate between the two. Similar studies, in which the same block has been used, have suggested irregularity of the support and the materials [144, 145]

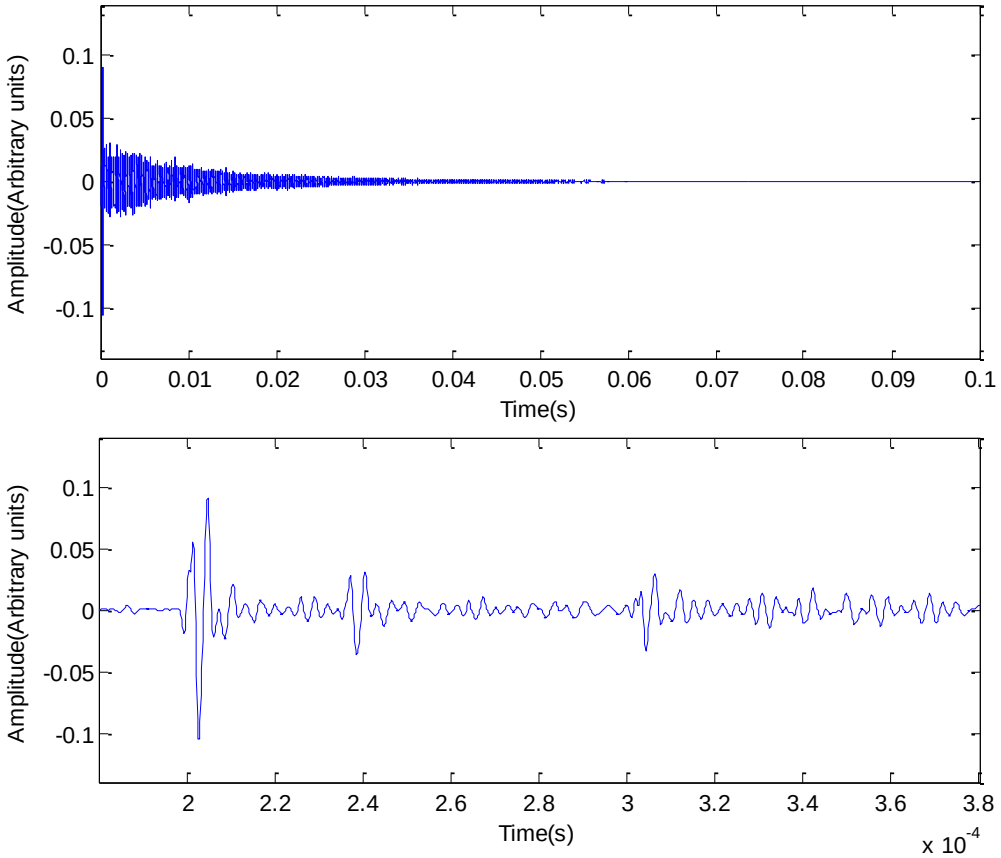

Figure 4.18: Typical raw AE signal of the sensor calibration experiment for AES1 with a 0.1 s record (top) and with window of 0.2 ms (bottom).

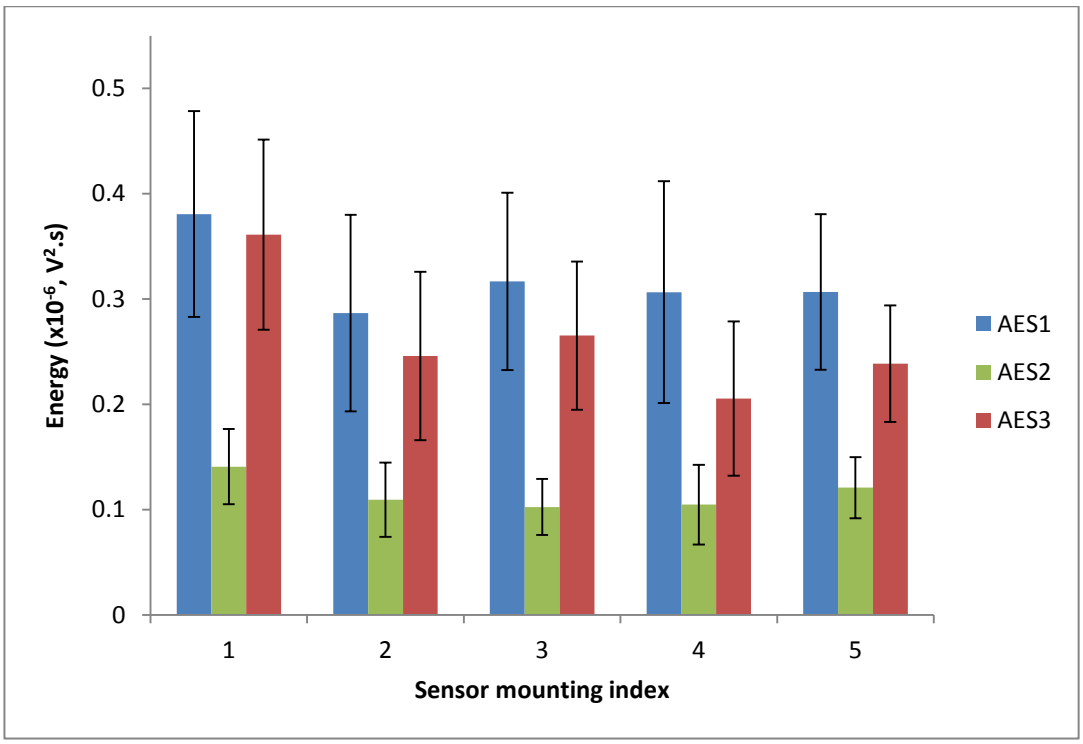

Figure 4.19: Effect of re-mounting and variation of pencil lead breaks for each of the sensors in first calibration test.

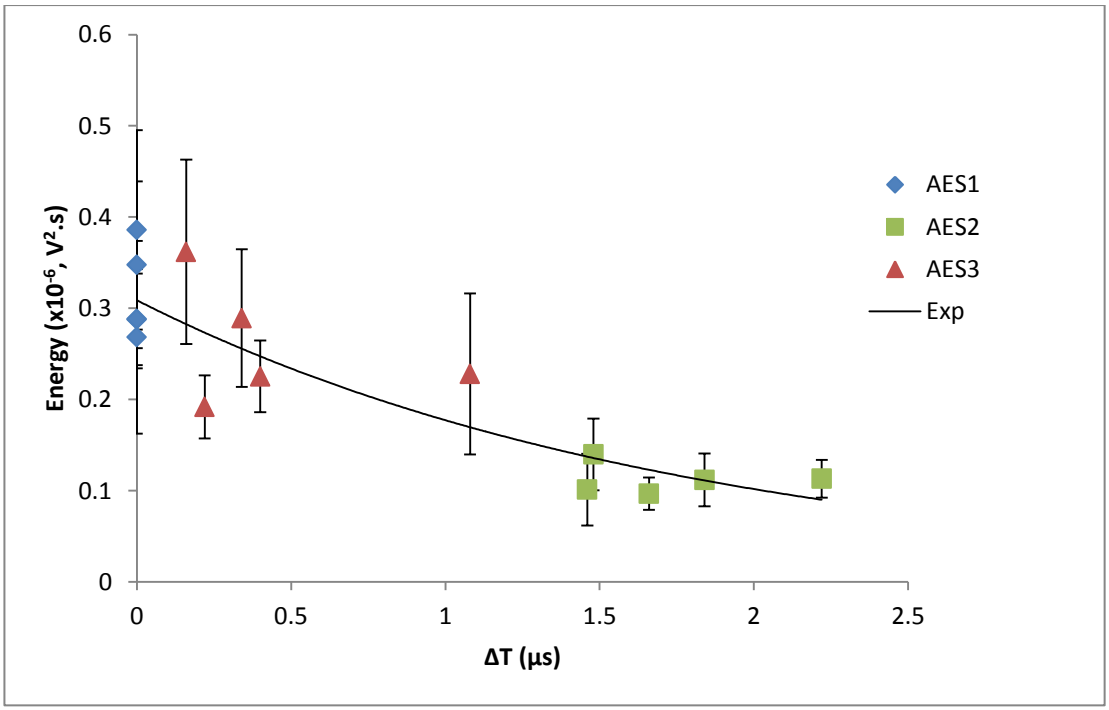

Figure 4.20: Data from Figure 4.19 re-plotted to show arrival time relative to AES1 along with best fit exponential function.

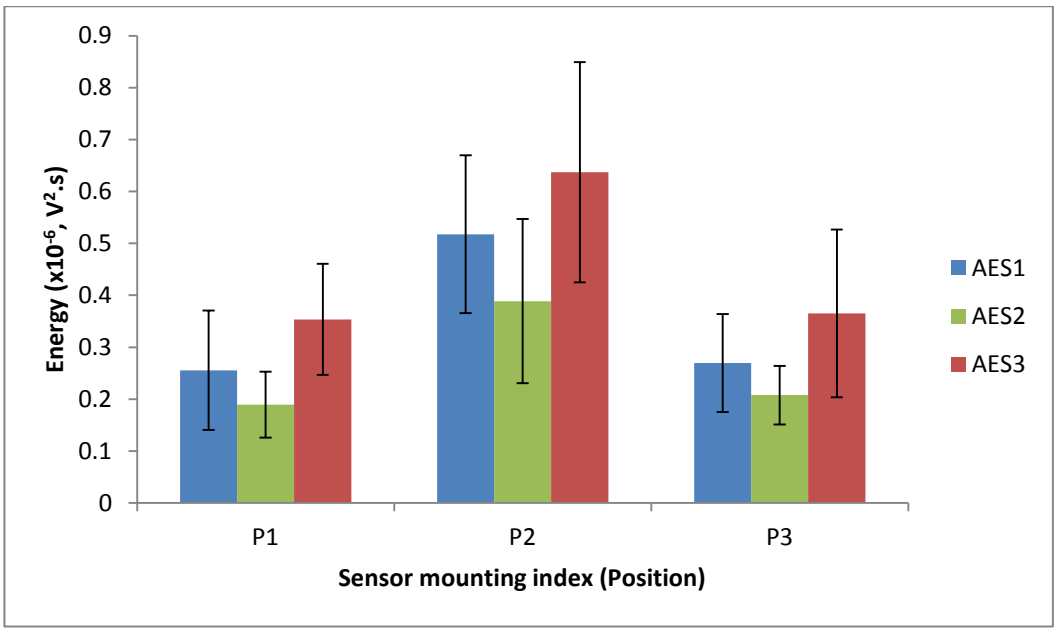

Figure 4.21: Effect of sensor position and variation of pencil lead breaks for each of the sensors in the second calibration test.

A 1m × 1m steel plate of thickness of 6 mm was used to assess arrival time estimation over longer distances. Two of the same sensors and preamplifiers as used in the cylinder test were also used here, although relative amplitude calibration is not important here as the first sensor merely acted as a trigger for capture at the second sensor. The two sensors were mounted 400 mm apart and the gap divided into seven segments of 50 mm spacing (Figure 4.22). Ten pencil leads were broken at each interval (Table B.2 in Appendix B), the AE signal at the target sensor being acquired and processed as before.

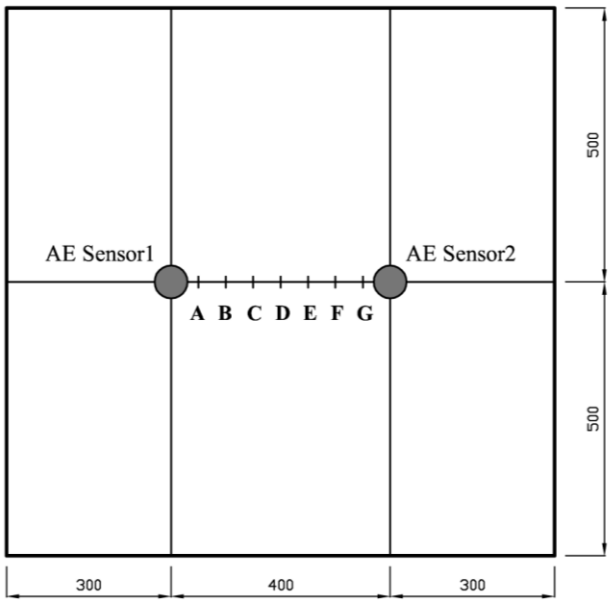

Figure 4.22: Schematic layout on thin steel plate with two AE sensors. (All dimensions in mm.)

Figure 4.23 shows an example of the recorded signal for the two sensors for a particular source position, illustrating how the difference in arrival time was estimated. As can be seen, each signal commences with a short segment of relatively low amplitude AE, followed by a second "arrival" of higher amplitude AE, and the length of the initial segment increases with source-sensor distance, implying that it is moving faster from the source. The arrival of two (or more) waves travelling at different speeds has been noted by a number of researchers, e.g. Shehadeh *et al.* [146] and algorithms have been suggested for separating the two. For the purposes of the current work, where there is significant background noise and the need is to pick out stronger locatable sources within this background, it is sufficient simply to find the first emergence of a source above the noise. Accordingly, the arrival time is estimated by calculating the absolute value of the signal since the cessation of the previous source and comparing this with the instantaneous amplitude, arrival being defined as the time at which the amplitude exceeds 1.5 of the maximum absolute value of the background noise which is estimated from the first 500 sampling points (of 1000 points pre trigger value). Figure 4.24 shows the resulting arrival time differences plotted against source-sensor distance difference and the best-fit straight line suggests a propagation speed of 5128 ms^{-1} which compares to the speed of the fast wave of 5119 ms^{-1} in similar steel plate reported by El-Shaib [144].

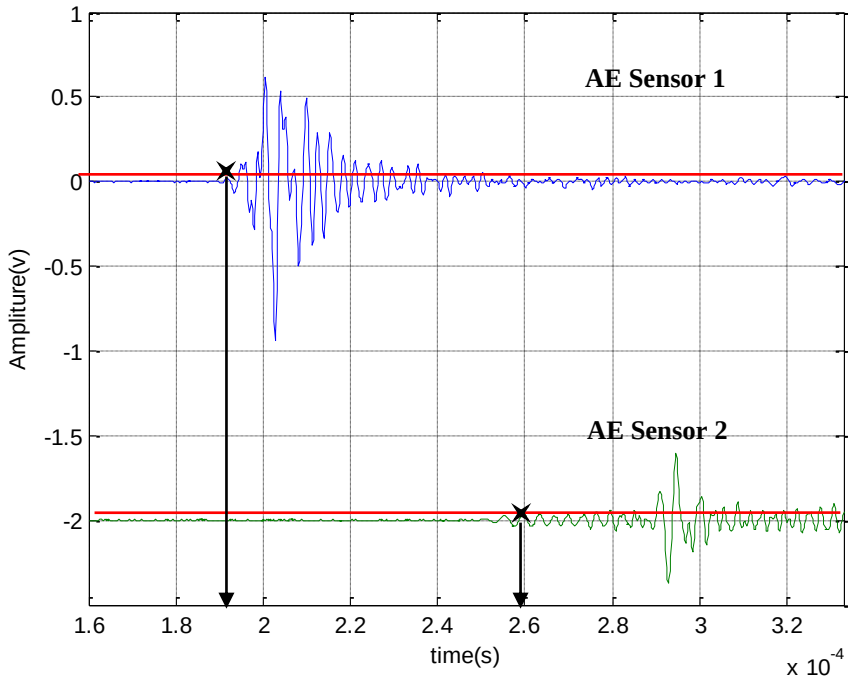

Figure 4.23: Raw AE signal of pencil lead break on a thin steel plate at the fifth position (A).

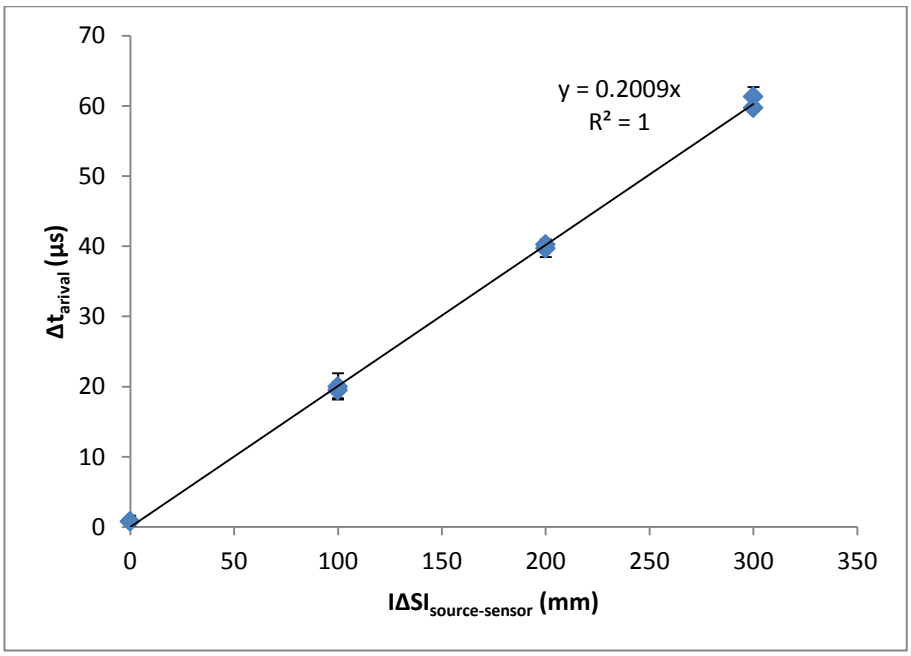

Figure 4.24: Measured arrival time difference *vs* source-sensor distance difference for thin plate.

4.3.2 Calibration on engines and injectors

As well as the calibration of the sensors and the development of thresholding algorithms, it was necessary to carry out some propagation studies on each of the experimental objects, the detail varying with the particular experiment envisaged.

4.3.2.1 Injector attenuation

One of the injectors was removed and cleaned and one sensor was mounted on the end which normally protrudes from the cylinder head as shown in Figure 4.25. Twenty five pencil lead records were then acquired at each of four source positions, using a sampling rate of 2.5MHz and a record length of 0.1 second (Table B.10 in Appendix B).

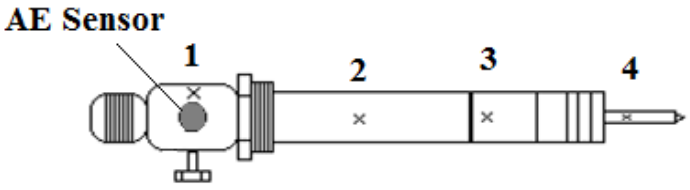

Figure 4.25: Attenuation measurements on injector body.

Figure 4.26 shows the results of the attenuation tests on the injector plotted against axial distance. Here the attenuation with distance along the injector is much smaller than for the cylinder head (as seen later), most likely because of the dimensions of the injector which will reduce geometric spreading.

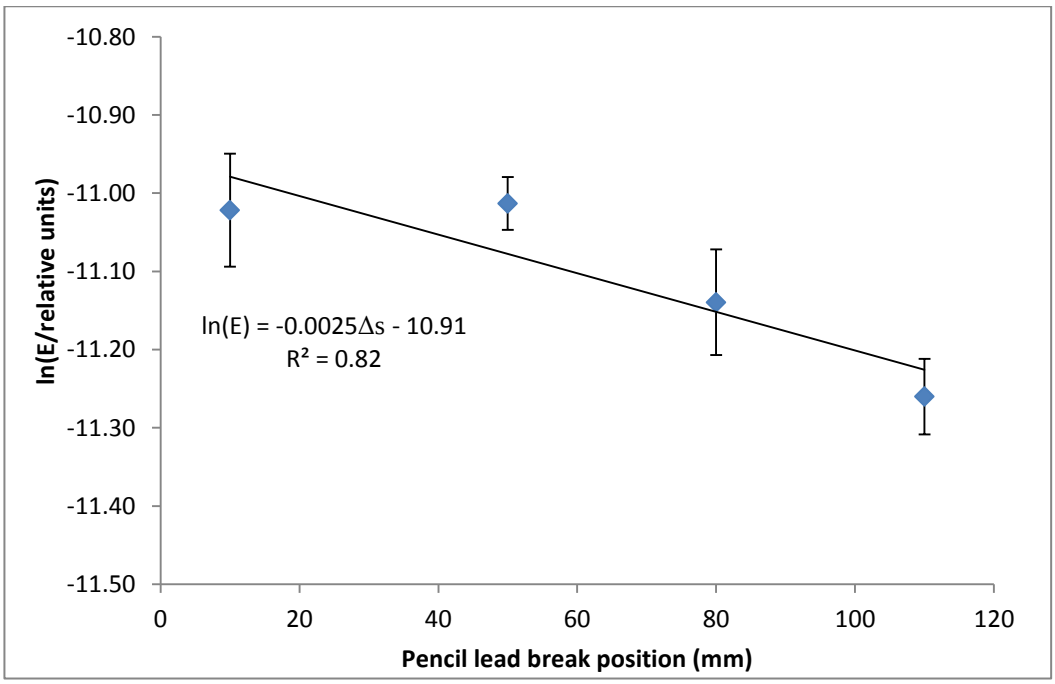

Figure 4.26: Attenuation measurements on injector body.

4.3.2.2 Calibration on Stuart Turner engine (Engine A)

Pencil lead break tests were performed on the cylinder head of Engine A with the engine cold, hot (immediately after a running engine test) and with the engine warm, approximately one hour after a test. At each temperature, a pencil lead was broken at nine different positions (P1-P9) with sensors at two positions (AES1 and AES2) as shown in Figure 4.27, and five records were captured for each source position. The AE signals were acquired at a sampling rate of 2.5MHz over a record length of 0.1 second, using a fixed signal gain of 28dB (Table B.3 in Appendix B).

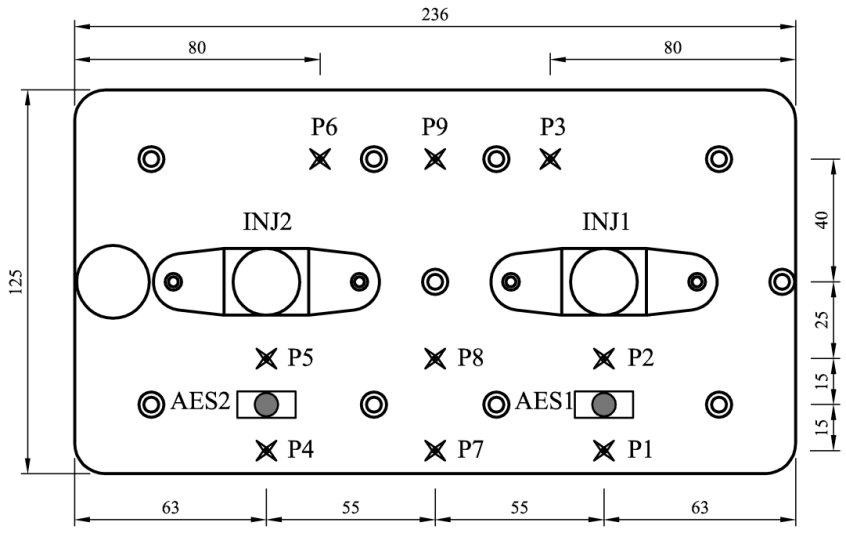

Figure 4.27: Schematic diagram of sensor array and positions of pencil lead break (x) in signal transmission test on Stuart Turner diesel engine (Engine A). (All dimensions in mm.)

Figures 4.28 and 4.29 show the resulting AE energy recorded at Sensor 1 and 2, plotted on logarithmic-linear axes for the cold (room temperature- approximately 20°C), warm (approximately 40°C) and hot (approximately 70°C) engine. As can be seen, the engine temperature has a noticeable effect on the overall transmission over the cylinder head surface, although the attenuation slopes are quite similar at the three temperatures, suggesting that the temperature simply reduces the sensitivity of the sensor [147-151].

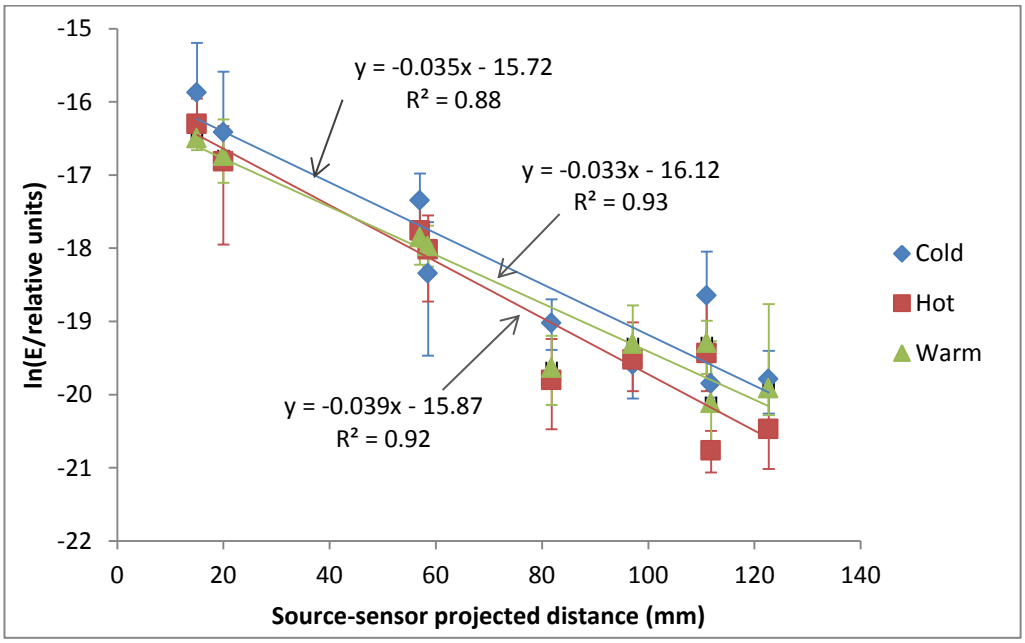

Figure 4.28: Attenuation of cylinder head (P1-P9) sources recorded at AES1 on Engine A *vs* source-sensor projected distance at three different surface temperature conditions; Cold (≈20°C), Warm (≈40°C) and Hot (≈70°C).

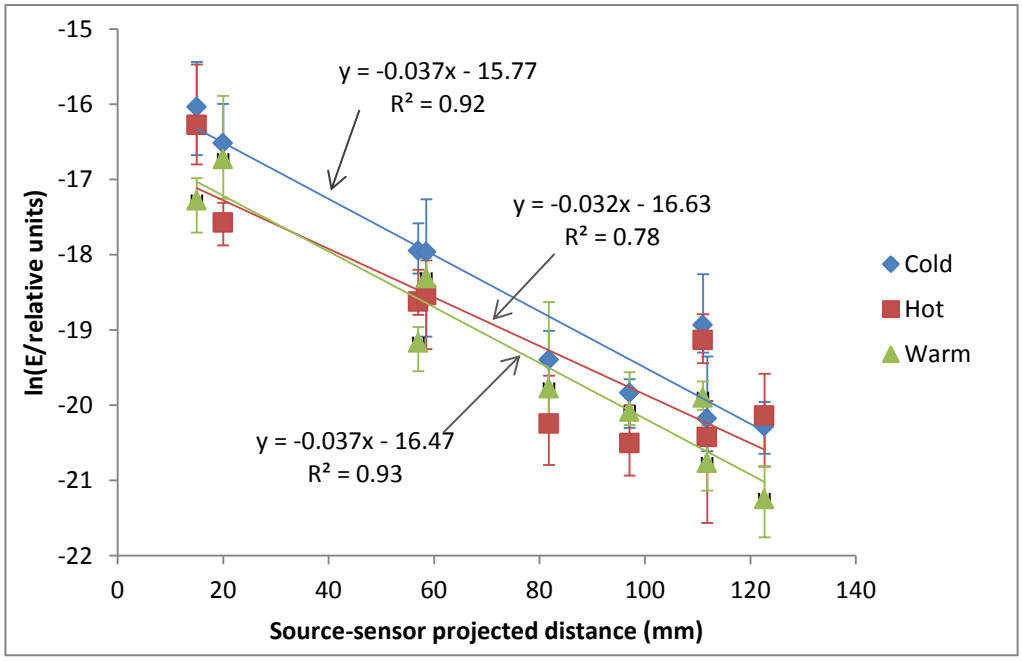

Figure 4.29: Attenuation of cylinder head (P1-P9) sources recorded at AES2 on Engine A *vs* source-sensor projected distance at three different surface temperature conditions; Cold (≈20°C), Warm (≈40°C) and Hot (≈70°C).

Figure 4.30 shows the arrival time difference at the two sensors plotted against the projected path difference. The apparent wave speed is somewhat higher than for the steel block, but consistent with the slower of two speeds (2650±41ms^{-1}) measured on a different cylinder head to the one studied here.

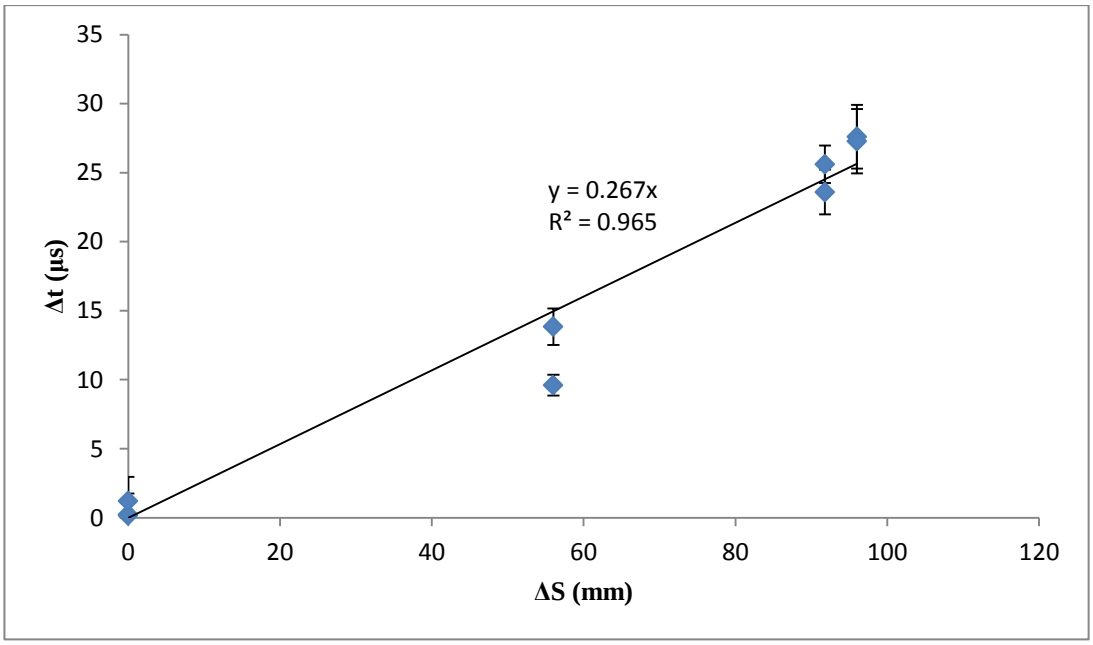

Figure 4.30: arrival time and the projected distances.

4.3.2.3 Perkins T1004 (Engine C): sensor array 1

Three sets of transmission tests were performed on the cylinder head of Engine C; cold (before running the engine; room temperature- approximately 20^{o}C), hot (immediately after the engine has run for 30 minutes, approximately 70^{o}C) and warm (30 minutes after turning off the hot engine, approximately 40^{o}C), Table B.4 in Appendix B. Pencil leads were broken at nine different positions (P1 to P9 , shown in Figure 4.31), five records being acquired at each sensor in the array, again using a sampling rate of 2.5MHz and a record length of 0.1 second. Because of the very wide range of attenuation across the cylinder head it was necessary to vary the gain settings between 28 and 60dB (as shown in Table 4.2). Figures 4.32 to 4.34 show the results of the energy transmission on the engine for the three surface temperatures for Sensors 1 and 2, respectively. The effect of engine surface temperature was not as distinct as it was in Engine B, and, in fact, in the Cylinder 3 window (Sensor 2) the effect of temperature in sensitivity appears to be opposite to what it is in Engine B.

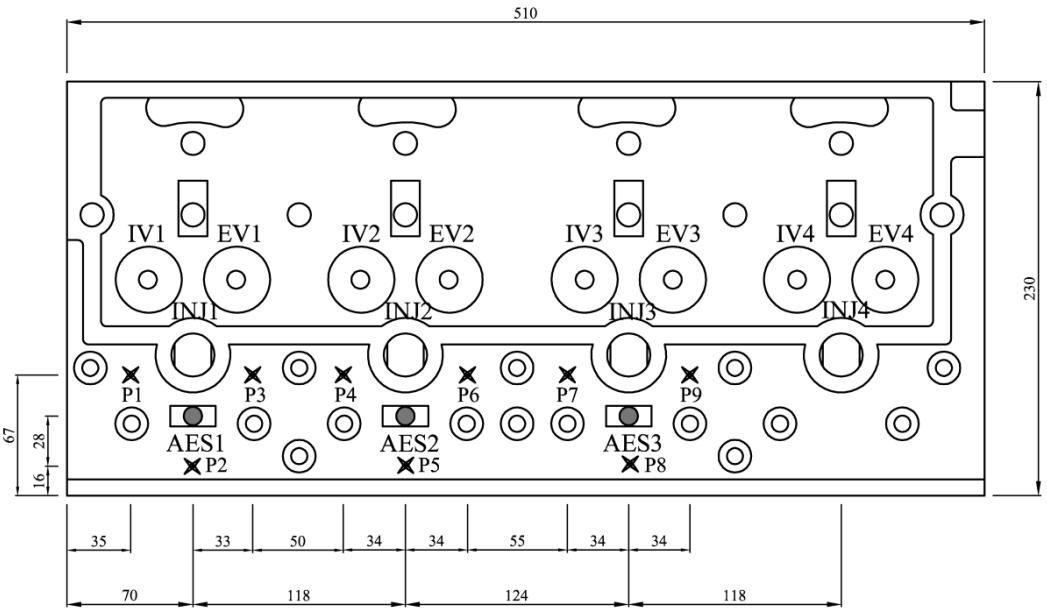

Figure 4.31: Schematic diagram of sensor array 1 on Perkins T1004 (engine C) and simulated source positions (P1-P9) for cylinder head calibration. (All dimensions in mm.)

Position	Signal Gain (dB)		
	Sensor1	Sensor2	Sensor3
P1	28	48	60
P2	34	46	60
P3	34	40	54
P4	40	28	48
P5	48	28	48
P6	48	28	40
P7	54	40	34
P8	60	46	34
P9	60	48	28

Table 4.2: Signal amplification gain settings of AE sensors in the signal transmission experiment of sensor array1 on Perkins T1004 (engine C).

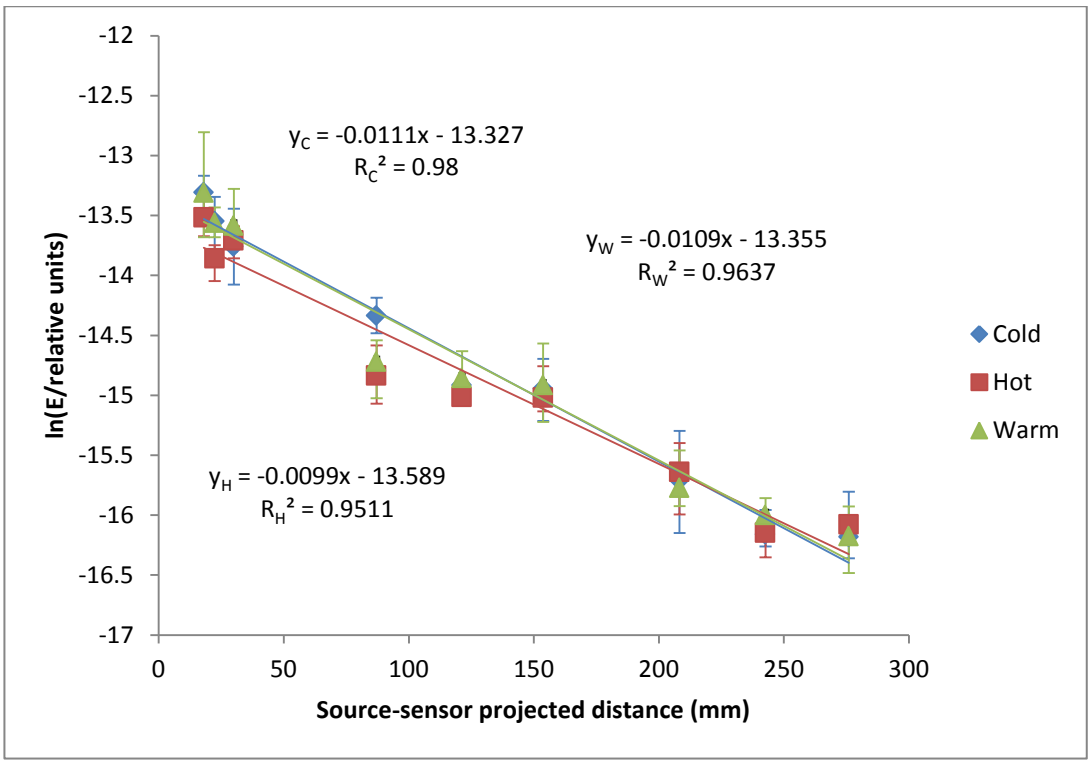

Figure 4.32: Attenuation of cylinder head (P1-P9) sources recorded at AES1 on Engine C (sensor array1) *vs* source-sensor projected distance at three different surface temperature conditions; Cold (≈20°C), Warm (≈40°C) and Hot (≈70°C).

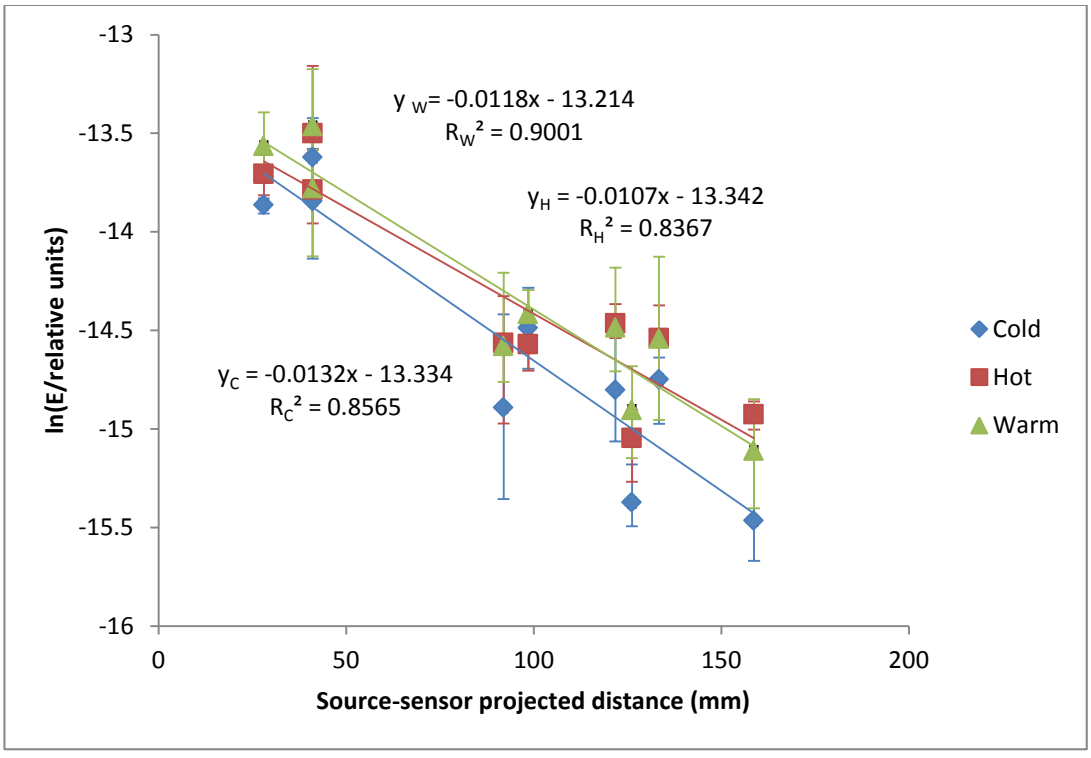

Figure 4.33: Attenuation of cylinder head (P1-P9) sources recorded at AES2 on Engine C (sensor array1) *vs* source-sensor projected distance at three different surface temperature conditions; Cold (≈20°C), Warm (≈40°C) and Hot (≈70°C).

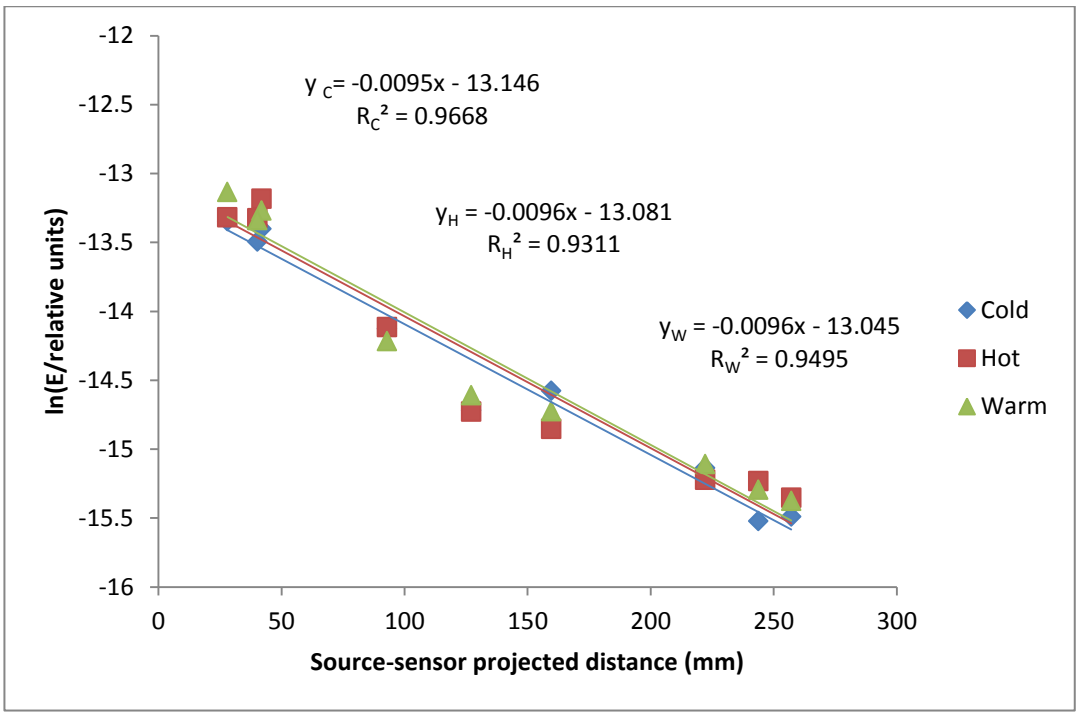

Figure 4.34: Attenuation of cylinder head (P1-P9) sources recorded at AES3 on Engine C (sensor array1) *vs* source-sensor projected distance at three different surface temperature conditions; Cold (≈20°C), Warm (≈40°C) and Hot (≈70°C).

4.3.2.4 Perkins T1004 (Engine C): sensor array 2

Two cylinder head calibration tests were carried out on this engine, one to check sensing reproducibility on the less regular (than the cylindrical steel block) structure of the engine and the other to measure time-of-flight and attenuation between various possible source locations and the sensor array shown in Figure 4.35. The sensing reproducibility test involved acquiring 10 records (2.5MHz sampling rate for 0.1 second using a fixed signal gain of 48dB) at each sensor of pencil leads broken at the position PR. This was repeated four more times, each time removing and replacing the sensors in the same positions. In the transmission tests (Table B.5 in Appendix B), pencil leads were broken at eight different positions (P1 to P8 in Figure 4.35), five records being acquired at each sensor in the array, again using a sampling rate of 2.5MHz and a record length of 0.1 second. Because of the very wide range of attenuation across the cylinder head it was necessary to vary the gain settings between 20 and 66dB (as shown in Table 4.3), and this had to be corrected after processing in order to plot the attenuation.

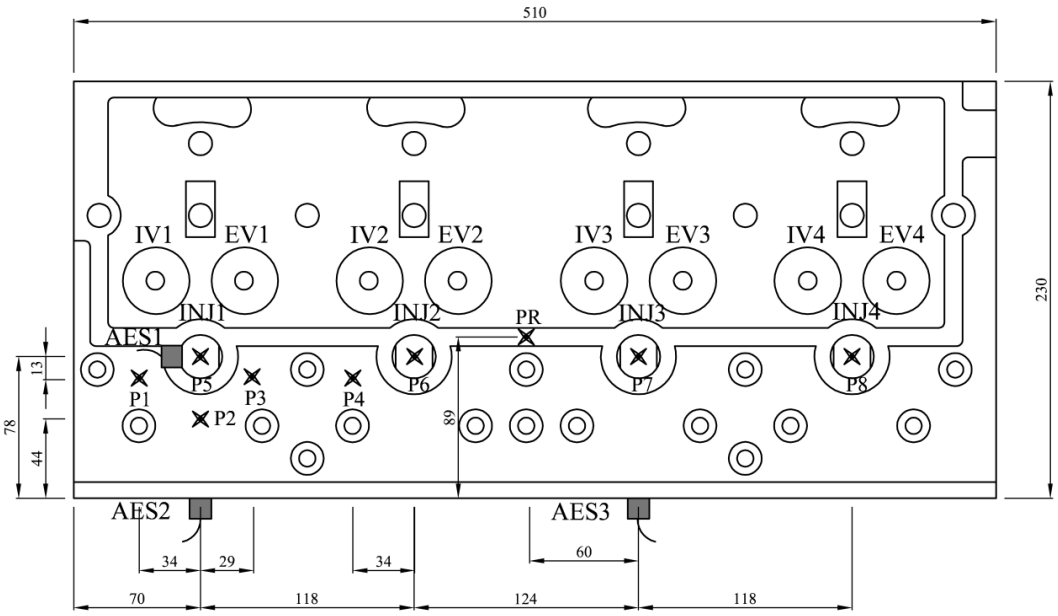

Figure 4.35: Schematic diagram of sensor array 2 on Perkins T1004 (engine B) and simulated source positions (PR and P1-P8) for cylinder head calibration. (All dimensions in mm.)

Position	Signal Gain (dB)		
	Sensor1	Sensor2	Sensor3
P1	48	34	54
P2	54	28	54
P3	46	34	54
P4	54	40	48
P5	20	54	66
P6	60	54	66
P7	66	66	60
P8	66	66	66

Table 4.3: Signal amplification gain settings of AE sensors in the signal transmission experiment of sensor array1 on Perkins T1004 (engine B).

Figure 4.36 summarises the results of the reproducibility tests on the cylinder block for the 10 breaks for each of the re-mounts for each of the sensor positions. The variation of about ±30% between individual breaks for a given mounting is similar to that found on the calibration block, but that between the means of the re-mounts is ±30-60% for the cylinder head positions and ±75% for the injector position. This reflects the relative difficulty of securing a good attachment and coupling on the cylinder head compared with the flat surface of the calibration block, although there may well be an effect of positioning error as well.

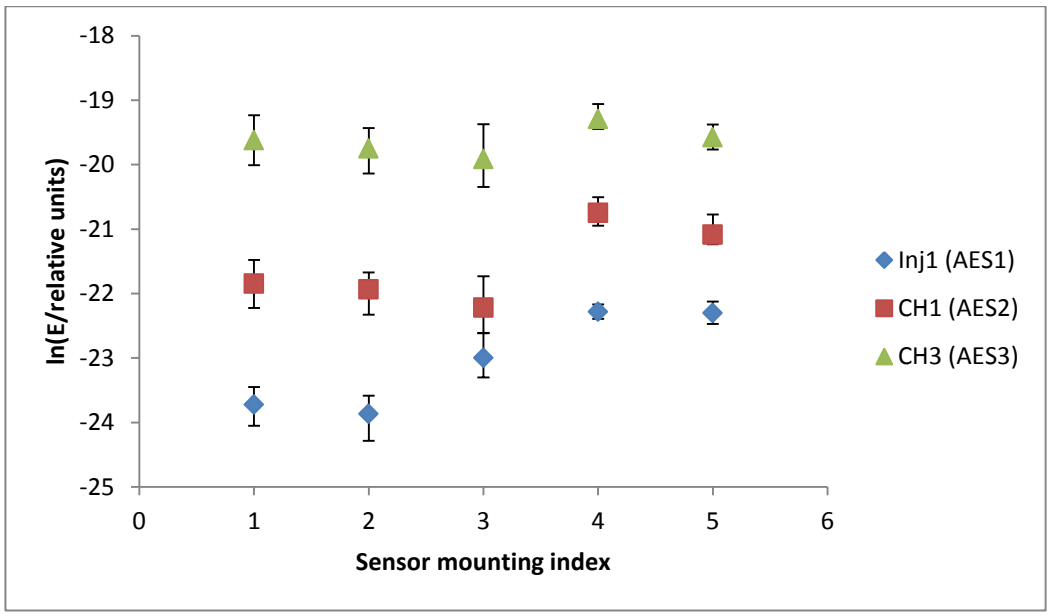

Figure 4.36: Averaged AE energy of the pencil lead break in the signal reproducibility experiment on the cylinder head of Perkins T1004 diesel engine.

The effective transmission path difference between AES3, and AES2 and AES1 was determined using the estimated arrival time (which was calculated using a threshold of 1.5 of the maximum absolute value of the background noise as per discussed in the thin plate experiment Figure 4.23) with the higher of the two speeds (4500ms^{-1}) obtained by Nivesrangsan *et al.* [152]. Figure 4.37 shows the same data as Figure 4.36 plotted as an attenuation curve, and it can be seen that the energy follows an exponential decay with effective path difference, within the variability apparent in Figure 4.37. The effective path differences can be estimated from Figure 4.35 by simply using the projected distances between the source and the sensors on the plan view of the cylinder head.

$$\Delta S_{proj}^{23} = (PR \rightarrow AES3) - (PR \rightarrow AES2) \cong 90mm$$

$$\Delta S_{proj}^{13} = (PR \rightarrow AES3) - (PR \rightarrow AES1) \cong 80mm$$

As can be seen from Figure 4.37, the effective path difference between AES2 and AES3 is very close to the projected distance across the cylinder head, whereas that for the injector-mounted sensor is much longer, far more so than could be accounted for by the additional distance out of plane. This discrepancy is likely to be a combination of the main transmission path not being over the surface of the block and an element of

"structural filtering", both of which would make the effective wave speed different to those obtained for the cylinder head surface.

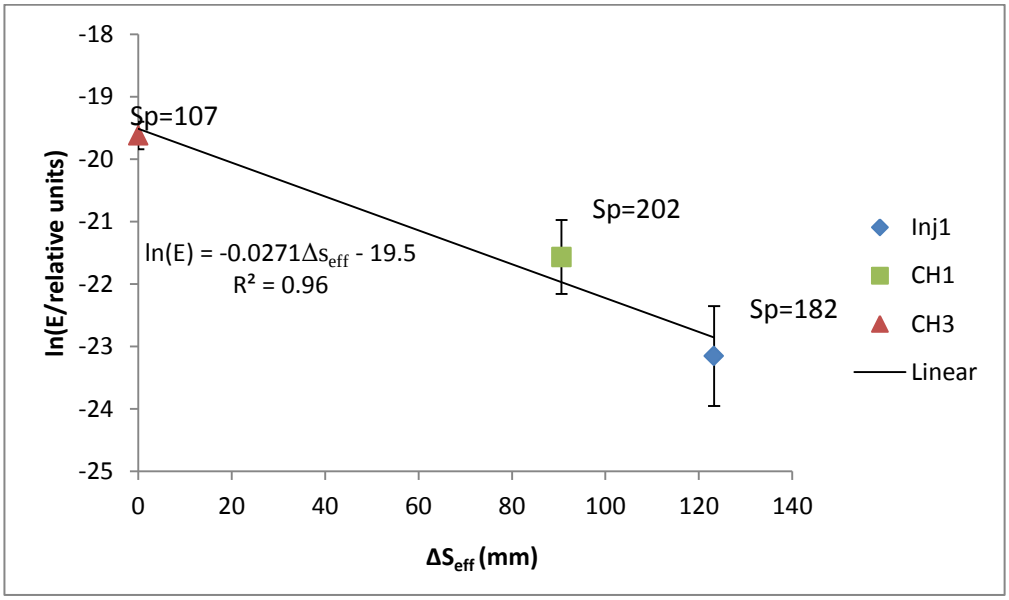

Figure 4.37: Average AE energy and effective path length difference of cylinder head attenuation experiment where the values of Sp represent the projected distances between PR and the sensors (in mm).

Figure 4.38 shows a similar plot to Figure 4.37, this time for the main transmission tests on the cylinder head (see Figure 4.35) where the source is on the surface of the cylinder head (P1-P4). As can be seen, sources on the surface of the cylinder head arrive last at AES3 and earliest at AES2, which is consistent with the projected distances (Figure 4.35), as was the case in the reproducibility tests. Also as was the case in the reproducibility tests, the effective path length difference is greater than the projected path length difference for the injector-mounted sensor.

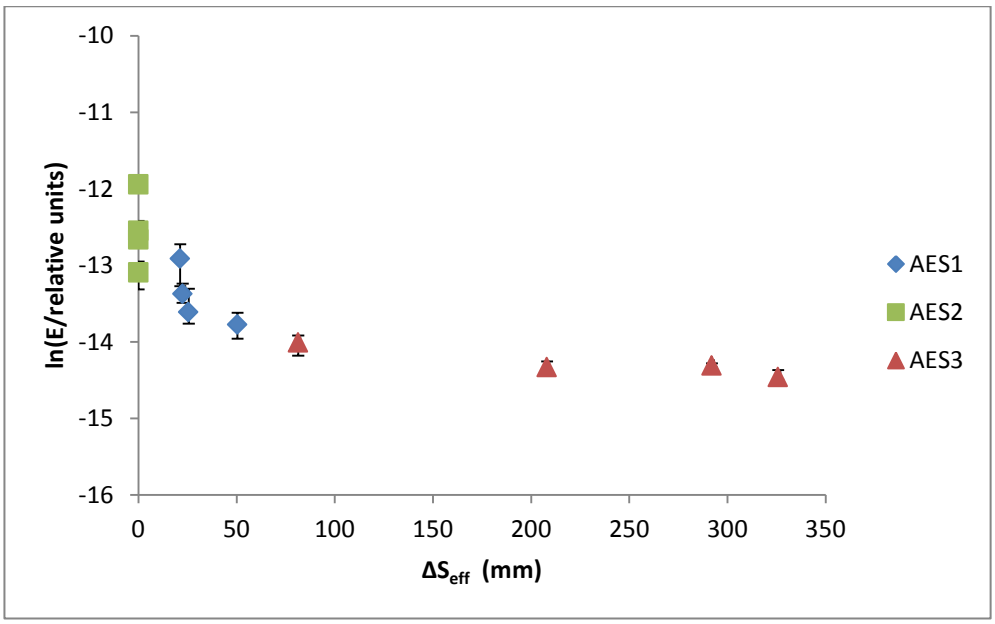

Figure 4.38: AE energy and effective path length difference for cylinder head attenuation experiment with source at positions P1-P4.

When the source is on an injector (P5-P8), the arrival times are broadly as would be expected from the projected distances, Figure 4.39a. However, the average energy arriving at the sensors in the array is dominated by the effect of crossing from an injector to the cylinder, other effects being relatively small. Interestingly, the injector-mounted sensor shows the highest energy for all injector sources, despite it being the least sensitive of the three, suggesting that there is an alternative transmission path on the injector side.

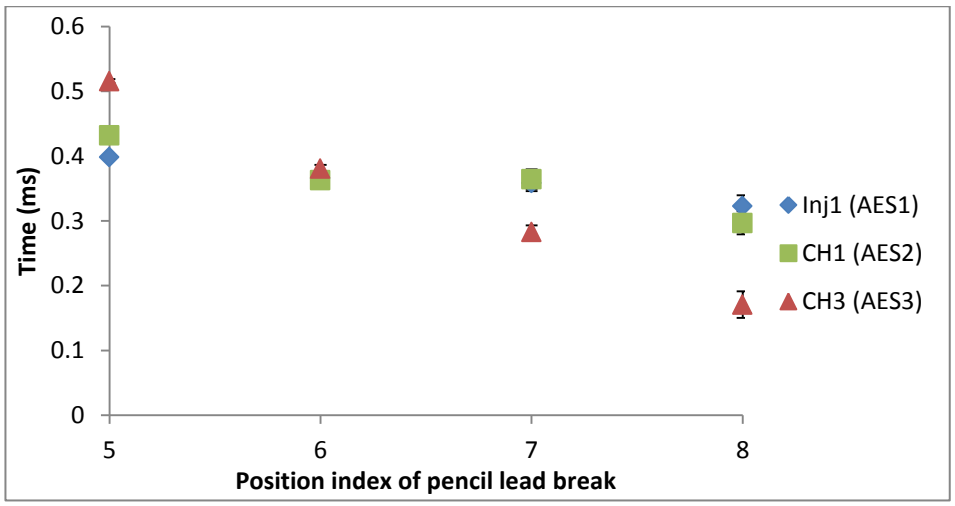

(a)

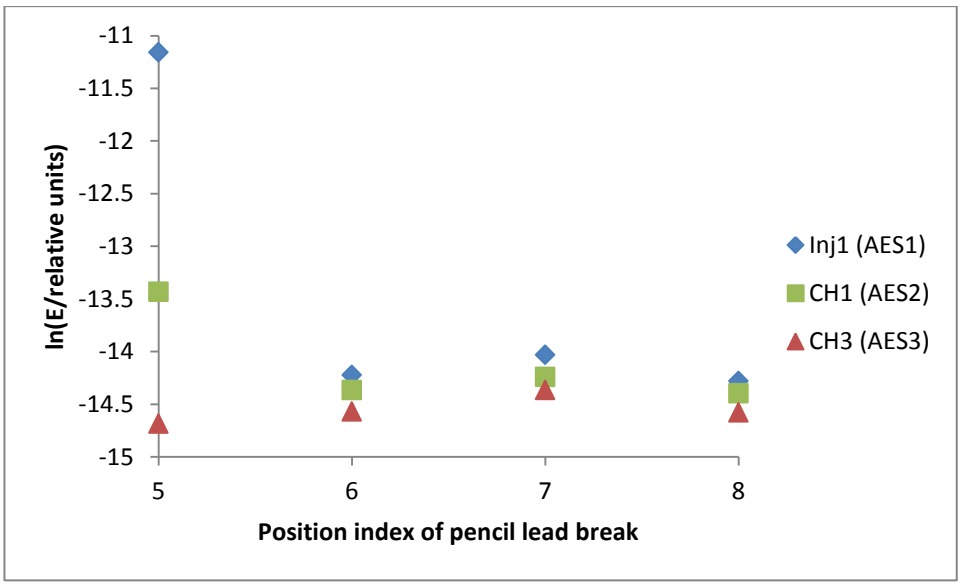

(b)

Figure 4.39: Arrival time (a) and average energy (b) for injector sources (P5-P8) at the sensor array in the cylinder head attenuation experiment.

Figure 4.40 shows the same energy data as in Figures 4.38 and 4.39, this time plotted against the measured source-sensor projected distance. In Figure 4.40a, only signals which do not cross between the cylinder head and the injectors are included (i.e. source positions 1 to 4 with sensors at CH3 and CH1, and source position 5 with sensor at Inj1). The slope of this (logarithmic) curve is reasonably compatible with that shown in Figure 4.37, given the additional effects of relative sensor sensitivity and the difference between projected and effective source-sensor distances. Figure 4.40b includes the data from Figure 4.40a (plus the regression line) as well as energies where there is a crossing between cylinder head and injector (i.e. source positions 5 to 8 with all sensors, except source position 5 with sensor at Inj1). The regression line through these latter energies

shows a much weaker correlation with source-sensor projected distance, both in terms of a lower slope and a reduced correlation coefficient.

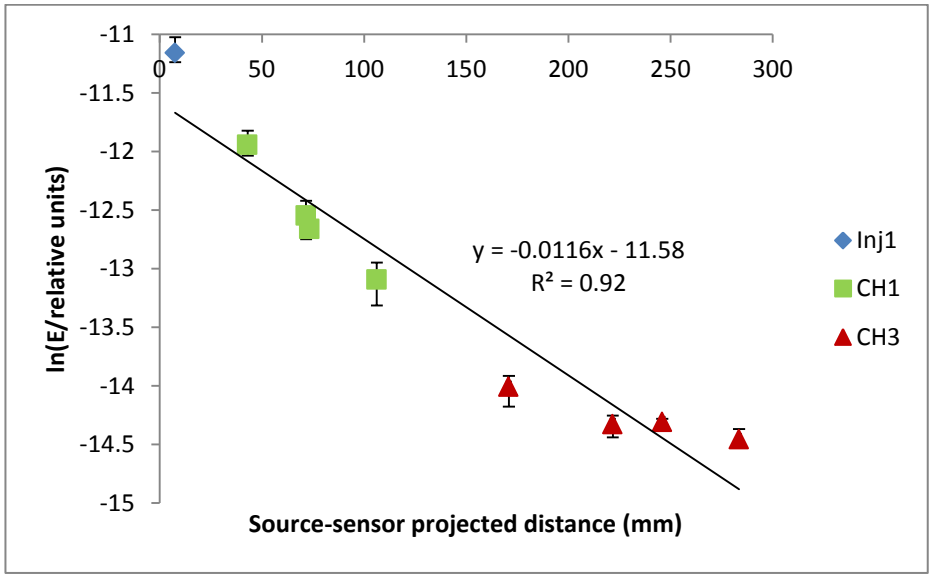

(a)

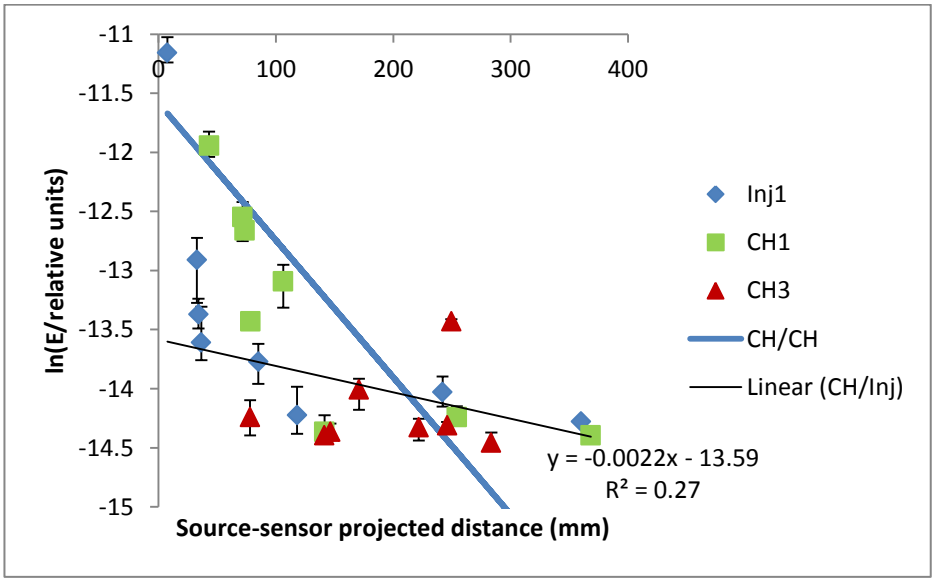

(b)

Figure 4.40: Attenuation of cylinder head (P1-P5) and injector (P5-P8) sources at the sensor array in the cylinder head attenuation experiment using projected distances from Figure 4.35: (a) where wave does not cross between injector and cylinder head (b) all data.

Taken together, the attenuation tests indicate that there are two sources of effective time delay in the cylinder head, one associated with projected distance travelled and one associated with crossing interfaces between engine components. Also each of these components is associated with a different type of attenuation, the first being "normal" attenuation with propagation distance and the second not being particularly sensitive to distance or, for that matter, number of apparent "crossings".

4.4 Running engine and injector rig experiments

The experimental strategy was to carry out a series of tests on structures of increasing complexity in order to identify the parts of the multi-source signal on a running engine that are associated with the fuel delivery processes. Thus, experiments were first carried out on an injector rig so that the AE associated with fuel flow through the injectors could be isolated from the other sources in a running engine. Next, running tests were carried out on a very simple 2-cylinder 2-stroke engine over a range of running conditions (speed and load). Next, experiments were carried out on normally-aspirated four-stroke diesel, before the most complex engine, a turbocharged four stroke, was studied.

4.4.1 Injector rig experiments

Three different sets of experiments were performed on this rig, with two sensor arrays and with and without a pressure transducer in the fuel line. Figure 4.41 shows the schematic diagram for the experimental rig used to simulate the diesel injection process. One AE sensor (Sensor 1) was attached to the shank of the monitored injector while a second sensor (Sensor 2) was attached to the pump outlet port. The monitored injector was connected to the pump using a 105 cm long feed line, where its rotational speed represented the engine operating at twice this speed. The first set of experiments (Experiment1) was carried out with a pressure transducer mounted onto the solid block half way along the fuel line as shown in Figure 4.42. In total, five different motor speeds were used, ranging from 1500 rpm to 2500 rpm with increments of 250 rpm, under two different fuel throttle positions (minimum and maximum, as shown in Table B.12). Experiment 2 used the same sensor array but without a pressure transducer installed to the feed line of Injector 1 and the range of motor speed was varied between 950 rpm to 2500 rpm. In Experiment 3, Sensor 2 was moved to the shank of one of the injectors mounted to the return tank and six motor speeds were used in the range of 700-2100 rpm. At each speed and each throttle position, 1 sec of raw AE at each sensor and shaft encoder input were acquired at sampling rate of 2.5MHz. The same 360-segment shaft encoder was used to record the average motor speed and to provide a measure of instantaneous speed of the motor shaft.

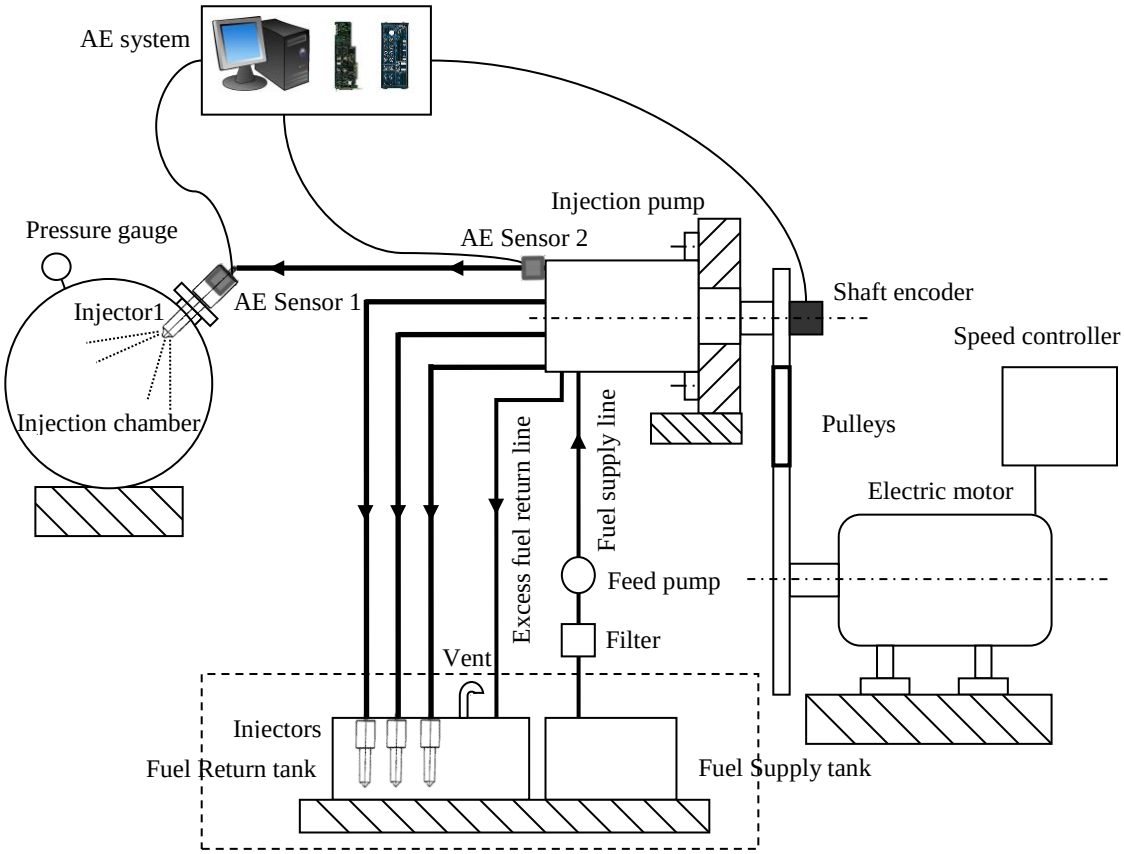

Figure 4.41: Schematic diagram of the experimental diesel injection rig showing sensor positions.

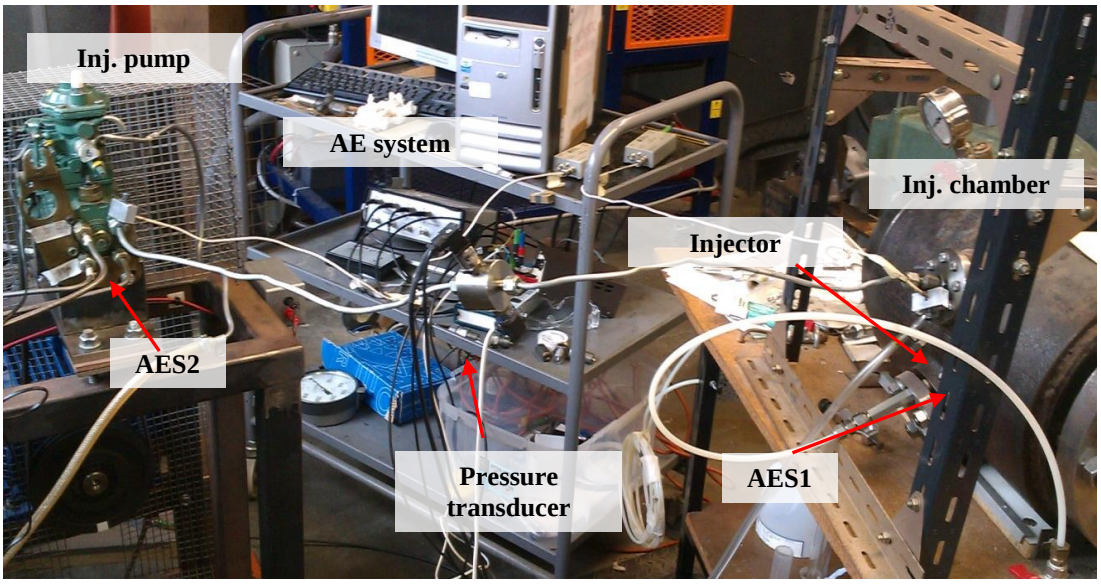

Figure 4.42: Experimental diesel injection rig with pressure transducer.

4.4.2 Stuart Turner engine (Engine A)

Two sets of experiments were performed on the running Stuart Turner engine, one using diesel fuel and the other using bio-diesel. Each set used 14 load settings where the engine was incrementally loaded from the no load condition and then unloaded at the

same nominal settings, each setting resulting in a specific engine speed, as shown in Table B.6 in Appendix B. After allowing the engine 5 seconds to settle at a given setting, five one-second records were captured for each condition using a sampling rate of 2.5MHz and a gain of 14dB. AE was recorded from two AE sensors; sensor 1 near Injector 1 and sensor 2 near injector 2 as shown in Figure 4.43 and the instantaneous speed of the crankshaft was recorded via the shaft encoder synchronously with the AE. The injection pump was set to deliver a constant amount of fuel during the experiment and the change in speed was simply due to the applied load from the eddy current dynamometer.

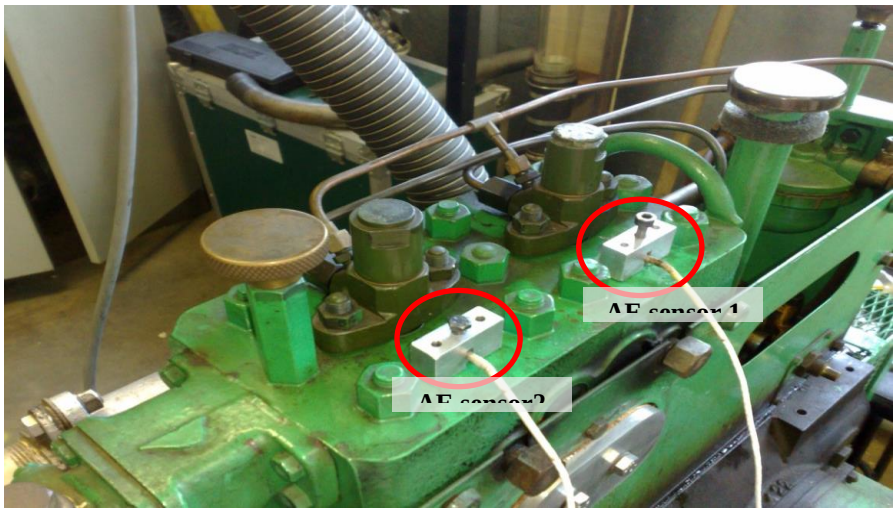

Figure 4.43: Sensor array set up on Stuart Turner diesel engine (Engine A).

4.4.3 Perkins A4.270 (Engine B)

This engine was very similar in design and construction to the turbo-diesel engine and used to give some comparative data for a normally-aspirated engine. Accordingly, experiments were performed with no load at five different nominal crankshaft speeds; 900, 1200, 1500, 1800, and 2100 rpm (equivalent to 450, 600, 750, 900, and 1050 rpm of the camshaft). AE was recorded for two sensors mounted on equivalent positions on the cylinder head, Sensor 1 being adjacent to Injector 1 and Sensor 2 adjacent to Injector 3 as shown in Figure 4.44. For each speed range, five records were captured at a sampling rate of 2.5 MHz for one second and using a total gain setting of 28dB for each sensor (Table B.7 in Appendix B). The same shaft encoder was connected to the shaft of the injector pump to record the angular position synchronously with the AE.

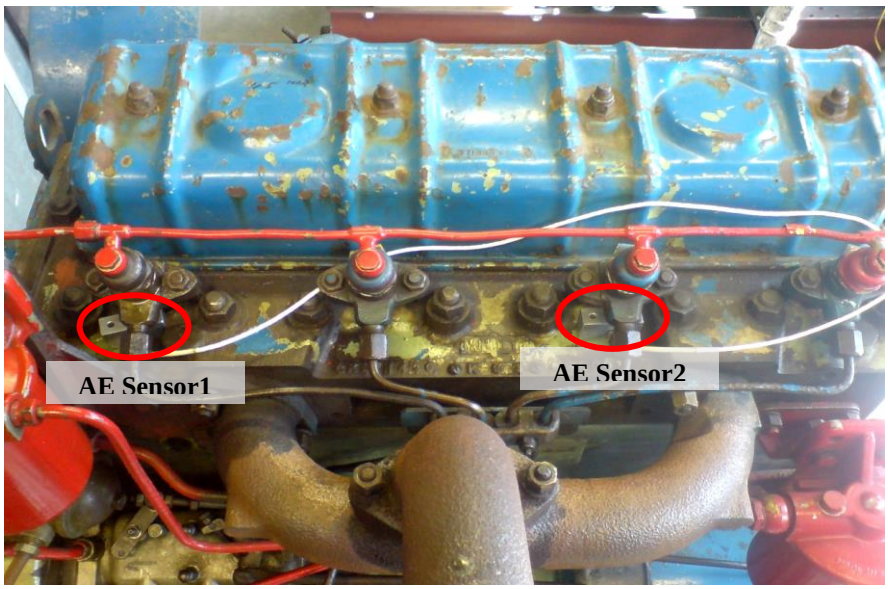

Figure 4.44: Sensor array set up for Perkins A4.270 diesel engine (Engine B).

4.4.4 Perkins T1004 (Engine C)

As the most sophisticated of those studied, this engine was subjected to the most intensive set of experiments, although the extent of the experiments was limited to the no-load condition. Two distinct sets of experiments were done, using two different sensor arrays.

The first set of experiments was performed on this engine with a linear sensor array (sensor array 1), in which sensors 1, 2 and 3 were placed on the top of the cylinder head surface next to injectors 1, 2 and 3, respectively (as shown in Figure 4.45) in a similar style to the tests on Engine C. The engine was again run with no load but with seven different throttle positions of the injection pump, delivering engine speeds of around 730, 850, 1050, 1430, 2060, 2250 and 2500 rpm. Five records were captured for each speed range at a sampling rate of 2.5 MHz for one second, using a total gain setting of 14dB for each sensor (Table B.8 in Appendix B).

The main series of experiments involved monitoring of the running engine using the sensor array shown in Figure 4.46 (sensor array 2), where AE Sensor 1 was placed on the protruding body of Injector 1, and AE Sensors 2 and 3 were placed on similar flat areas on the cylinder head adjacent to Cylinders 1 and 3, respectively. The engine was run with no load at five different throttle positions of the injection pump associated with five camshaft speed ranges around 420, 530, 735, 995 and 1130 rpm. At each speed range, five records were captured at a sampling rate of 2.5 MHz for one second,

corresponding to between seven and nineteen cycles depending on the engine speed. Sensor AES1 used 8dB total signal gain while both AES2 and AES3 required a total signal gain of 14dB (Table B.9 in Appendix B). Again, the crankshaft angular position was acquired synchronously with the AE using the shaft encoder on the injector pump.

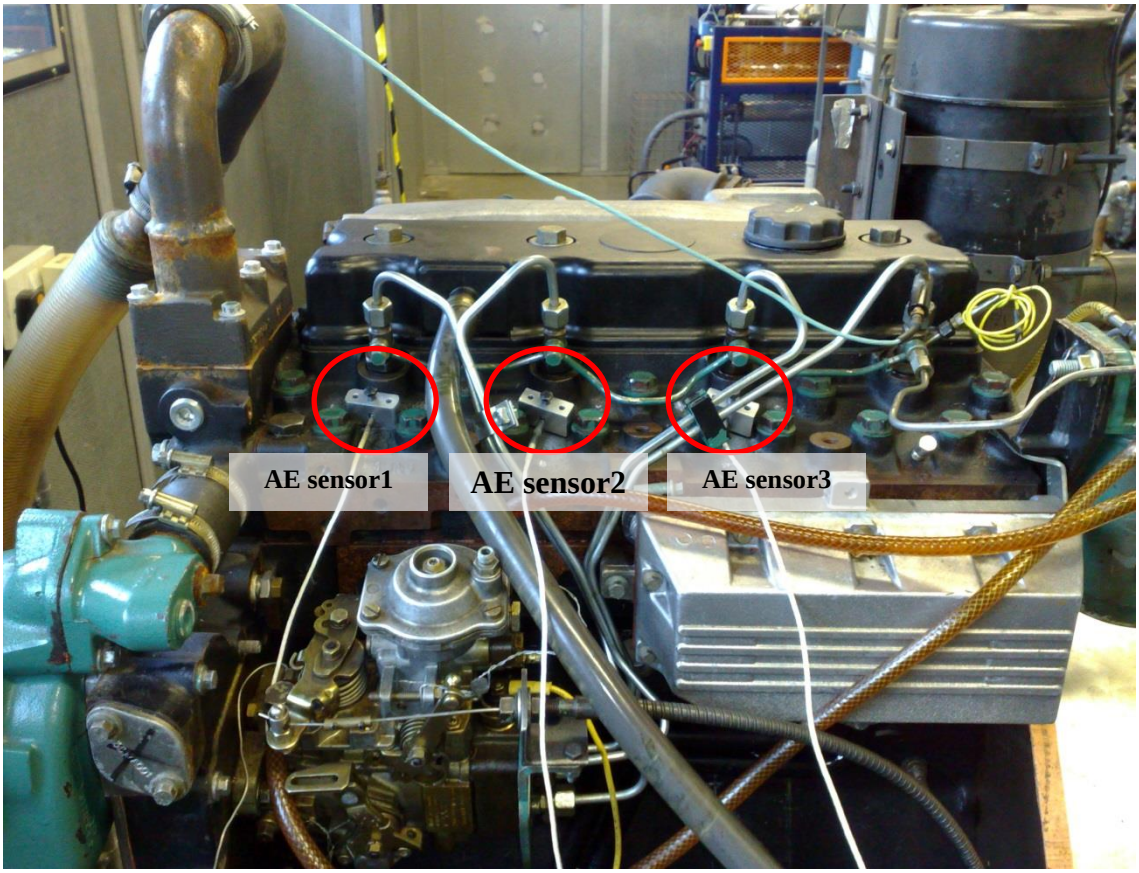

Figure 4.45: Cylinder head linear sensor array 1 set up on Perkins T1004 (Engine C).

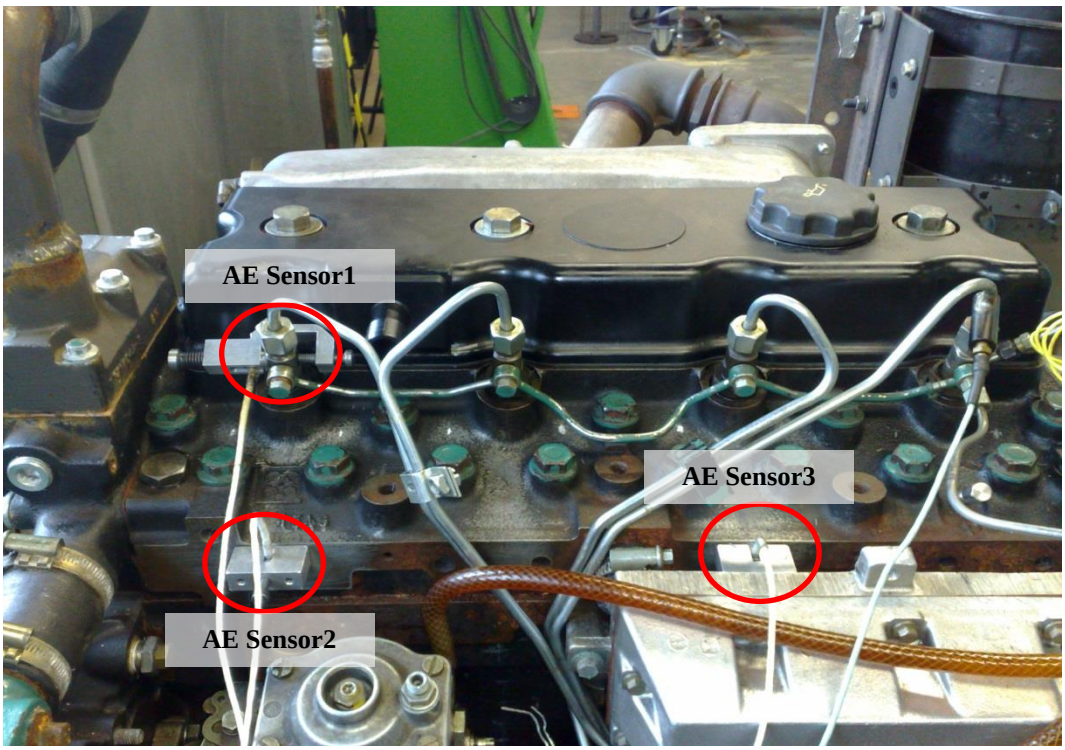

Figure 4.46: Sensor array 2 set up on Perkins T1004 (Engine C).

4.5 Signal Processing

The signal processing used in this work was developed specifically to address the source identification problem for multi-sensor data where there may be multiple sources distributed in time and space. Another feature of the data is that it is structured in a way that is dictated by the (known) behaviour of the engine.

The techniques are described below in three sub-sections, firstly those which have been applied to a single sensor time-series, involving averaging, thresholding, re-sampling, energy analysis and demodulating. Next, a novel application of the canonical correlation technique is described as a way of cross-correlating two time series which are known to represent the same processes.

4.5.1 Single time-series methods

All of the data were acquired above the Nyquist frequency for raw AE, given that the preamplifiers contained analogue filters between 0.1 and 1MHz. This gives enough time resolution to capture the complete waveform of an impulsive source (important in the calibration and time-of flight measurements) as well as providing 3-channel continuous raw capture for around ten cycles in the running engine tests (governed by the performance of the data acquisition system). For such a time series of *y* as a function of *t*, the average energy over a time interval from T_1 to T_2 can be calculated as the root mean square voltage (RMS) [54]

$$y_{RMS} = \sqrt{\frac{1}{N}\sum_{i=1}^{n} {y_i}^2} = \sqrt{\frac{1}{T_1 - T_2}\int_{T_1}^{T_2} [y(t))]^2 dt} \qquad \textbf{4-1}$$

In all of the measurements, it is necessary to determine the energy of all or part of a time series, and this was done using the area under the AE waveform

$$E = \int_0^{t_{lim}} V^2\,(t)dt \qquad \textbf{4-2}$$

where E is the acoustic emission energy in V^2.s, V(t) is the amplitude of the AE signal in volts as a function of time t and t_{lim} is the length of the time period of interest in seconds. Before any processing, all of the signals were re-scaled to unit gain so that the energy is comparable across all tests.

Often, it is of more interest to view signal in the crank angle domain, since most of the processes of interest in the engine are related to angle. Since shaft encoder data was sampled synchronously with AE, it was possible to re-sample the data for constant angle difference (as opposed to time difference) using the scheme shown in Figure 4.47, which is a short segment of raw shaft encoder data, which contains n points, depending on engine speed.

First, two thresholds were set, one of which is only crossed in the upward direction every 360° of engine rotation and the other being crossed every degree of engine rotation. An algorithm was written, which searched for the first upward crossing of

Threshold 1, assigning to that point an angle of 0°. Subsequent crossings of Threshold 2 were assigned to 1°, 2° and so on. Next, the intermediate points were assigned angles by linear interpolation. In general, points will now no longer be an equal angle apart, and so each angle was resampled to a length of 800 points.

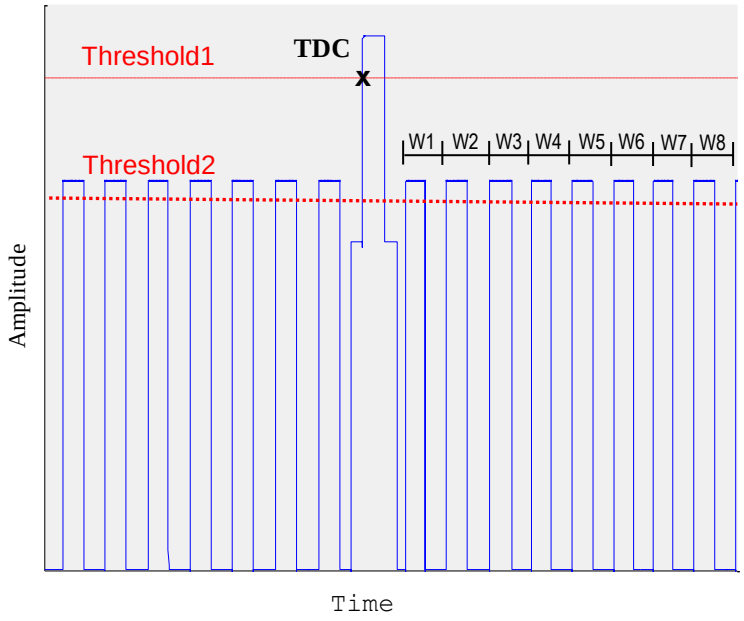

Figure 4.47: Identifying the position of the TDC signal and individual angles using threshold crossing.

Once the AE has been resampled, it is then possible to re-cast the AE energy equation as:

$$E_\theta = \int_{\theta 1}^{\theta 2} V^2(\theta) d\theta \qquad \textbf{4-3}$$

When dealing with the propagative aspect of AE, two key pieces of signal processing are of considerable value. The first of these is about relating the energy content of the signal measured at a specific place on a structure to the energy of the corresponding event(s) [153-156], which needs to take into account various mechanisms of attenuation. In this work, the simplifying assumption is made that most of the AE energy is transmitted in surface waves with the block (solid cylinder, plate or cylinder head) as a semi-infinite medium, and that attenuation can be expressed by a simple absorption law [157]

$$E(x) = E_o e^{-kx} \quad \textbf{4-4}$$

where E(x) is the AE energy a distance x (m) from the source (V^2.s), Eo is the effective AE source energy (V^2.s) and k is an attenuation factor (m^{-1}). Rewriting Equation 4-4:

$$\ln E(x) = \ln E_o - kx \quad \textbf{4-5}$$

which allows k to be determined for a given structure by placing multiple sensors at various distances from a source of fixed energy and short duration (e.g. a pencil lead).

The second important technique in spatial analysis is the location of an "arrival time". More generally, and of more relevance to engine signals where there are a succession of arrivals from different sources with different locations relative to the sensor, this reduces to finding local peaks in the input data [158].

Finally, there are a few instances where a frequency domain analysis of the signal is useful. For the raw AE, where the signal is biopolar, this is a simple matter of performing an FFT on the analogue-filtered signal, yielding a spectrum over the bandwidth of 0.1 to 1MHz. However, the signals in an engine are also modulated at the engine speed, where specific sources appear in a periodic fashion once (or more) per engine revolution and it is of interest to carry out a demodulated spectral analysis. This was done by averaging the signal within a time/angle window to obtain the RMS convolution of the signal which maintains the fundamental features of the original signal, followed by an FFT.

4.5.2 Analysis of pulse train signals

Using Fourier analysis, any periodic signal, *x*(*t*), can be represented as a series of cosine and sine waves, which can be written [159]

$$x(t) = a_o + \sum_{n=1}^{\infty} a_n \cos(2\pi f t n) - \sum_{n=1}^{\infty} b_n \sin(2\pi f t n) \quad \textbf{4-6}$$

where:

$$a_o = \frac{1}{T}\int_{-T/2}^{T/2} x(t)\,dt$$

$$a_n = \frac{2}{T}\int_{-T/2}^{T/2} x(t)\cos\left(\frac{2\pi tn}{T}\right)dt$$

$$b_n = \frac{-2}{T}\int_{-T/2}^{T/2} x(t)\sin\left(\frac{2\pi tn}{T}\right)dt$$

Figure 4.48 illustrates an example of a pulse train signal which has a time period of T (between -T/2 to T/2) and duty cycle $d = k/T$. The frequency domain shows the fundamental frequency and harmonics of the waveform.

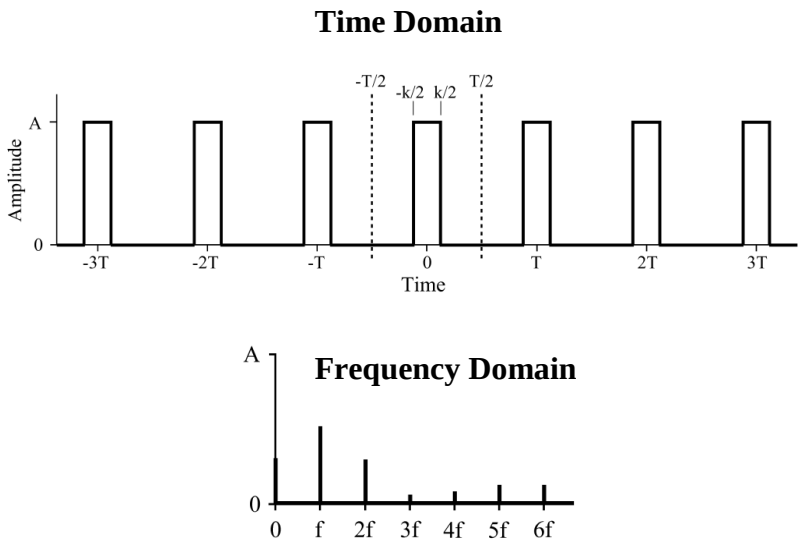

Figure 4.48: Pulse train representation in time and frequency domains. [159]

4.5.3 Canonical correlation analysis (CCA)

Statistical analysis approaches which deal with multivariable problems, such as Principal Component Analysis (PCA) and Partial Least Squares (PLS), have been used widely in process monitoring and fault diagnosis [160]. This study explores a new AE signal processing approach, canonical correlation analysis (CCA), traditionally used in learning applications, particularly image recognition [161]. As far as the author is aware, this application is novel and so it has been named Source Identification using Canonical Correlation Analysis (SICCA).

Canonical correlation analysis (CCA) finds the optimum linear relationship between two multidimensional variables, and can be seen as an extension of Principal Component Analysis, where principal components are first identified from a data set and CCA is a kind of cross-correlation between the PCs of two (or more) data sets [162]. The proposed technique uses CCA to compare two signals at different relative windows to find the optimum relation between these two signals and the corresponding matching features. The important thing about this technique is how it links the multivariate analysis in terms of CCA and the allocation of the signal sources/events in a very accurate manner. In this technique, a set of multi-layer analyses has been implemented to scan the signal where there is very little information provided (e.g. TDC position). The output from each layer was used to improve the next stage, in which the values of the key parameters such as the shift window were improved to increase the accuracy of the output.

The algorithm for the CCA operates to describe the correlation between two sets of variables by finding the optimal bases for the corresponding maximum correlation. For given two sets of variables X and Y, the general form of the canonical correlation can be written as

$$X_1 + X_2 + X_3 + .. + X_n = Y_1 + Y_2 + Y_3 + .. + Y_n \qquad \textbf{4-7}$$

Two sets of canonical coefficients (one for each set of variables) will be calculated to obtain the maximum bases. By applying $a_1, a_2, \ldots, a_n$ to X_n and $b_1, b_2, .., b_n$ to Y_n the maximum correlation will be obtained as

$$CU_1 = a_1X_1 + a_2X_2 + a_3X_3 + .. + a_nX_n$$

$$CV_1 = b_1Y_1 + b_2Y_2 + b_3Y_3 + .. + b_nY_n \qquad \textbf{4-8}$$

where CU_1 and CV_1 are the first canonical variates (bases) and *a* and *b* are the canonical coefficients.

The residuals of the first pair of the canonical variates are then processed similarly to obtain the second pair of the canonical variates. This process will continue until the number of pairs equals n or a significant set point has been achieved.

Similarly, this concept can be applied to two sets of data matrices, x of size ($m \times n_1$) and y of size ($m \times n_2$). First, both x and y need to be normalised

$$\sum_{i=1}^{m} x_{ij} = 0, \quad j = 1, \dots, n_1$$

$$\sum_{i=1}^{m} y_{ij} = 0, \quad j = 1, \dots, n_2$$

4-9

The applied CCA algorithm runs through the data matrices to find the best correlation where the best matched linear combination pair of the x and y coordinates has been found. This will be achieved by obtaining the largest coefficient of correlation which maximises the correlation between the linear composites (canonical variates). The search for other best pairs (second-best, third-best, tec.) will continue in the orthogonal subspaces until the number of pairs is d= min [n_1, n_2]. The result will be two matrices representing the canonical variates; *u* of size $n_1 \times$ d and *v* of size $n_2 \times$ d [163]

$$u = xa, \qquad v = yb$$

4-10

where *a* and *b* are the canonical coefficients.

Both *u* and *v* are orthogonal matrices in successive orthogonal subspaces, so it can be represented as

$$u^T u = 1_d, \quad v^T v = 1_d$$

4-11

where 1_d is the identity matrix in d dimensions

Furthermore, all the columns of *u* and *v* are cross-orthogonal. Thus,

$$u^T v = D$$

4-12

where D is a diagonal matrix in d dimensions.

The best single linear correlation located in the first columns of *a* and *b*, expressed as a_1 and b_1, and can be represented as [163]

$$(a_1\ b_1) = argmax\left[\frac{u_1^T\ v_1}{\sqrt{u_1^T\ u_1}\sqrt{v_1^T\ v_1}}\right] \qquad \textbf{4-13}$$

where u_1 and v_1 are the representation of the maximum canonical variates corresponding *a* and *b*, respectively.

The ***canoncorr*** MATLAB function has been used to calculate the coefficients and variates of the canonical correlation for the data matrices *x* and *y*. The function can be represented as [164]

$$[A, B, r, U, V] = canoncorr(x, y)$$

Where A and B are the canonical coefficients for *x* and *y*, respectively, r is the column matrix containing the canonical correlations and U and V are the canonical variates for *A* and *B*, respectively

The *U* and *V* are n by d matrices computed as [164]

$$U = \big(x - repmat(mean(x), N, 1)\big) * A$$

$$V = (y - repmat(mean(y), N, 1)) * B$$

Figure 4.49 show the results of applying the algorithm to a pair of signals, from a running Perkins T1004 engine (sensor array 2), in which an angle shift has been applied to examine the correlation. The values of the corresponding *U* and *V* were shown (right) along with the confections of regression which are summarised in Figure 4.50, in which there is a significant decrease in the correlation as the angle shift increases. Similarly, shifting the signals in the opposite direction has the same effect as shown in Figures 4.51 and 4.52. This outcome has shown a clear advantage of using CCA to demonstrate a clear correlation which was the inspiration of developing the SICCA algorithm.

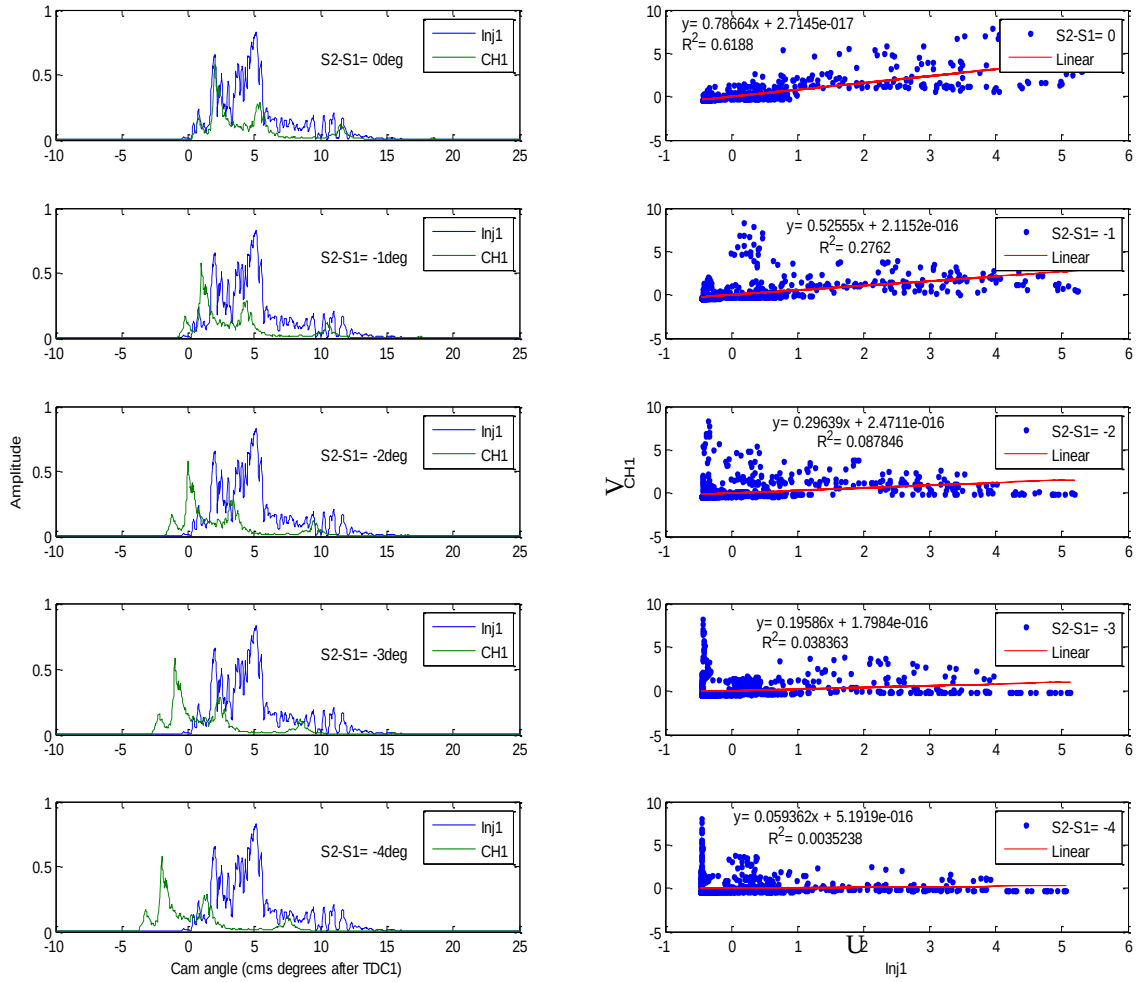

Figure 4.49: Running engine RMS signals (Engine C sensor array2) with different angle shift (left), and the corresponding regression of U-V using canonical correlation (right).

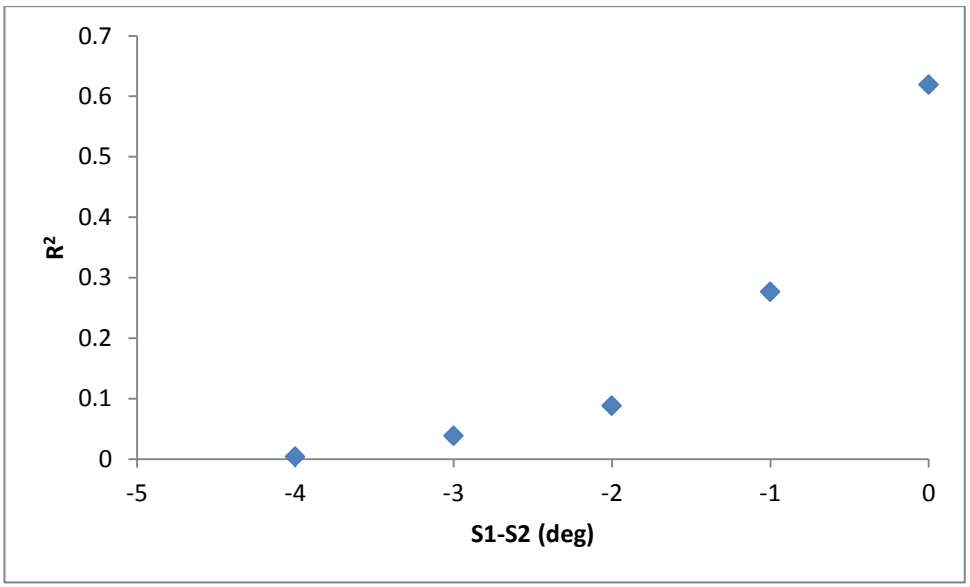

Figure 4.50: Coefficients of regression for the different values of the angle shift in Figure 4.49.

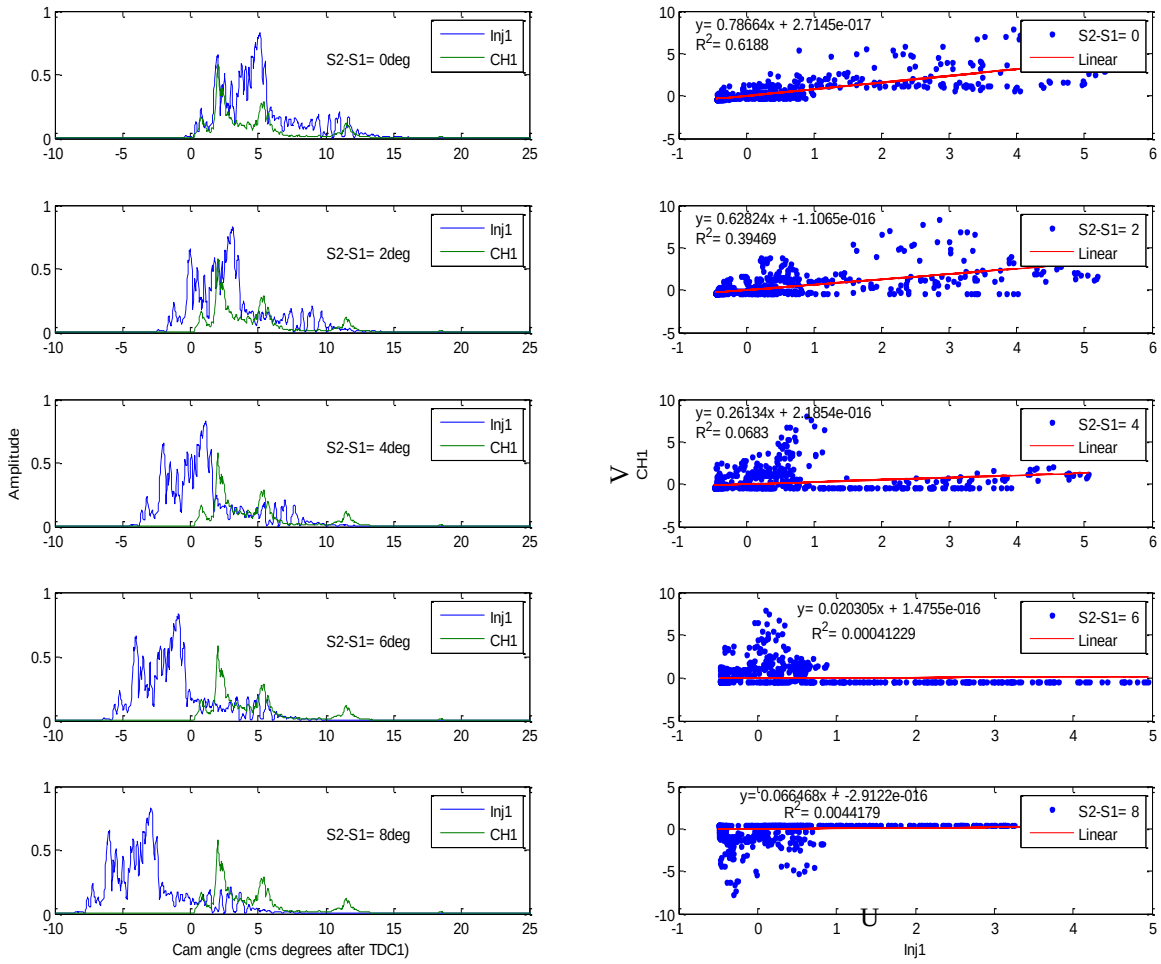

Figure 4.51: Running engine RMS signals (Engine C sensor array2) with different angle shift (left), and the corresponding regression of U-V using canonical correlation (right).

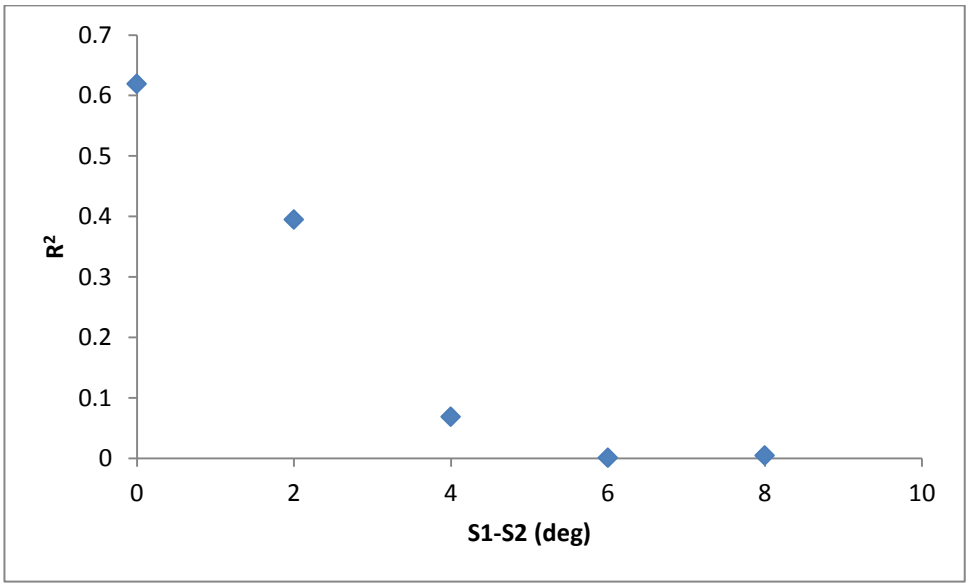

Figure 4.52: Coefficients of regression for the different values of the angle shift in Figure 4.51.

The essential problem to which the SICCA algorithm is to be applied is to take two time series (recorded at two sensor locations) both of which contain transient features arising from one or more sources, potentially at different distances from each of the sensors. Thus, these features will be shifted in time (and angle) as seen by the two sensors, will have different amplitudes (due to attenuation) and multiple features may even have different arrival time differences within each of the time series. Because it is essentially a correlation technique, it was felt best to assess how the analysis performs by simulating a set of different time series, finally testing the algorithm on a well-defined segment of real engine data.

The simplest test consisted of two identical Gaussian pulses with zero mean:

$$y = \frac{A}{\sigma\sqrt{2\pi}}\, e^{\frac{-(x)^2}{2\sigma^2}}$$

and unit standard deviation (σ), unit amplitude (A), with a 160^{o} phase shift. Figures 4.53 and 4.54 show the time series of two pairs of signals with A = 1,1 and A = 3,1, respectively. These figures also show the SICCA output, expressed as the R^2 value for the correlation as the angle difference is stepped (0.08^{o}) from 0 to 360°. As can be seen, each signal pair generates the same narrow peak centred at 160° with a height of R^2 = 1 and a peak width approximately the same as the width of the original peaks in the time series, indicating a perfect correlation at the simulated angle shift, irrespective of the relative "attenuation" of the signals.

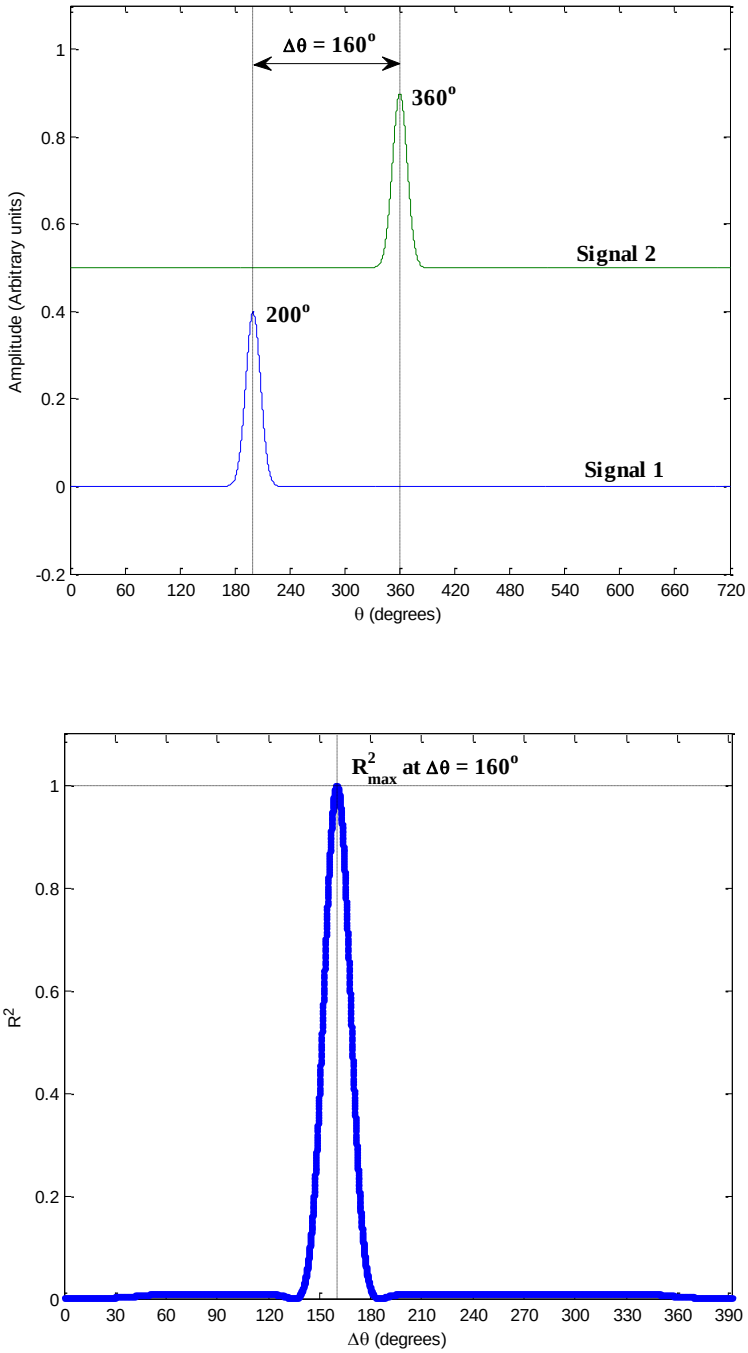

Figure 4.53: Simulated signals (Gaussian pulses) with a phase shift of 160° where both signals have same amplitude (top) along with the corresponding regression using canonical correlation analysis (bottom).

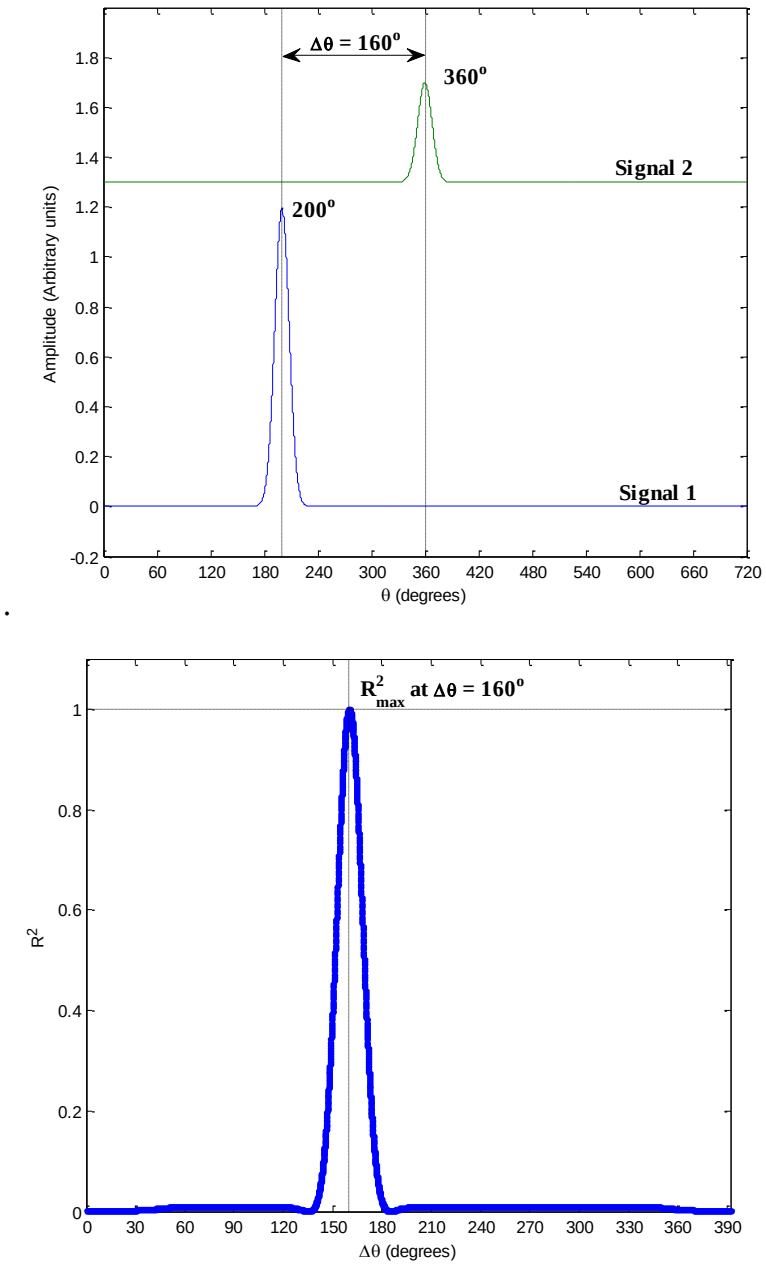

Figure 4.54: Simulated signals (Gaussian pulses) with a phase shift of 160° where signals have different amplitudes (top) along with the corresponding regression using canonical correlation analysis (bottom).

Next, a set of damped oscillations of the form:

$$y = A\, e^{(-Bx)}\, \sin(2\pi f x)$$

were simulated, these being more representative of the shape of an AE burst. Figures 4.55 to 4.59, show the results of applying the SICCA algorithm to a series of signal pairs, all with the same maximum amplitude, *A*, and angle difference (103°), but with varying damping coefficient, *B*, and frequency, *f*. As can be seen, all simulations

produce a precise identification of the angle difference, but with maximum values of R^2 which vary from 0.9 to 0.43. The highest value R^2 occurs when the signals are identical (Figure 4.55), although it might be noted that the peak is very narrow with side peaks arising from the damped oscillations. If the frequency remains the same but one signal is more heavily damped (Figure 4.56), the maximum value of R^2 reduces a little and the peak becomes asymmetric. If the frequencies are different but the attenuation coefficient remains the same, the maximum value of R^2 reduces significantly, although the magnitude of the frequency change appears to have little effect, Figures 4.57 and 4.58. Finally, if both the frequency and attenuation coefficient are changed (Figure 4.59), the maximum value of R^2 reduces still further.

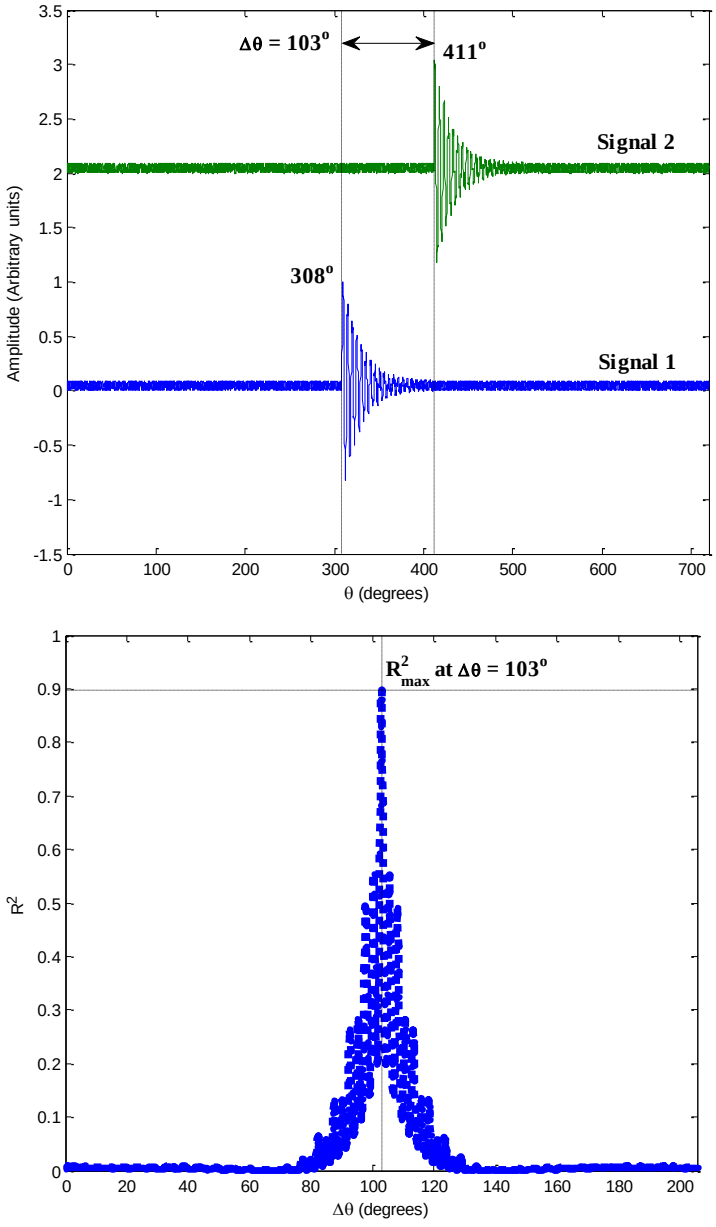

Figure 4.55: Simulated identical damped waveform signals with a phase shift of 103° (top), and the corresponding regression using canonical correlation (bottom).

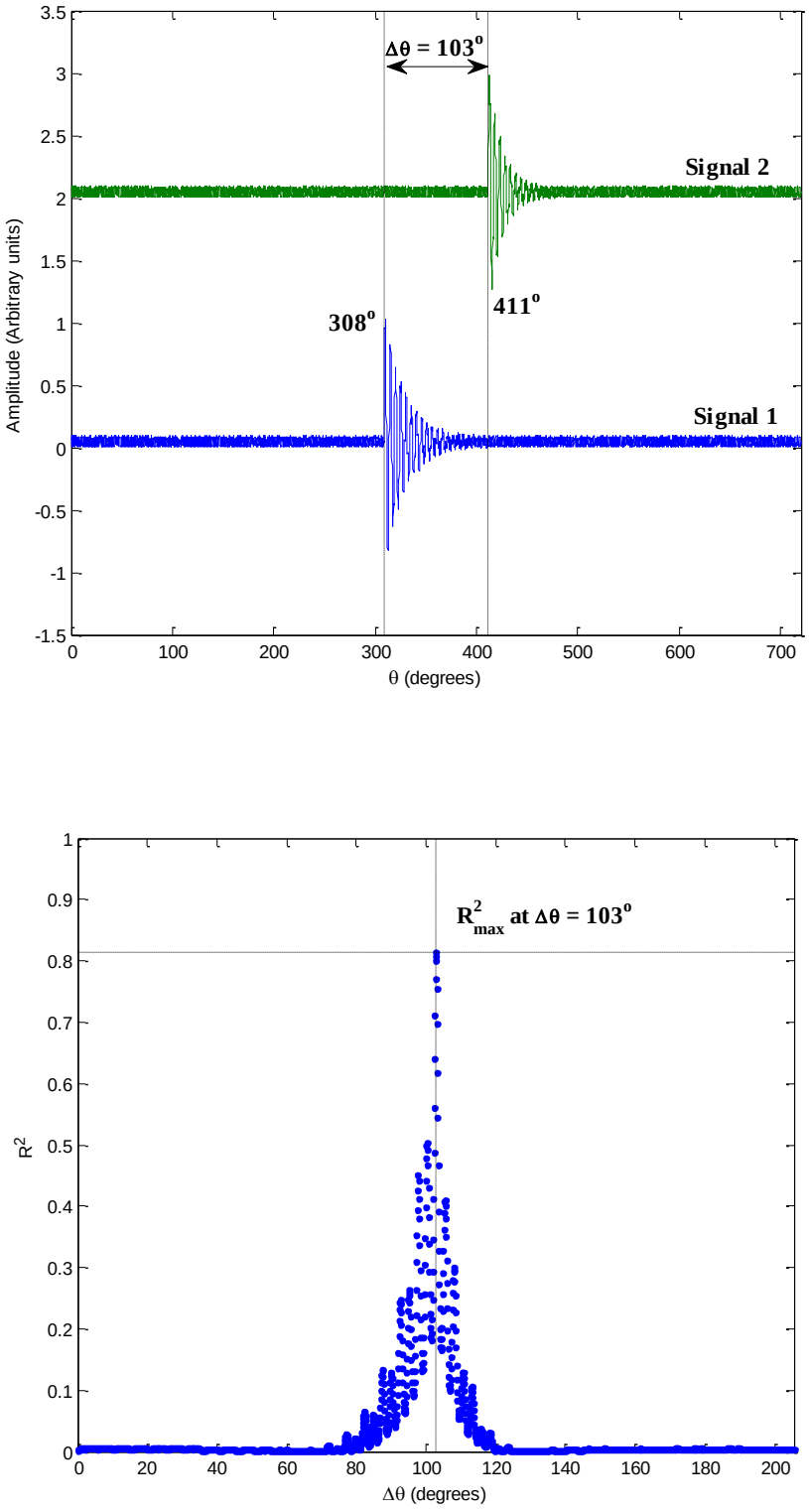

Figure 4.56: Simulated damped waveform signals with a phase shift of 103° and different attenuation factors $B_1 = 5$ and $B_2 = 10$ (top), and the corresponding regression using canonical correlation (bottom).

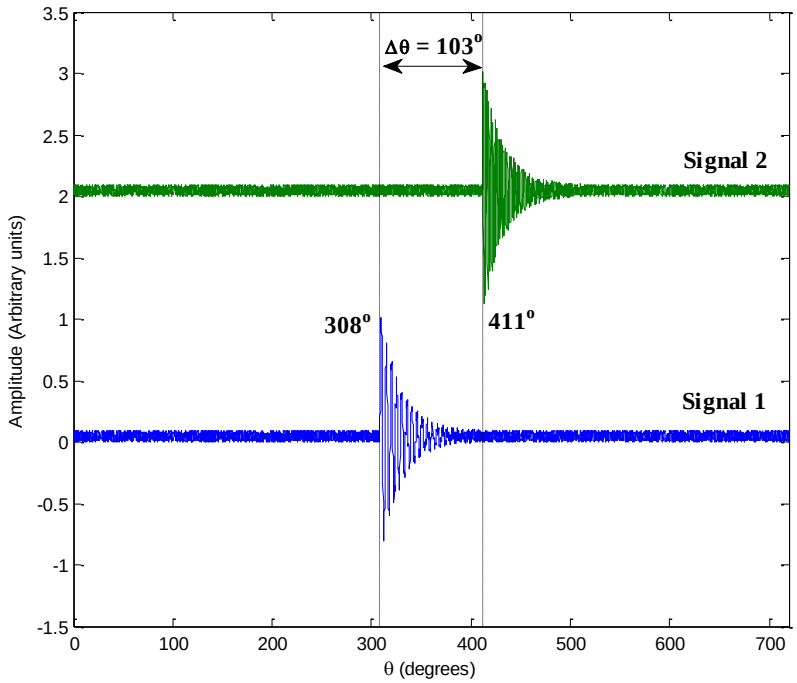

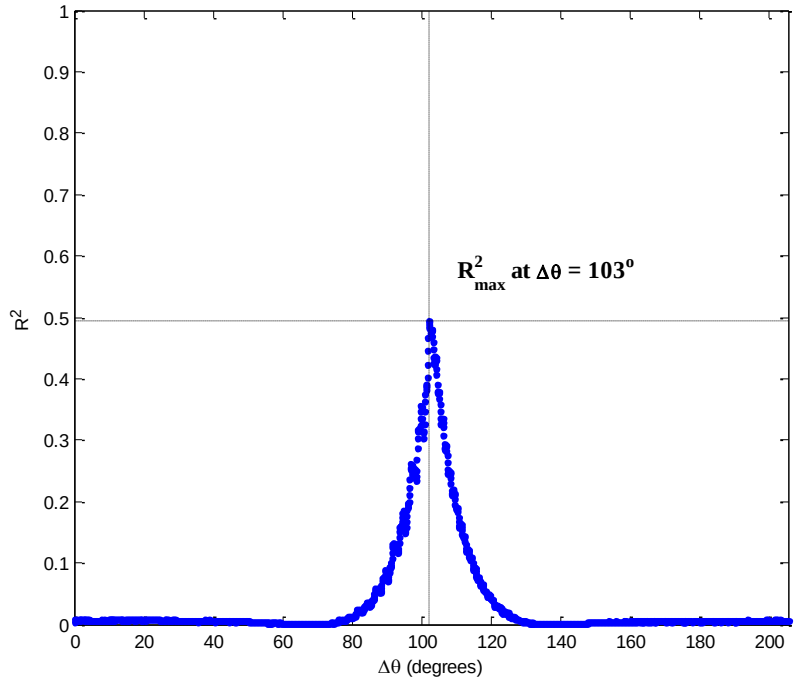

Figure 4.57: Simulated damped waveform signals with a phase shift of 103° with f_1 = 20Hz, f_2 = 50Hz and the same attenuation coefficient B = 5 (top), and the corresponding regression using canonical correlation (bottom).

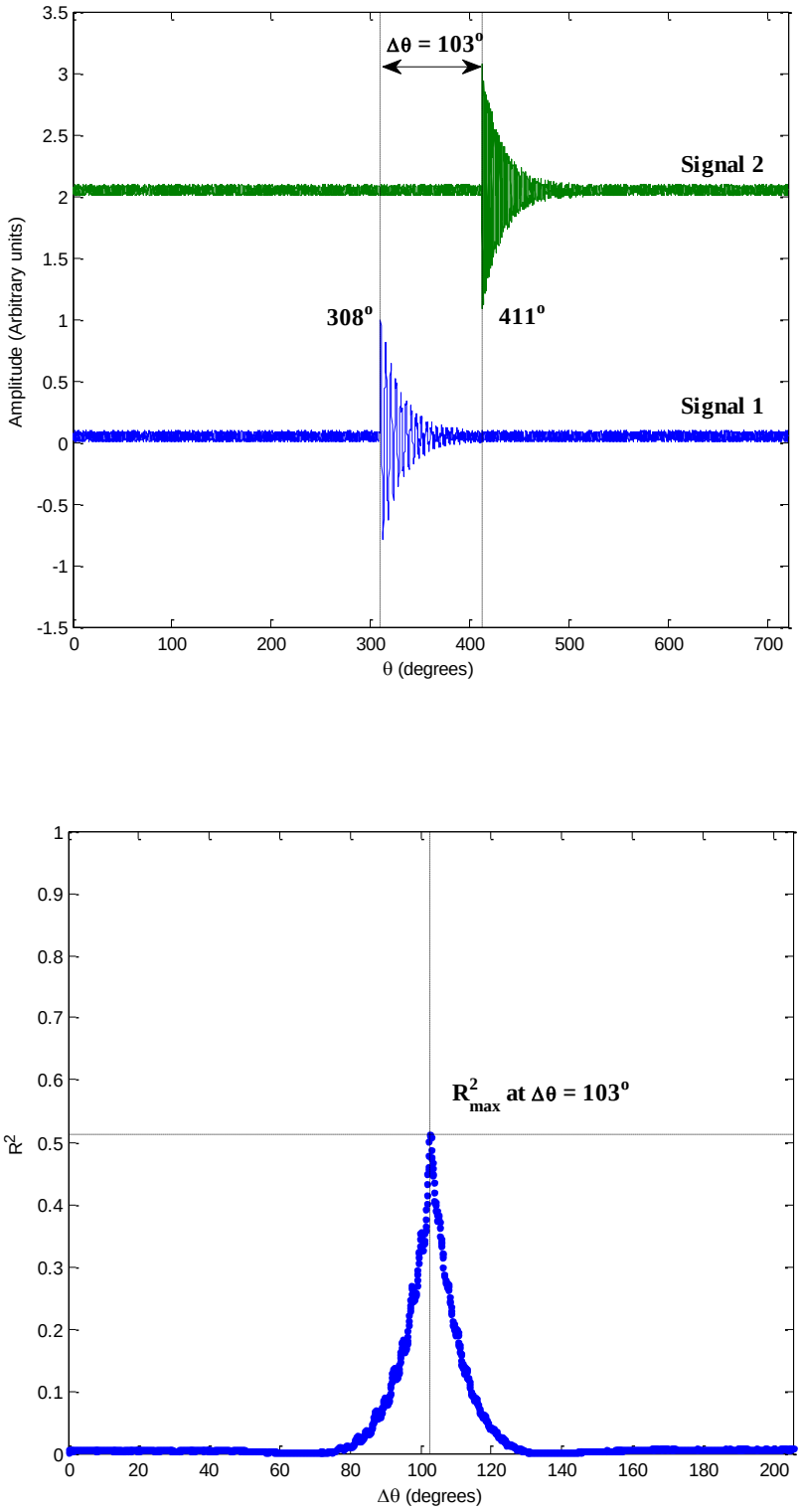

Figure 4.58: Simulated damped waveform signals with a phase shift of 103° with f_1 = 20Hz, f_2 = 120Hz and the same attenuation coefficient B = 5 (top), and the corresponding regression using canonical correlation (bottom).

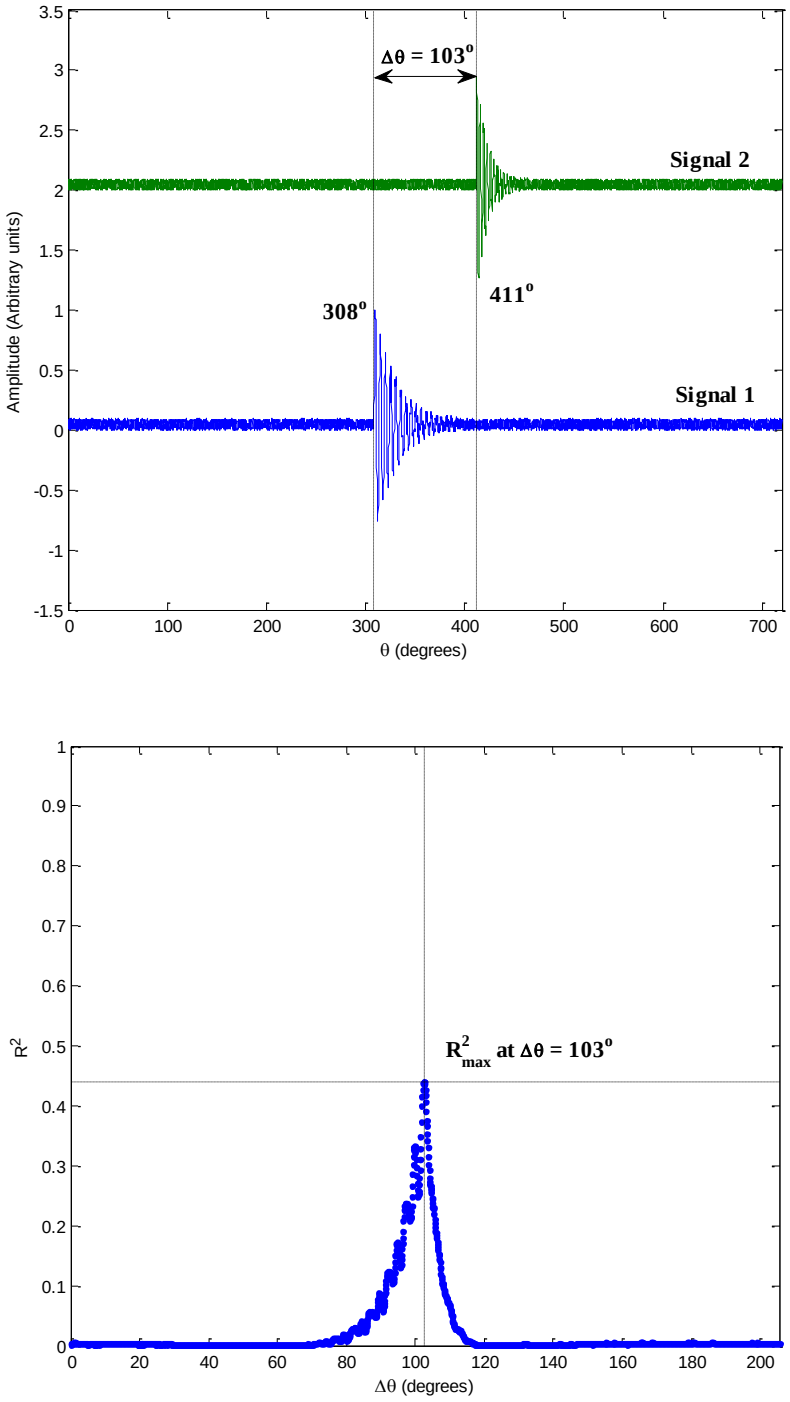

Figure 4.59: Simulated damped waveform signals with a phase shift of 103° with f_1 = 20Hz, f_2 = 30Hz and attenuation coefficients B_1 = 5 and B_2 = 10 (top), and the corresponding regression using canonical correlation (bottom).

The next level of testing involves the more realistic case where the simulated signals contain more than one pulse, thus introducing ambiguities in the correlation, Figures 4.60 to 4.62.

$$y = A_1\, e^{(-Bx)}\, \sin(2\pi f x) + A_2\, e^{(-Bx)}\, \sin(2\pi f x + \varphi)$$

For convenience, all of these simulations used the same frequency and damping coefficient (f = 20Hz and B = 5) while the amplitude factors and phase delays are varied. Figure 4.60 illustrates the case where $A_2 = 0.7A_1$ and φ = 39º for both simulated signals with the second signal lagging by 133º. As can be seen, the SICCA algorithm shows $R^2 = 1$ at the expected phase shift, but also shows two secondary peaks with $R^2 \approx 0.2$, corresponding to the matching of the second peak in Signal 1 with the first peak in Signal 2 and the matching of the first peak in Signal 1 with the second peak in Signal 2.

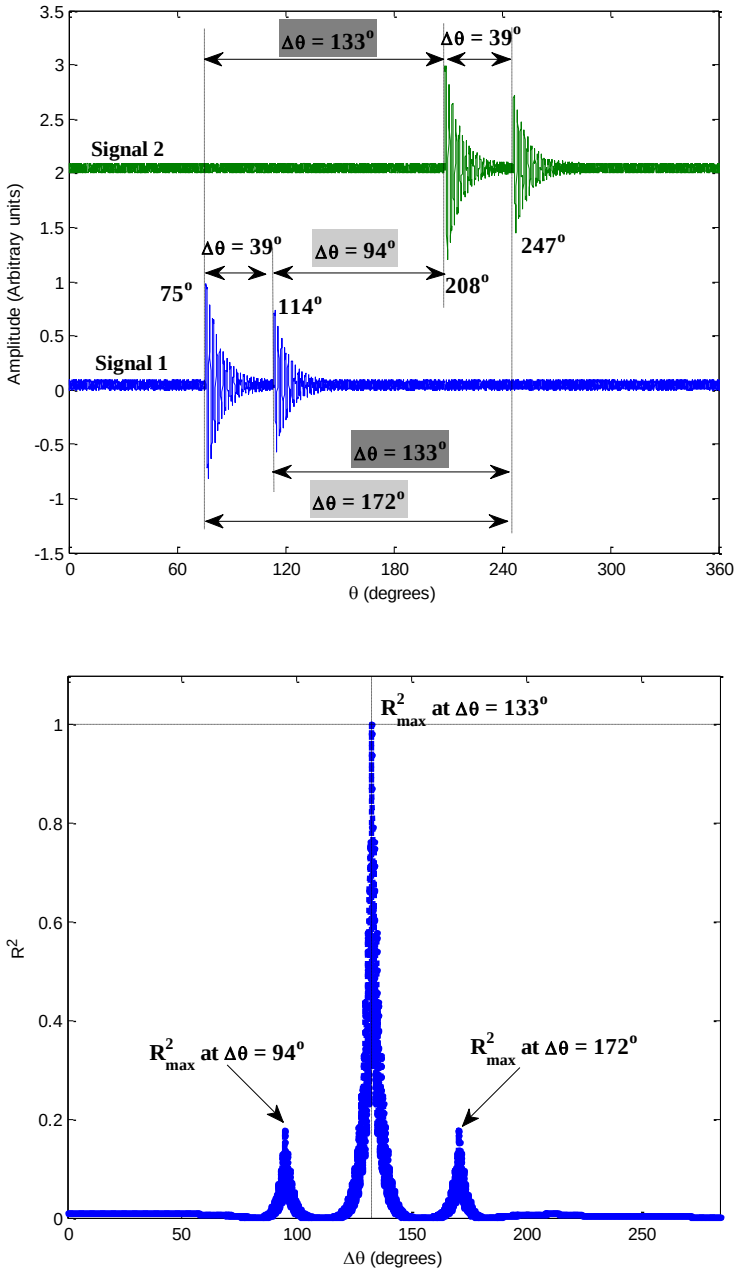

Figure 4.60: Simulated two-component compound damped waveform signals (top), and the corresponding regression using canonical correlation (bottom). $A_2 = 0.7A_1$ and φ = 39º for both simulated signals with the second signal lagging by 133º

In Figure 4.61, the second waveform of Signal 2 has been shifted to φ = 76° retaining φ = 39° for the first waveform. Since the signal can no longer be made to map exactly by a single phase shift, the R^2 value at 133° is considerably reduced (just below 0.4). There are now three alternative (incorrect) mappings, two corresponding to the mapping of the second peak in Signal 1 with the first peak in Signal 2 and the mapping of the first peak in Signal 1 with the second peak in Signal 2, as before, again with $R^2 \approx 0.2$. The third mapping is at a slightly lower R^2 value and corresponds to the mapping of the second peak in Signal 1 with the second peak in Signal 2.

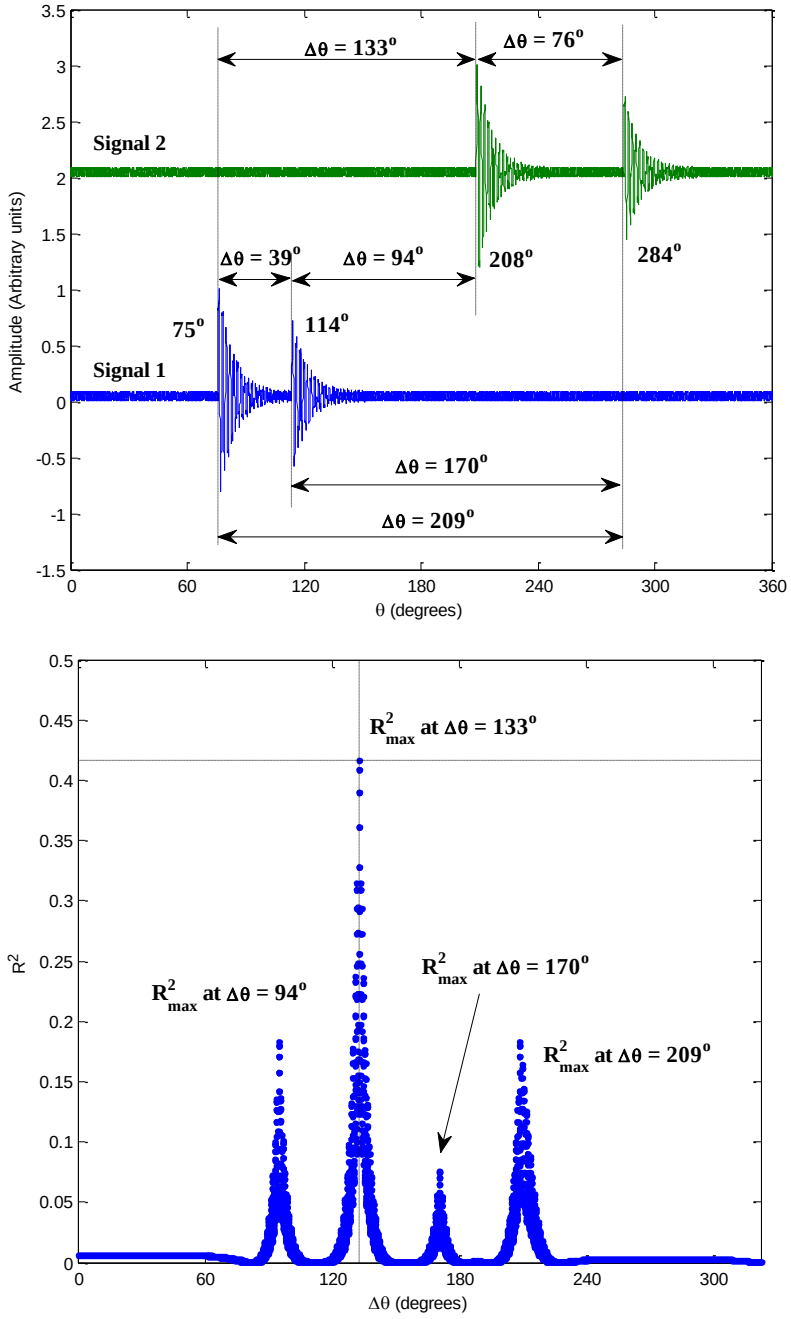

Figure 4.61: Simulated two-component compound damped waveform signals with the second signal lagging by 133° (top), and the corresponding regression using canonical correlation (bottom). $A_2 = 0.7A_1$ for both simulated signals, φ = 39° for Signal 1 and φ = 76° for Signal 2.

Figure 4.62 shows the effect of reducing the significance of the second waveform in the series, keeping the other parameters the same. As can be seen, this increases the confidence of the correct interpretation to $R^2 \approx 0.7$, whereas the incorrect interpretation values are diminished, the correlation between the two minor peaks being almost zero (as the square of the two minor amplitudes). It might be noted that the focus could be put on the minor peaks simply by windowing the time (or angle), as will be discussed later.

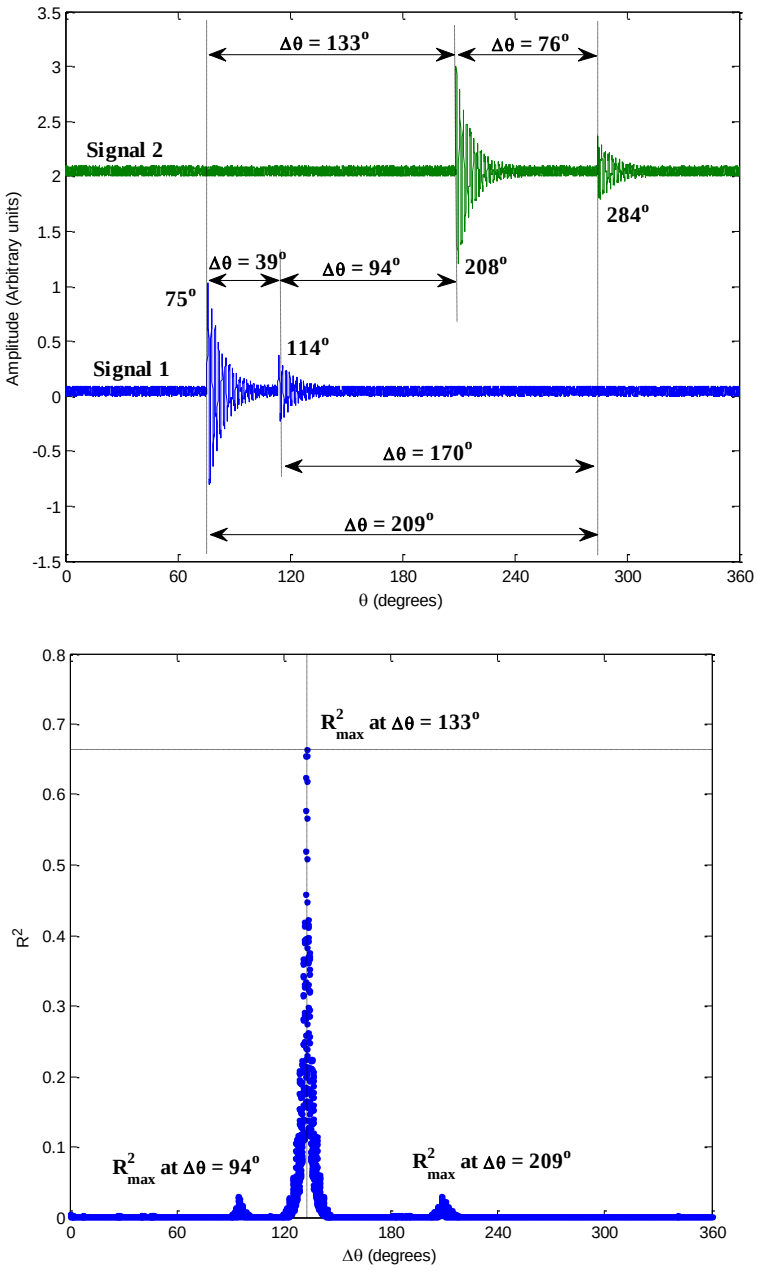

Figure 4.62: Simulated two-component compound damped waveform signals with the second signal lagging by 133° (top), and the corresponding regression using canonical correlation (bottom). Parameters as for Figure 4.61, except that $A_2 = 0.3A_1$ for.

The final stage of testing the algorithm was carried out using an example of actual AE signals captured from a running engine. Figure 4.63 shows a half-cycle angle series of raw AE from Engine B, for sensors mounted on the side face of the cylinder head adjacent to cylinders 1 (CH1) and 3 (CH3). At this relatively coarse angle scale it can be seen that there are two pulses, separated by 90^o, corresponding to TDC in Cylinder 1 and Cylinder 3 (firing order 1, 3, 4, 2). The SICCA algorithm has indicated a high ($R^2 \approx 0.7$) confidence that the two series are either separated by 0^o or 90^o, as opposed to the known outcome that they are approximately 0^o apart. The reason for the ambivalent answer is that, unlike the simulation shown in Figure 4.60, the smaller and larger peaks are in the opposite sequence. This shows the need to combine calibration data with CCA, which, in this case would have been able to correct the two series to show pulses of approximately equal height in each series. However, as will be seen later, the strength of CCA lies in a more detailed analysis at the event level to explore the structure of the two sub-peaks visible in Figure 4.63, where the source location is unknown.

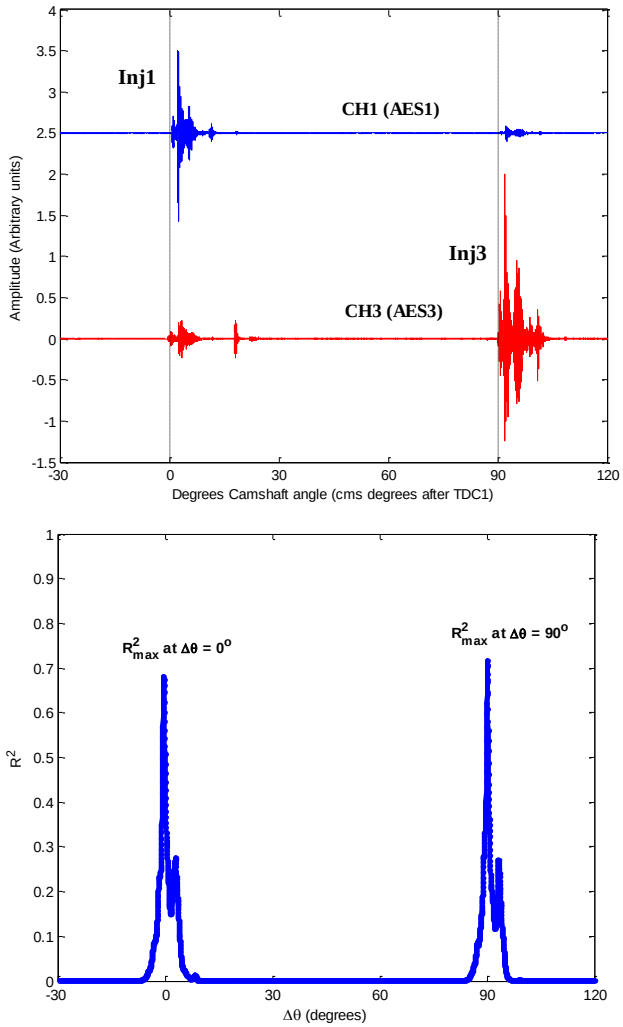

Figure 4.63: Running engine signals (Engine C sensor array1) (top), and the corresponding regression using canonical correlation (bottom).

Chapter 5

Analytical discussion of the results of a two stroke Diesel engine and injector rig experiments

Despite the fact that AE has been found useful in engine condition monitoring, there remain challenges in detailed, automated AE signal interpretation from more complex sources such as the injection and combustion events in diesel engines. In this chapter the experiments with the fewest sources/events are considered; the injector rig, where there is only fuel injection event and associated activity in the pump, and the two stroke engine which is less complex than the four stroke engines considered in the next chapter.

First, the results from injector rig experiments are discussed with a view to isolating the AE characteristics of diesel injection, isolated from the closely related valve and combustions events. Next, the two stroke engine is considered using both conventional time and frequency domain techniques and also to introduce the SICCA algorithm to study the injection/combustion events.

5.1 Injector rig experiments

Figures 5.1 to 5.3 show the three sensor arrays used on the injector rig; Experiments 1 and 2 using sensors on the output part of the pump and on the injector with and without a pressure transducer in the line, and Experiment 3 using sensors mounted on one of the dummy injectors as well as the test injector. The injection events, identifiable from the shaft encoder signal, were observed clearly for all pump (camshaft) speeds at both sensors (Figures 5.4 to 5.6). Figure 5.4 shows clear pulses at the injector shortly after the pulse in the pressure in the delivery pipe, but also shows significant AE recorded at the pump, not only associated with delivery to Injector 1. This can be seen more clearly in Figure 5.5 (where the pressure transducer is absent) re-cast into the angle domain. The pulses at the pump are quite complex, but are clearly spaced about 90° apart and are probably associated with the opening and closing of the respective pressure ports. There are clearly also seen (much attenuated) at the injector, but there is additional AE at the injector around its expected opening. Comparing two different injectors over a longer timescale (Figure 5.6) shows the injector signal closer to the pump to be more heavily contaminated by AE from the pump.

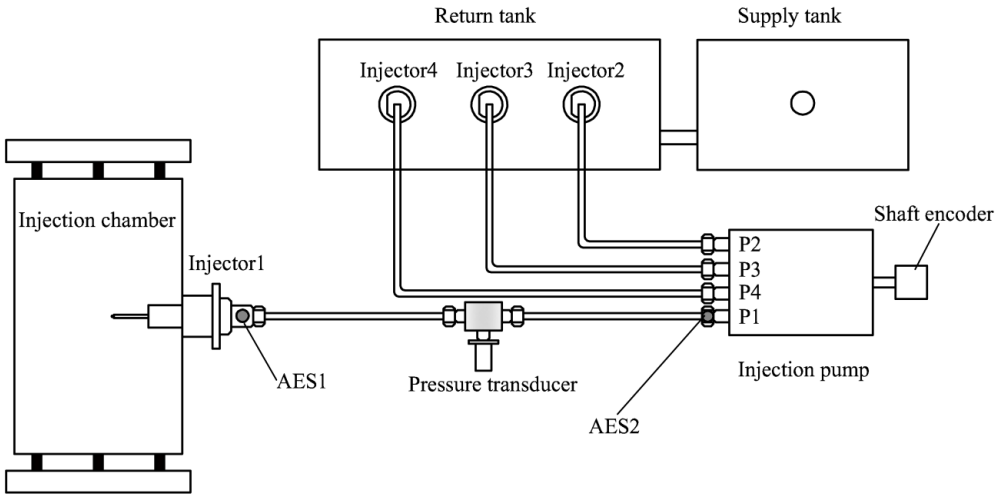

Figure 5.1: Schematic diagram of the experimental injector rig for Experiment 1 showing the AE sensor array.

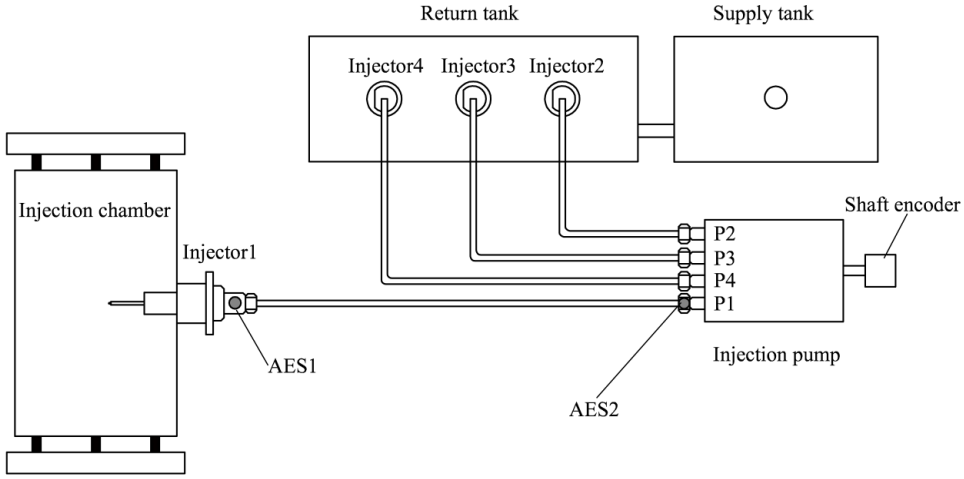

Figure 5.2: Schematic diagram of the experimental injector rig for Experiment 2 showing the AE sensor array.

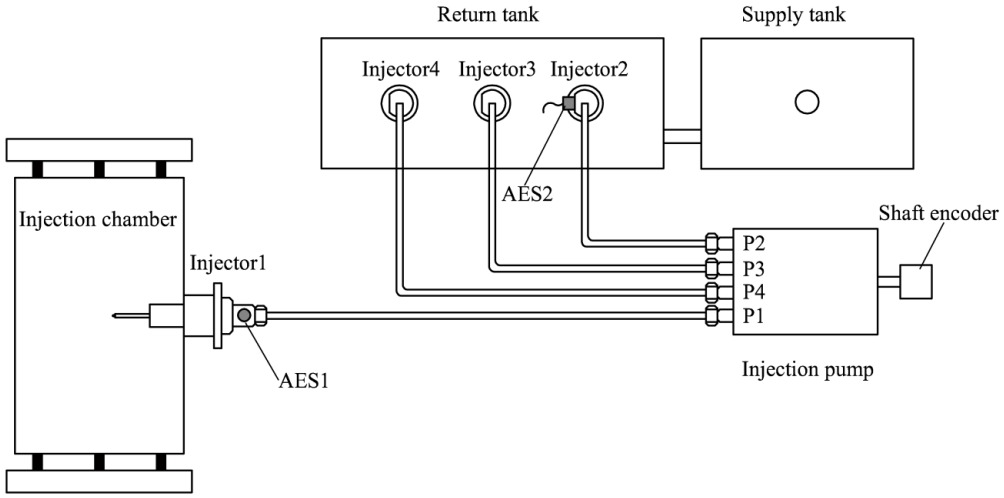

Figure 5.3: Schematic diagram of the experimental injector rig for Experiment 3 showing the AE sensor array.

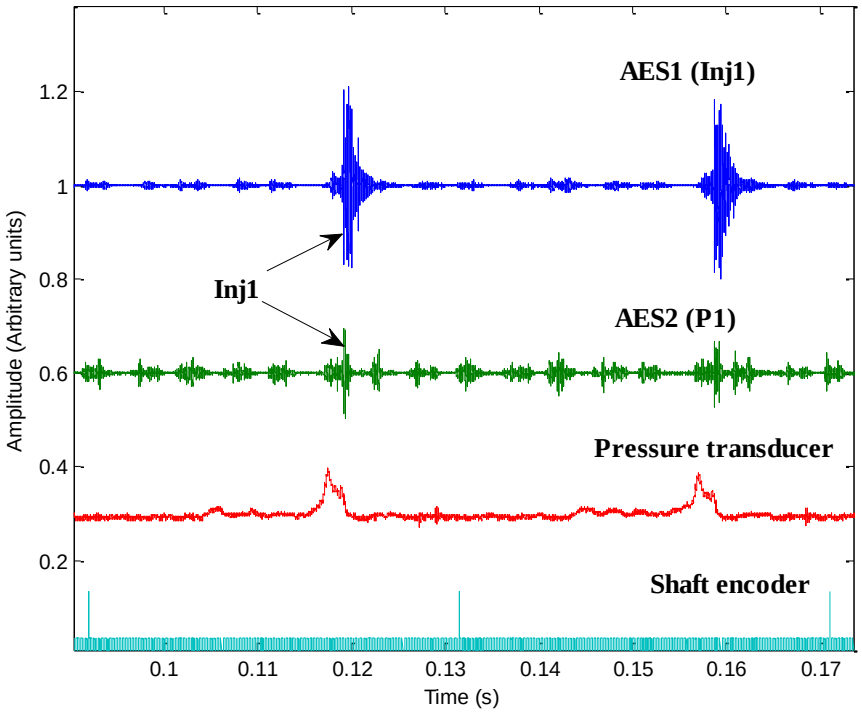

Figure 5.4: Raw AE signals acquired from the injector rig (Experiment 1) at a pump (camshaft) speed of 1525rpm.

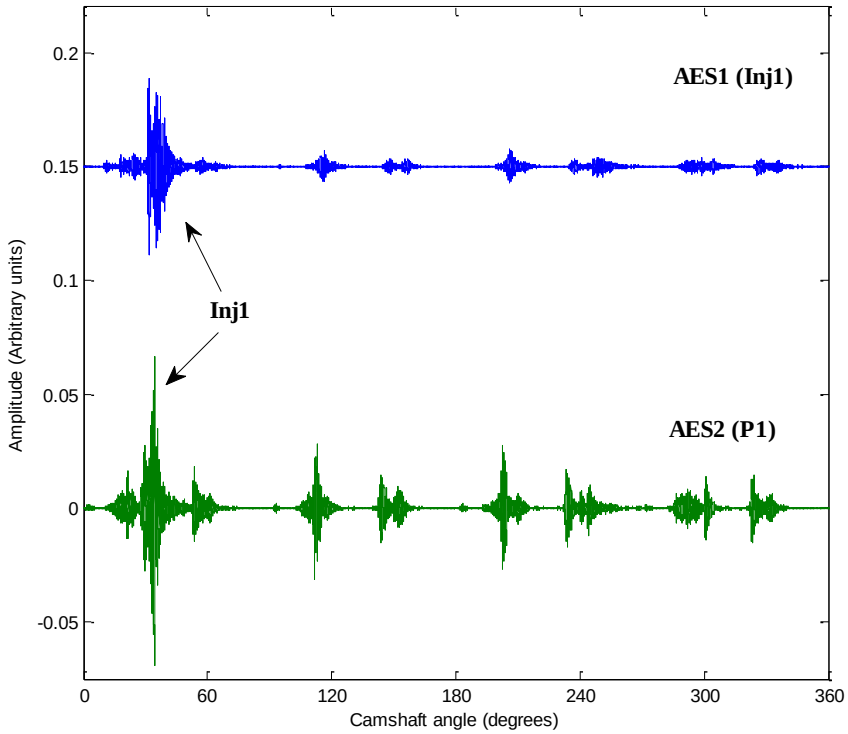

Figure 5.5: Example of the raw AE signal for one complete injection pump cycle from the injector rig, Experiment 2 at a pump (camshaft) speed of 1272rpm.

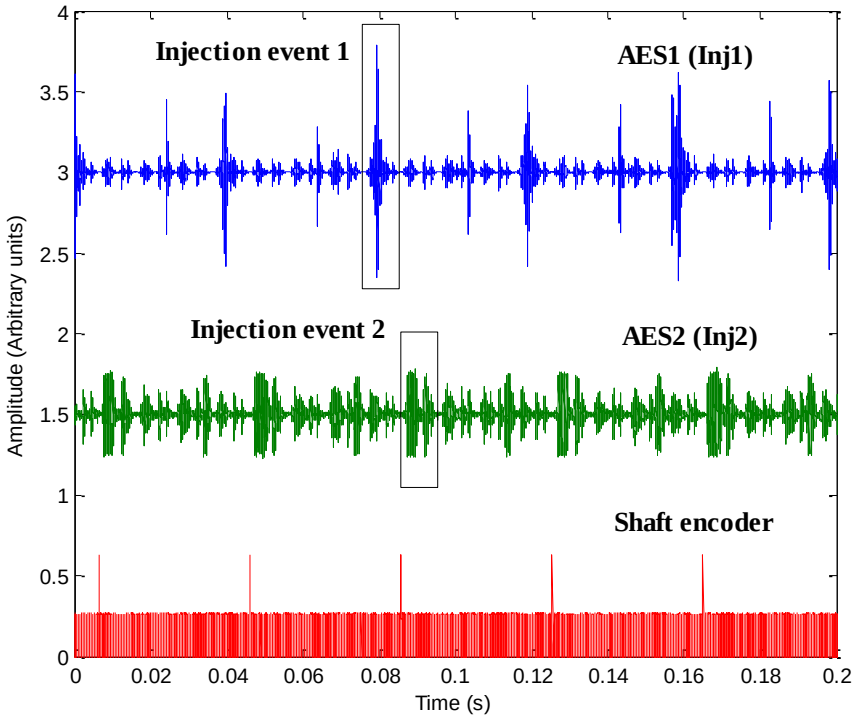

Figure 5.6: Raw AE signals acquired from two injectors on the injector rig, Experiment 3 at a pump (camshaft) speed of 1517rpm.

5.1.1 AE energy analysis for injector rig

Figure 5.7 shows example records from the pressure transducer on the fuel line to Injector 1 (the monitored injector) for the effective cam angle range from 200° to about 350°, covering the period when Injector 1 opens and also when the following injector (Injector 3) drains into the return tank. In this experiment, the electric motor operated at two speed settings where the fuel throttle were varied between partial and fully opened positions. As a result, four settings can be seen in Figure 5.7 where the high motor speed with partially and fully open throttle settings were shown as 2210 rpm and 2200 rpm, respectively, and the lower motor speed with partially and fully open throttle settings were shown as 1525 rpm and 1458 rpm, respectively. Clearly, the port-opening in the pump corresponds to a rise in pressure in the fuel line being monitored, followed by a fall back to the baseline value. Both the rise and fall in pressure are somewhat erratic but the peak pressure appears to be higher at the higher pump speeds.

Figure 5.8 shows example AE records equivalent to the pressure records in Figure 5.7. Although the AE is clearly related to the pressure trace, it is both delayed and extended in duration relative to it. The delay might be explained by the fact that the pressure

pulse has to travel from the transducer (mid-way along the fuel line) to the injector and this is consistent with the delay being longer (in crank angle terms) when the motor is running faster. The extended duration is more apparent at the higher speeds and seems to be associated with the secondary peaks seen in the pressure traces. These secondary peaks could be caused by reflections of the primary pressure wave causing re-opening of the injector. Overall, the evidence seems to be consistent with the AE resulting from flow of fuel through the injector, although a contribution from spring rubbing or scratching cannot be ruled out.

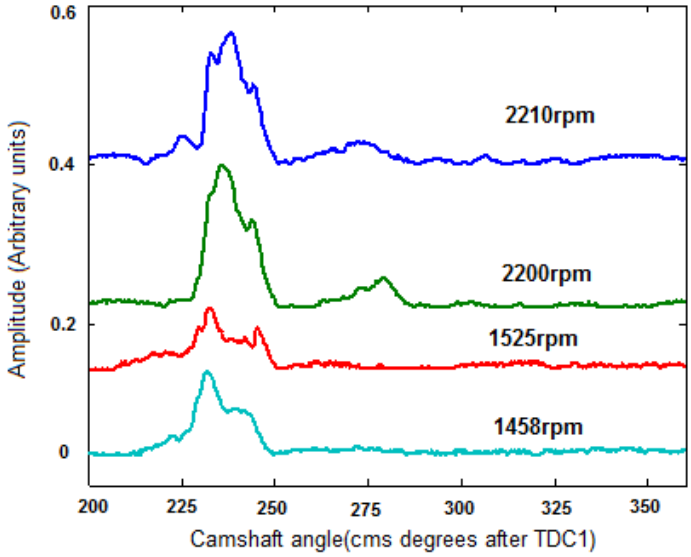

Figure 5.7: Pressure transducer outputs around the time of opening of the monitored injector on the injector rig Experiment 1. (Curves offset vertically for clarity.)

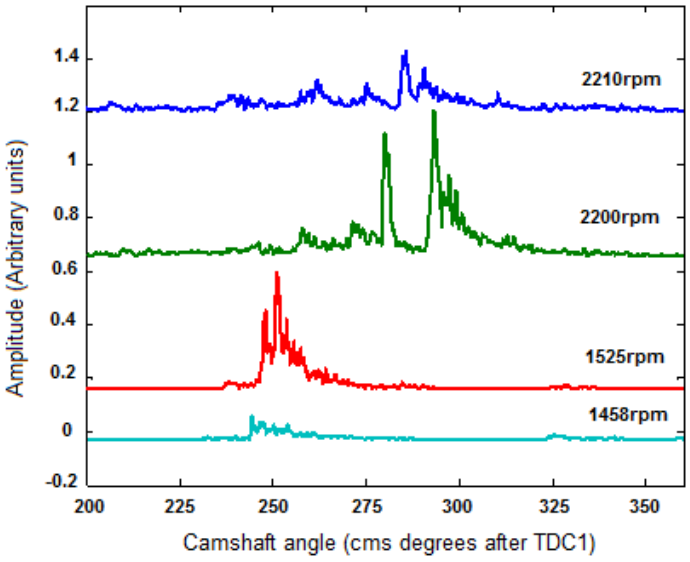

Figure 5.8: Acoustic emission recorded at Sensor 1 around the time of opening of the monitored injector in the injector rig Experiment 1. (Curves offset vertically for clarity.)

Figure 5.9 shows a typical raw AE angle series for the region around injection for each of the speeds used in Experiment 3 and it is clear that increased speed leads to increased amplitude and duration, suggesting that a simple energy analysis would show a clear effect with speed. To study each individual injection event, a constant time window of 9.5 ms was applied to the peak raw AE signal corresponding to injection event 1 which was selected based on the information acquired from the shaft encoder signal, Figure 5.10. A more automated algorithm was implemented to detect the individual injection events which used the RMS convolution obtained by applying a moving average of 100 points to the raw signal and split the event window, auto-selected based on the detected engine speed, into two adjacent phases, representing the starting and ending of the event, as shown in Figure 5.11. A different adaptive threshold was then applied to each of these phases, its value depending on the running speed, the type of the window (start or end), the peak value of the event window and the positions of the local maximum and minimum signal values within each phase. This provides an objective and automatable way of identifying the start and end points of the injection event and the AE energy calculated in this way is compared with that determined by inspection.

Figures 5.12 and 5.13 show, for Experiments 1 and 3, the effect of camshaft speed on energy of the injection event using a fixed time window as well as the adaptive threshold time window. Although there are some differences between the two types of threshold, it is clear that the adaptive one, which can be used automatically, is adequate for showing evolutions of energy in a way that does not involve the (subjective) judgement of the user.

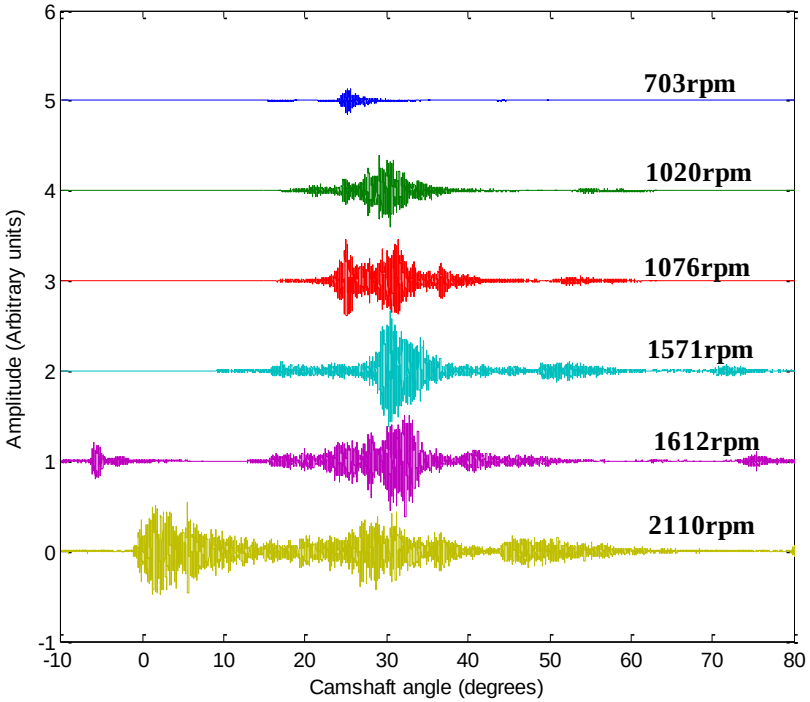

Figure 5.9: Raw AE signal recorded at Injector1 from Experiment 3 showing the injection window for all the acquired speeds in the angle domain.

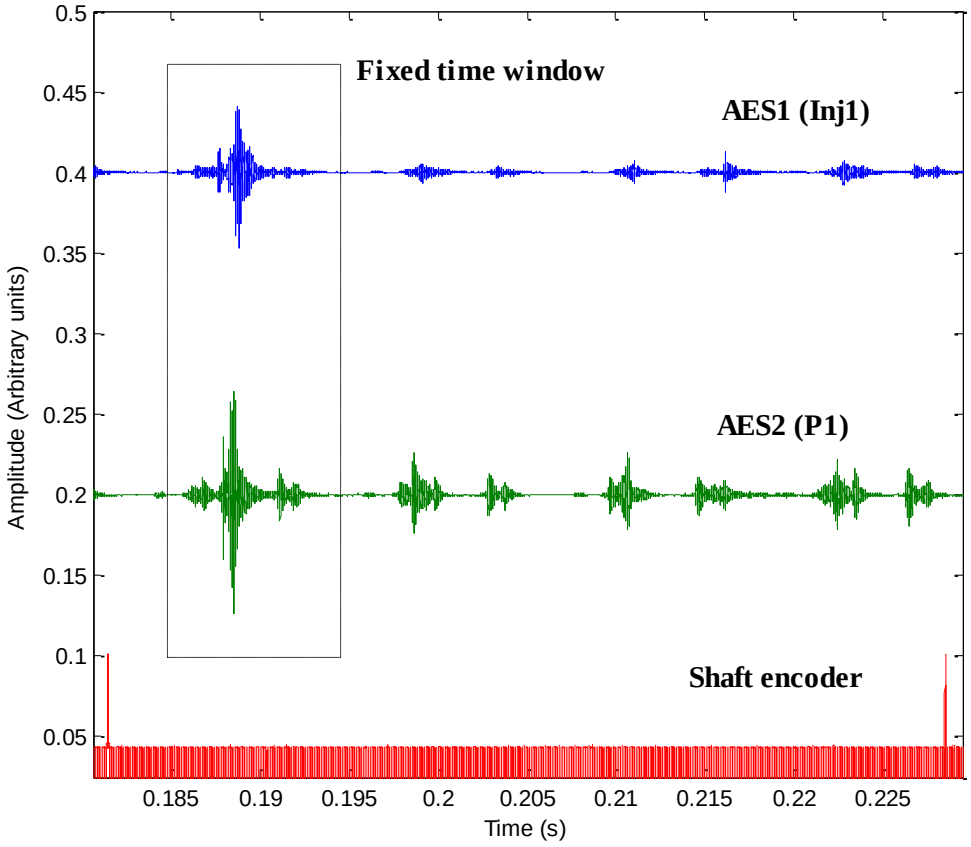

Figure 5.10: Fixed time window of 9.5ms applied to the raw AE signal from injector rig Experiment 2 at 1272 rpm in the time domain.

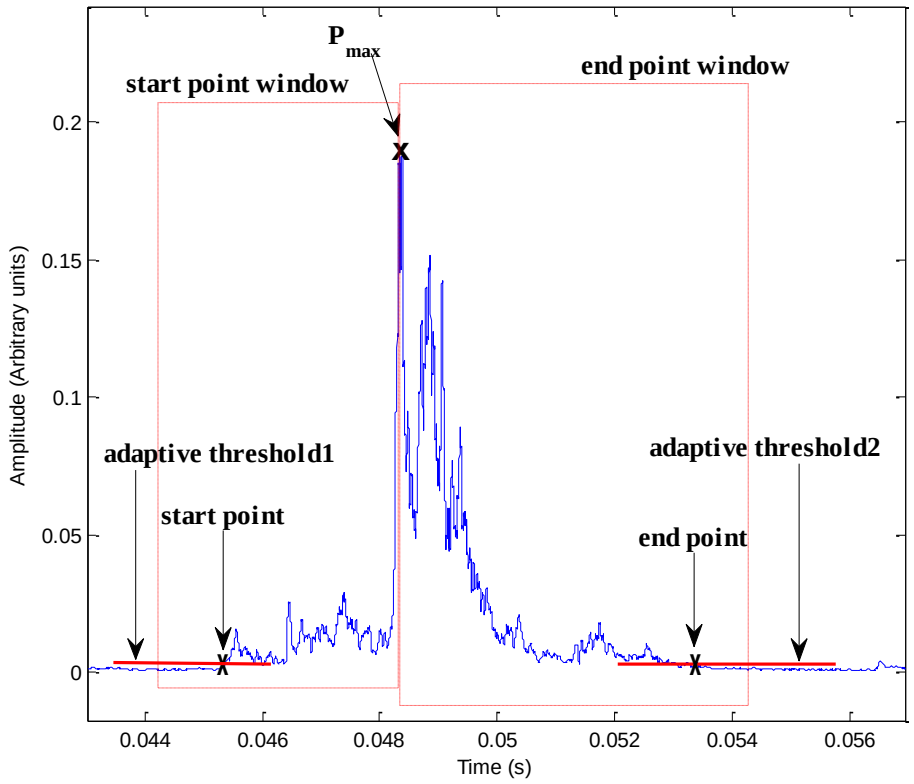

Figure 5.11: Adaptive threshold technique applied to the 100-point RMS signal from injector rig Experiment 2 at 1272 rpm in the time domain.

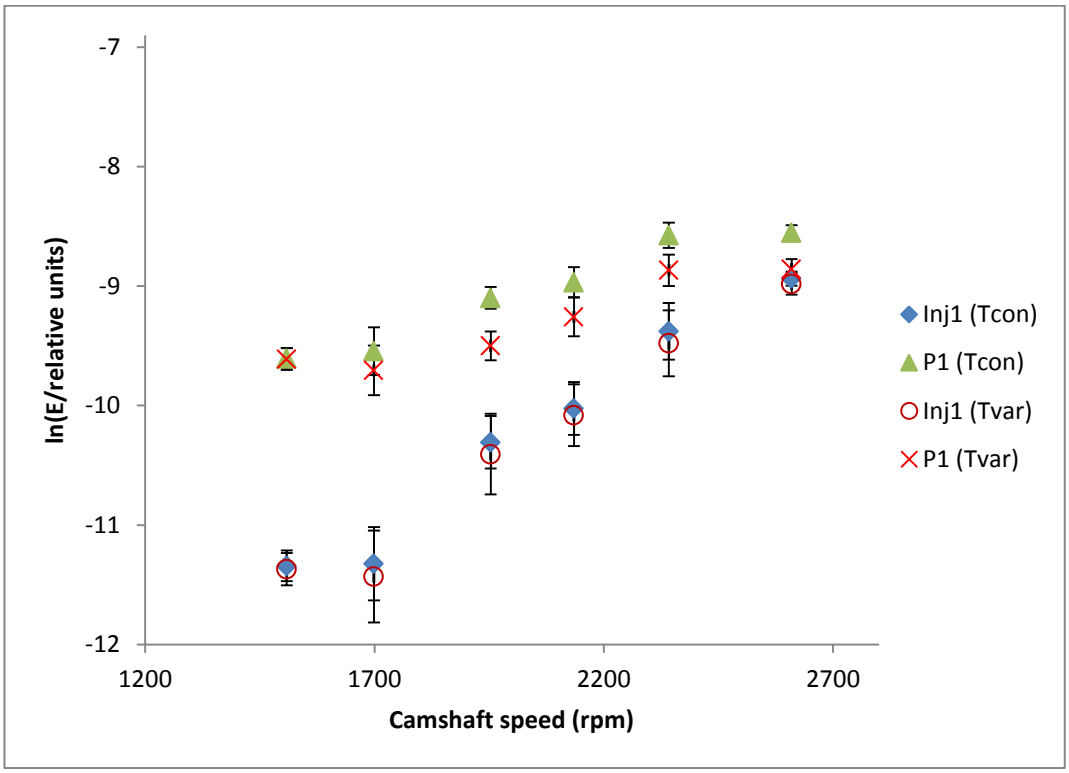

Figure 5.12: Averaged AE energy of the Injector1 event recorded at pump and injector during injector rig Experiment 1, calculated using fixed-time (Tcon) and adaptive threshold (Tvar) windows.

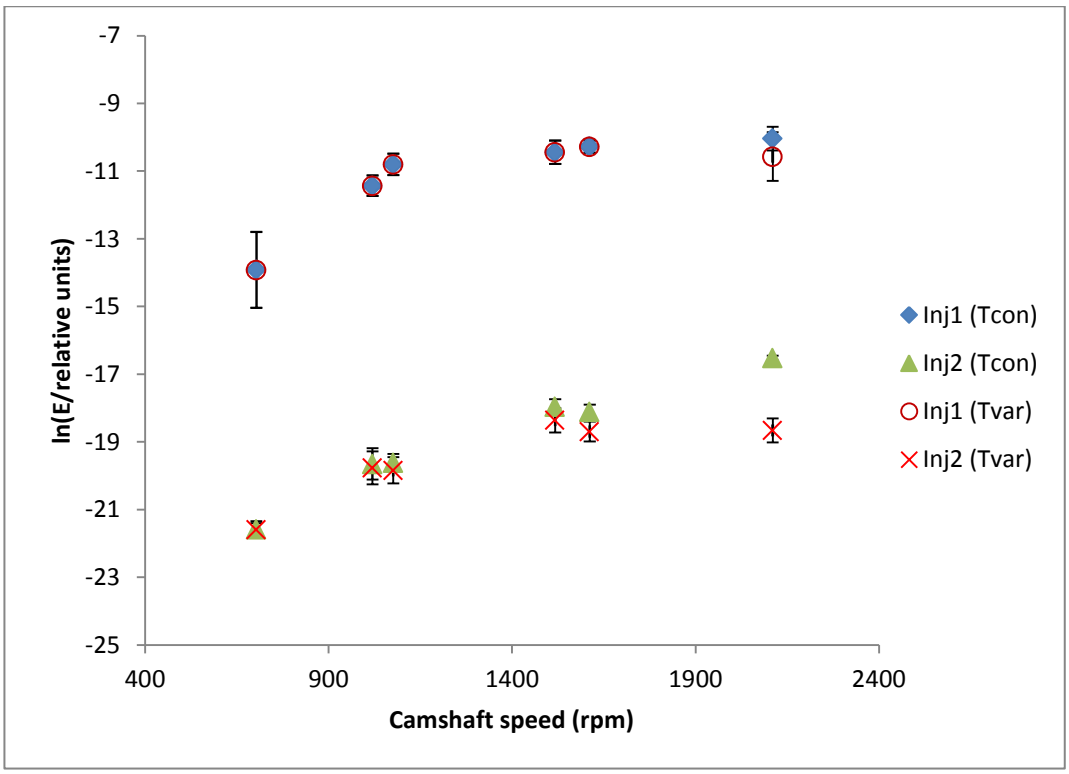

Figure 5.13: Averaged AE energy of the Injector 1 and Injector 2 events recorded during injector rig Experiment 3, calculated using fixed-time (Tcon) and adaptive threshold (Tvar) windows.

Finally, Figure 5.14 shows the variation of AE energy (on an angular basis, over a fixed angle window of 45^{o} camshaft) with speed for the two injectors and, although the absolute values are very different, it is clear that the variation of angular energy with speed is very similar.

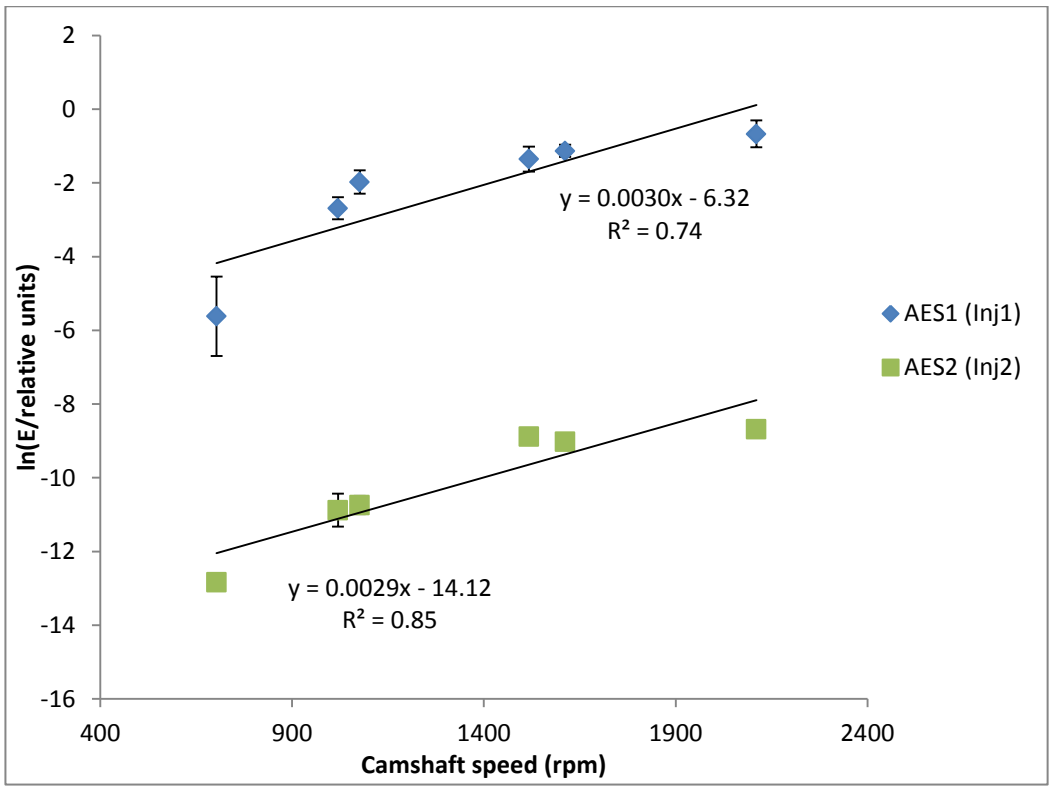

Figure 5.14: Angular AE energy of the Injector 1 event (for a fixed 45° camshaft window) for injector rig Experiment 3.

5.1.2 Demodulated frequency analysis for injector rig

If the AE is related to engine cycling, the signal should show some periodicity associated with the mechanical events which are tied into the engine cycles. To reveal this periodicity, it is necessary to demodulate the signal by averaging it. Because the injector rig is driven by an electric motor of fixed rotational speed (at least on a cycle-to-cycle basis), it is sufficient to carry out the demodulation on a time basis (rather than a re-sampled angle basis). An example of this averaging of 2ms is shown in Figure 5.15, where the periodicity in the shaft encoder is clearly reflected in the AE records from both injectors. Figures 5.16 and 5.17 show a summary of the resulting frequency domain analyses of Experiments 3 and 2, respectively for sensors located on Injector 1, Injector 2 and the pump outlet for Injector 1. As can be seen, all of the spectra contain the pump rotational speed as the lowest frequency peak but, like bearing and wheel AE signatures [165] the spectra contain complex harmonic patterns, which are typical of pulse trains. As can be seen, the inter-pulse "noise" (actually competing sources to the injector being monitored) seen in Figures 5.5 and 5.6 is reflected in a reduced spectral

density at the fundamental (running) frequency, so this aspect alone could be used in diagnostics, for example to filter out the main source of interest.

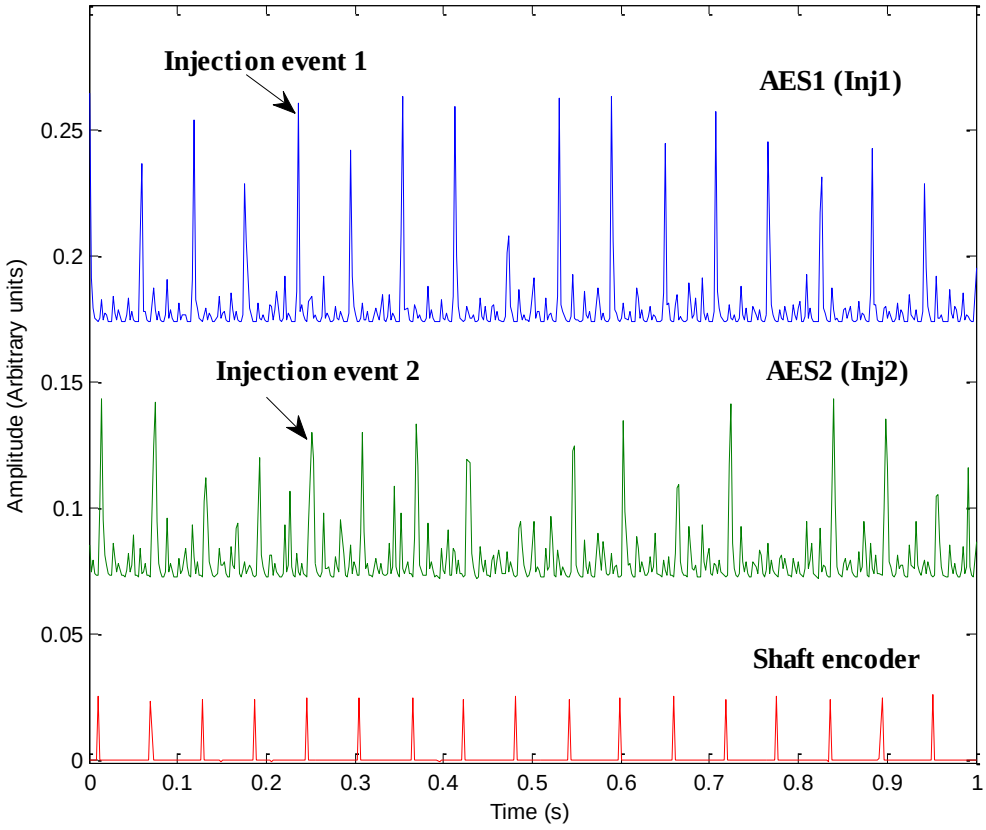

Figure 5.15: Demodulated AE signals recorded at Injectors 1 and 2 in injector rig Experiment 3 for injection pump (camshaft) speed of 1517rpm.

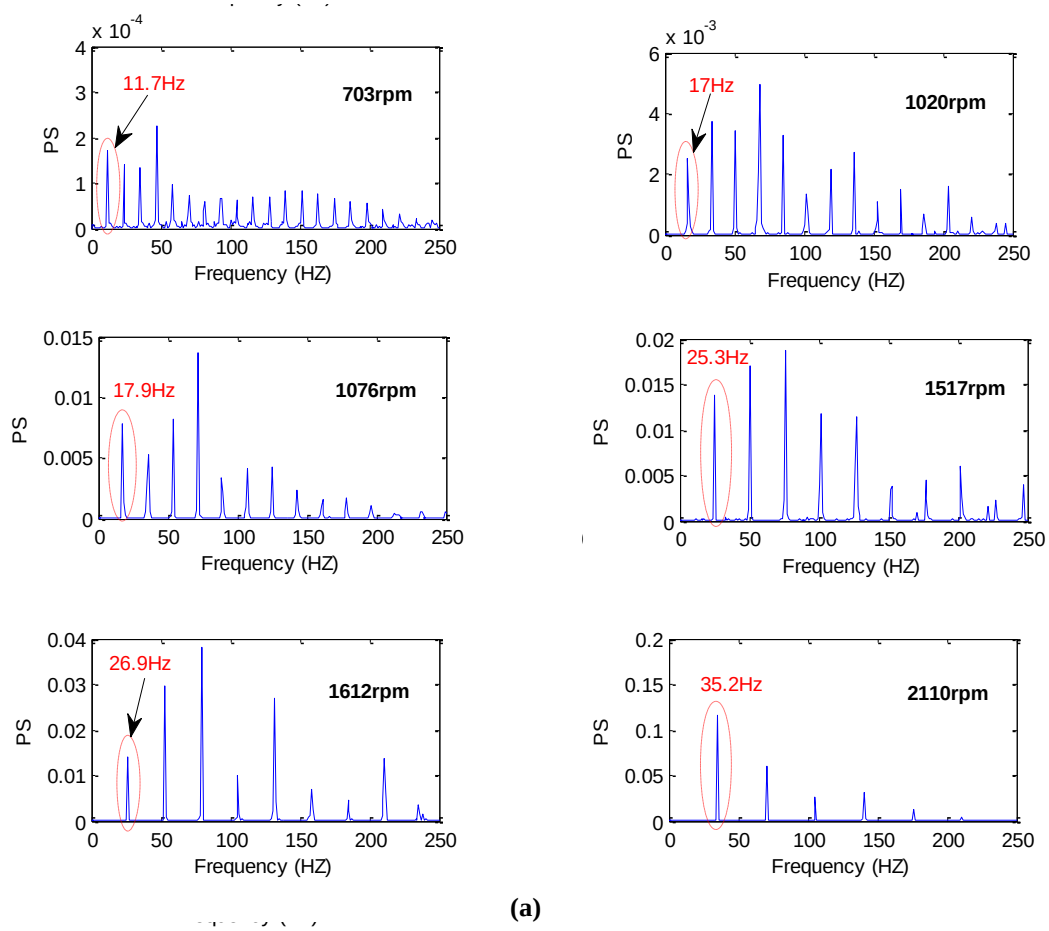

(a)

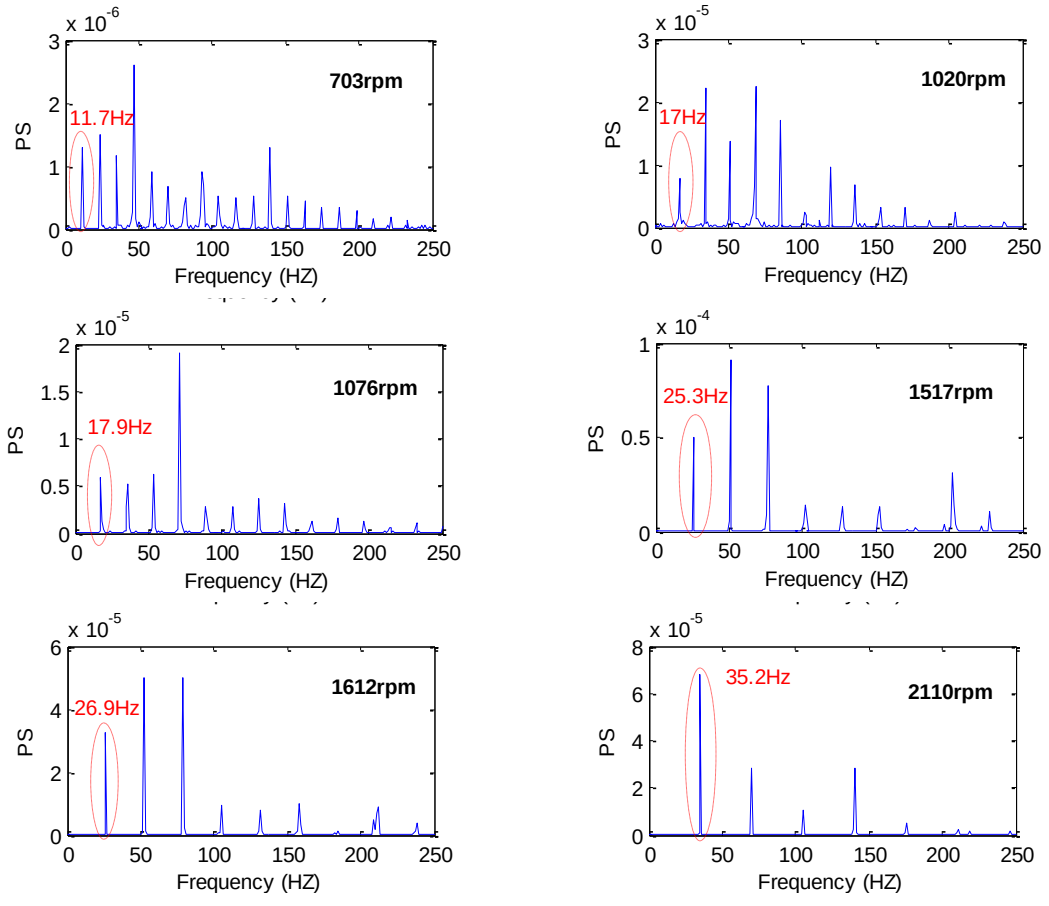

(b)

Figure 5.16: Frequency content of the demodulated AE signals from injector rig Experiment 3 for each pump (camshaft) speed used: (a) sensor on Injector 1 and (b) sensor on Injector 2.

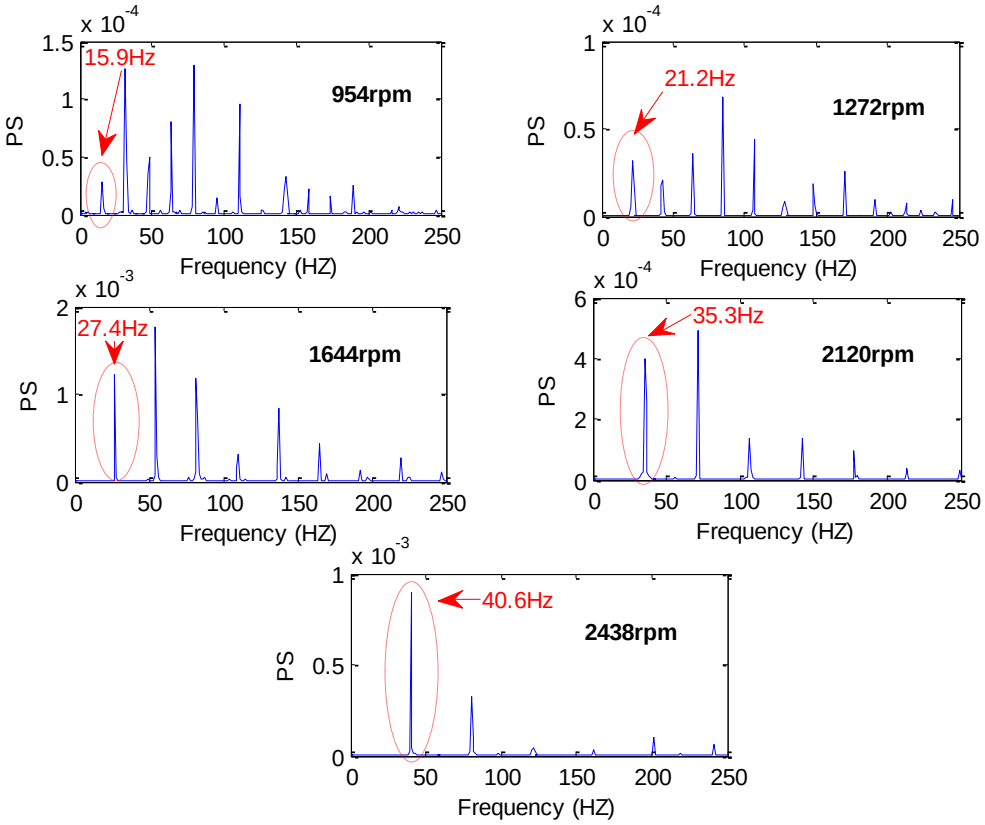

(a)

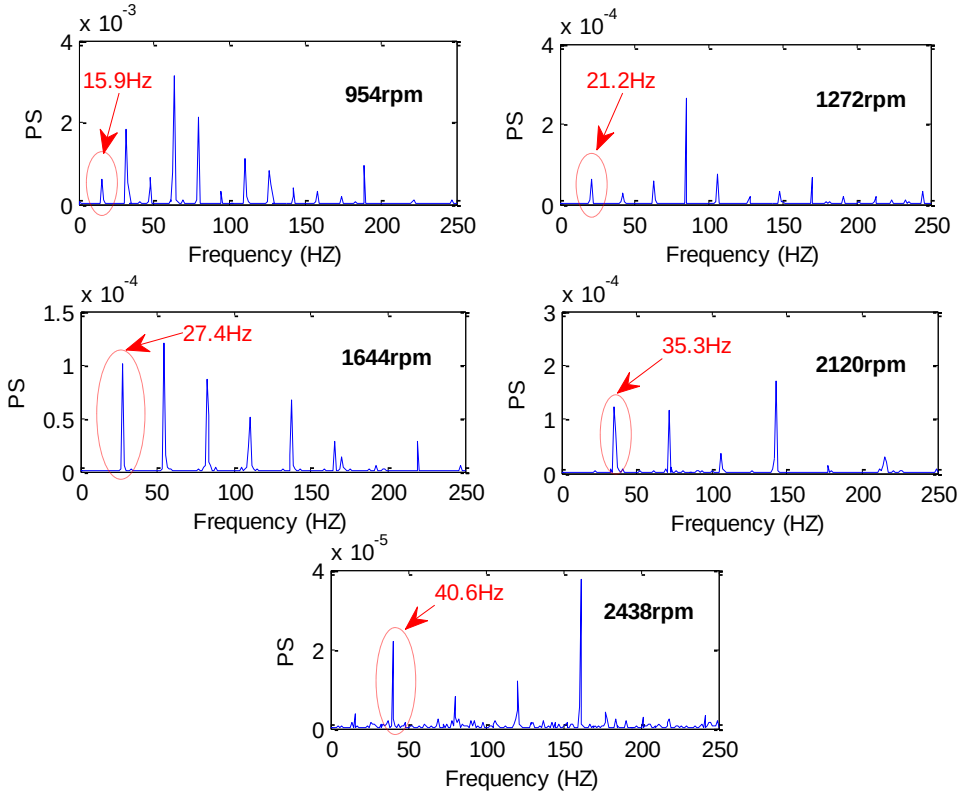

(b)

Figure 5.17: Frequency content of the demodulated AE signals from injector rig Experiment 2 for each pump (camshaft) speed used: (a) sensor on Injector 1 and (b) sensor on pump port at Injector 1 outlet.

Figures 5.18 and 5.19 show the instantaneous injector pump speed versus angle for injector rig Experiments 2 and 3. At the higher average rotational speeds, the instantaneous speed oscillates around the average, but with a strong dip at the port opening followed by an oscillatory return to the controlled value. At the lower speeds the pressure becomes almost sinusoidal with a period equal to the injector opening period and not strong dip and recovery, which could indicate that the pump is not delivering sufficient pressure to open the injector. The secondary oscillations (approximately every 15° camshaft angle) are thought to be an interaction between the motor rotational stiffness and the hydraulic properties of the fuel line and are hence of limited interest in terms of engine performance.

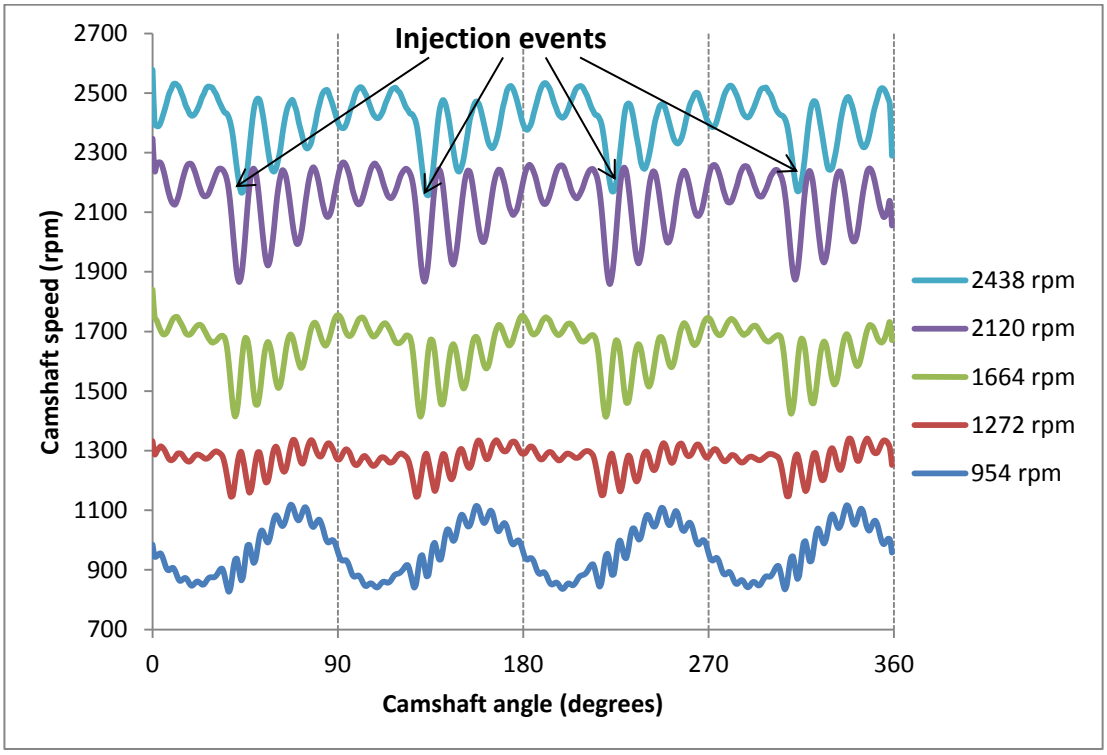

Figure 5.18: Angular speed versus angle (expressed as equivalent camshaft values) for injector rig Experiment 2.

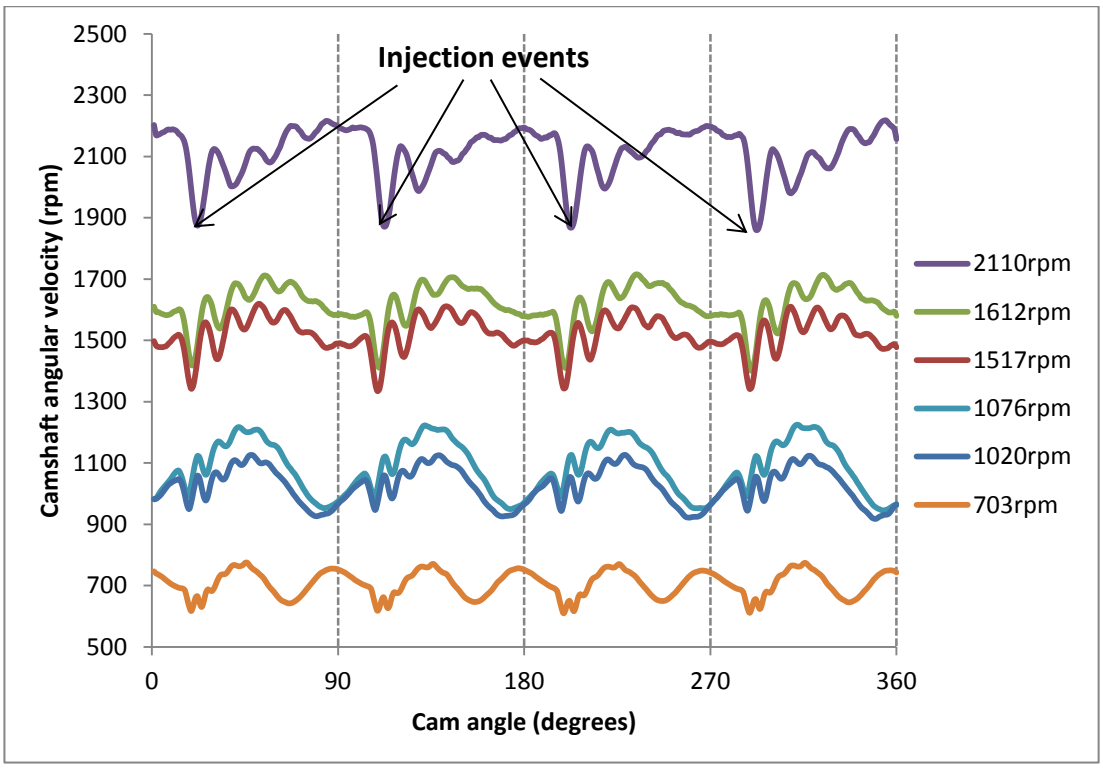

Figure 5.19: Angular speed versus angle (expressed as equivalent camshaft values) for injector rig Experiment 3.

5.1.3 Summary findings from injector rig

The foregoing analysis has shown that the injection process itself generates a significant amount of acoustic emission, which can be recorded by mounting a sensor on the injector. It is also seen that the injection pump generates AE and some of this can travel to the injector to be recorded there.

The energy associated with the injection process can be quite simply calculated using a fixed (by inspection) time or angle window and this energy increases in a fairly reliable way with pump (hence crankshaft) speed. The duration of the injection process also changes with speed, being drawn out over a longer angle window as pump speed increases. The observations on energy and window indicate that the AE is generated by the passage of fuel through the injector.

5.2 Running engine experiments: Engine A

Engine A was the simplest of the three examined in this work, having only two cylinders and also being a two-stroke. As shown in Figure 5.20, the sensors were identically positioned with respect to the two cylinders.

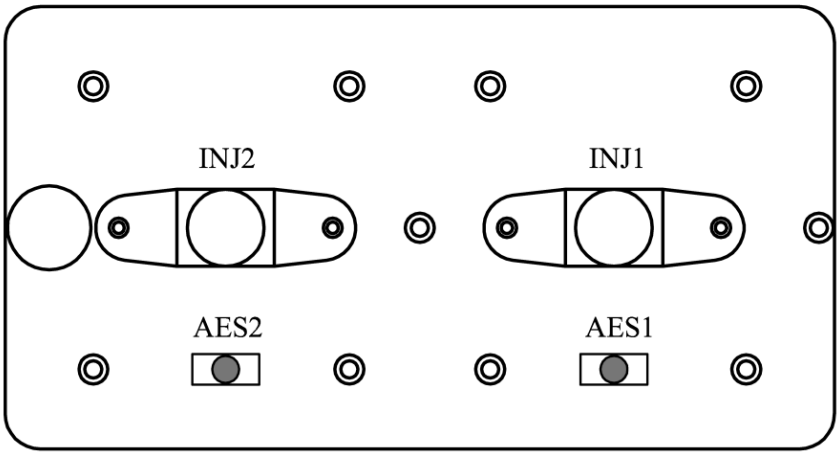

Figure 5.20: Schematic diagram of the running Stuart Turner engine (Engine A) experiment showing the positions of AE sensor array.

Figures 5.21 and 5.22 show typical time- and angle-series for the two sensor positions. These are broadly as might be expected, with Sensor 1 showing a stronger signal associated with Cylinder 1 and Sensor 2 showing Cylinder 2 more strongly. There are also clear similarities (albeit attenuated) between the same events as viewed by the two sensors. It is also evident that, despite a certain cycle-to-cycle variation, the "fingerprint" of Cylinder 2 is distinct from that of the nominally identical Cylinder 1.

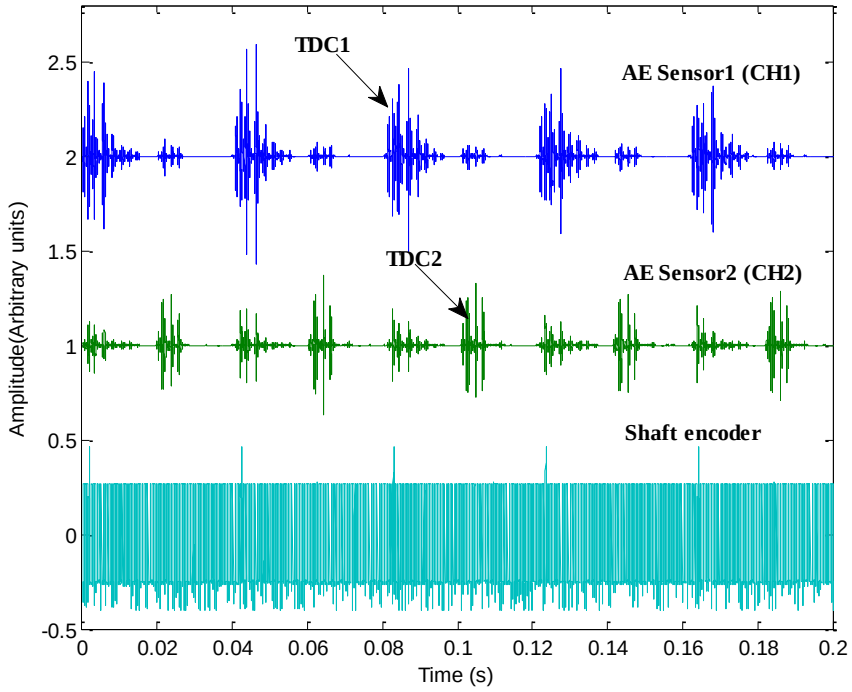

Figure 5.21: Typical AE signal from Stuart Turner engine (Engine A) at a camshaft speed of 738 rpm in the time domain (0.2 second window).

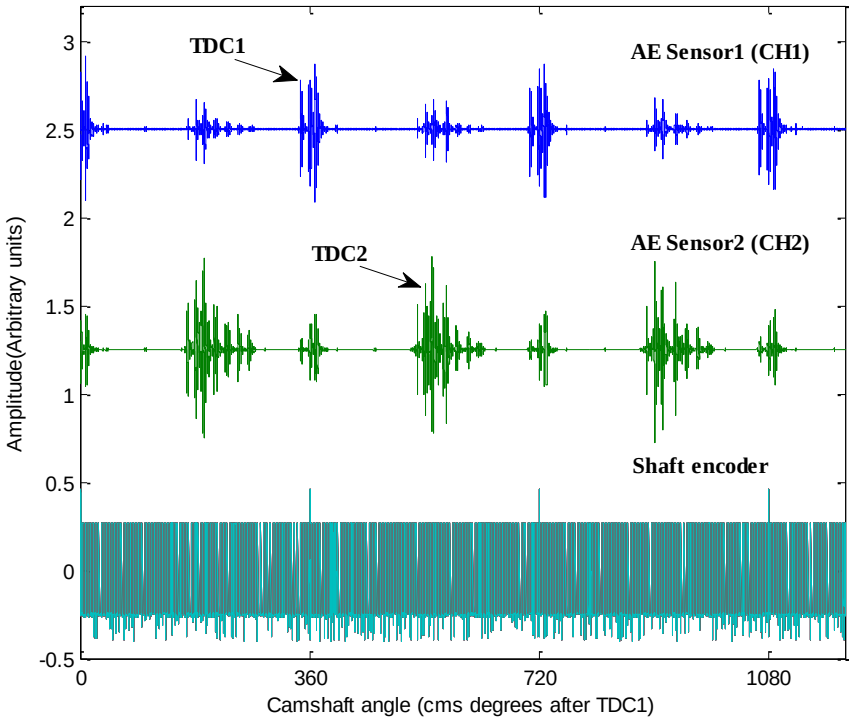

Figure 5.22: Typical AE signal from Stuart Turner engine (Engine A) at a camshaft speed of 738 rpm in the angle domain (three complete engine cycles).

Figure 5.23 shows one cycle in a bit more detail with an engine event map superimposed on the angle series. The cycle for Cylinder 1 starts at about -120° when

the exhaust port closes (EPC1, shown for the succeeding cycle in Figure 5.23) and compression of the air taken in between IPO1 and IPC1 (again shown for the succeeding cycle in Figure 5.23) commences. The AE activity commences shortly after injection with a very low amplitude pulse which suggests this to be linked to the fluid flow and the build up pressure associated with the injection event (the sensor placement affected the signal attenuation where a direct placement on the injector body should reveal more detailed injection information), followed by three strong pulses and then some minor, seemingly erratic activity up to the opening of the exhaust port (EPO1). This pattern is reflected at AE sensor 2 with a small angle delay which seems to be slightly different for each of the main pulses, possibly indicating that they are associated with different locations. The relative attenuation of the three pulses between Sensors 1 and 2 is also different, again suggesting different source locations. The AE activity associated with Cylinder 2 shows similar characteristics, except that there are four strong pulses and at least four substantial but weaker ones. The effect of closing and opening the exhaust ports can be seen more clearly in the signal from Sensor 2 where the position of the exhaust manifold close to the cylinder 2 as shown in Figure 5.24. The time delays are this time in the opposite direction, as would be expected for sources located nearer to Sensor 2.

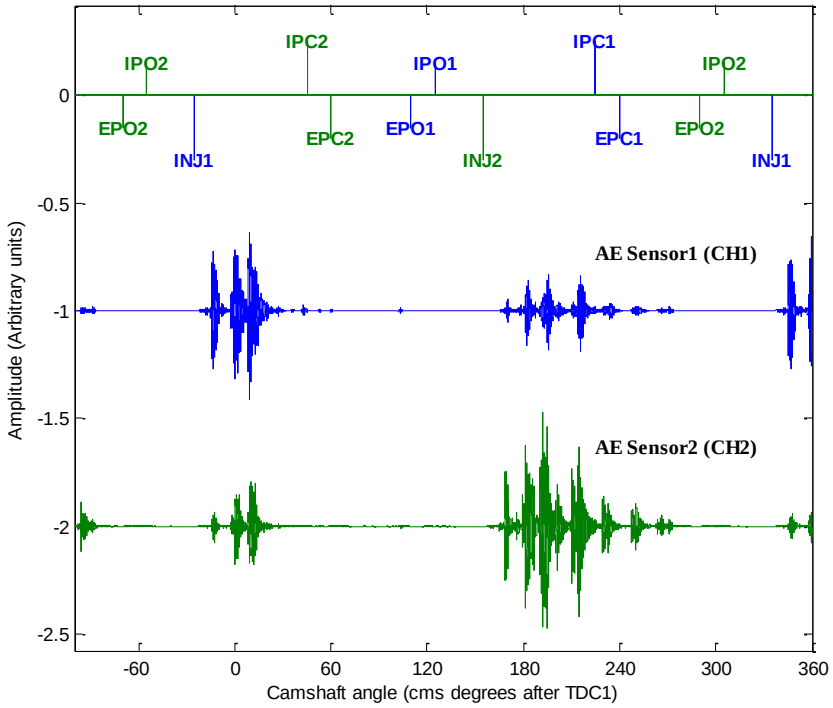

Figure 5.23: One complete engine cycle in the angle domain showing the engine event map and the AE signals from both sensors on the Stuart Turner engine (Engine A) at a camshaft speed of 738 rpm.

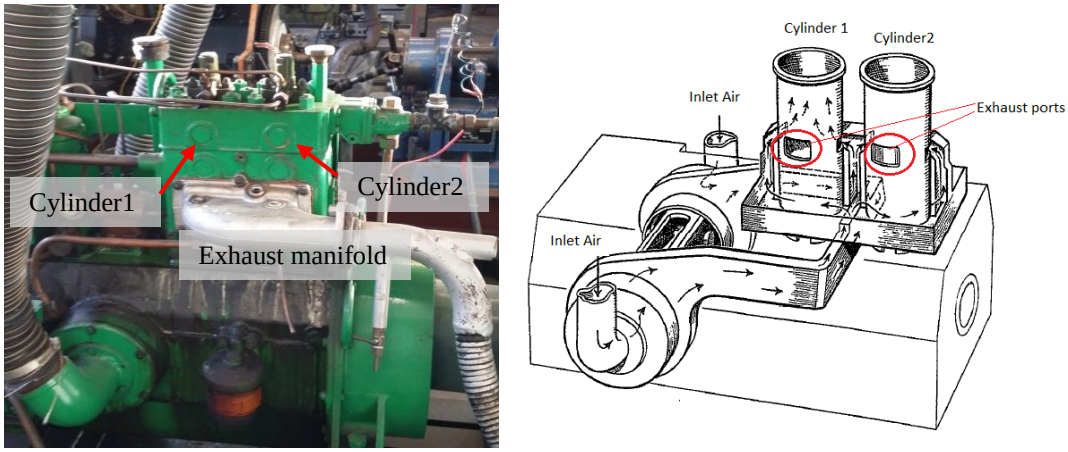

Figure 5.24: Side view of the Stuart Turner engine showing the air intake and exhaust gas systems (left) and schematic diagram shows the flow of the air inside the cylinder blocks [166] (right).

5.2.1 AE energy analysis; Engine A

Figures 5.25 and 5.26 show typical angle series for each of the speeds for the local sensor recording on Cylinders 1 and 2, respectively. These behave in a broadly similar way to the injector rig measurements, with the amplitude and duration of the AE activity increasing with speed although, in the case of the engine, there are some anomalies in this progression.

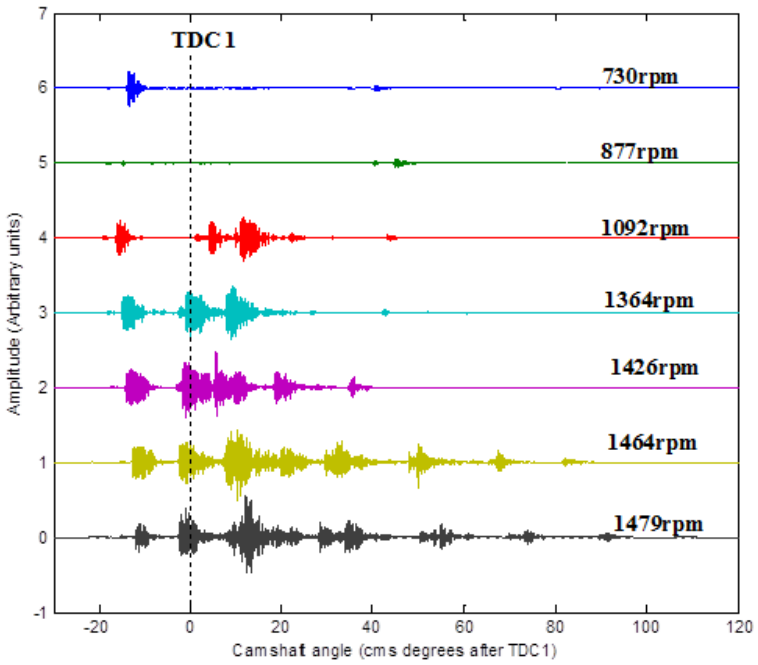

Figure 5.25: Raw AE signal recorded by sensor 1 from Engine A showing the Cylinder 1 injection window for all the acquired speeds in the angular domain.

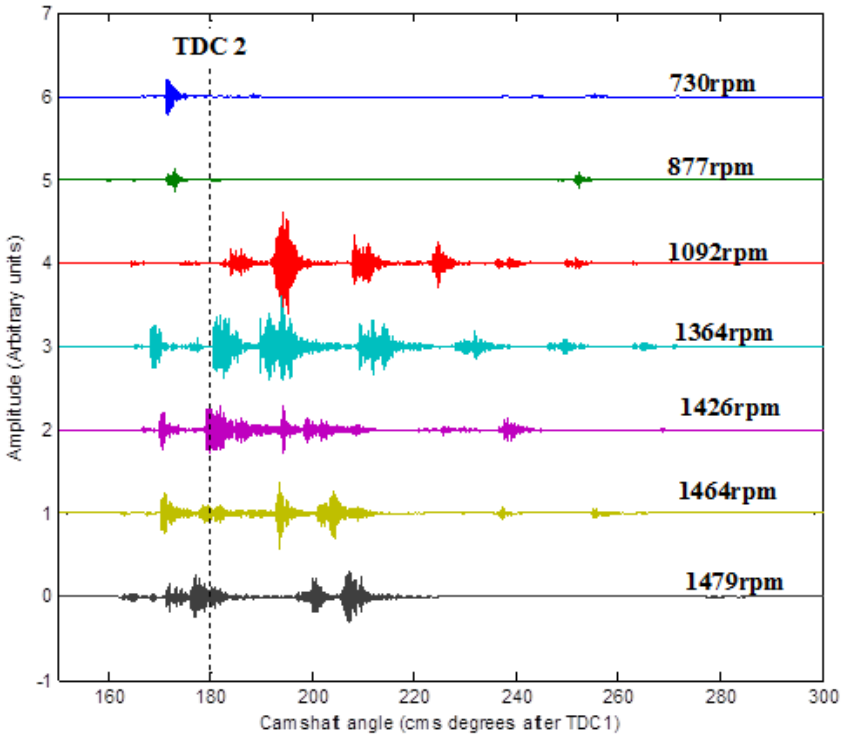

Figure 5.26: Raw AE signal recorded by sensor 2 from Engine A showing the Cylinder 2 injection window for all the acquired speeds in the angular domain.

As described previously, the AE energy of each raw signal was calculated over a constant time window of 20 ms within the longer TDC1 window, selected by inspection only to include the injection-combustion event of cylinder 1 where the energy results were compared to those obtained using the adaptive thresholding method.

Figures 5.27 and 5.28 show the averaged energy (for 175 cycles) on a time basis using both fixed and adaptive threshold windows for both sensors over the Cylinder 1 active stroke and the Cylinder 2 active stroke, respectively. Clearly, both sensor positions record the same evolution and the same relative attenuation is seen between the respective curves in the two figures. Also, the fixed and variable windows show similar results for average energy. A slightly puzzling aspect of these results is the reversal of the generally increasing trend at low speeds in Cylinder 1 and at high speeds in Cylinder 2, reflecting the anomalies visible in Figures 5.25 and 5.26. Given that these are measured by both sensors, they must be associated with a genuine aspect of engine behaviour, and so some further analysis is merited.

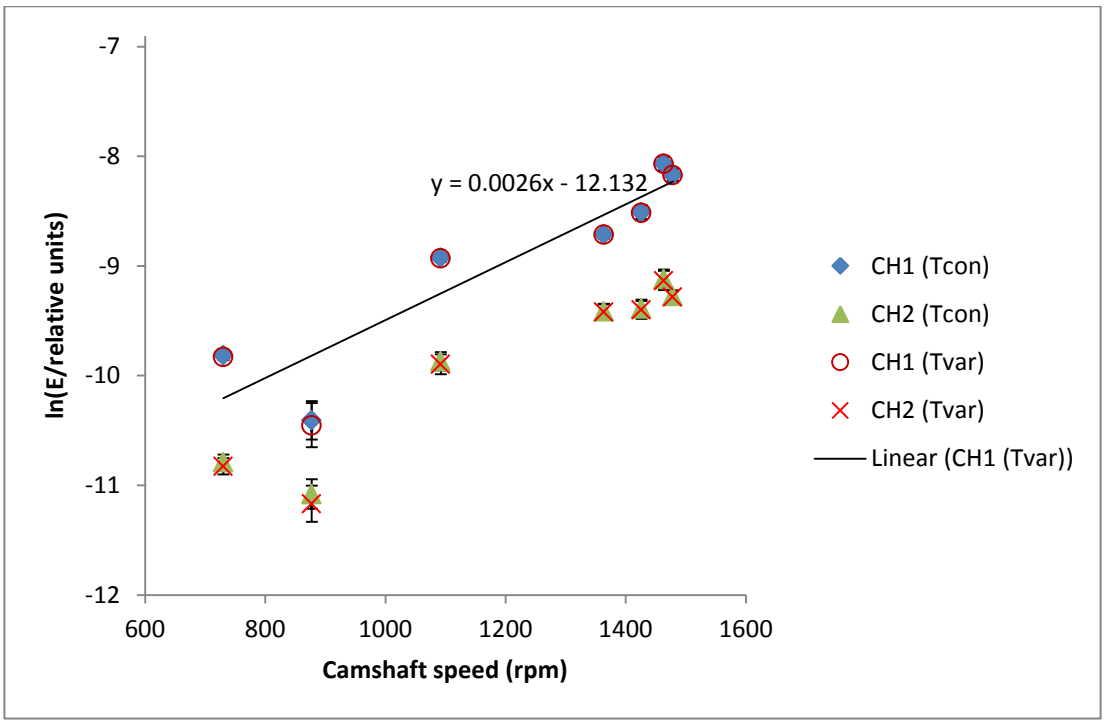

Figure 5.27: Averaged AE energy (time basis) in the injection/combustion event for Cylinder1 calculated using fixed-time (Tcon) and adaptive threshold (Tvar) windows for Engine A.

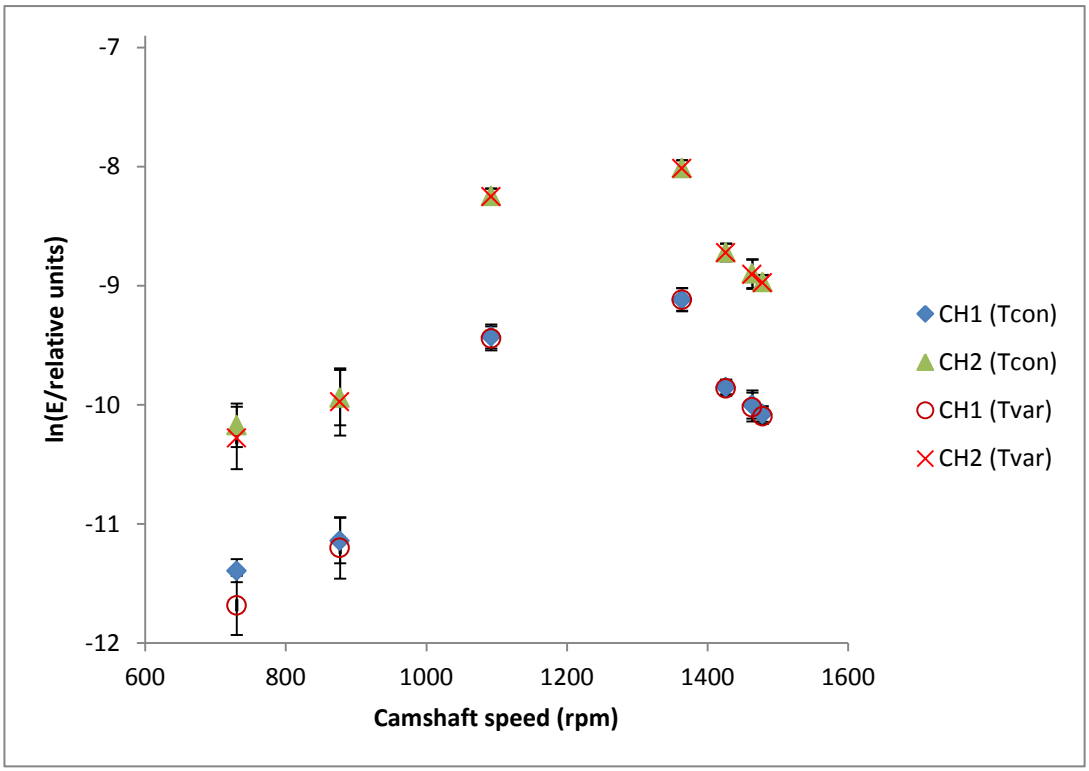

Figure 5.28: Averaged AE energy (time basis) in the injection/combustion event for Cylinder2 calculated using fixed-time (Tcon) and adaptive threshold (Tvar) windows for Engine A.

Figures 5.29 and 5.3 show a fixed (approximately 90°) camshaft window as applied to the Cylinder 1 and Cylinder 2 data, respectively. This window was used to calculate the

AE energy on an angle basis for each of the cylinders and each of the sensors. The result of this is shown in Figures 5.31 and 5.32 and these can be directly compared with Figure 5.14 for the injector rig. The main thing to note is that, although the correlation is poorer in all cases, the slope of the logarithm of angle-based energy is very similar for the two cylinders and also between the engine and the injector rig.

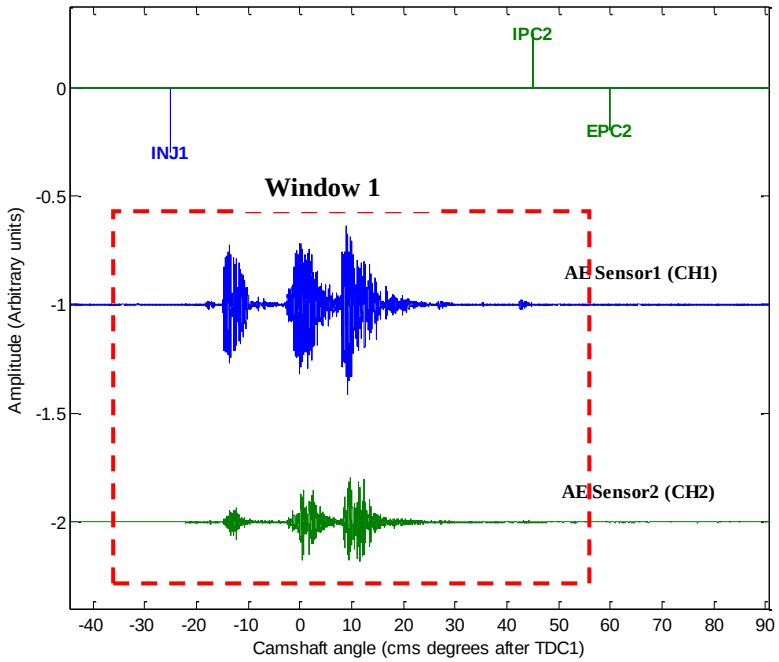

Figure 5.29: Typical AE signal from Stuart Turner engine (Engine A) showing the window of injection/combustion events of Cylinder 1.

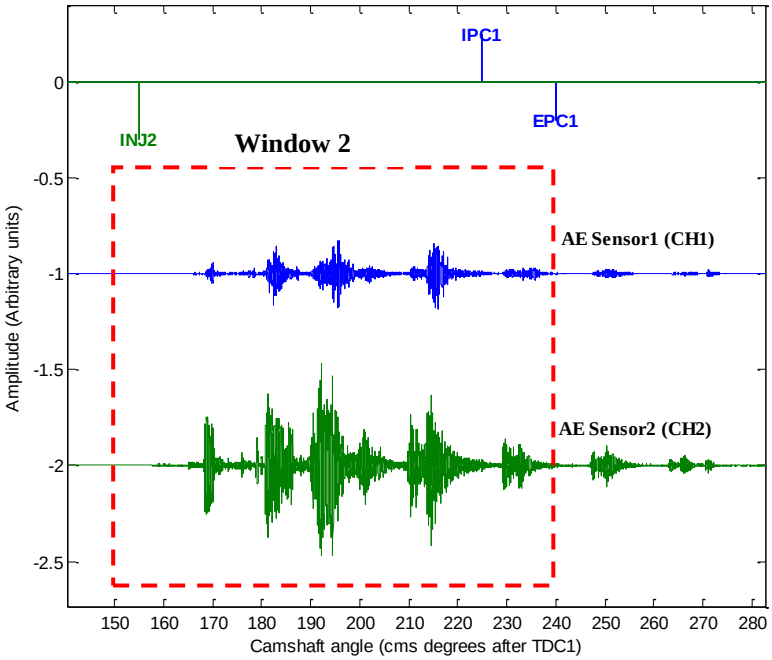

Figure 5.30: Typical AE signal from Stuart Turner engine (Engine A) showing the window of injection/combustion events of Cylinder 2.

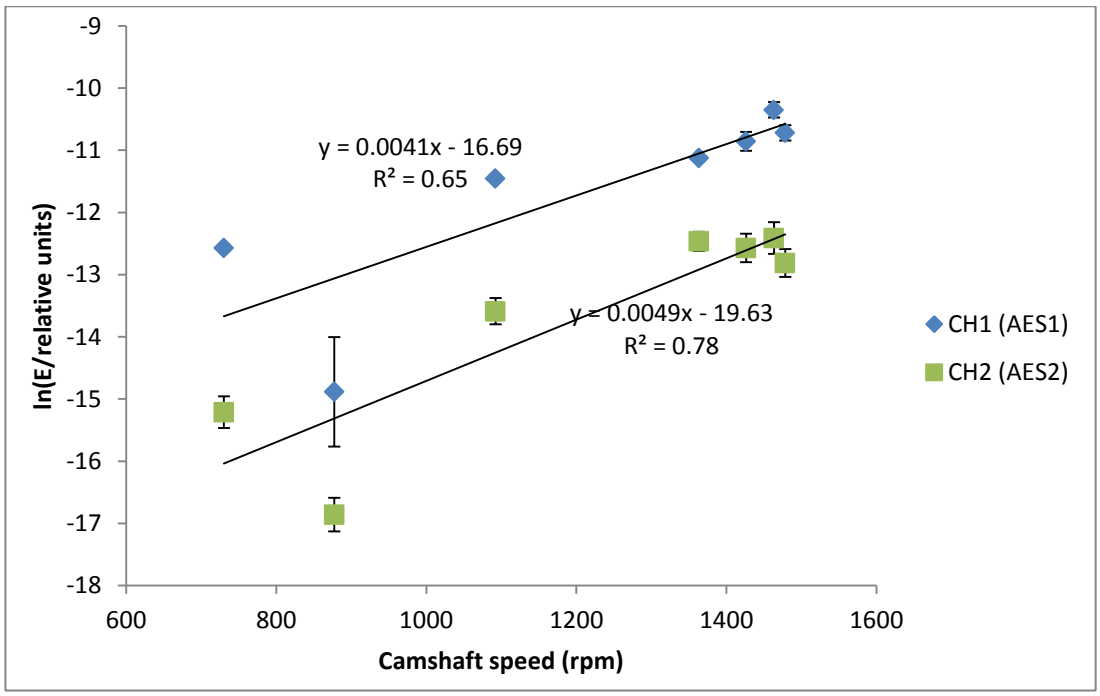

Figure 5.31: Angular AE energy of the Cylinder 1 event (for a fixed 90° camshaft window) for Engine A.

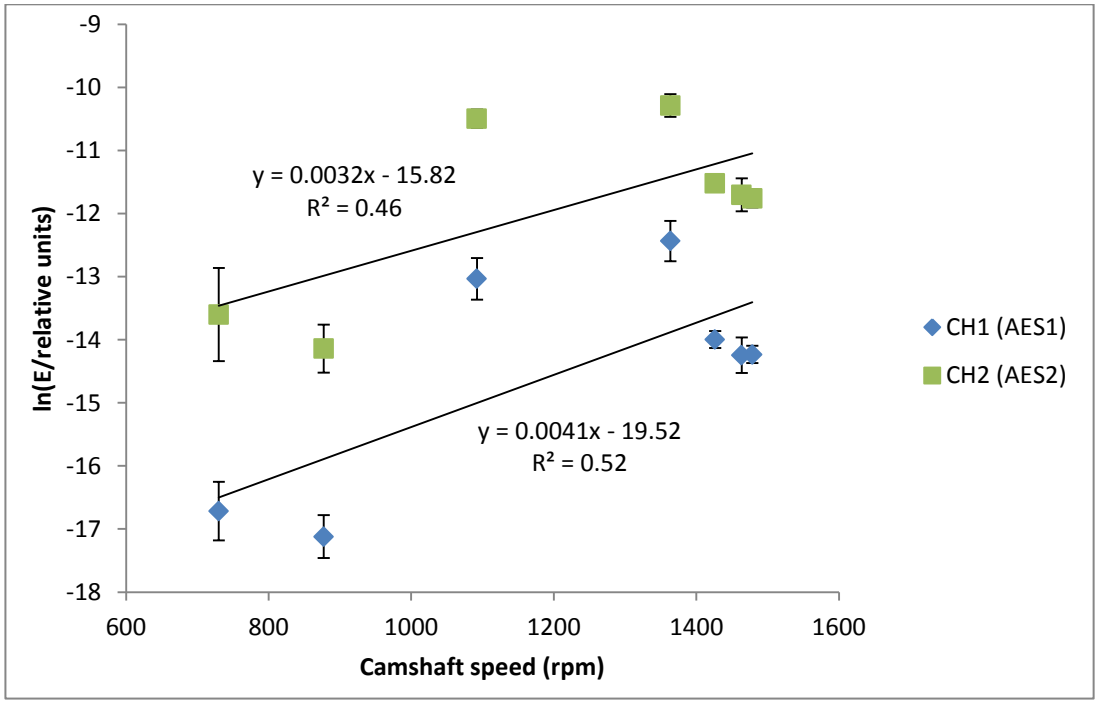

Figure 5.32: Angular AE energy of the Cylinder 2 event (for a fixed 90° camshaft window) for Engine A.

5.2.2 Demodulated frequency analysis; Engine A

As for the injector rig, the AE signals from Engine A were averaged using an averaging time of 2ms, an example being shown in Figure 5.33. As can be seen from the shaft encoder output, the cycle-to-cycle engine speed is relatively constant, so it was decided to proceed with the averaging on a time-basis. The resulting spectra are shown in Figure 5.34 for each of the sensor positions, with the fundamental frequency (running speed) circled. As for the injector rig, these spectra are typical of pulse trains and are slightly less complex since the inter-pulse "noise" this time comes from the second cylinder. Thus, many of the spectra have a stronger second harmonic and the ratio of first to second harmonic (compensating for the inter-cylinder attenuation and relative sensitivity of sensors) could, in principle, be used to characterise the relative characteristics of the two cylinders. Also, it might be expected that the 3-pulse and 5-pulse fingerprints of the two cylinders, observed in Figures 5.22 and 5.23, might also be reflected in the spectra, although some type of pattern recognition would probably be required to achieve the diagnosis. The demodulated frequency analysis has shown a significant strength in using the frequency analysis as a signal encoder with high accuracy.

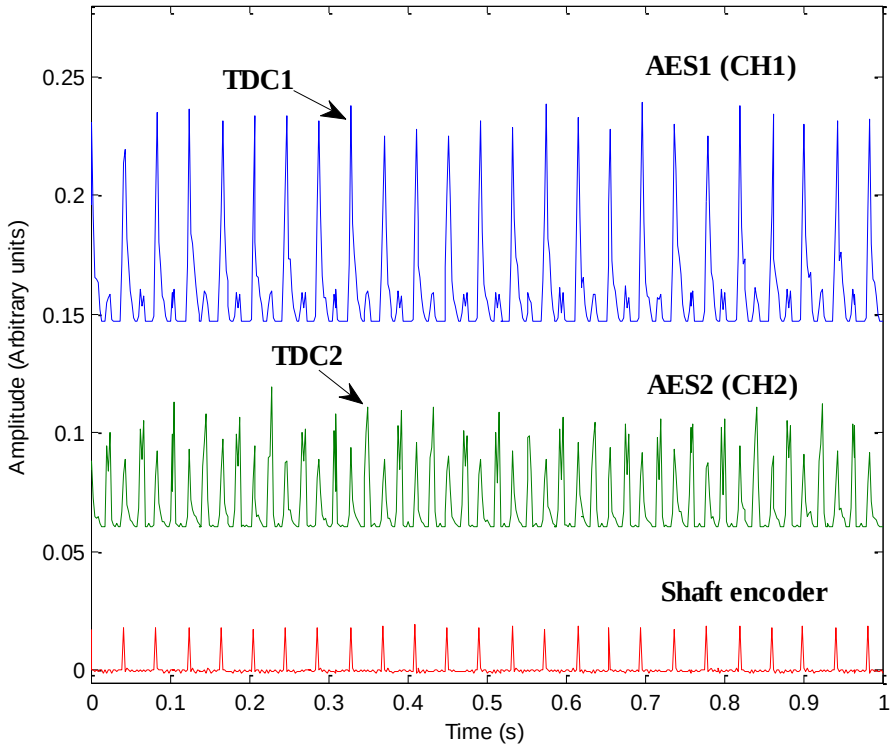

Figure 5.33: Demodulated AE signal from Engine A at a camshaft speed of 1479 rpm.

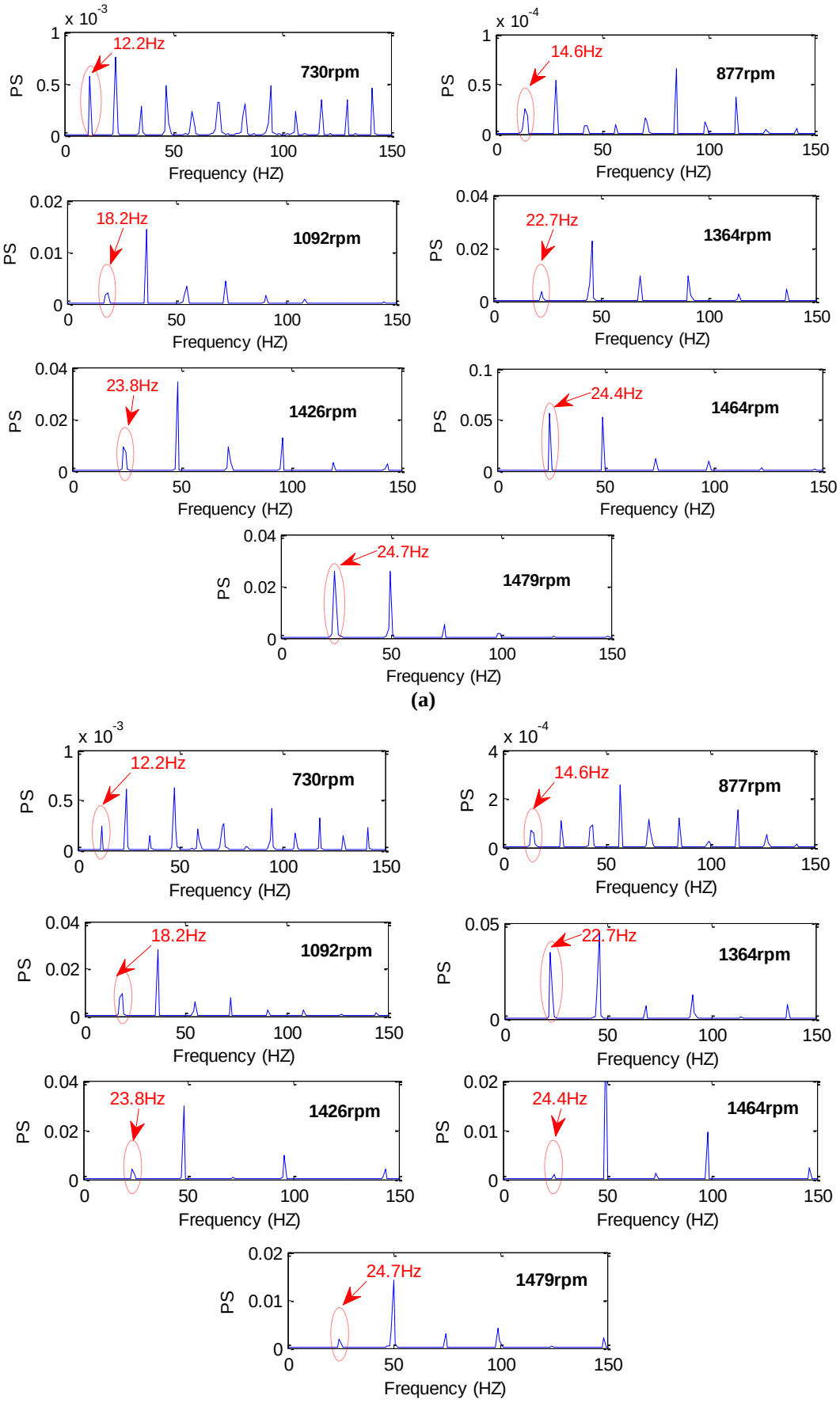

Figure 5.34: Frequency content of the demodulated AE signals acquired in the running experiment of Engine A over the range of camshaft speed; (a) recorded at Sensor1, and (b) recorded at Sensor2.

5.2.3 Identification using canonical correlation analysis; Engine A

Figures 5.35 and 5.36 show the result of applying the SICCA algorithm to the RMS AE angle series over the Cylinder 1 and Cylinder 2 windows, respectively. The curves of R^2 versus angle shift, over the range of -12^o to $+12^o$ camshaft angle, are superimposed for 175 cycles, depending on the engine speed. Clearly all correlations have a strong peak close to zero and this corresponds to the small angle differences seen in Figure 5.23. As well as the main peak with an R^2 close to unity, there are a number of secondary peaks over the range ±10° which are indicative of various false mappings of the multiple pulses seen in Figure 5.23. These could, in principle, be used to carry out a more detailed diagnosis, but it is more useful to subdivide the window to allow different angle shifts for different sources as seen in the next chapter.

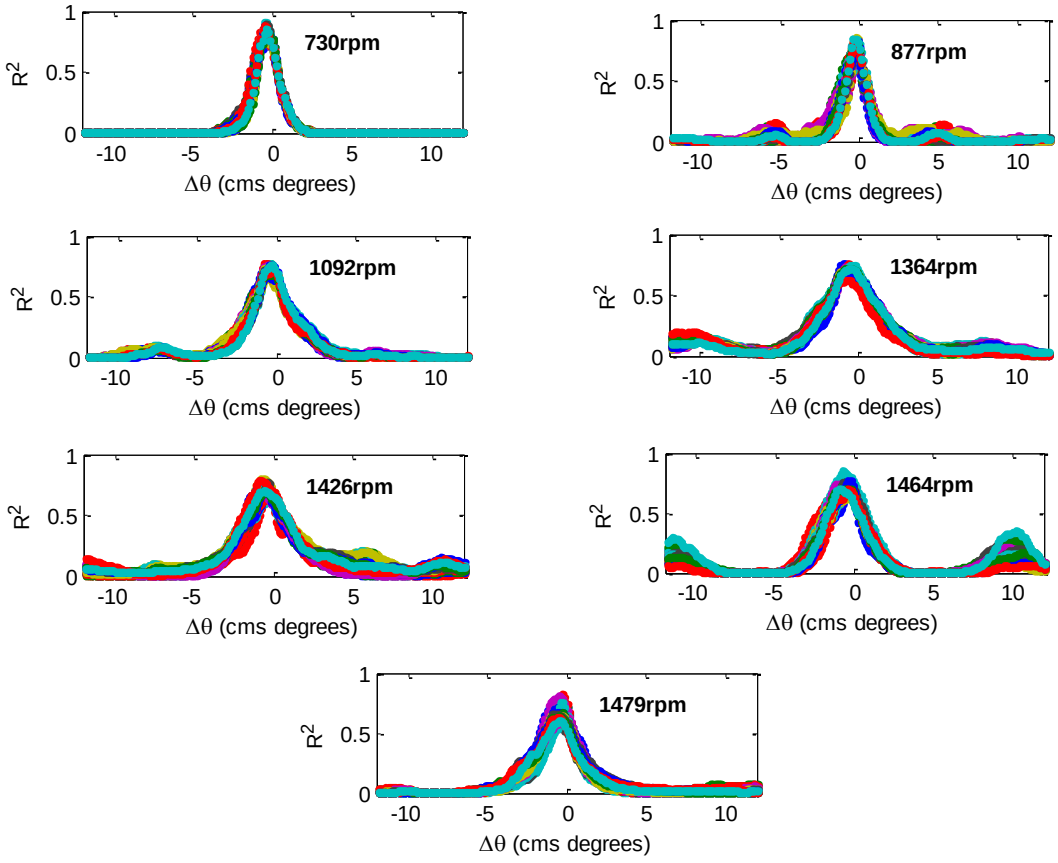

Figure 5.35: Distribution of R^2 with camshaft angle (over the range -12^o to $+12^o$) for Cylinder 1 window (35^ocms BTDC1 - 55^ocms ATDC1) for the running Engine A.

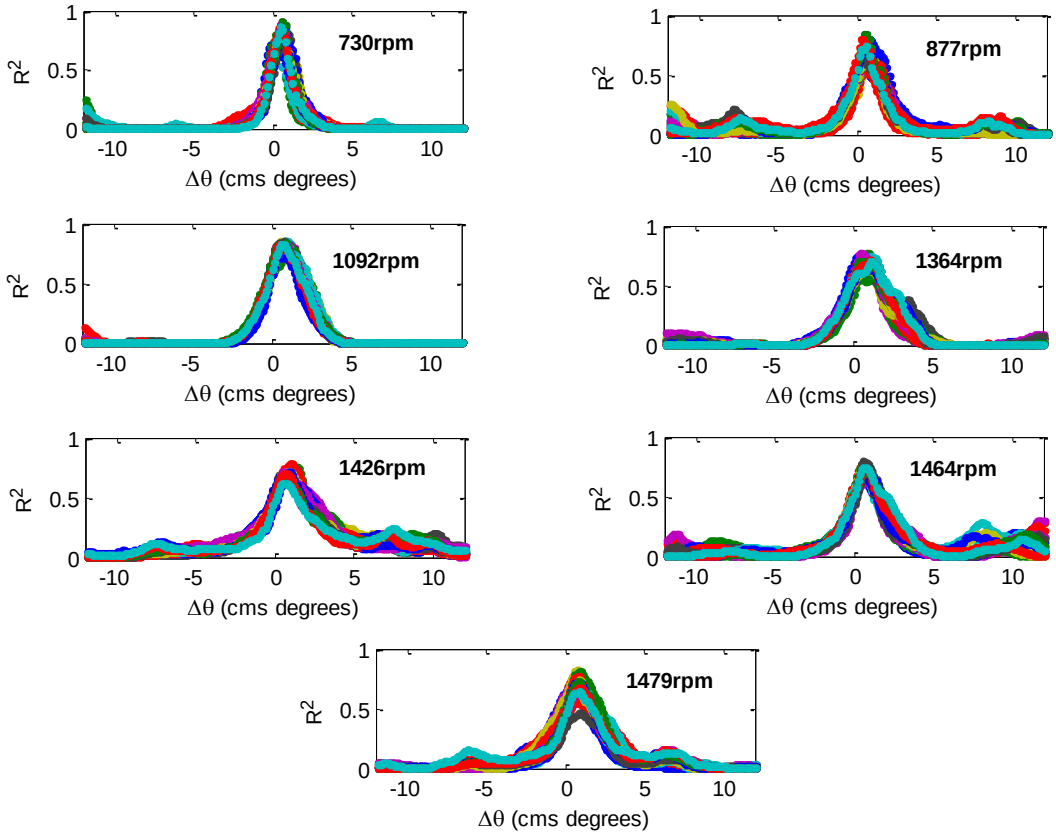

Figure 5.36: Distribution of R^2 with camshaft angle (over the range -12° to +12°) for Cylinder 2 window (35°cms BTDC1 - 55°cms ATDC1) for the running Engine A.

Figure 5.37 shows the maximum R^2 values from the canonical correlation which are relatively constant at around 0.7, slightly deteriorating with engine speed. Figure 5.38 shows the angle shift to be around ±0.6°cms, increasing slightly with speed. Figure 5.39 shows the angle shifts converted to time differences by detecting the time required for each 45° and assigning the corresponding angle shift.

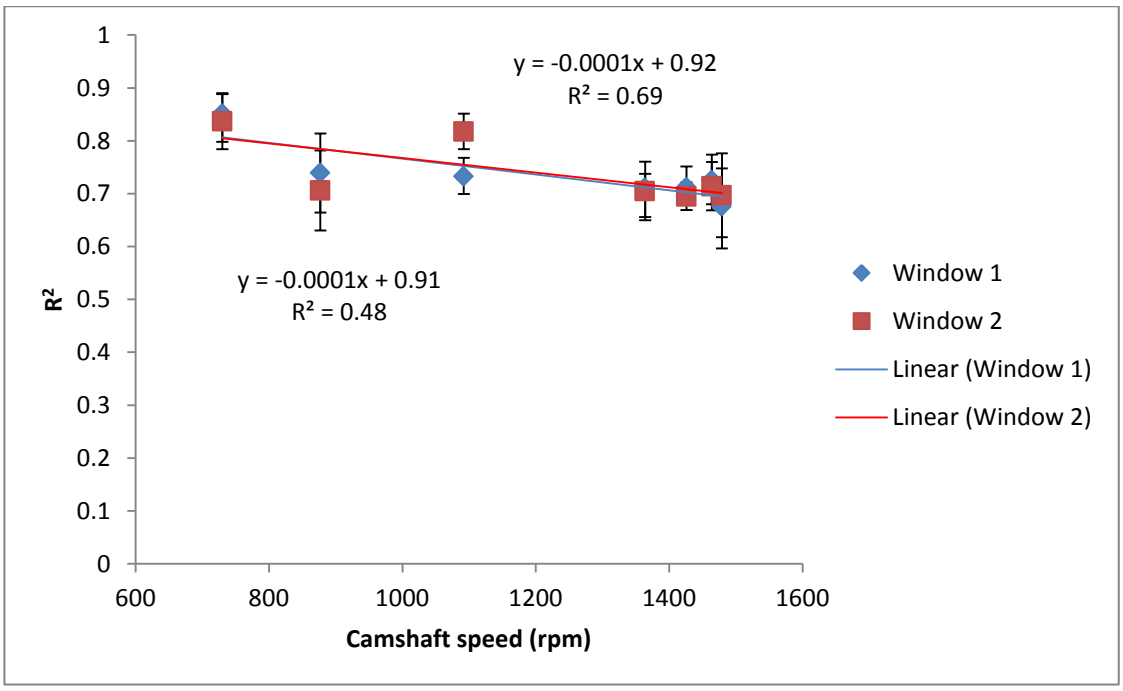

Figure 5.37: Averaged maximum regression coefficients between Cylinder 1 and 2 windows from the canonical correlation of the running experiment on Stuart Turner engine (Engine A).

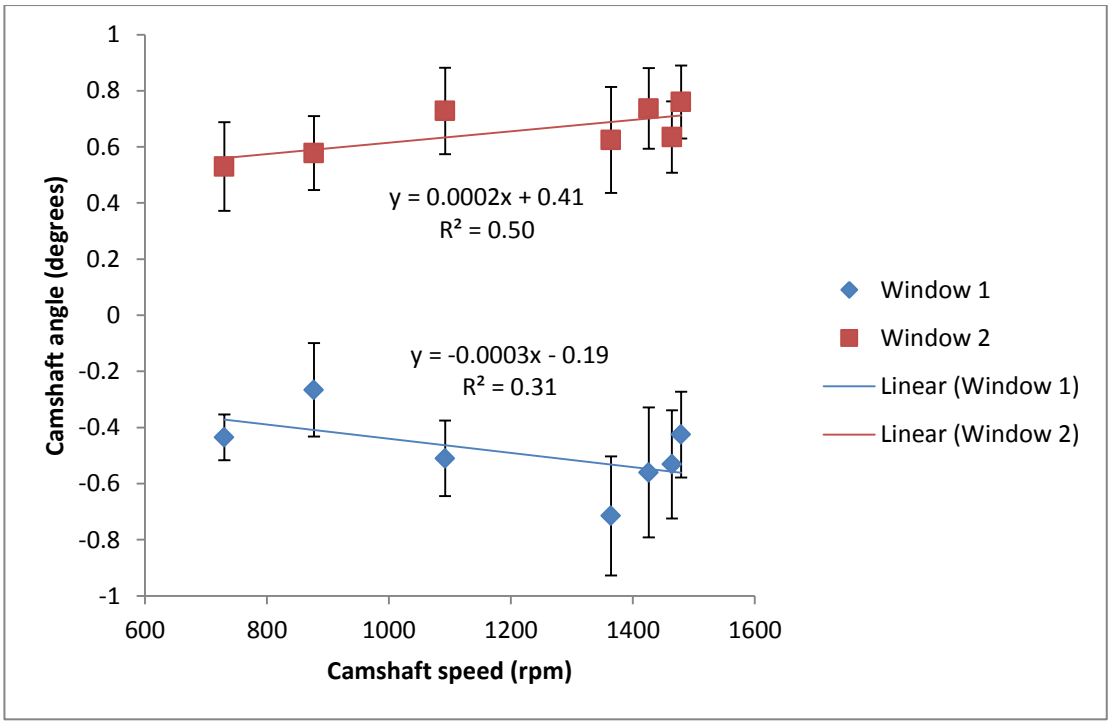

Figure 5.38: Corresponding camshaft angle shifts for maximum regression coefficients between Cylinder 1 and 2 windows from the canonical correlation of the running experiment on Stuart Turner engine (Engine A).

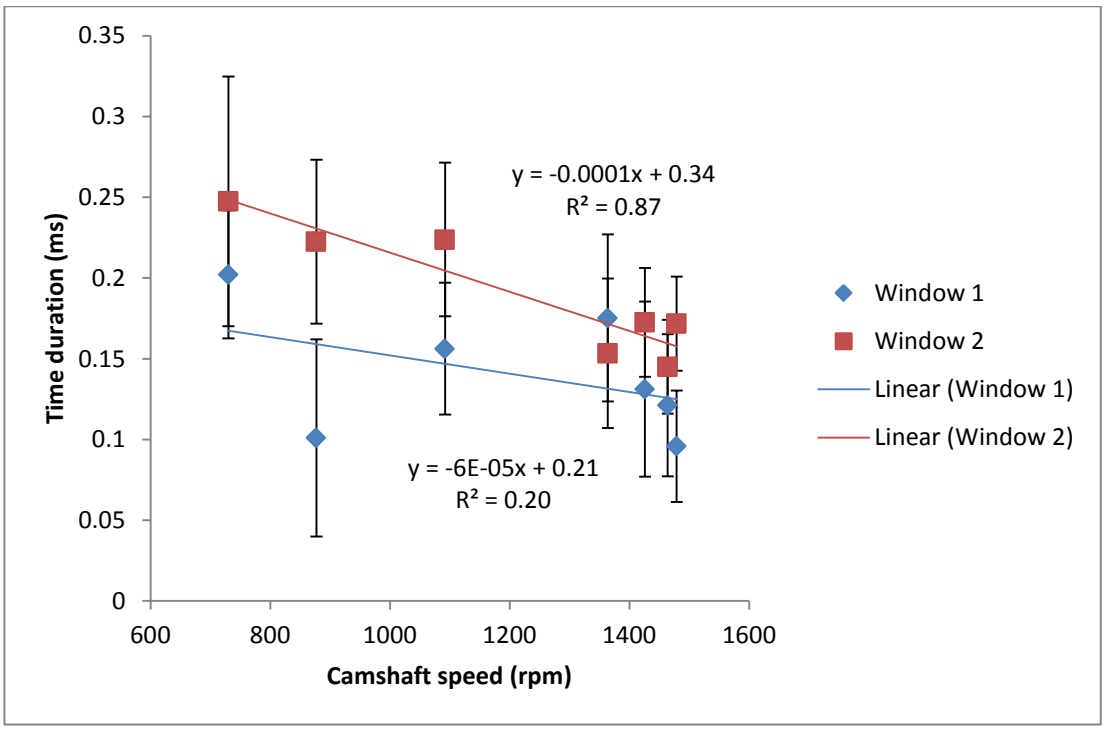

Figure 5.39: Corresponding time shifts for maximum regression coefficients between Cylinder 1 and 2 windows from the canonical correlation of the running experiment on Engine A.

5.2.4 Summary of findings on Engine A

The analysis of this relatively simple engine has allowed a further set of observations beyond those made on the injector rig.

First of all, the signals are a little "cleaner" than some of those recorded on the injector rig (less inter-pulse noise) and the cylinders each seem to have their own distinct characteristics, with time and amplitude shifts between sensor locations which correspond well with the calibration experiment.

Demodulated resonance analysis can be used to decode the cyclic behaviour of the engine, although, for the most sophisticated analysis, a pattern recognition technique will be required.

Canonical correlation has been demonstrated at the cycle level, providing an accurate measure of time- and angle-shifts between the same cylinder event recorded by two sensors at different locations. The approach has not yet been applied at the sub-cycle level, since it is not sufficiently clear that multiple sources exist at sub-cylinder level in this simple engine.

Chapter 6

Analytical discussion of the results of four stroke engine experiments

This chapter builds on the analysis carried out in Chapter 5 on the injector rig and on the simple two-stroke engine. Both engines considered here are four-stroke, four-cylinder engines, and potentially have several sources even within one stroke of the engine cycle. The most intensive study has been reserved for Engine C, the most sophisticated of all the engines studied and the one on which canonical correlation has most to offer. For Engine B (discussed first) the analysis is less detailed, concentrated on assessing the differences in signal nature and potential sources when moving from two-stroke to four-stroke engines.

6.1 Running engine experiments: Engine B

Figure 6.1 shows a reminder of the sensor positions and Figure 6.2 shows a typical record of raw AE, highlighting events around the top dead centre (TDC) of Cylinders 1 and 3 as recorded at Sensors 1 and 2, respectively. There is an ambiguity in four-stroke signals, in that it is not known which of the two TDC positions is associated with firing and which associated with inlet and exhaust valve movements. However, Figure 6.3, which includes an engine event map, taken with Figure 6.1, shows that the most likely interpretation is the one indicated, where events at firing diminish in amplitude in the order 1, 2, 3, 4 when seen from AES1 and in the order 3, 2, 4, 1. The nature of the signals, with multiple pulses, is also similar to that seen for Engine A, which does not have valve movements.

A preliminary indication of multiple sources within the TDC1 and TDC3 windows is given by Figures 6.4 and 6.5. There is a relatively strong pulse at about 3°ATDC1 in the CH3 record in Figure 6.4, which is either absent or buried in the CH1 record. Similarly, the pulse at about 3°ATDC1 in the CH1 record in may or may not be present in the CH3 record. These secondary pulses could be associated with the closure of EV4 and EV2, respectively, although this can only be tested by looking at a larger set of the data.

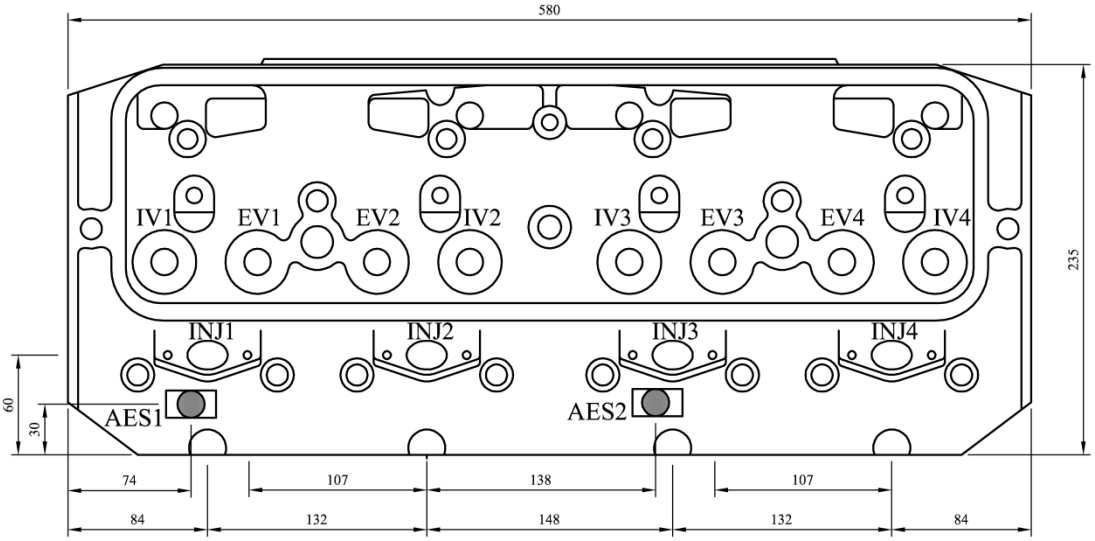

Figure 6.1: Schematic diagram of the Perkins A4.270 engine (Engine B) showing the positions of the AE sensors. (All dimensions in mm.)

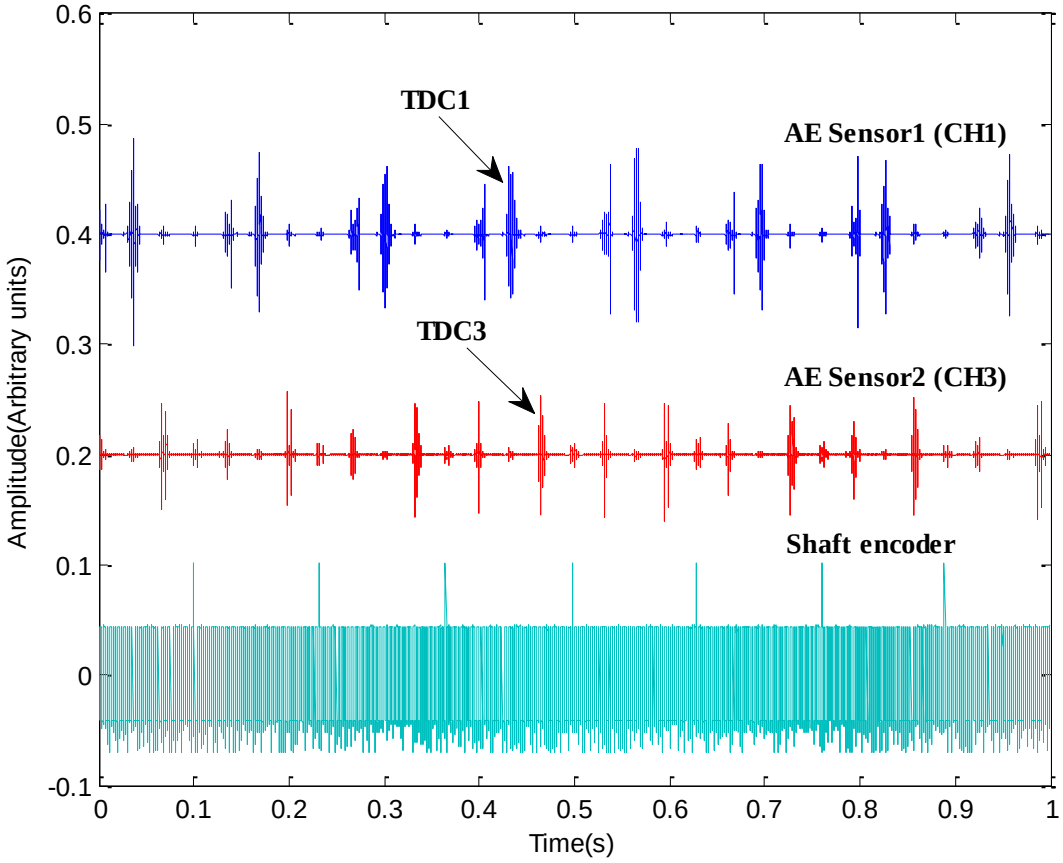

Figure 6.2: Raw AE signals acquired from Perkins A4.270 engine (Engine B) at a camshaft speed of 600 rpm for a time record of one second.

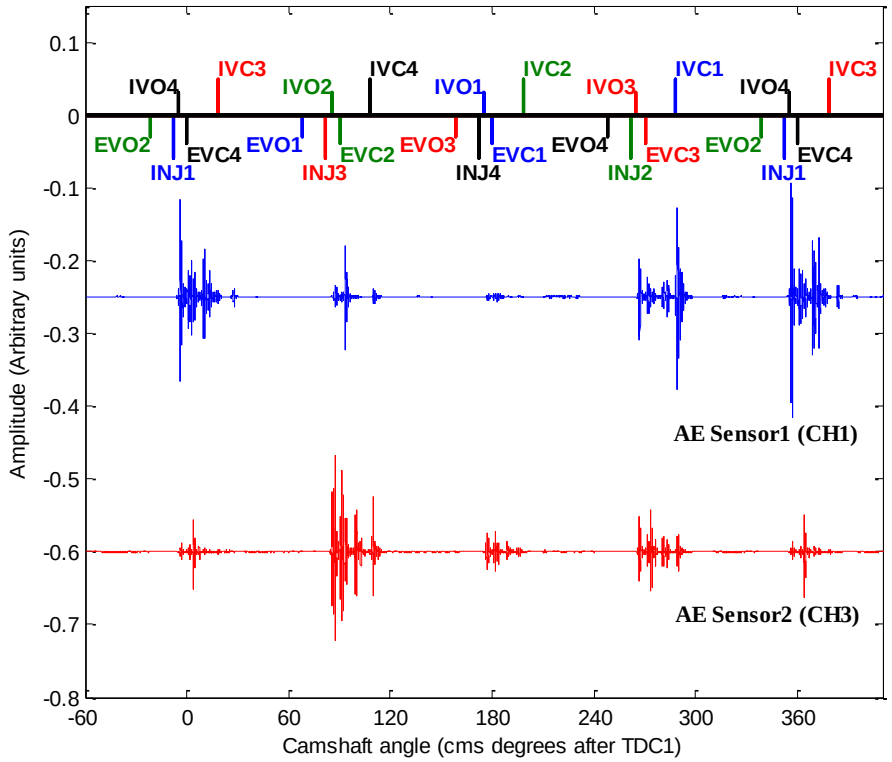

Figure 6.3: Example of one complete engine cycle of the running Perkins A4.270 engine (engine B) in angular domain. (Camshaft speed is 600 rpm)

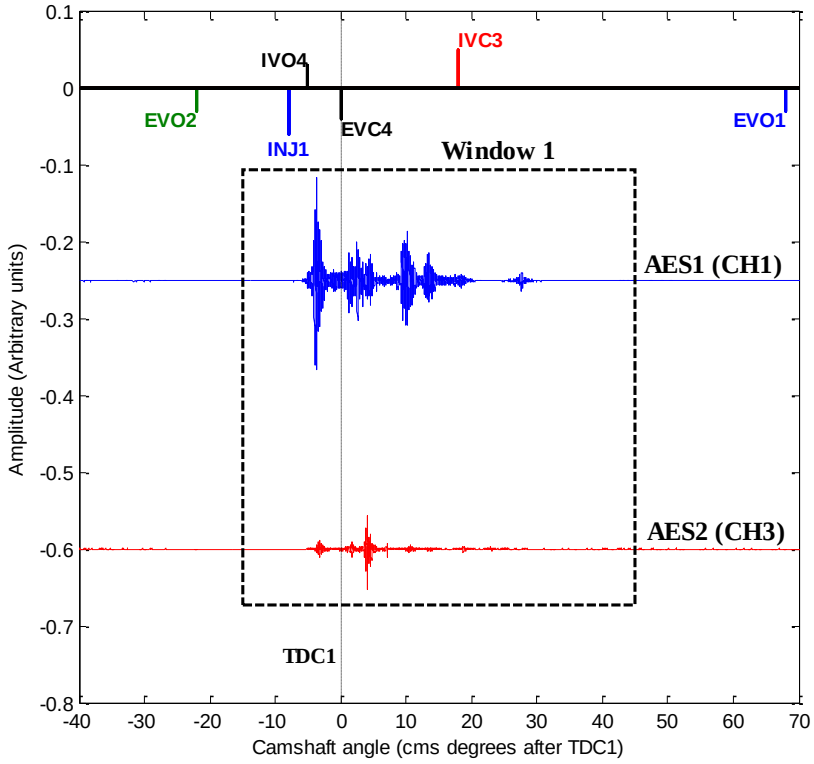

Figure 6.4: Example of Perkins A4.270 (Engine B) Cylinder 1 window. (Camshaft speed is 600 rpm)

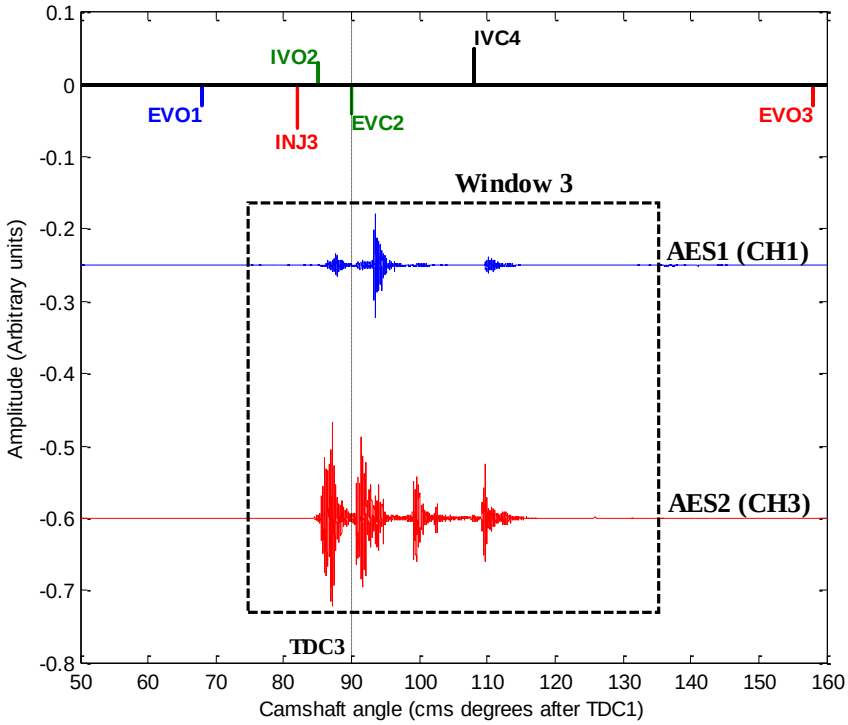

Figure 6.5: Example of Perkins A4.270 (Engine B) Cylinder 3 window. (Camshaft speed is 600 pm)

6.1.1 AE energy analysis for engine B

Figures 6.6 and 6.7 show typical records of the TDC windows for Cylinders 1 and 3, as recorded by the nearby sensor. These show a similar picture to Engine A, with the duration of the signal, even in angle terms, increasing with speed. As before, a fixed camshaft window (this time 45°) was used to obtain the angle-based energy or each of the Cylinders recorded at each of the positions, shown for Cylinder 1 in Figure 6.8 and for Cylinder 3 in Figure 6.9. The energy increases with speed at approximately the same rate as in the injector rig and Engine A when the nearby sensor is considered, but, rather surprisingly, the rate of increase with speed for the more remote sensor is higher than for the nearby sensor. This adds further indication that the remote sensor is measuring something different to the nearby sensor in the relevant window.

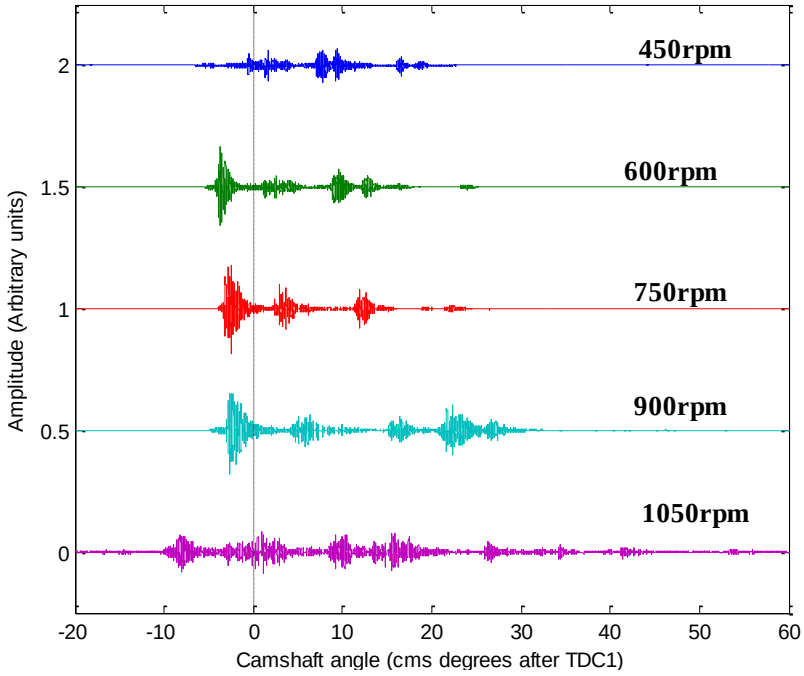

Figure 6.6: Raw AE signal recorded by sensor1 from Engine B showing the Cylinder 1 injection window for all the acquired speeds in the angular domain.

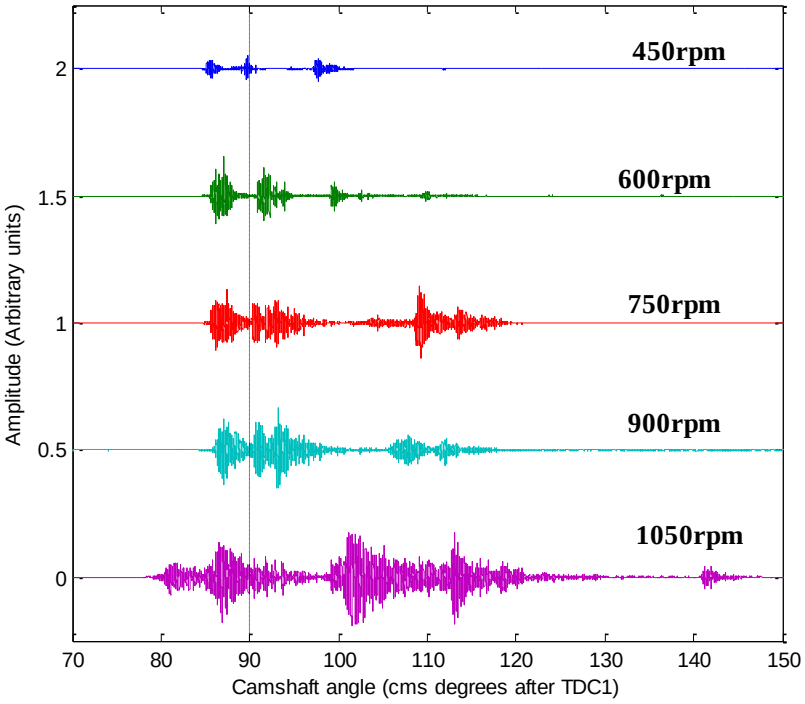

Figure 6.7: Raw AE signal recorded by sensor2 from Engine B showing the Cylinder 3 injection window for all the acquired speeds in the angular domain.

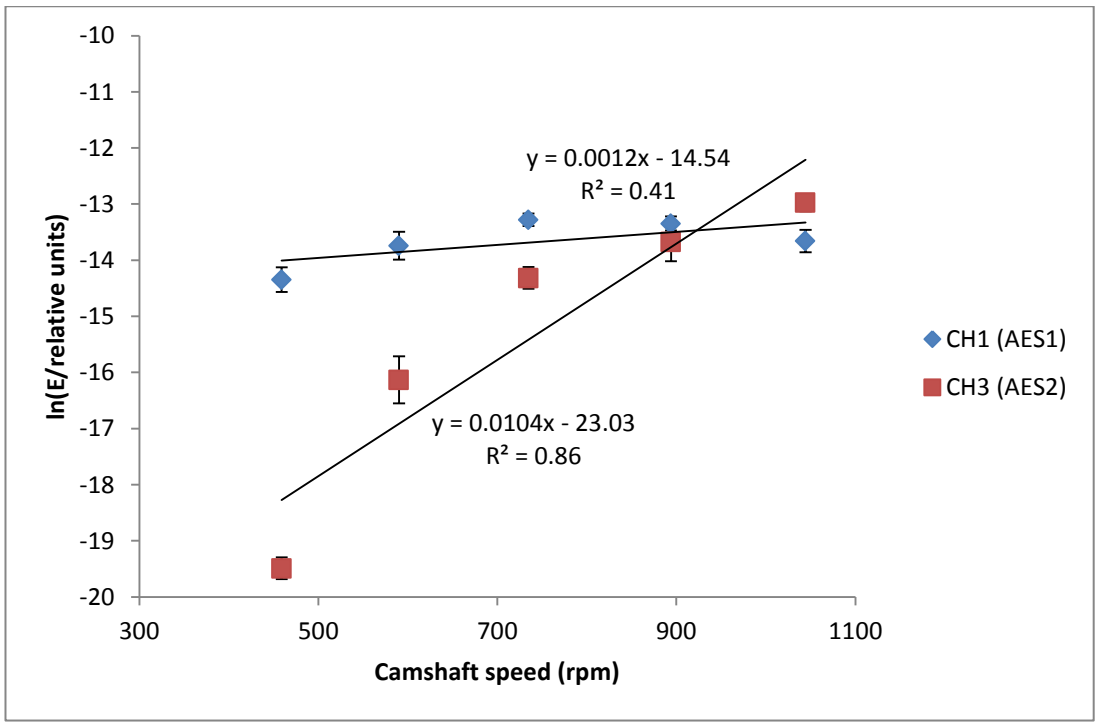

Figure 6.8: AE energy and time duration of the injection/combustion event (45° camshaft) at cylinder 1 in the running Perkins A4.270 engine (engine B) experiment.

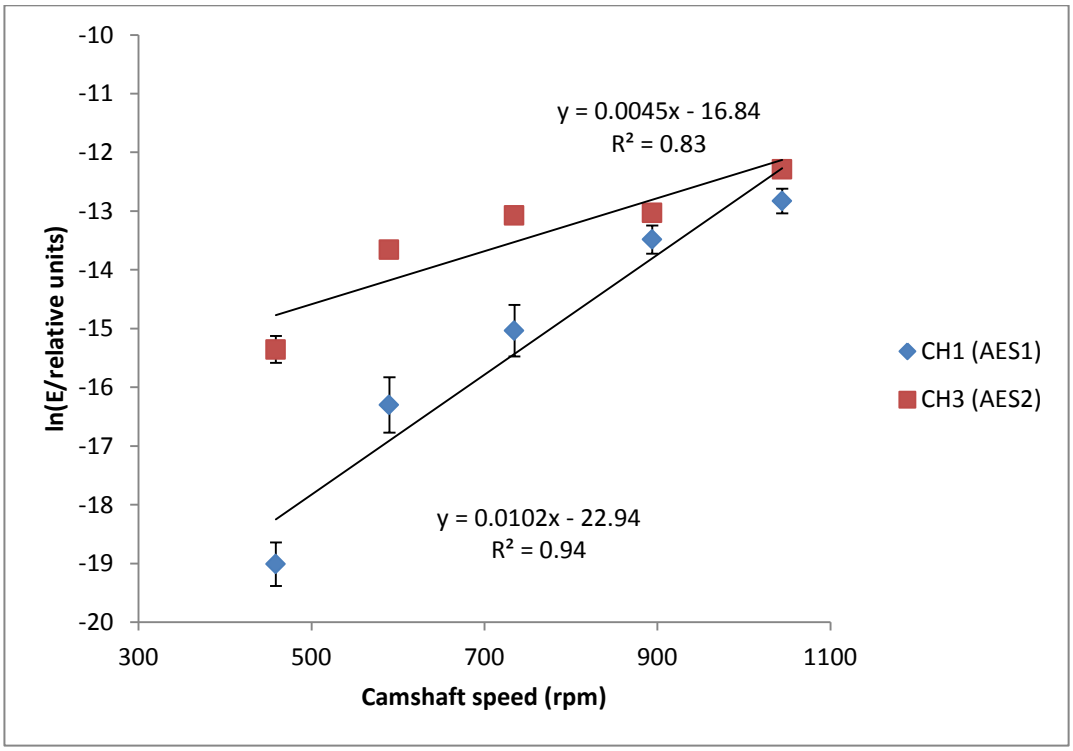

Figure 6.9: AE energy and time duration of the injection/combustion event (45° camshaft) at cylinder 3 in the running Perkins A4.270 engine (engine B) experiment.

6.1.2 Signal frequency demodulation analysis for engine B

Figure 6.10 shows the signal from Figure 6.2 averaged to reveal frequencies in the range of the engine running speed. As might be expected, the demodulated spectra (Figure 6.3) are more complex, although it is possible to see a secondary periodicity. The fundamental frequency is clearly reflecting the camshaft speed while four harmonics are evident with the fourth harmonic always having the maximum power (as shown in Figure 6.11). It has been seen in the two stroke engine that the second harmonic has the maximum peak value.

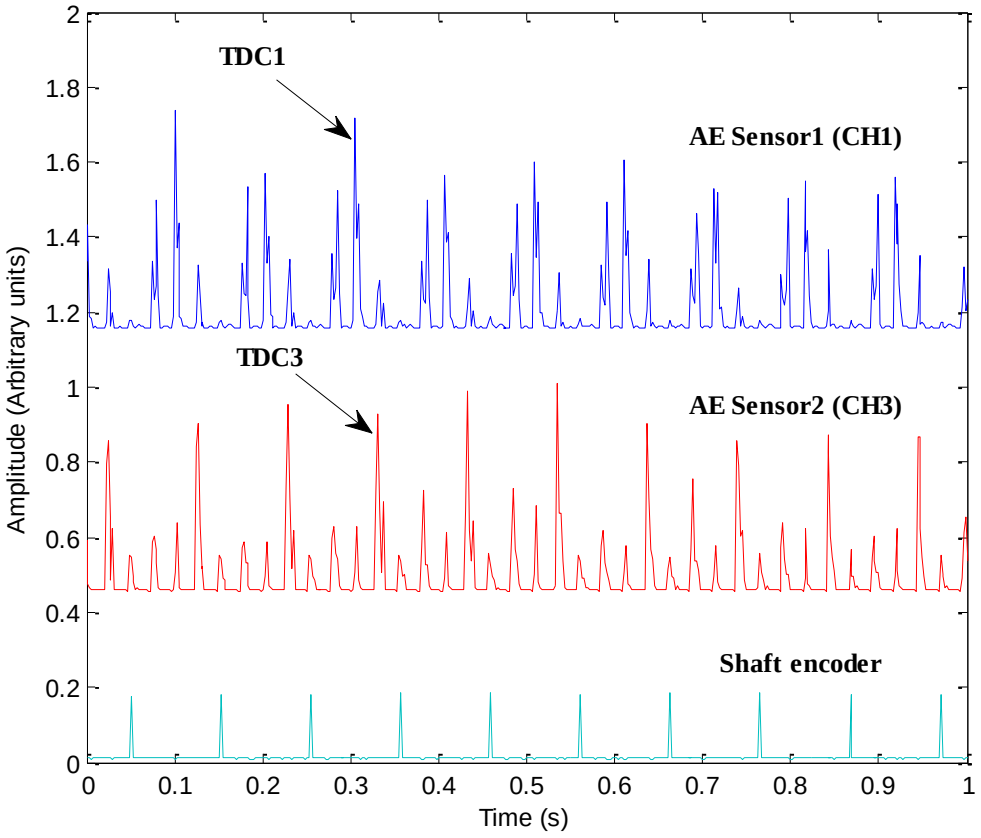

Figure 6.10: Demodulated AE signal for injection pump speed of 588 rpm.

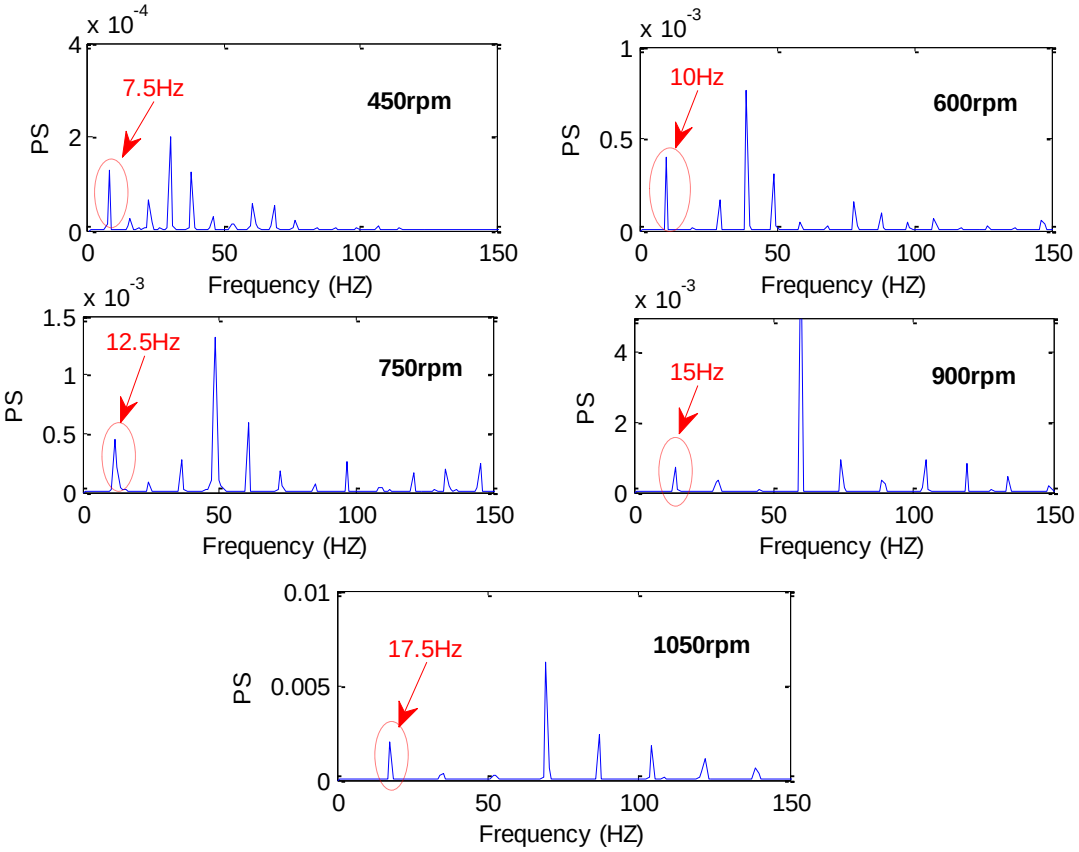

(a)

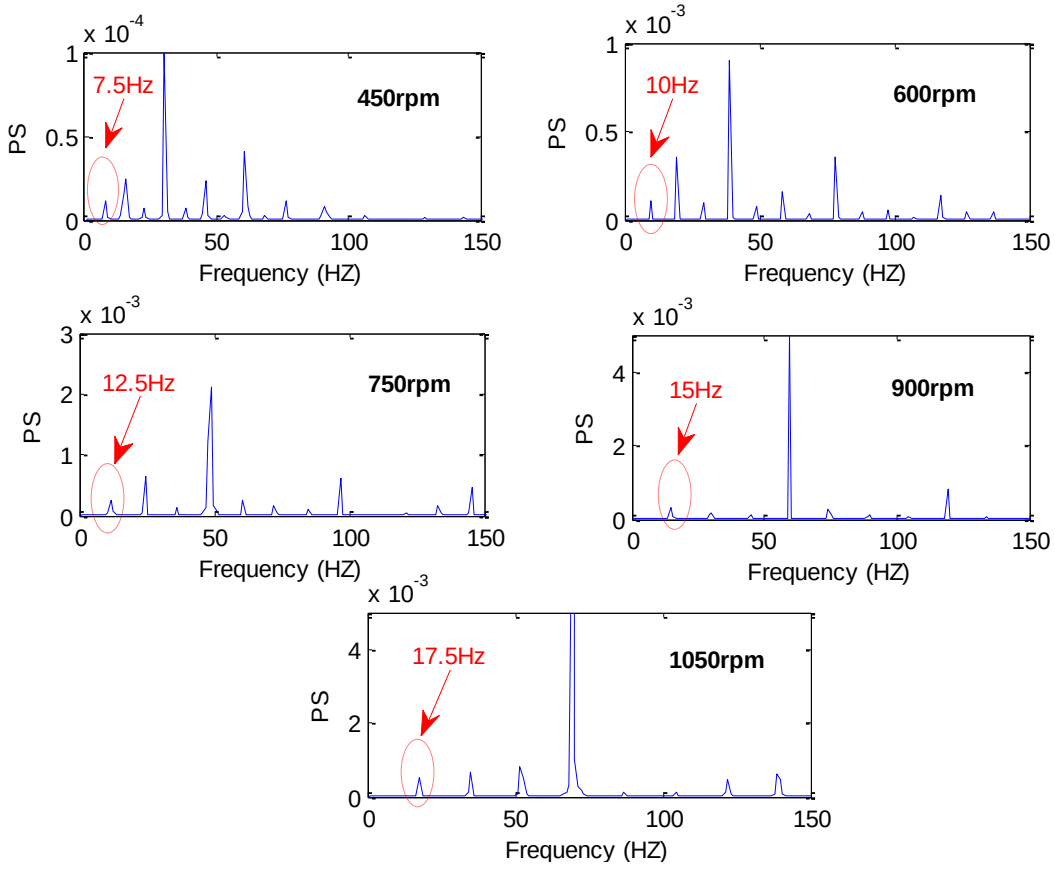

(b)

Figure 6.11: Frequency domain of demodulated AE signal from sensor1 (a) and sensor2 (b).

6.1.3 Identification of diesel engine events using canonical correlation analysis; Engine B

The Cylinder 1 and Cylinder 3 windows shown in Figures 6.4 and 6.5 were used to apply the SICCA algorithm to the RMS AE signal. Figures 6.12 and 6.13 show examples of the canonical correlation analysis in which the distribution of R^2 over the range of shift in camshaft angle from -12^o to $+12^o$ for the different engine running speeds. Figure 6.14 shows the maximum values of R^2 for both windows where Cylinder 3 has relatively constant, but poor, value, whereas, for Cylinder 1, the correlation deteriorates significantly with speed. As can be seen from Figure 6.15 the maximum correlation peak is always between -1° and 3° shift for Cylinder 3 but this is only valid for Cylinder 1 at the lowest and the highest speeds, the maximum being found at a larger angle shifts for the three intermediate speeds. Figure 6.16 shows the corresponding time shifts for maximum regression by converting the angle shift using the ICAV values.

In order to improve the results, a finer angle shift range (-5^o to $+5^o$ camshaft angle) was introduced to focus on more localised sources and avoid the interference with other engine events. As seen in Figure 6.17, this had very little effect on the results from Cylinder 3 or the results at the lowest and highest speed Cylinder 1, as it would be expected. Figures 6.18 and 6.19 show that the angle shift corresponding to the maximum regression for the three intermediate speeds in Cylinder 1 are now consistent with the remaining results, albeit with lower maximum regression values.

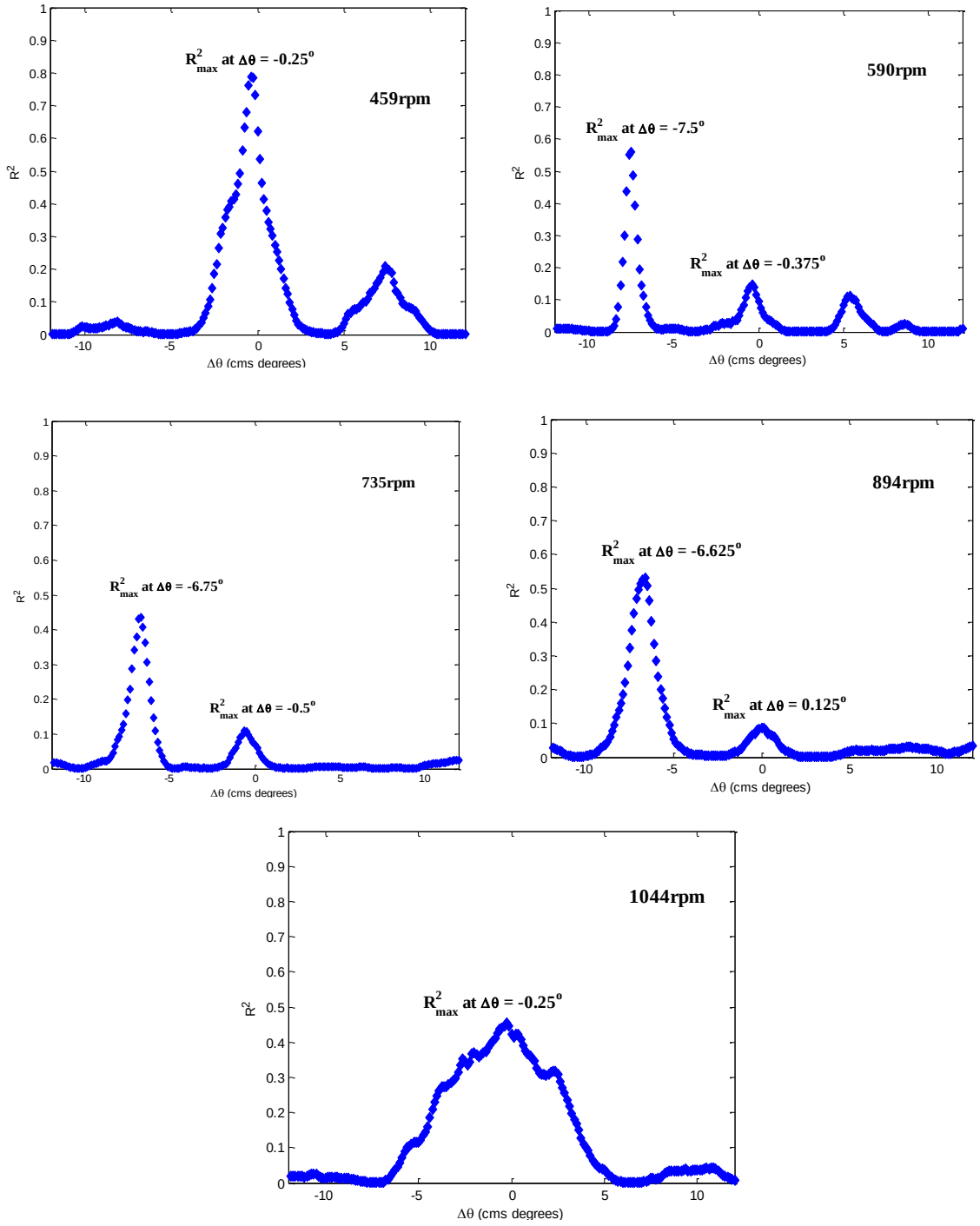

Figure 6.12: Example of the distribution of the regression coefficients over the Cylinder 1 window (15^ocms BTDC1 - 45^ocms ATDC1) from the canonical correlation (range of -12^o to $+12^o$ cms shift) in the running experiment for Engine B.

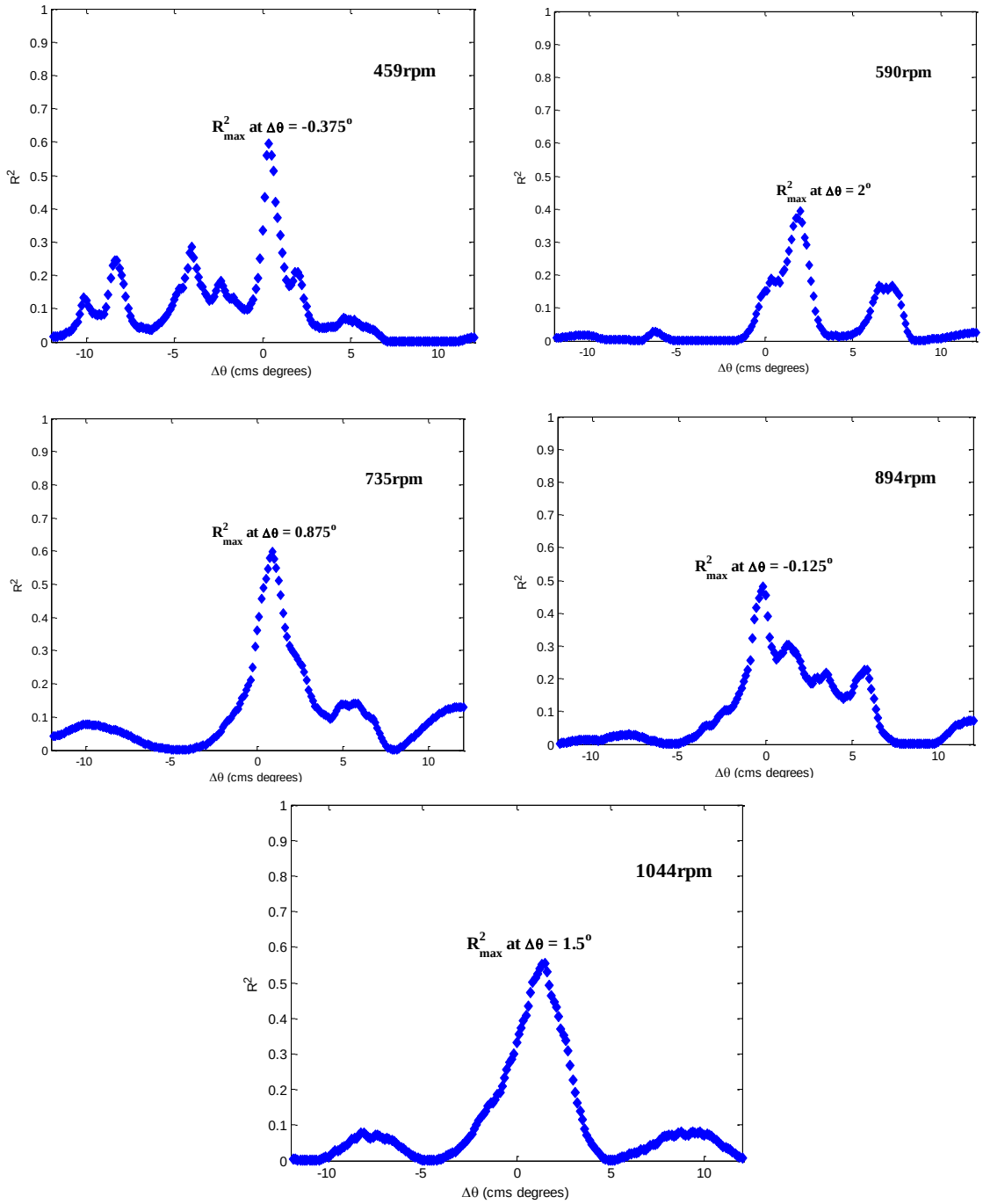

Figure 6.13: Example of the distribution of the regression coefficients over the Cylinder 3 window (15^ocms BTDC1 - 45^ocms ATDC1) from the canonical correlation (range of -12^o to $+12^o$ cms shift) in the running experiment on Engine B.

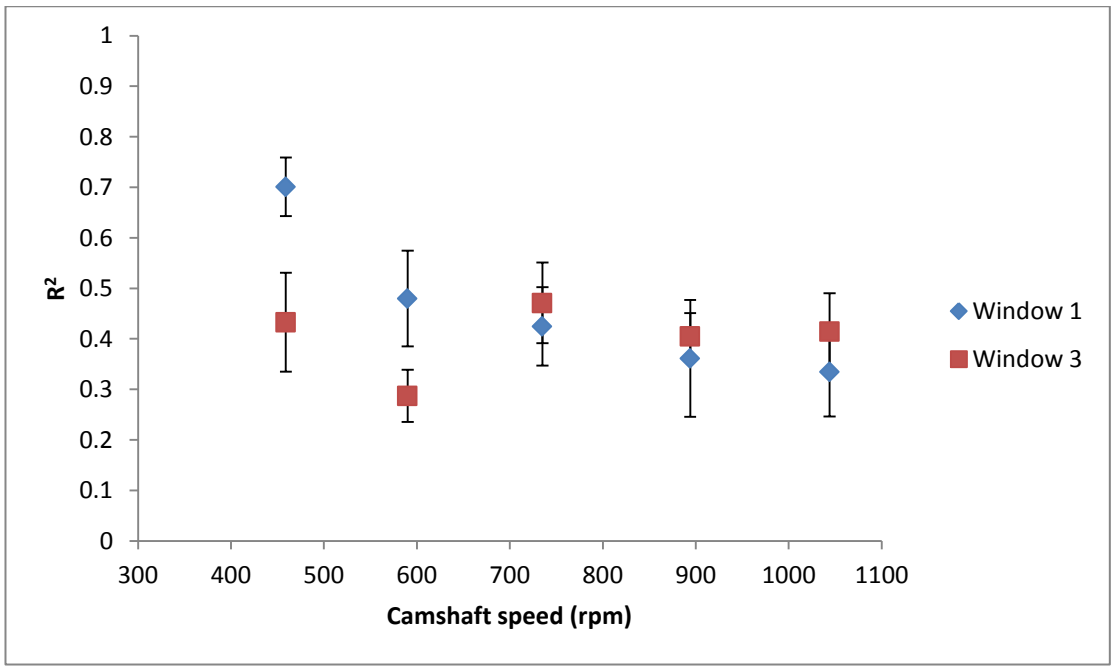

Figure 6.14: Regression coefficients of Cylinder 1 and 3 windows (15°cms BTDC1 - 45°cms ATDC1) from the canonical correlation (range of -12° to +12° cms shift) in Engine B.

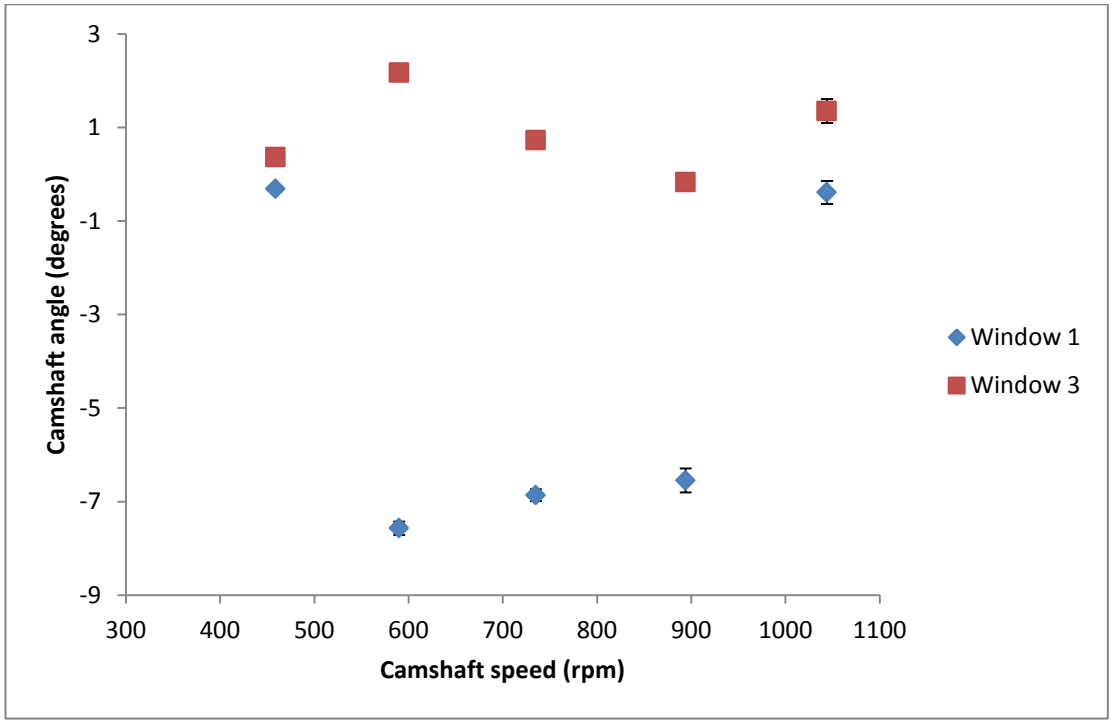

Figure 6.15: Corresponding camshaft angle shift for the maximum regression coefficients for Cylinder 1and 3 windows (15°cms BTDC1 - 45°cms ATDC1) from the canonical correlation (range of -12° to +12° cms shift) in Engine B.

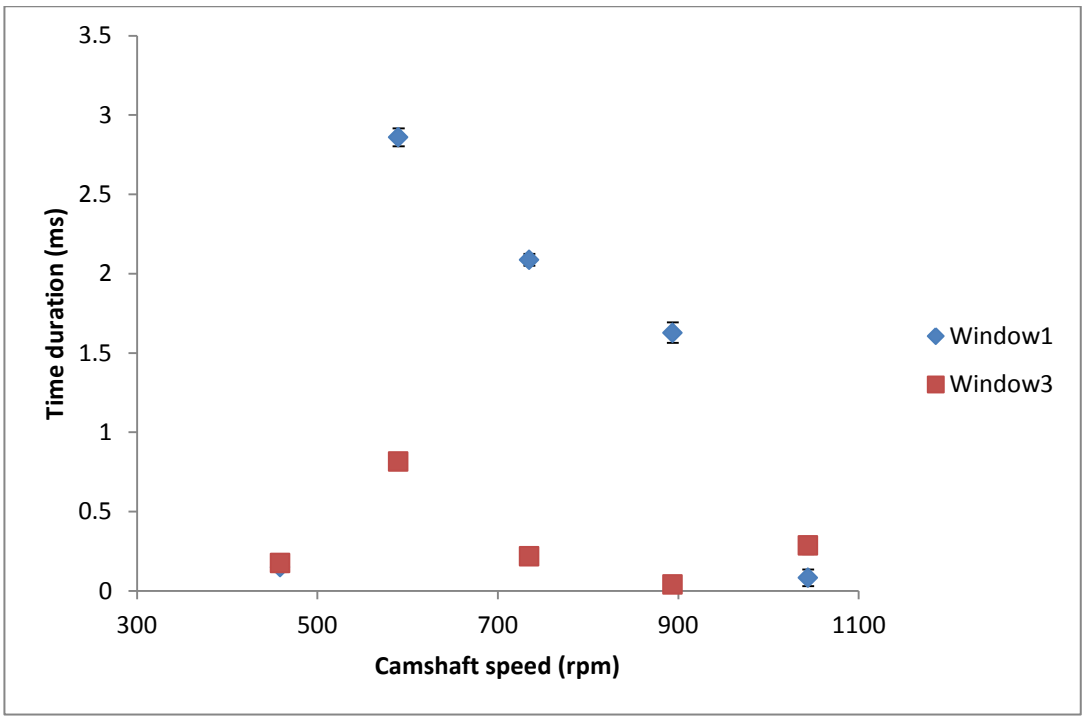

Figure 6.16: Corresponding time shift for the maximum regression coefficients for Cylinder 1 and 3 windows (15°cms BTDC1 - 45°cms ATDC1) from the canonical correlation (range of -12° to +12° cms shift) in Engine B.

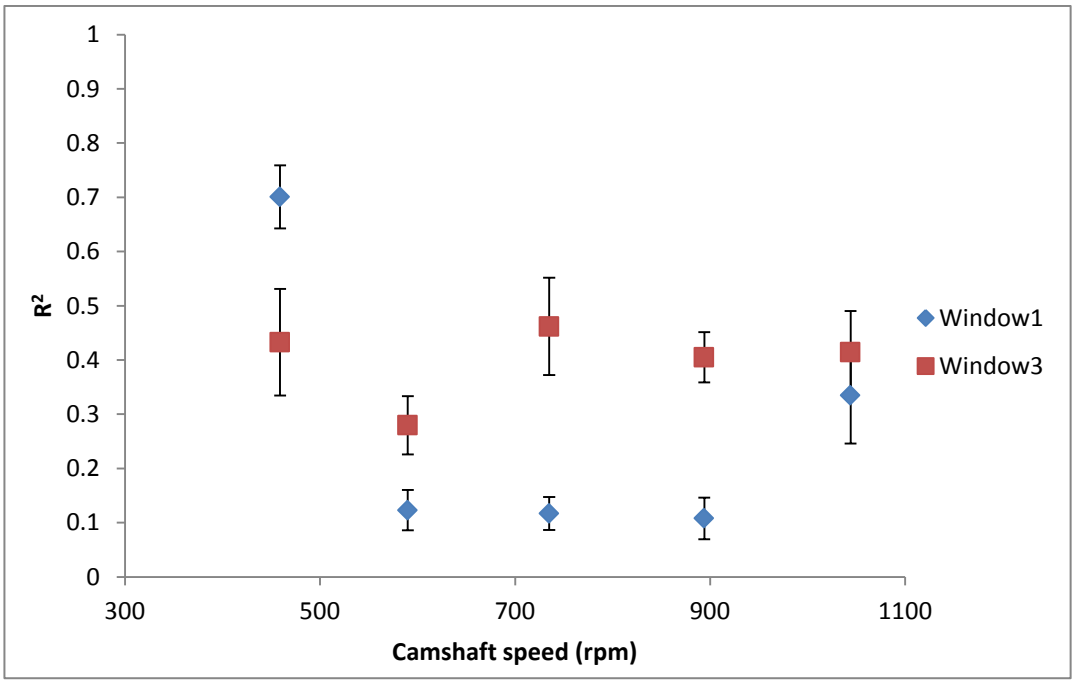

Figure 6.17: Regression coefficients for Cylinder 1 and 3 windows (15°cms BTDC1 - 45°cms ATDC1) from the canonical correlation (range of -5° to +5° cms shift) in Engine B.

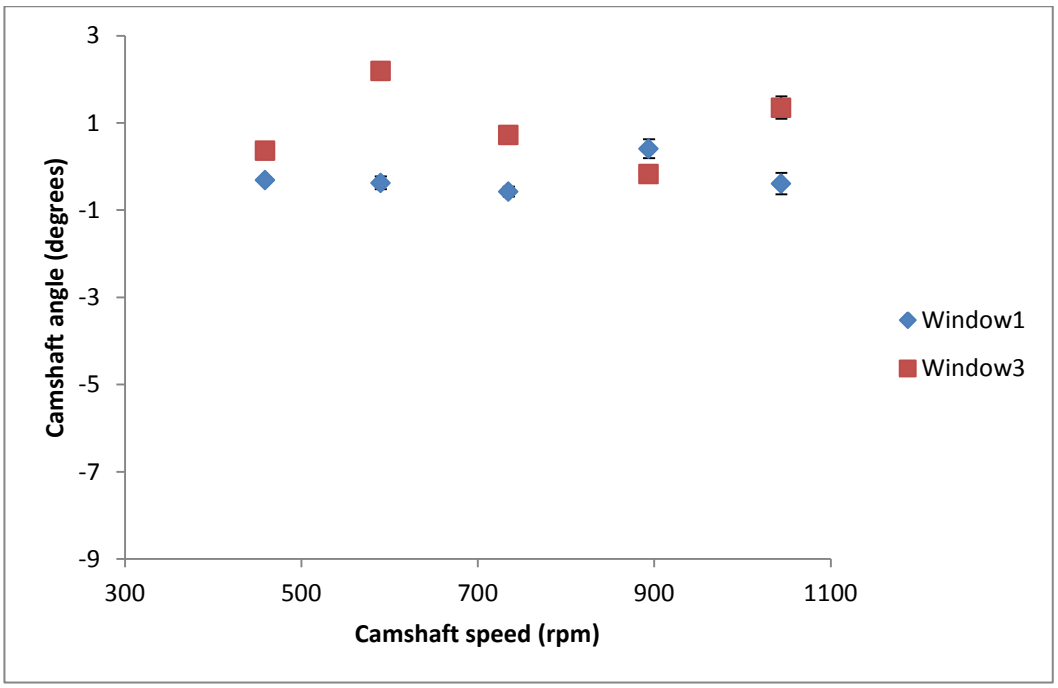

Figure 6.18: Corresponding camshaft angle shift for the maximum regression coefficients for Cylinder 1and 3 windows (15°cms BTDC1 - 45°cms ATDC1) from the canonical correlation (range of -5° to +5° cms shift) for Engine B.

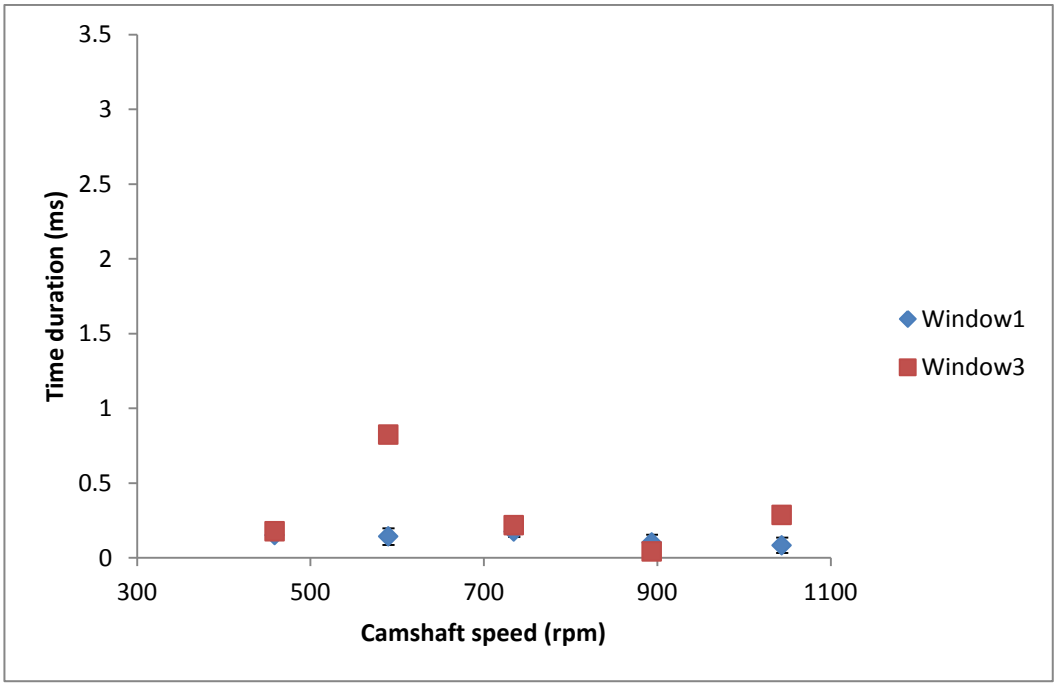

Figure 6.19: Corresponding time shift for the maximum regression coefficients Cylinder 1 and 3 windows (15°cms BTDC1 - 45°cms ATDC1) from the canonical correlation (range of -5° to +5° cms shift) in Engine B.

6.1.4 Summary of findings on Engine B

The analysis of Engine B has shown the added complexity associated with identifying the events in four-stroke four-cylinder engines which highlights the need for a more robust identification technique to tackle the problem of multiple sources more effectively. This is seen in particular from the results of the energy analysis which is affected by event overlap with increase in speed in some cylinders.

The application of the SICCA algorithm has provided promising results in terms of the identification of sources in engines. However, the technique requires further development as will be demonstrated on Engine C.

6.2 Running engine experiments: Engine C (sensor array1)

The first set of experiments on the Perkins T1004 engine (Engine C) used three sensors placed on the top surface of the cylinder head in an inline arrangement, similar to the experiments on Engines A and B, as shown in Figure 6.20. Figure 6.21 shows an example of a typical raw AE signal for four complete engine cycles in the angular domain where the maximum peaks are seen to occur according to the firing order, as expected.

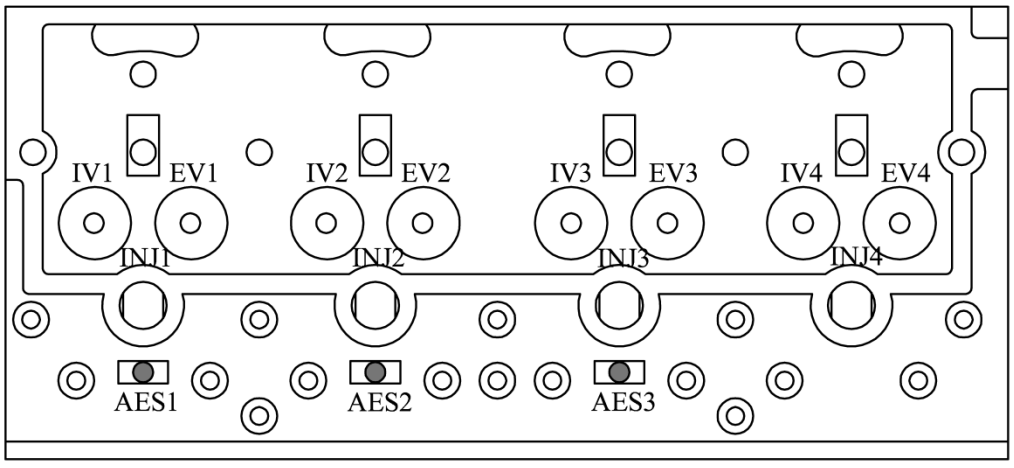

Figure 6.20: Schematic diagram of the running PerkinsT1004 (Engine C) sensor array1 experiment showing the positions of AE sensor array.

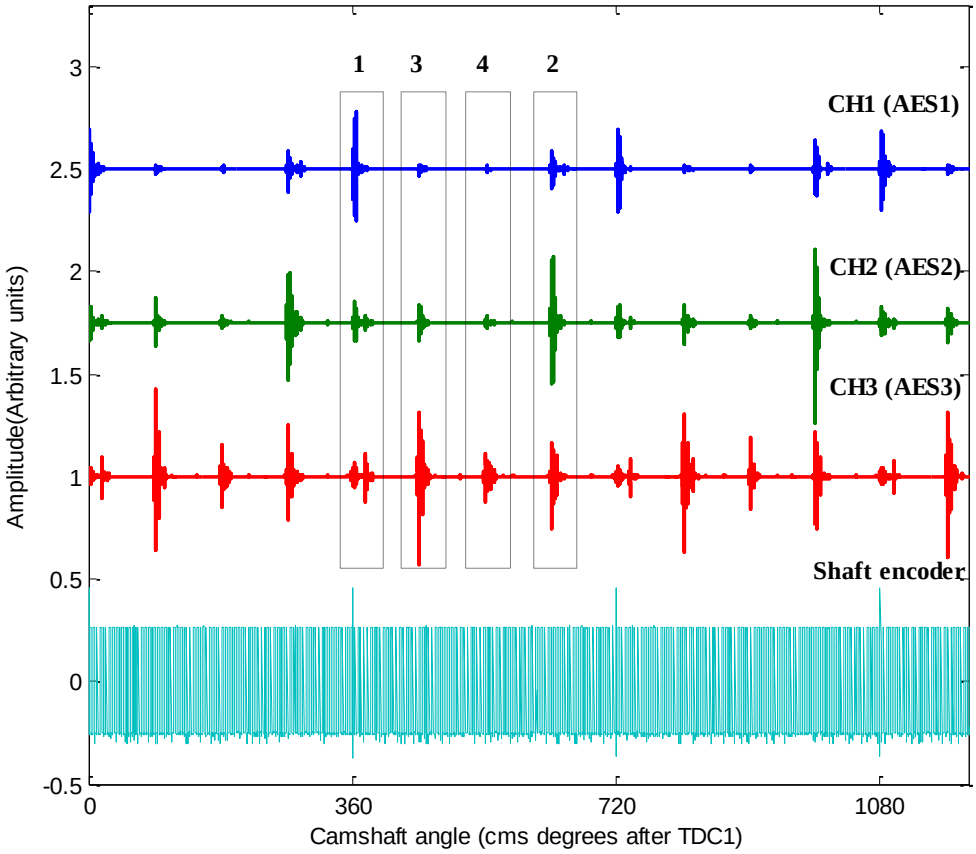

Figure 6.21: Typical AE signals from PerkinsT1004 (Engine C) sensor array1 experiment showing each cylinder window in the firing order 1-3-4-2.

6.2.1 AE energy analysis for engine C (sensor array1)

Figures 6.22 to 6.24 show typical raw AE angle series for the injection/combustion windows for Cylinders 1, 2 and 3, respectively. In all series, the advance in injection is evident for speeds over 1000 rpm (as per VE Bosch pump [7]), when the advance device starts to work, and the length of the signal increases in the angular domain due to the constant injection and ignition time lags.

Figures 6.25 to 6.27 show the results of the AE energy calculated using the 9.5 ms fixed time window for Cylinders 1, 2 and 3, respectively. It is clear that the energy values reflect the sensor position with the exception of Cylinder 1 at higher speeds which could mean further energy analysis is required.

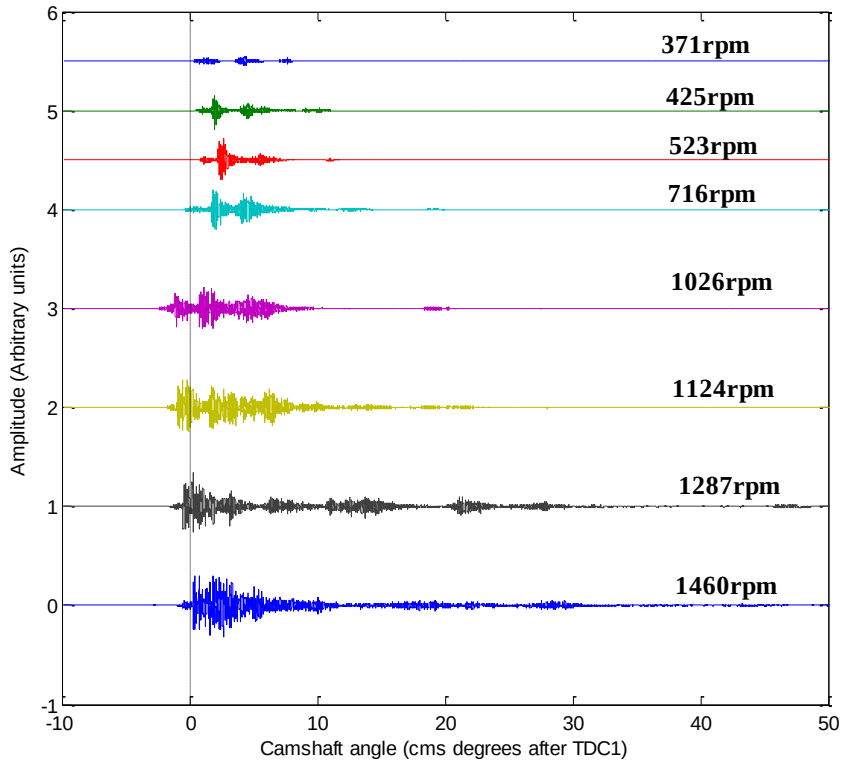

Figure 6.22: Raw AE signal recorded by Sensor1 from Engine C (sensor array1) showing the Cylinder 1 injection window for all the acquired speeds in the angular domain.

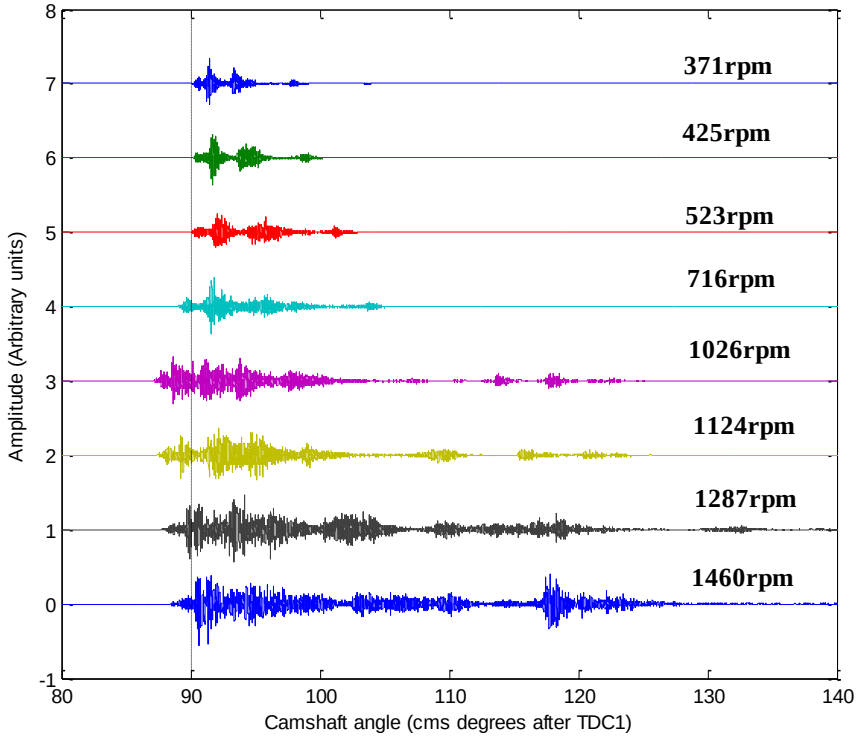

Figure 6.23: Raw AE signal recorded by Sensor2 from Engine C (sensor array1) showing the Cylinder 2 injection window for all the acquired speeds in the angular domain.

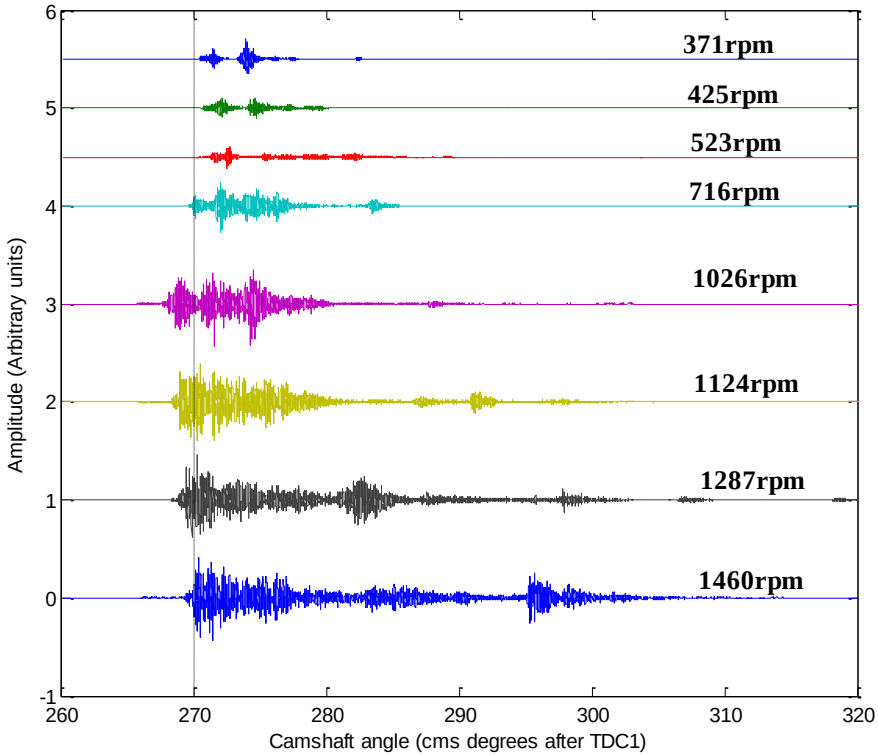

Figure 6.24: Raw AE signal recorded by Sensor 3 from Engine C (sensor array1) showing the Cylinder 3 injection window for all the acquired speeds in the angular domain.

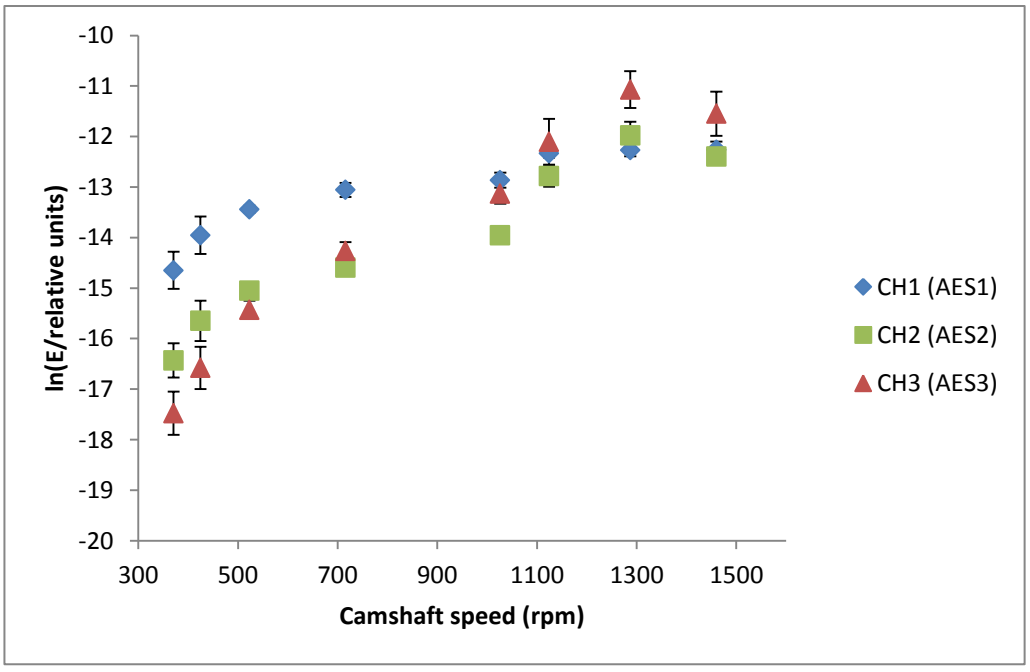

Figure 6.25: Averaged AE energy in the injection/combustion event for Cylinder1 calculated using a fixed-time window for PerkinsT1004 (Engine C), sensor array1.

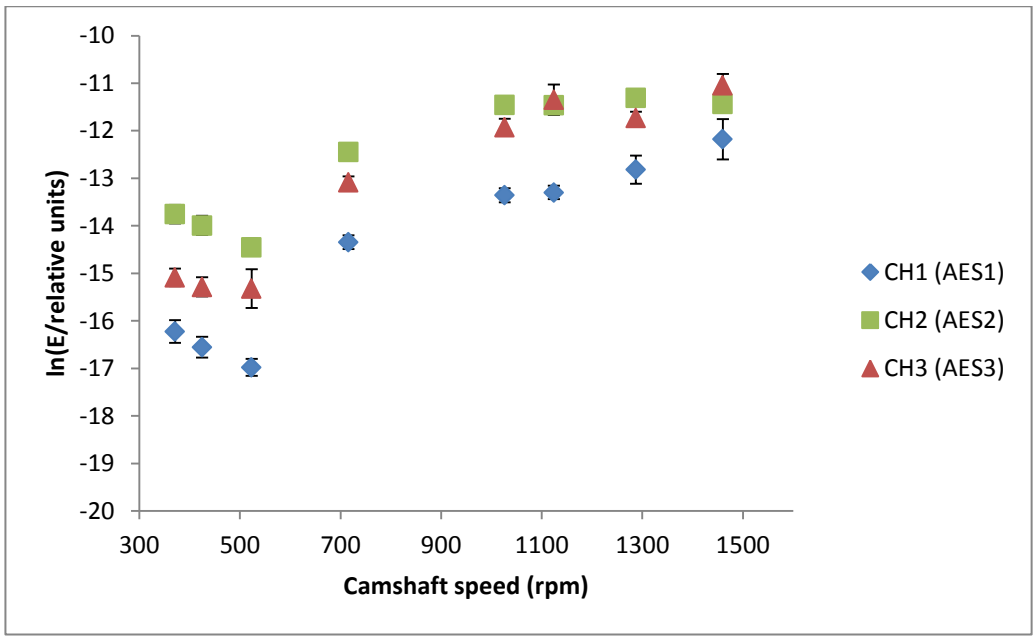

Figure 6.26: Averaged AE energy in the injection/combustion event for Cylinder 2 calculated using a fixed-time window for PerkinsT1004 (Engine C), sensor array1.

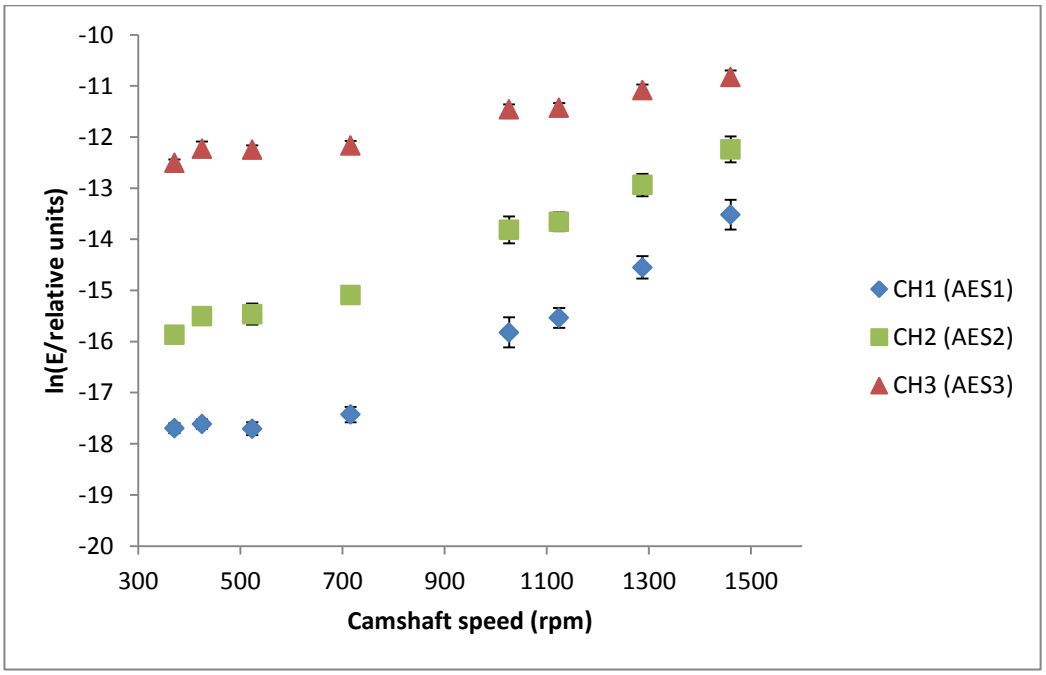

Figure 6.27: Averaged AE energy in the injection/combustion event for Cylinder 3 calculated using a fixed-time window for PerkinsT1004 (Engine C), sensor array1.

6.2.2 Signal frequency demodulation analysis for engine C (sensor array1)

The demodulated AE signal (Figure 6.28) highlights the injection/combustion events clearly as a pulse train. Again, the frequency analysis of the demodulated signals exhibits the fundamental frequency (associated with the running speed) as shown in Figures 6.29 to 6.31. As with Engine B, a four-peak pulse train characteristic is seen in all demodulated signals irrespective of the sensor used.

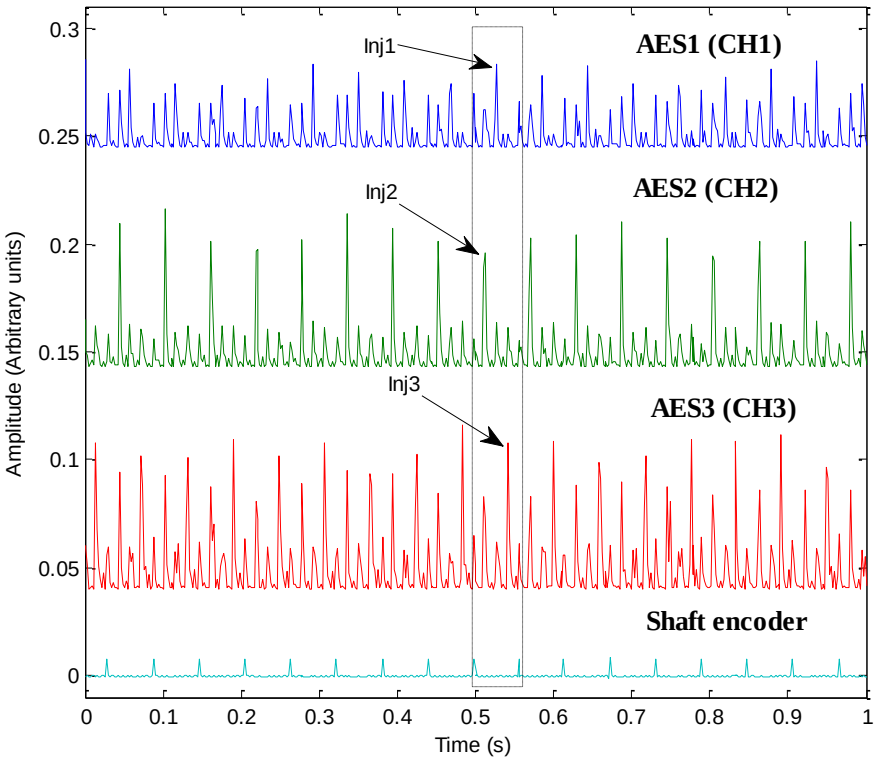

Figure 6.28: Demodulated AE signal from Engine C (sensor array1) at a camshaft speed of 1026rpm.

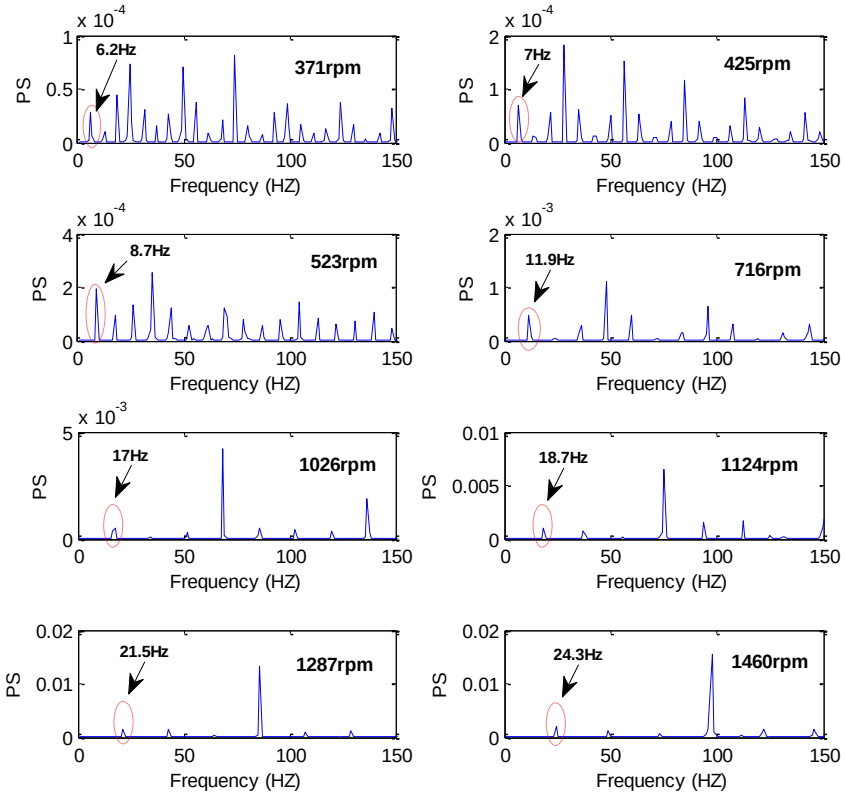

Figure 6.29: Frequency content of the demodulated AE signals acquired in the running experiment of Engine C (sensor array1) over the range of camshaft speed recorded at Sensor 1.

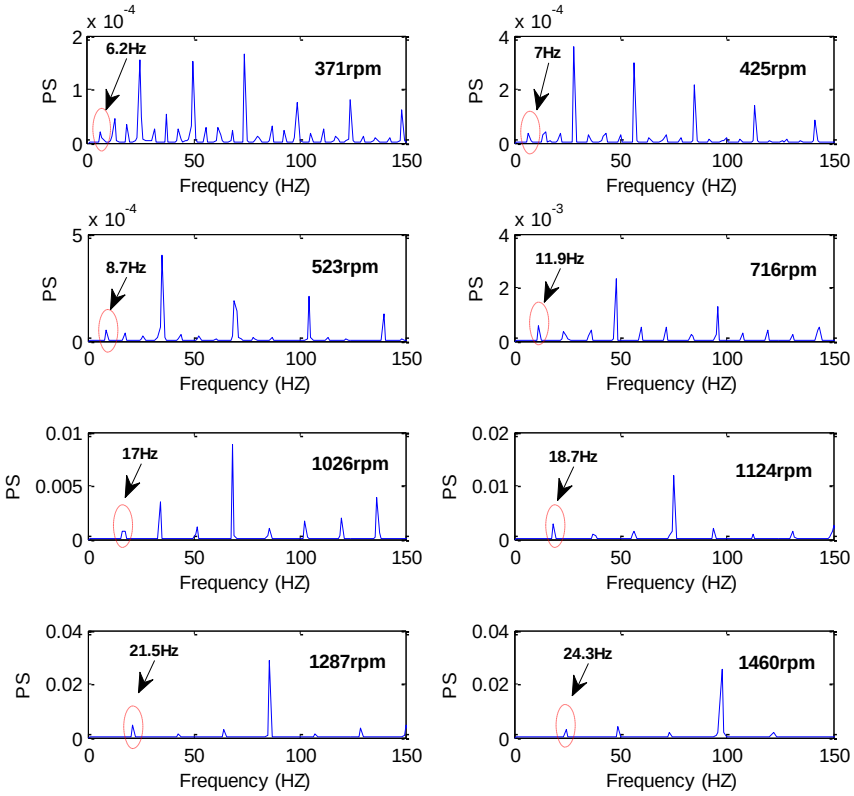

Figure 6.30: Frequency content of the demodulated AE signals acquired in the running experiment of Engine C (sensor array1) over the range of camshaft speed recorded at Sensor 2.

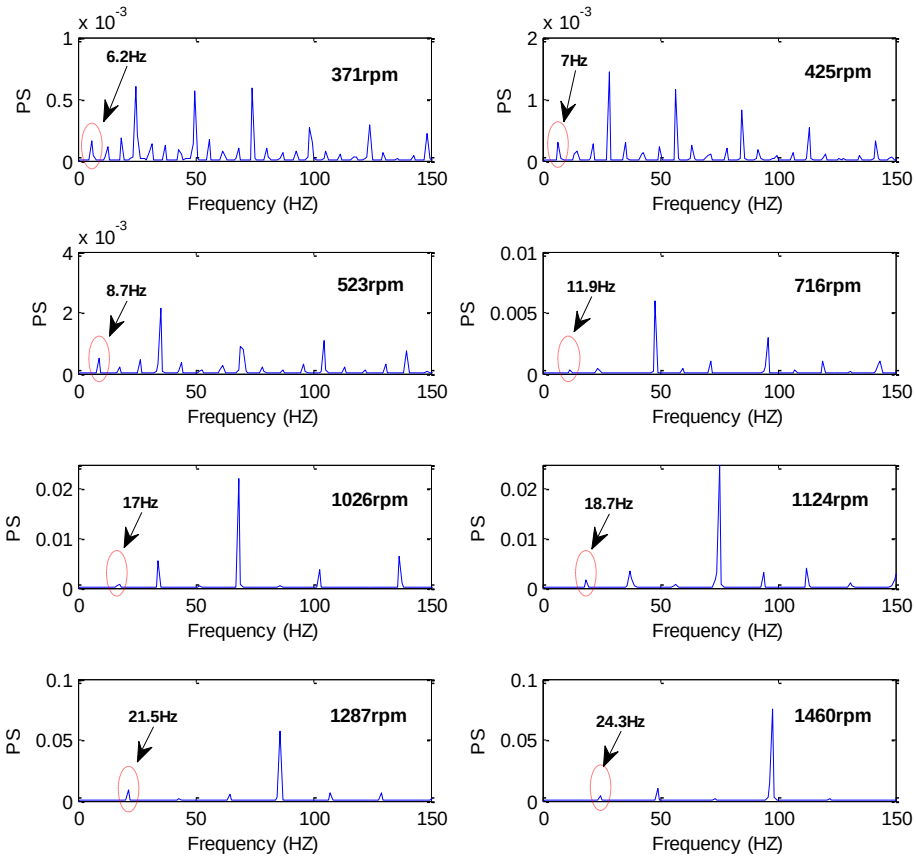

Figure 6.31: Frequency content of the demodulated AE signals acquired in the running experiment of Engine C (sensor array1) over the range of camshaft speed recorded at Sensor 3.

6.2.3 Identification of diesel engine events using canonical correlation analysis; Engine C (sensor array1)

Figure 6.32 shows the regression distributions for 200 cycles, in which CCA has been applied to compare the signal acquired at Cylinder 2 to the signal acquired at Cylinder 1 over the Cylinder 1 injection/combustion window. The use of SICCA here is far more complex than the previous experiment particularly because there are now three sensors, giving three groups of output (sensor pairs), each group having a subgroup representing the event window studied. A summary of the maximum regression values is presented in Figures 6.33 and 6.34 for the Cylinder 1 and 3 windows, respectively. It can be seen that the correlation between Cylinders 2 and 1 is best and that between Cylinders 3 and 1 is poorest for both windows. This can be represented more clearly by plotting the corresponding angle shift values as shown in Figures 6.35 and 6.36. There are two possible reasons for this difference, the first being that the most remote sensor is the weakest signal which, as shown in Chapter 4, does not in itself result in poorer canonical correlations. The other explanation is there are multiple sources at different locations and their times of arrival, as well as amplitude, change most significantly with

relative sensors distance. This effect is examined more closely with reference to array 2, which has a sensor mounted on one of the injectors.

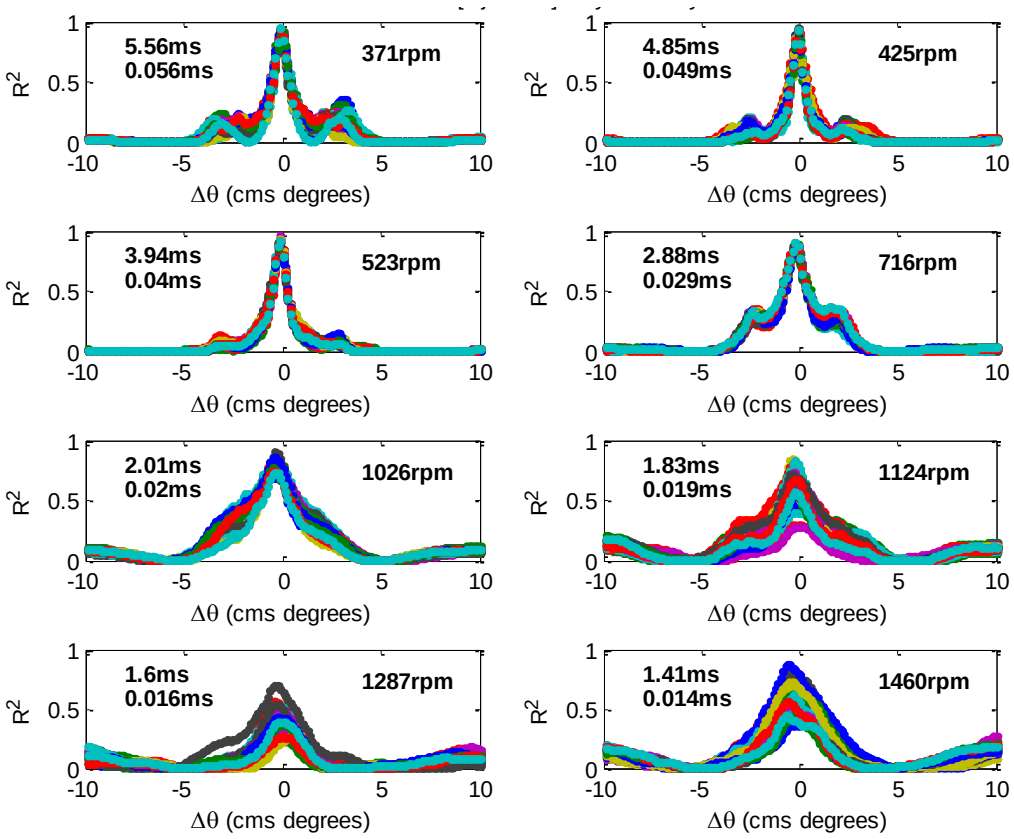

Figure 6.32: Correlation coefficients of AES2 (Cylinder 2) vs. AES1 (Cylinder 1) from the canonical correlation of the injection/combustion event of Cylinder 1 (10°cms BTDC1 - 35°cms ATDC1) for PerkinsT1004 (Engine C) sensor array1 experiment.

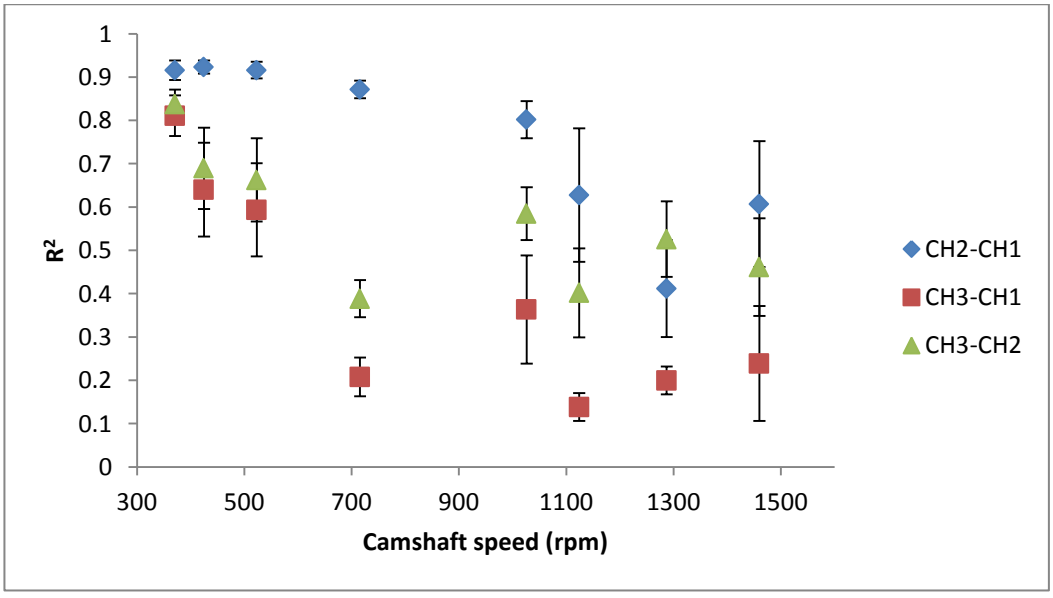

Figure 6.33: Regression coefficients of cylinder head 1 window from the canonical correlation of the injection/combustion event of cylinder 1 (10°cms BTDC1 - 35°cms ATDC1) for PerkinsT1004 (engine C) sensor array1 experiment.

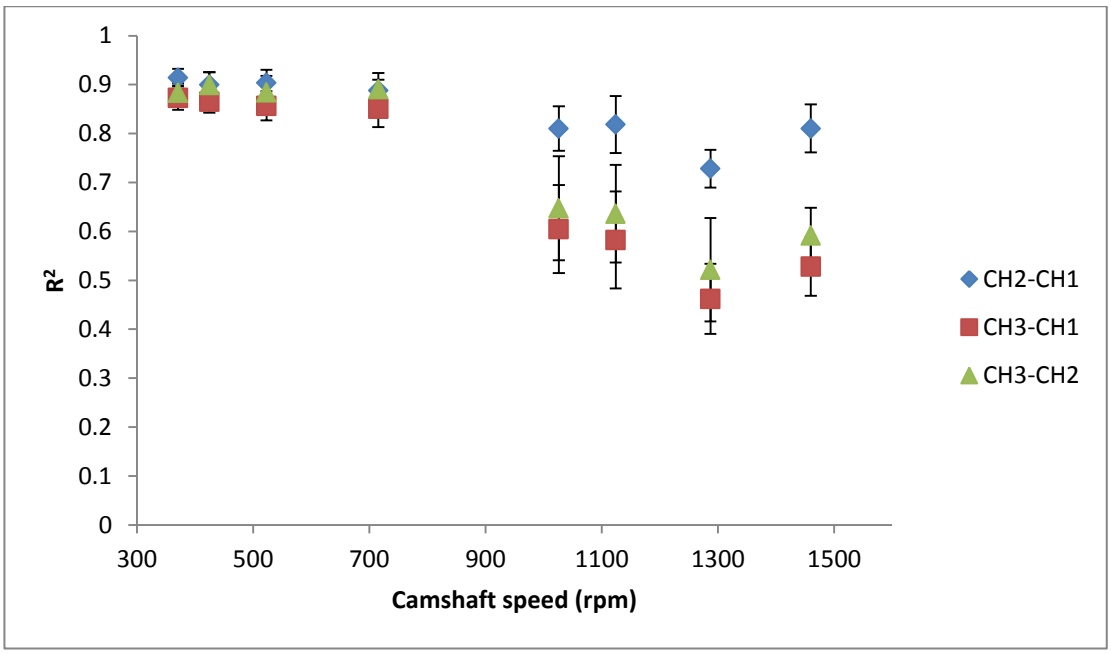

Figure 6.34: Averaged regression coefficients of cylinder head 3 window from the canonical correlation of the injection/combustion event of cylinder 1 (10°cms BTDC1 - 35°cms ATDC1) for PerkinsT1004 (engine C) sensor array1 experiment.

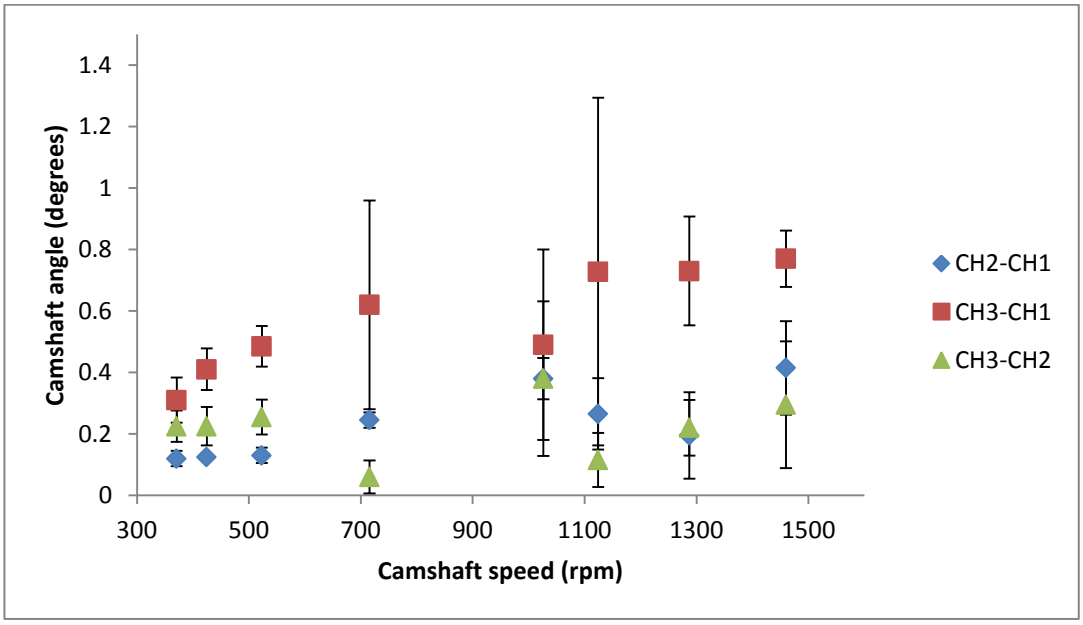

Figure 6.35: Averaged cam angle difference corresponding to maximum regression coefficients of cylinder head 1 window from the canonical correlation of the injection/combustion event of cylinder 1 (10°cms BTDC1 - 35°cms ATDC1) for engine C sensor array1 experiment.

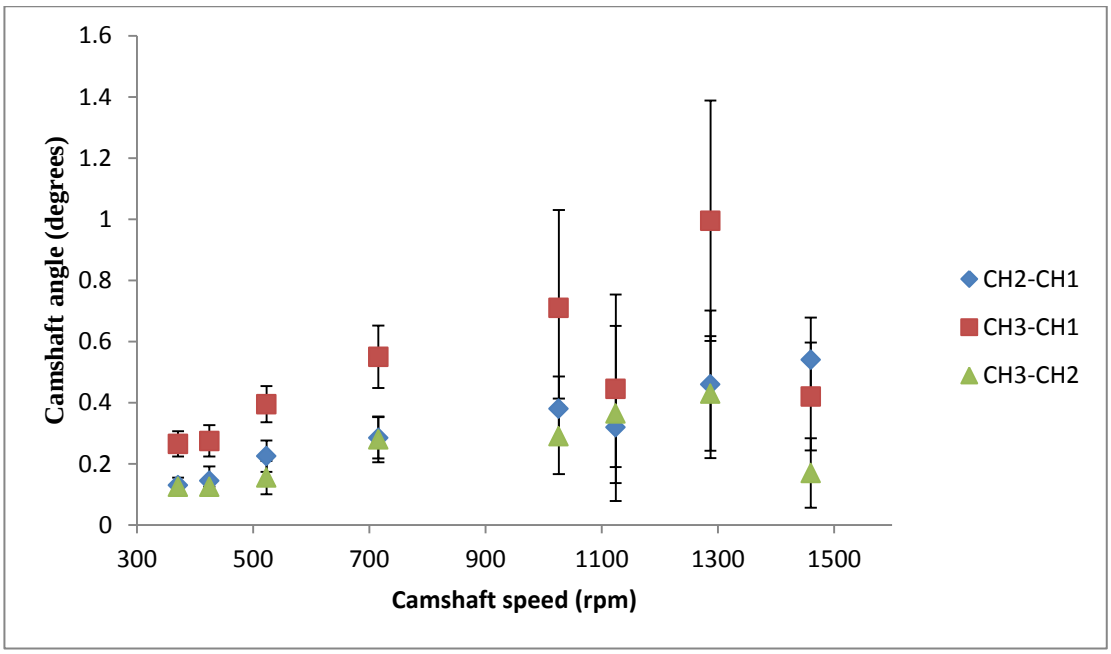

Figure 6.36: Averaged cam angle difference corresponding to maximum regression coefficients of cylinder head 3 window from the canonical correlation of the injection/combustion event of cylinder 1 (10°cms BTDC1 - 35°cms ATDC1) for engine C sensor array1 experiment.

6.2.4 Summary of findings on Engine C (sensor array1)

This experiment complemented the experiments on Engine B, in that an inline sensor array was used, although 3 sensors were used instead of 2. In contrast, the physical arrangement of the engine components (e.g. valve, ports, etc.) varies from one engine to another which cause signal variability, although clear pulse trains are still indicated in the demodulated signal. This application of SICCA highlighted the different results obtained from different sensor pairs examining the same events indicating that it is likely that multiple sources can be separated using triangular arrays. This is investigated in the next experiment with particular reference to injection and combustion by using an asymmetrical array.

6.3 Running engine experiments: Engine C (sensor array2)

Figure 6.37 shows the second set-up on Engine C (sensor array 2), the main difference being that there is now a sensor on the injector, identically placed to that in the injector rig experiment. As can be seen from Figure 6.38, the engine AE pattern is reasonably reproducible in amplitude and timing over a number of cycles, although neither can be

considered to be exact. To maintain a common treatment across all the data, 5 cycles were processed for each record, and analysis was carried out in both the angle and time domains. Figure 6.39 shows a typical record for all four sensors (3 AE plus shaft encoder) for a single cycle along with an engine map of the main mechanical events, noting that the injection (and hence combustion) timing is subject to variations with engine speed. Figure 6.39 also identifies the four "injection-combustion windows", constituting the angle (or time) period over which fuel enters and is burned in a given cylinder. It might be noted that other engine events occur within this window, but none of them concern the cylinder in question. Focusing on the cylinder 1 window, it can be seen that the highest amplitude signal is shown by the sensor mounted on injector 1 (AES1), especially significant given that the sensor mounted on the cylinder head adjacent to cylinder 1 (AES2) is about twice as sensitive as AES1, suggesting that the main source of AE in the window propagates more easily to the injector than to the cylinder head. It is also clear (for example by comparing AES3 and AES1) that the structure and the relative amplitudes of parts of the window are different as seen by different sensors. Finally, comparing AES3's response in the cylinder 3 window with AES1's response in the cylinder 1 window shows the structure to be different for nominally identical source-sensor relationships. These last two observations indicate that a given window contains contributions from more than one source, not necessarily all of which are within the given cylinder. It might also be noted that one event (e.g. injection) may have more than one source (e.g. contact during needle lift and spray formation) at different locations (e.g on the injector body and within the cylinder).

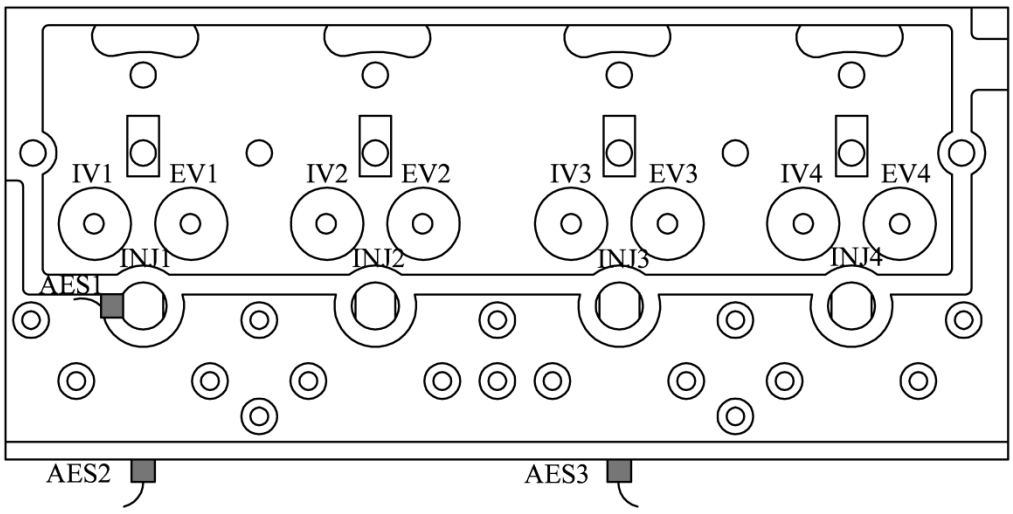

Figure 6.37: Schematic diagram of the running PerkinsT1004 (engine C) sensor array2 experiment showing the positions of AE sensor array.

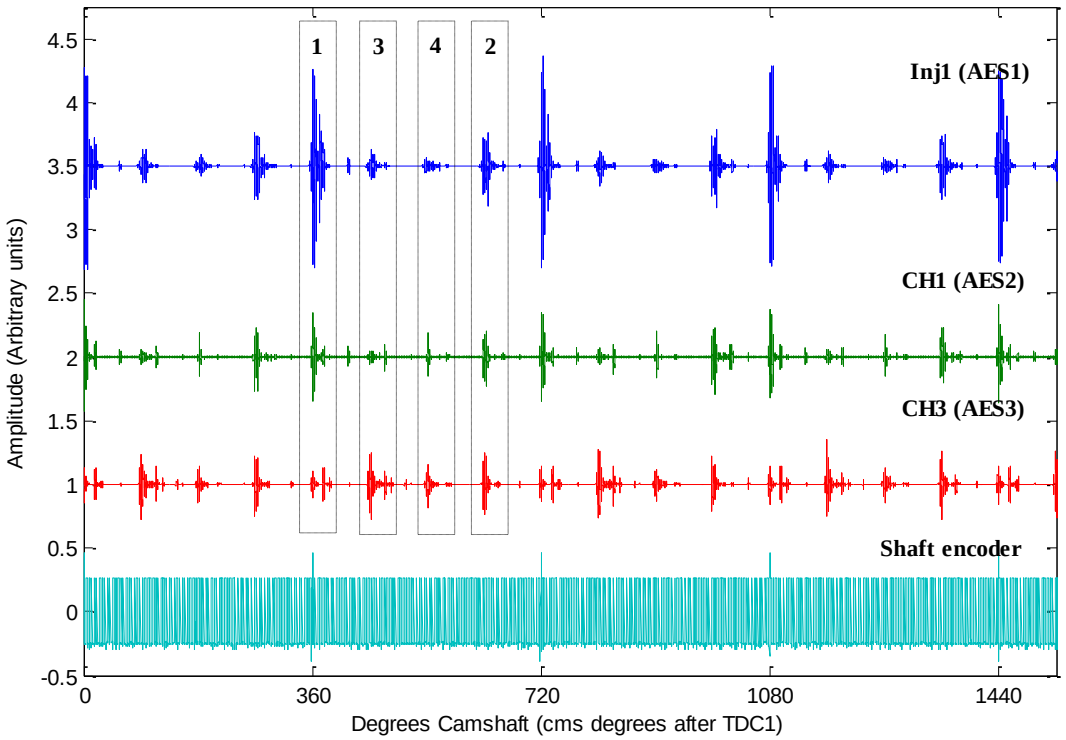

Figure 6.38: Raw AE signal of four complete engine cycles at camshaft speed of 997 rpm in the angular domain.

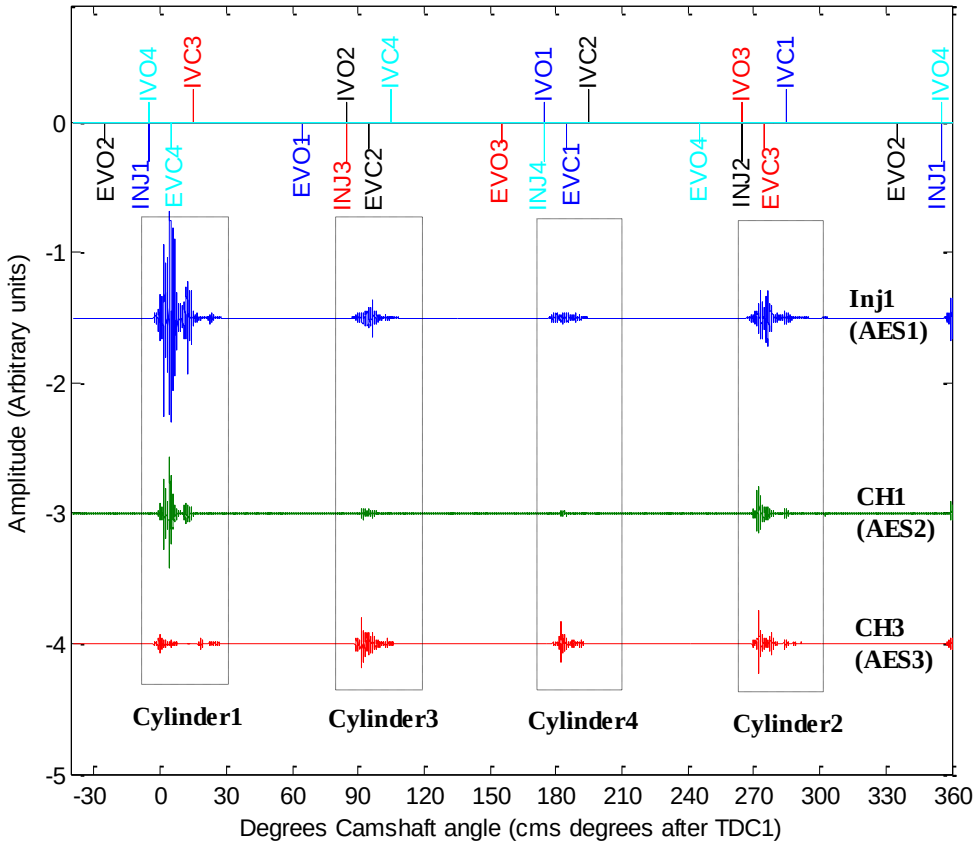

Figure 6.39: Raw AE signals for one complete engine cycle at camshaft speed of 736 rpm in the angular domain.

6.3.1 AE energy analysis for engine C (sensor array2)

Figure 6.40 shows examples of records of the cylinder 1 window as seen by the injector-mounted sensor for the range of engine speeds examined, and includes a magnified version of the relevant part of the engine map. Figure 6.41 shows the corresponding records as seen by the sensor mounted on the cylinder head adjacent to cylinder 1. These two sets of records show some important similarities, in that, with increasing engine speed, the general signal level increases, the signal commences earlier, and the trailing, low amplitude activity is spread out over later angles. There are also important differences between the two sensor record sets in both the timing and relative amplitudes of sections of the records, suggesting that there is more than one source location in the window. It is unlikely that there is a significant contribution from other cylinders; for example, EVC1 does not give a very strong signal at AES1 (Figure 6.39) and so EVC4 is even less likely to contribute significantly to the energy in the cylinder 1 window for this sensor.

As a first analysis, Figure 6.42 shows the AE energies of parallel records in the cylinder 1 window (10^{o}BTDC to 35^{o}ATDC) versus engine speed for each of the sensor locations, along with an (arbitrarily chosen) exponential fit. As might be expected, more AE energy is generated within this window as the engine speed increases and, interestingly, the growth constants for both the inj1 and CH1 sensors are very close, the injector sensor giving significantly higher AE levels across the whole speed range. Also interesting is the fact that the growth constant for the CH3 sensor is significantly higher than for the other two and this may be associated with an increasing contribution from the IVC3 event, which also occurs within the cylinder 1 window. Figure 6.42 also shows the angular duration of the activity in the cylinder 1 window, again with an arbitrarily chosen exponential fit, this time of decay.

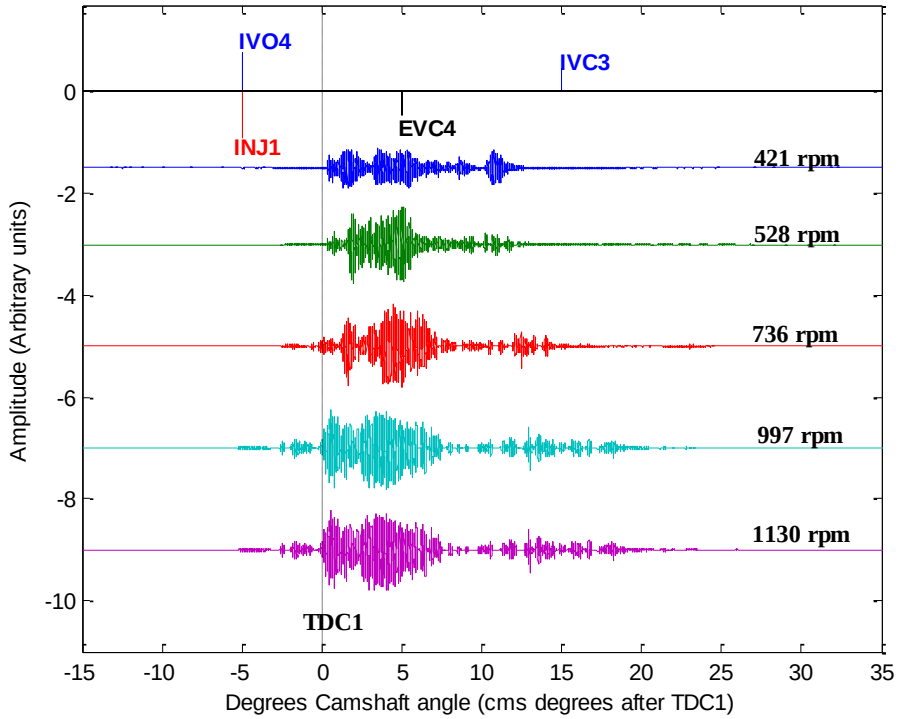

Figure 6.40: Raw AE signal recorded at Injector 1 over the Cylinder 1 window for all five speeds in the angular domain.

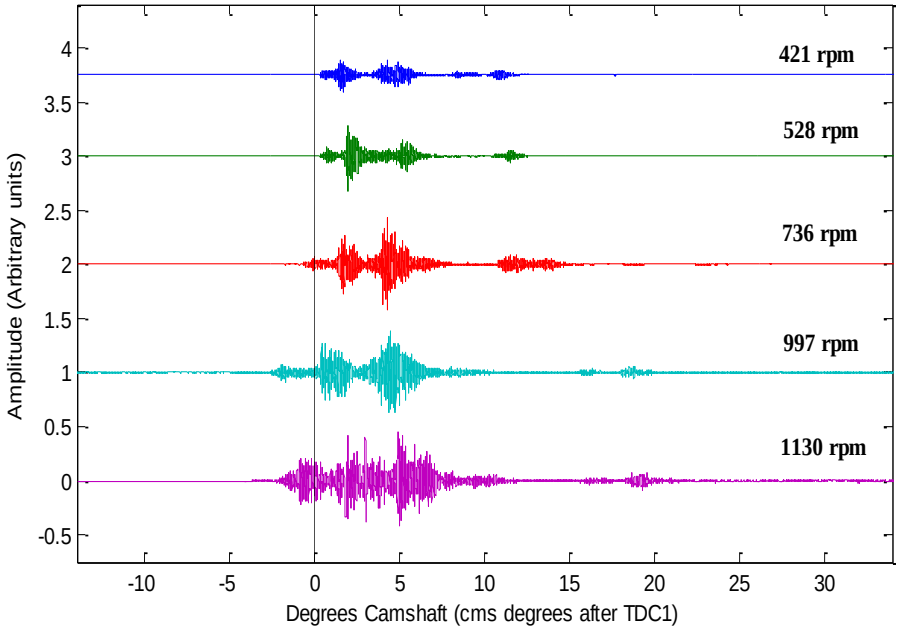

Figure 6.41: Raw AE signal recorded at Cylinder Head 1 over the Cylinder 1 window for all five speeds in the angular domain.

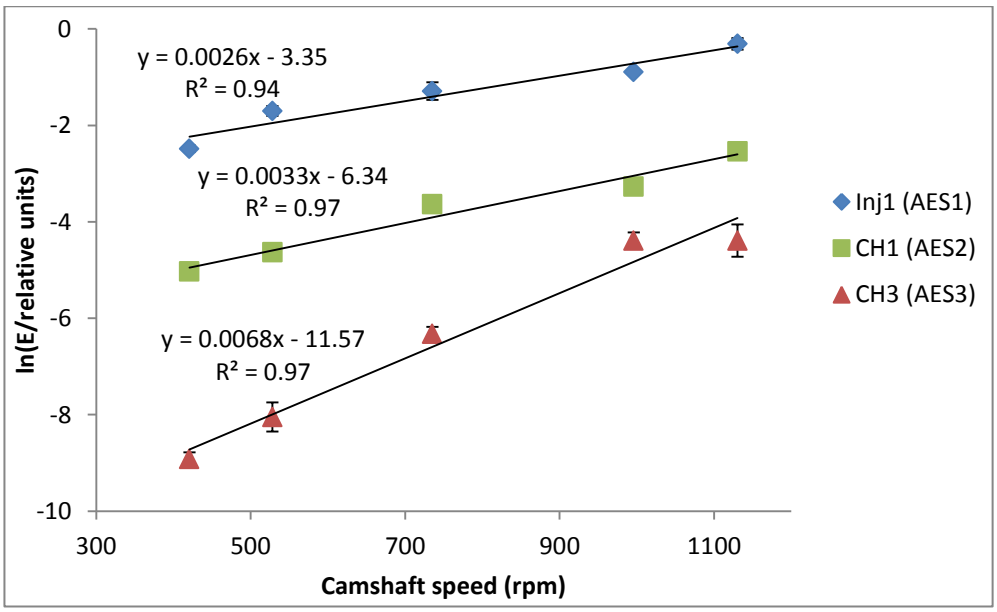

Figure 6.42: AE energy and time duration of the injection/combustion event (45° camshaft) at cylinder 1.

Figure 6.43 shows the AE energy from the three sensors using fixed time window and adaptive thresholding, where they can be seen to be almost identical, except for the measurements made adjacent to cylinder 3, where the lower signal-to-noise ratio (SNR) affects the performance of the automated algorithm slightly. However, all methods and sensor positions show the AE energy content of the event window to increase with an increase in the amount of fuel added (which is also increases the engine speed). The behaviour with engine speed is, of course, not entirely passive, due to the extra advance introduced by the VE injection system [62].

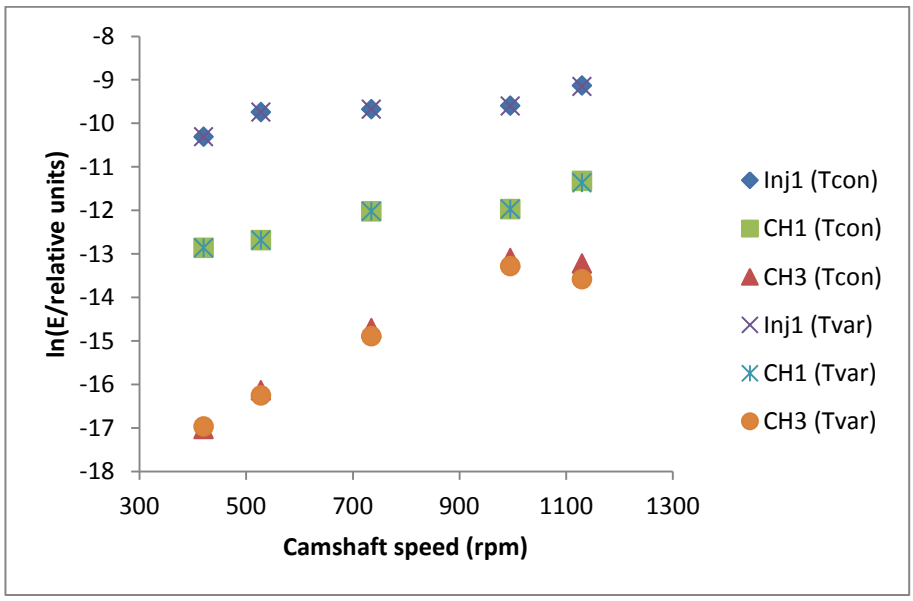

Figure 6.43: Averaged AE energy in the injection/combustion event for cylinder1 calculated using fixed-time (Tcon) and adaptive threshold (Tvar) windows.

6.3.2 ICAV and peak analysis

Instantaneous crankshaft angular velocity has shown to correlate well with average AE energy in diesel engines under a range of operating conditions, on the basis that the combustion of fuel generates the relevant accelerations of the pistons [167]. To test this hypothesis at a more detailed level in the injection/combustion event, the data from the shaft encoder was used to calculate the ICAV, instantaneous camshaft angular velocity (Figure 6.44), used here in preference to the more conventional crankshaft angular velocity to maintain consistency with the rest of the analysis. The ICAV waveform within the event window at TDC1 (10^{o}BTDC1-35^{o}ATDC1), highlighted in Figure 6.44, has been extracted for more detailed analysis. Figure 6.45 shows one example of the ICAV response and the corresponding AE signals from the two cylinder 1 sensors over the 45^{o} event window around TDC1. As can be seen, there is a peak in the AE recorded at the injector, which seems to correlate with the minimum ICAV.

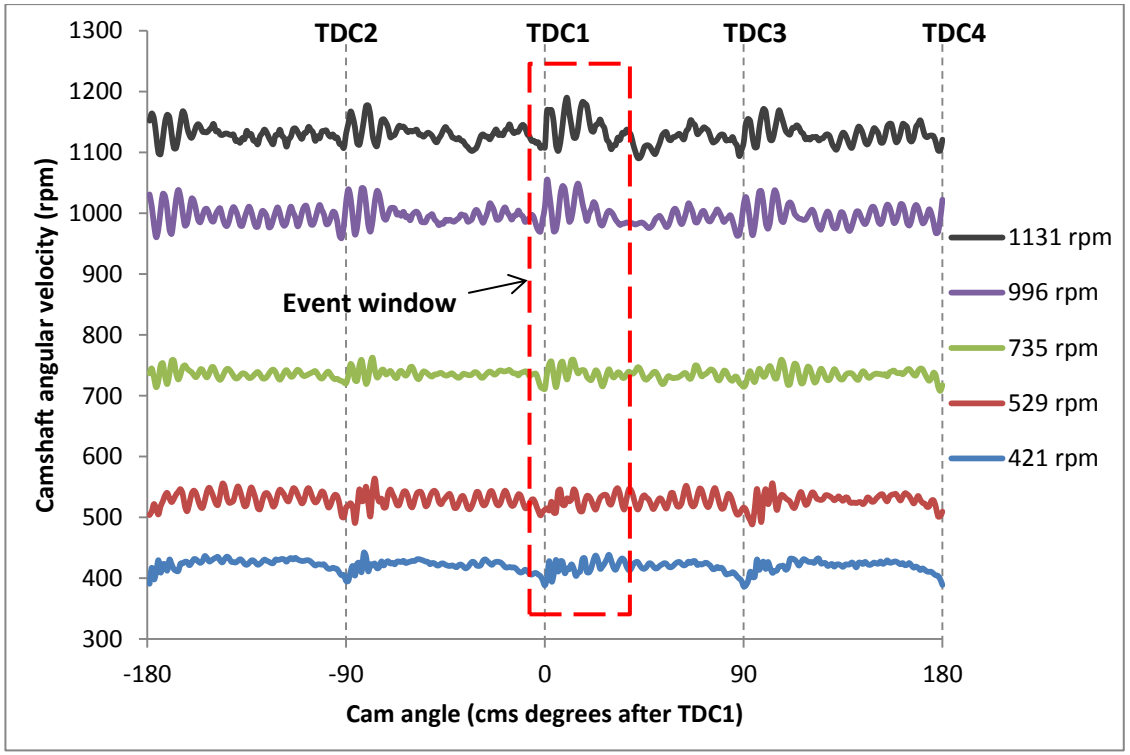

Figure 6.44: Averaged instantaneous camshaft angular velocity of one complete engine cycle for all five different speeds.

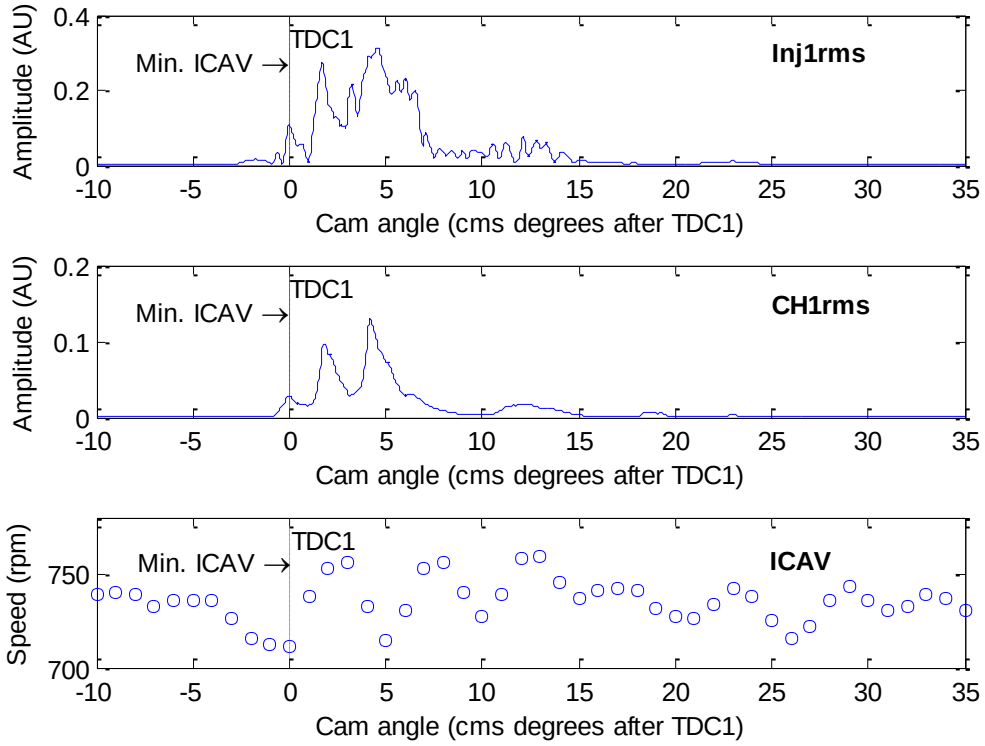

Figure 6.45: Averaged values of AE RMS signal from sensors mounted near cylinder 1 and ICAV waveform at a camshaft speed of 735rpm.

To investigate further the relationship between the AE signals and the ICAV waveform, a narrower window (between 2ºBTDC and 2ºATDC) was chosen and a cross-correlation algorithm applied between the AE records and the ICAV using [168]:

$$C_k = \begin{cases} \sum_{i=1}^{n-k} x_{i+k} y_i^* , & k \geq 0 \\ C_{-k}^*, & k \leq -1 \end{cases} \qquad \textbf{6-1}$$

where x and y are the vectors of n numbers, C_k is the cross-correlation function and k represents the period [-n : n]. Because the AE and ICAV time series have different resolutions, it was necessary to further average the AE to match the ICAV resolution before applying the cross-correlation. The resulting functions shown in Figure 6.46 show that there is a definite peak at TDC for both cylinder 1 sensors but the resolution of the ICAV is not sufficiently good to be able to identify the individual peaks in the AE, although it can be seen that the approach to the peak becomes steeper as the engine speed increases.

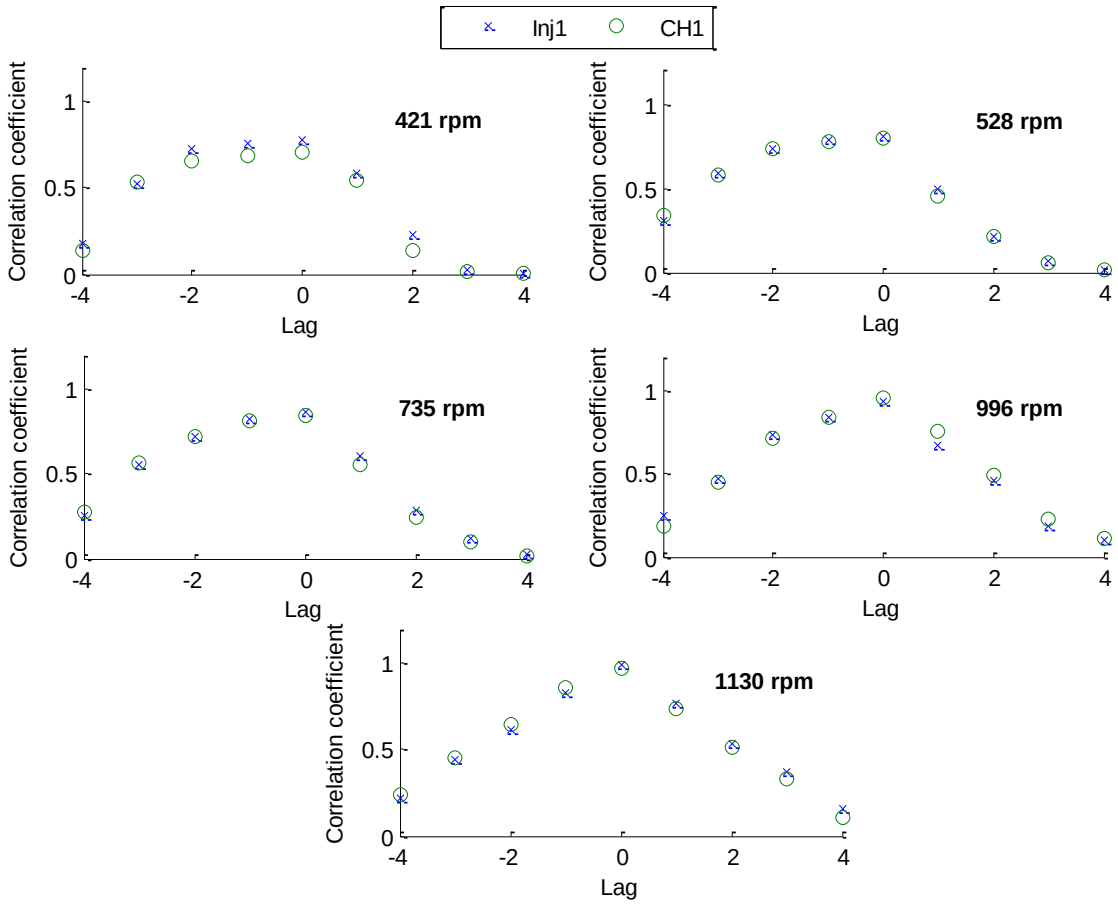

Figure 6.46: Averaged cross-correlation between AE signals at cylinder1 and the corresponding ICAV waveform over the cam angle range (-2^{o}) to 2^{o}.

A more successful approach is shown in Figure 6.47, which shows the cam angle positions of the minimum ICAV values along with the cam angle positions of the starting points of the cylinder 1 AE signals (obtained using the adaptive threshold method). Here it can be seen that the AE start is associated with the minimum ICAV, and that both are advanced relative to TDC as the engine speed increases. The lower slope and reduced correlation coefficient for the ICAV minimum are probably due to its lower angular resolution relative to the AE, represented by the larger error bars.

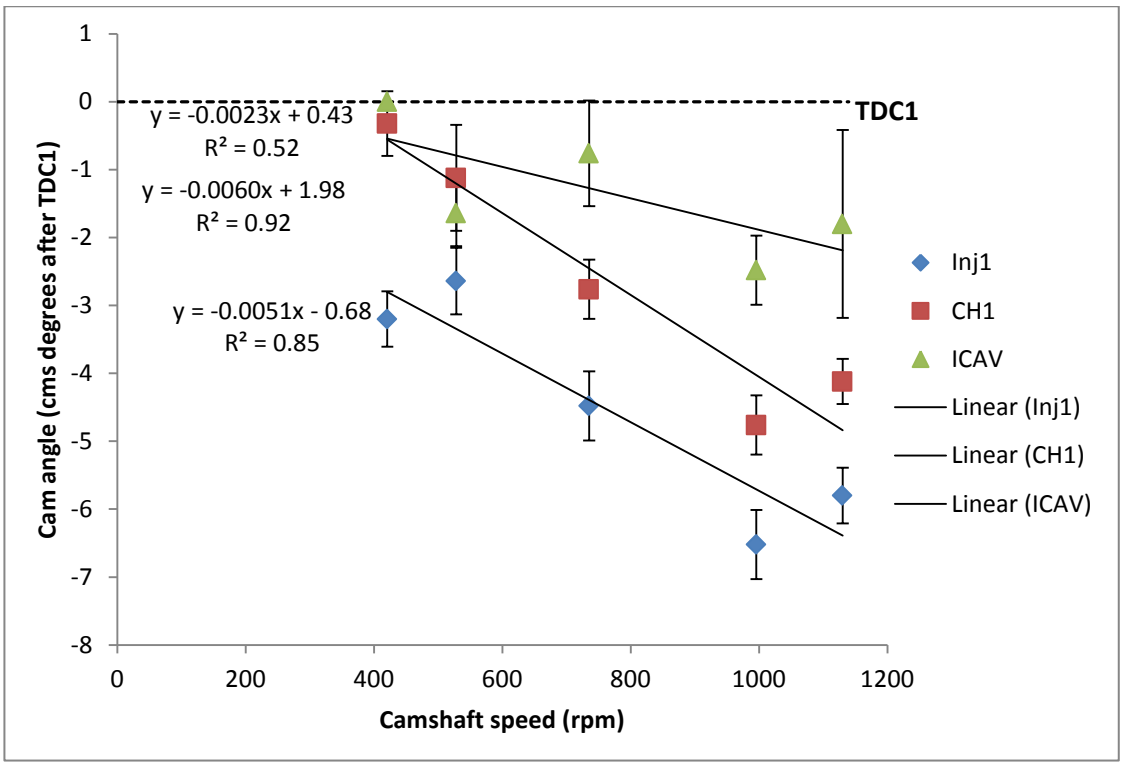

Figure 6.47: Averaged cam angle positions of the starting points of AE signals and the minimum value of ICAV around TDC1. Error bars indicate range of values over the 6 cycles analysed.

6.3.3 Diesel engine events and signal peaks interpretation

Having established that at least two features of the AE signal correlate with two different features of the ICAV, it remains to be seen if further diagnostic information can be obtained by comparing the AE sensor responses with each other. One simple way in which this can be done is illustrated by the example in Figure 6.48 where the sensor record on the cylinder head has been re-scaled to give the same total energy in the TDC1 window as does the sensor record for the injector-mounted sensor. In this way, the effects of attenuation and sensor sensitivity are eliminated and the energy distribution across the window can be compared simply by subtracting one record from the other. Figure 6.49 shows the effect of this subtraction averaged across all of the data for each speed, and it can clearly be seen that the injector sensor generally records less energy at the start of the injection-combustion event and more towards the end. This is somewhat contrary to what might be expected, but is consistent with the time lag seen between cylinder head sources and injector sensors in the calibrations, suggesting that the source for most of the early AE is within the cylinder rather than in the body of the injector.

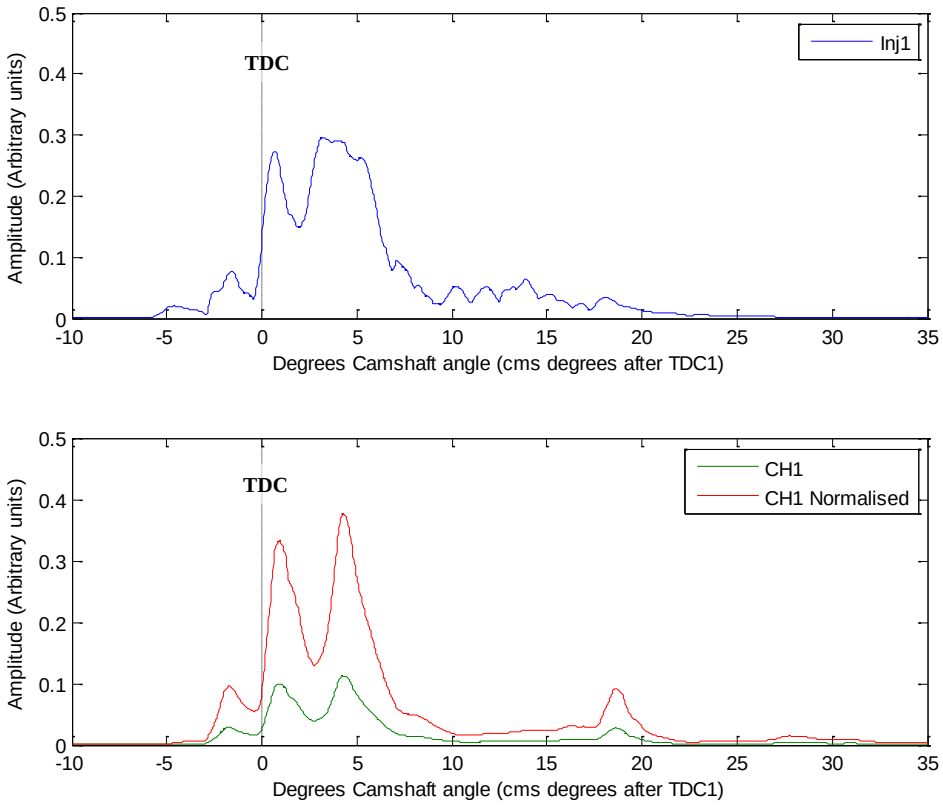

Figure 6.48: Examples of AE RMS signals from CH1 and Inj1, showing re-scaling of CH1 signal. (Camshaft speed is 996 rpm)

As can be seen from Figure 6.48 the signal from the injector-mounted sensor has a more detailed structure than the one mounted on the cylinder head, although the latter has clearer peaks, so it was used to segment the injection-combustion window. This was done using an algorithm which located the local peaks of the RMS signal by applying a sliding window with a width of 0.50 cam angle (1 crank angle). Figure 6.50 shows ten local peaks (M1 - M10) and the concomitant segmentation into five event windows (A, B, C, D and E) which are assumed to be linked to the injection/combustion stages under different operating conditions.

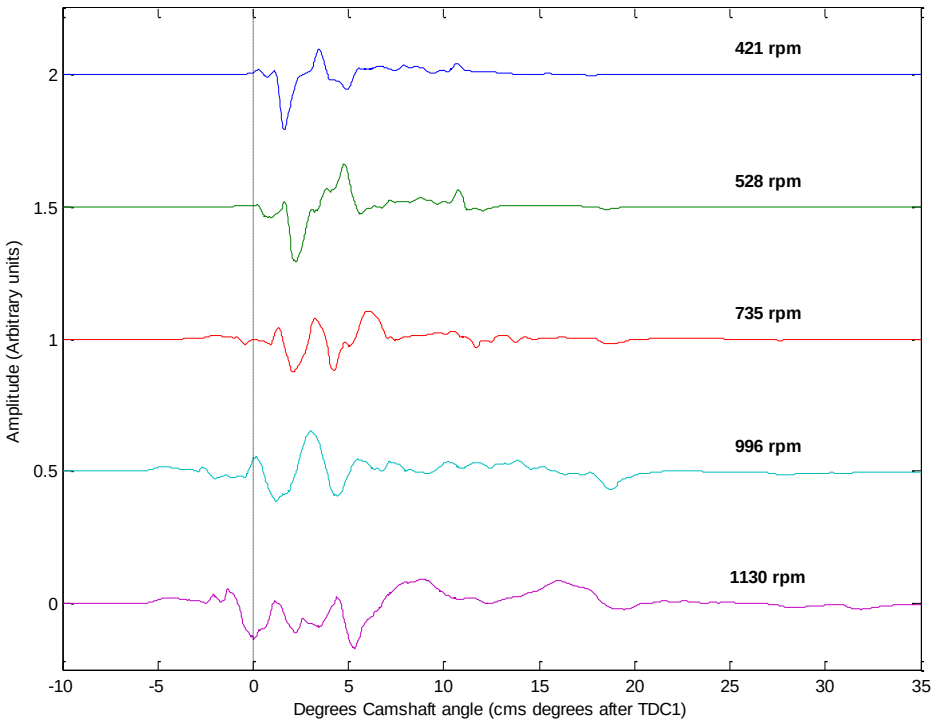

Figure 6.49: Averaged values of difference between Inj1 and re-scaled CH1 records for each camshaft speed.

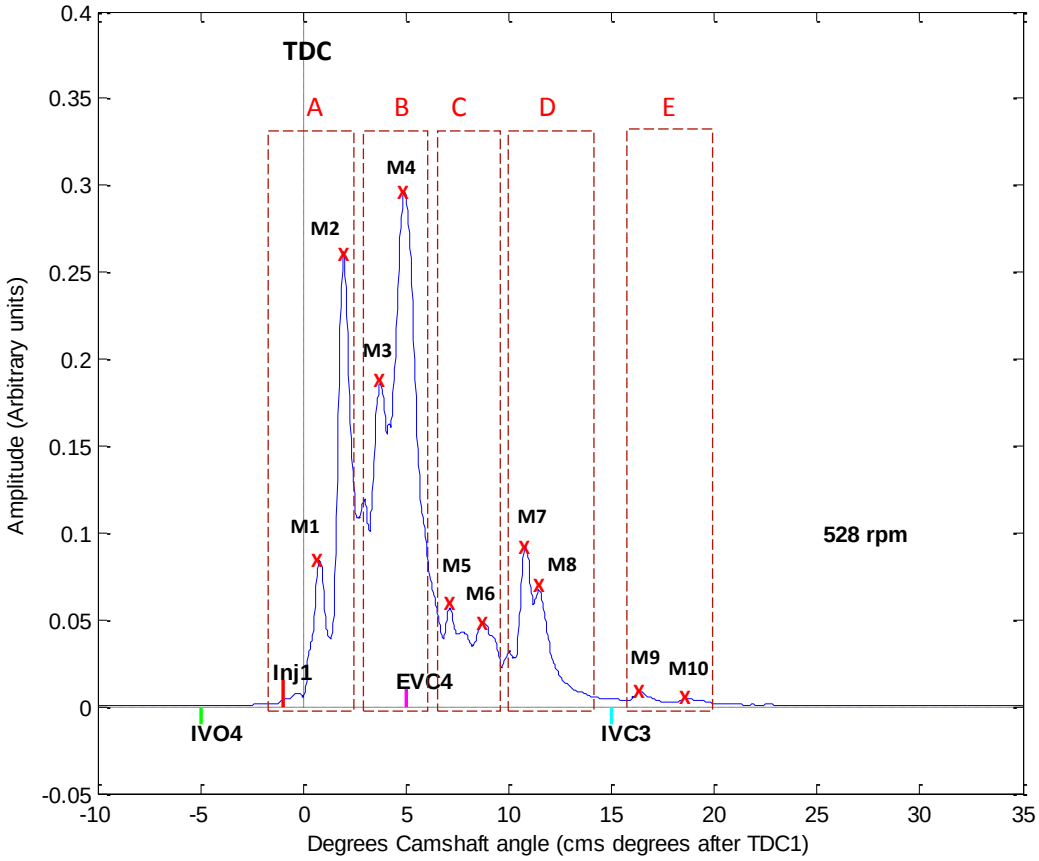

Figure 6.50: Example of AE RMS signal from sensor mounted near cylinder 1 showing segmentation of window and local peaks.

Figures 6.51 and 6.52 show how the AE peaks are distributed (as cumulative height over the 0.50 cam angle increment) for the 125 complete engine cycles over the five different speeds for each of the sensors. The bar charts are overlain rather than added in order to highlight areas of the crankshaft window in which peaks are concentrated and, as can be seen, the distribution is much broader for the injector mounted sensor than for that mounted on the cylinder head. With both sensors, there are clear changes in the peak pattern with speed, but the pattern is much more marked with the cylinder head mounted sensor, which moves from a concentration in three zones at low speed, to between four and six zones at higher speed.

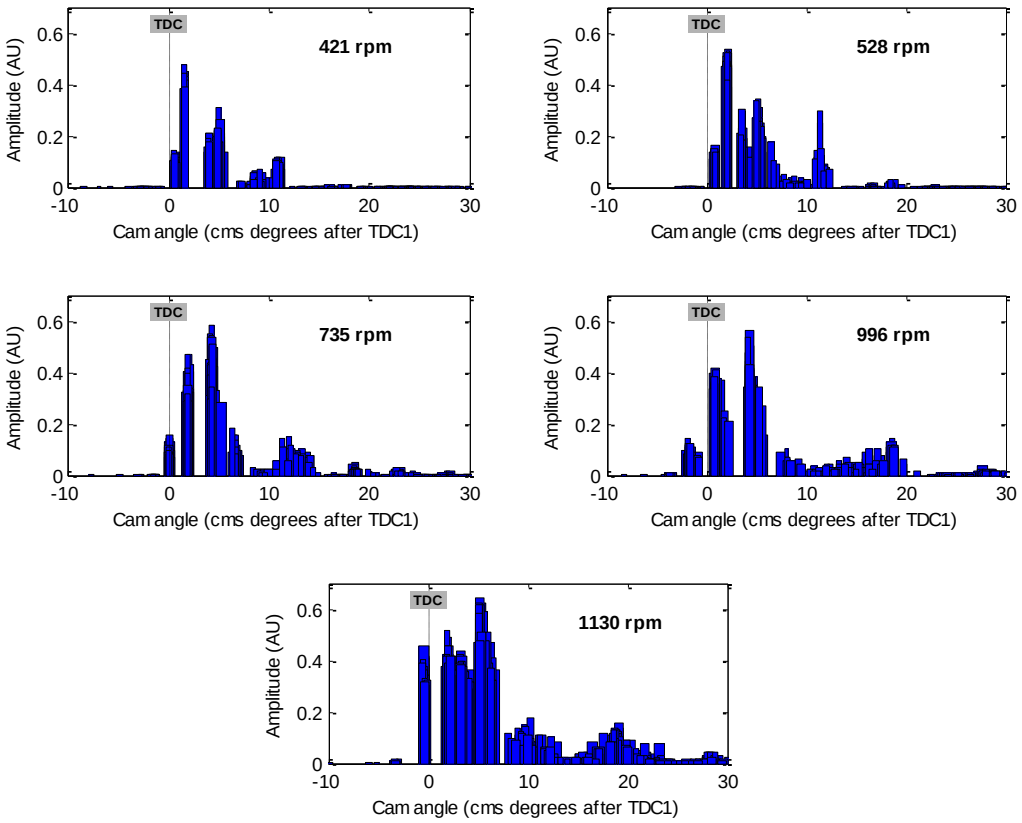

Figure 6.51: Re-scaled AE peak distribution at CH1 for each of the running speeds.

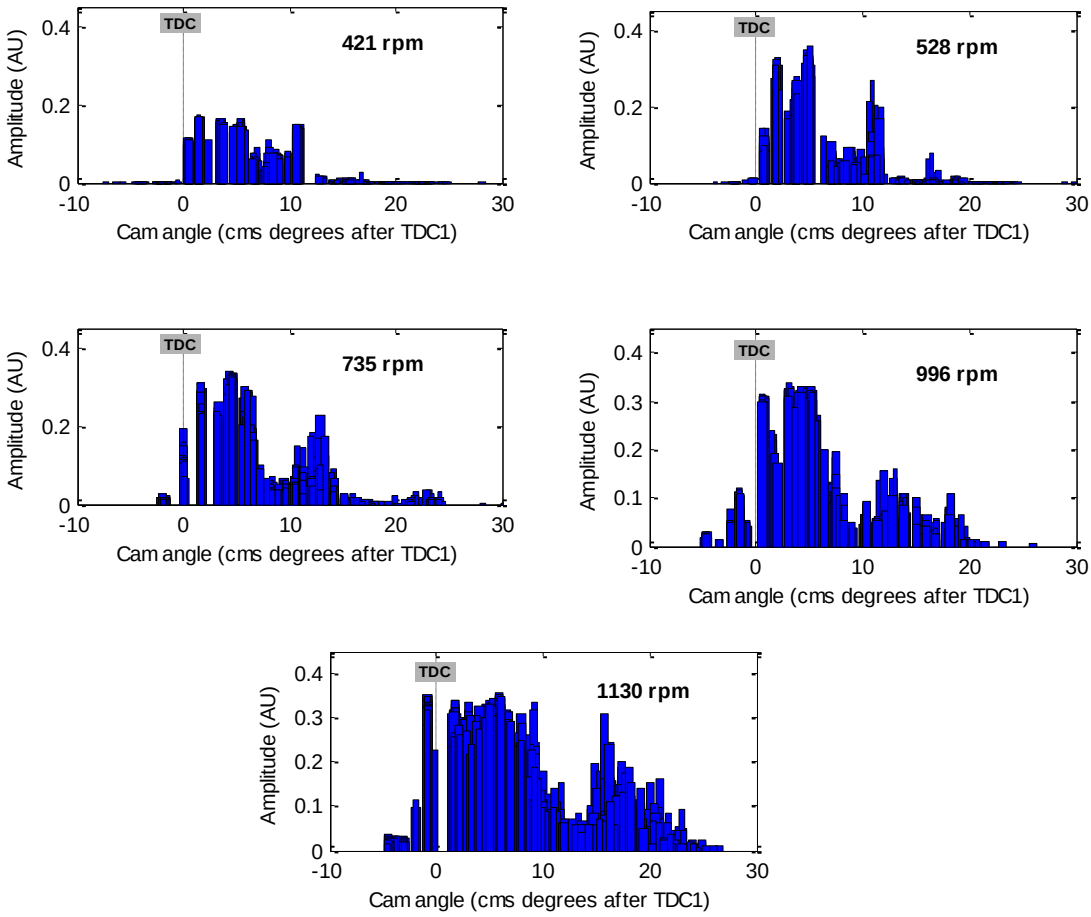

Figure 6.52: AE peak distribution at Inj1 for each of the running speeds.

The narrower distribution of peaks at CH1, allowed a more systematic investigation of the temporal structure across the TDC1 window and its changes with engine running speed. To do this, the cam angle position of each local peak (M1 to M10 in Figure 6.50) was automatically detected and stored in a matrix, each pair of peaks (M1/M2, M3/M4 etc.) being assigned to an event window (A to E in Figure 6.50). The event windows were decided by inspection of representatives of all records as being likely to indicate different processes in the engine. The position of each event (the mean angle of its two peaks), the average energy (angular integral over the event window) and the angular difference between the event peaks were then calculated for each example of each window at each speed and the results are shown in Figures 6.53-6.55.

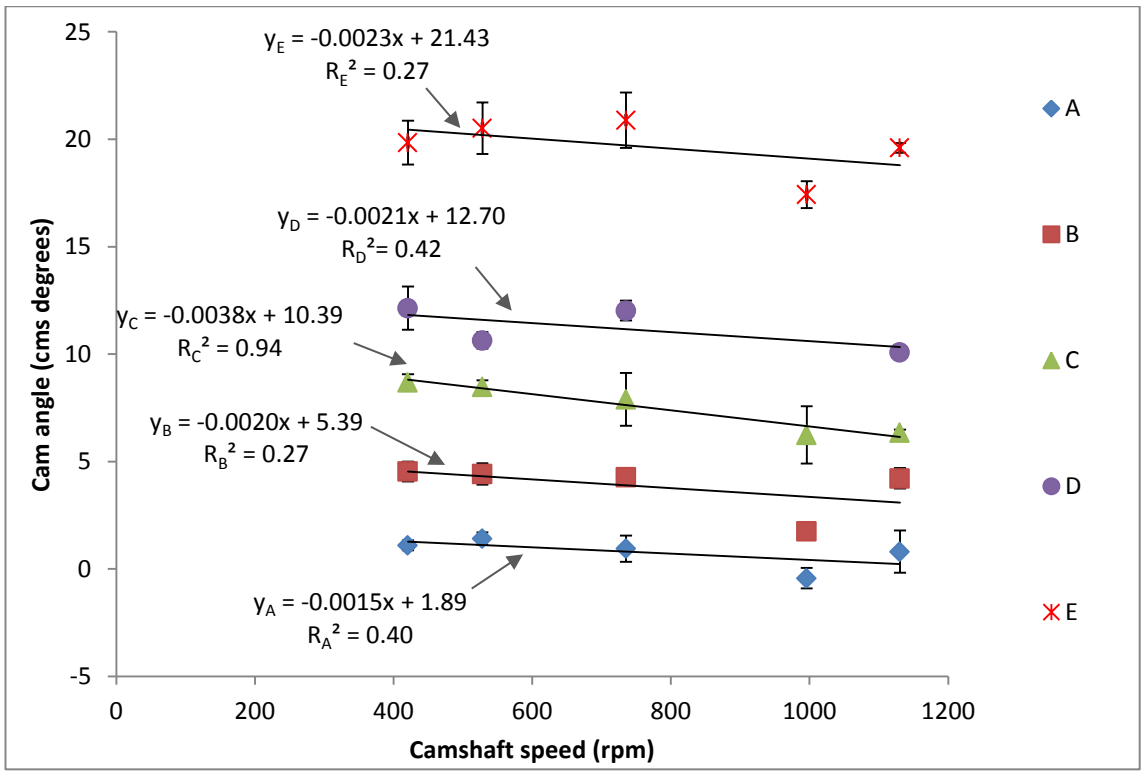

Figure 6.53: Averaged cam angle positions of the five event windows from AE RMS records at CH1.

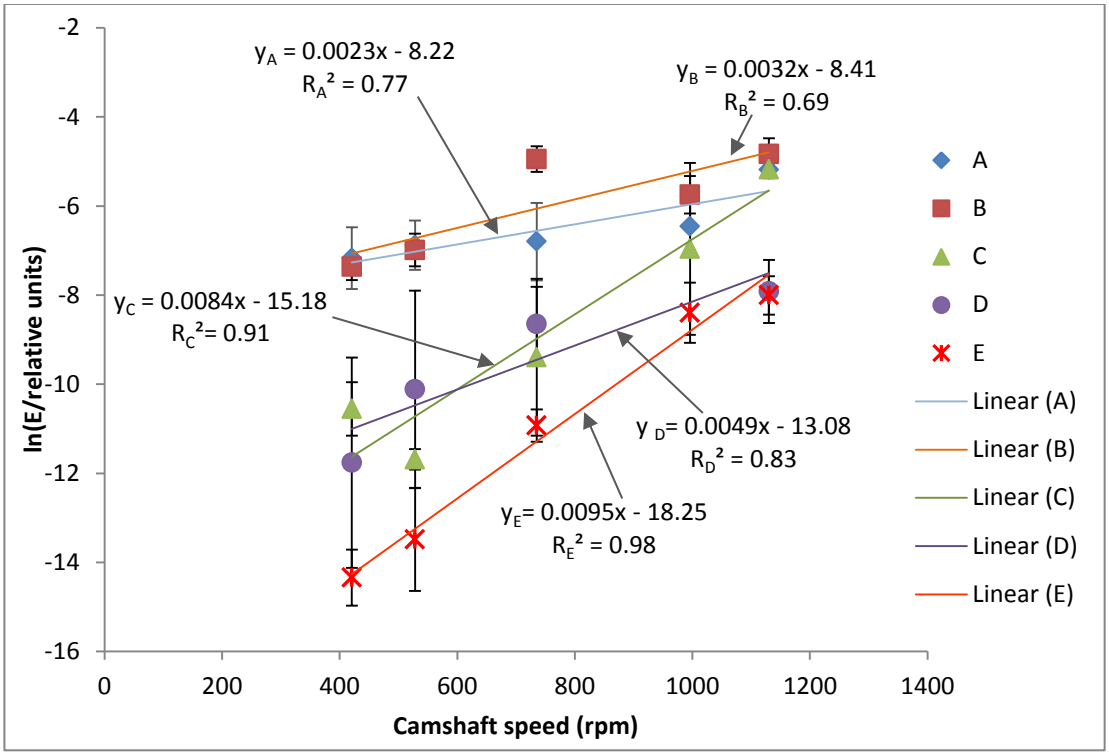

Figure 6.54: Averaged angular AE energy of the five event windows from AE RMS records at CH1.

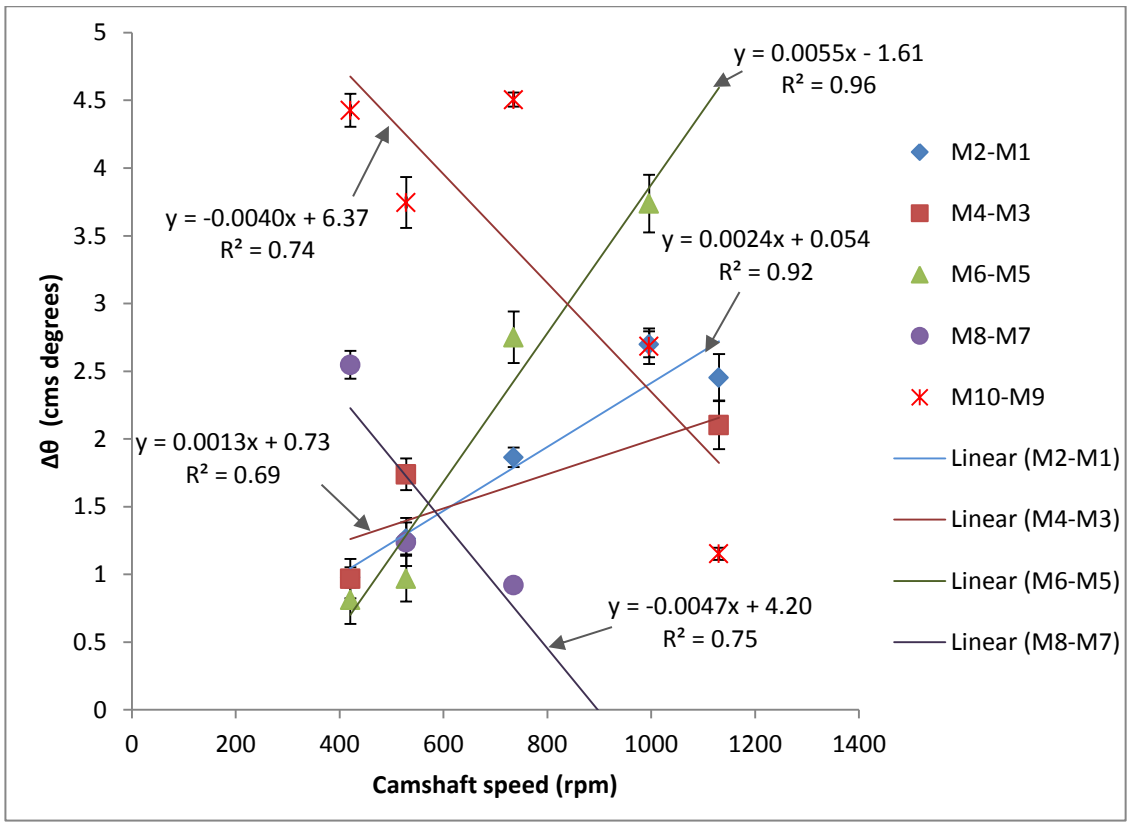

Figure 6.55: Averaged cam angle peak angular separation for the five event windows from AE RMS records at CH1.

The rather complicated behaviour exhibited in Figures 6.53 to 6.55 is summed up in Table 6.1, which shows how each of the event window indicators changes with engine speed.

	Rate of change with camshaft speed (10^4 r.p.m.$^{-1}$)		
Event window	**Angular position**	**Angular energy**	**Relative peak position**
A	-15	23	24
B	-20	32	13
C	-38	84	55
D	-21	49	-47
E	-23	95	-40

Table 6.1: Trends with camshaft speed of each of the event indicators derived from the AE RMS records at CH1.

Consideration of Table 6.1 shows the events that are least sensitive to engine speed to be A and B. Given that these are the two first events, it is likely that they are associated with the injection process, their position advancing relatively slowly with engine speed and their energy increasing when measured over a constant engine angle. This would suggest that the energy of events A and B would be indicative of the amount of fuel

injected, hence being more to do with spray formation than the mechanical movement of the injector parts. The longer and wider duration of the corresponding angular window recorded on the injector (Figures 6.51 and 6.52) would tend to support the suggestion that the Inj1 sensor is recording more than the spray formation, probably also the injector mechanical movements. The event window that is most sensitive to engine speed is C and its position within the overall TDC1 window, its rapid increase in energy and its relatively rapid angular advance would all suggest that this event window is associated with combustion. Event windows D and E show a similar rate of advance to A and B, suggesting that they are also associated with the injectors. However, in contrast to A and C, D and E show a rapid increase in energy with engine speed and, exceptionally, the two peaks move closer to each other as engine speed increases, suggesting that they are separated by a fixed time. One explanation of these events, which occur rather late in TDC1 window, that they are associated with pressure waves between the pump and the injector, which are known to travel at a speed of sound [9]. The pressure waves may be wholly or partially reflected back at the nozzle as a compression wave if the nozzle is closed which would lead to a fixed time difference, and the intensity of the waves might be expected to increase with the rate of closure of the injector valve.

6.3.4 Identification of diesel engine events using canonical correlation; engine C (sensor array2)

Figures 6.56 to 6.58 show the distribution of the maximum regression values for the three sensor pairs in a 45^o camshaft window for Cylinder 1, using shift angles in the range of (-10^o) to 10^o camshaft. The correlation results for each of the pairs in the Cylinder 1 and Cylinder 3 windows are summarised in Figures 6.59 and 6.6. As for sensor array 1 there is a substantial difference in correlation between the sensor pairs across the entire window, indicating that a more detailed analysis is needed, particularly in Cylinder 1. Figure 6.61 shows an example of raw AE signal recorded around TDC on Cylinder 1 by the two cylinder head mounted sensors. Figure 6.62 shows the correlation distribution over this window indicating four distinct peaks, with different heights, suggesting multiple events. Accordingly, the injection/combustion window was divided into three sub-windows (this was done by inspection Figure 6.63, although the process could easily be automated) and CCA has been applied to each sub-window separately. Figure 6.64 shows the results of this second CCA, showing three distinct angle shifts.

Repeating the process with the other sensor pairs and the other windows can easily be seen to be able to provide a set of arrival time differences which could be related to the time differences recorded in the attenuation experiments.

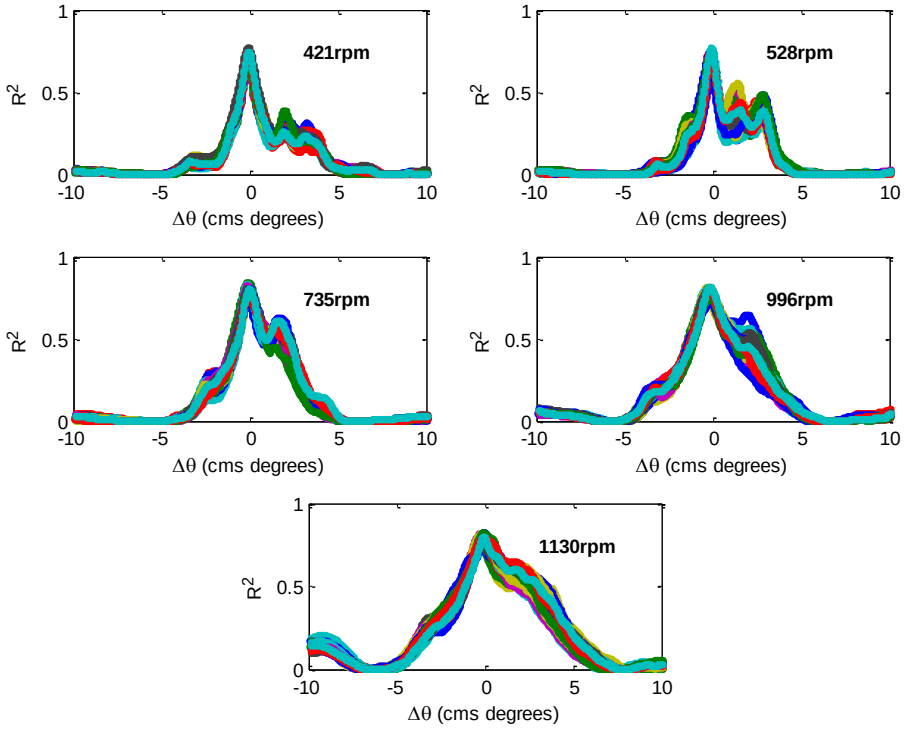

Figure 6.56: Regression coefficients of AES2 vs. AES1 from the canonical correlation of the injection/combustion window for Cylinder 1 (45° camshaft).

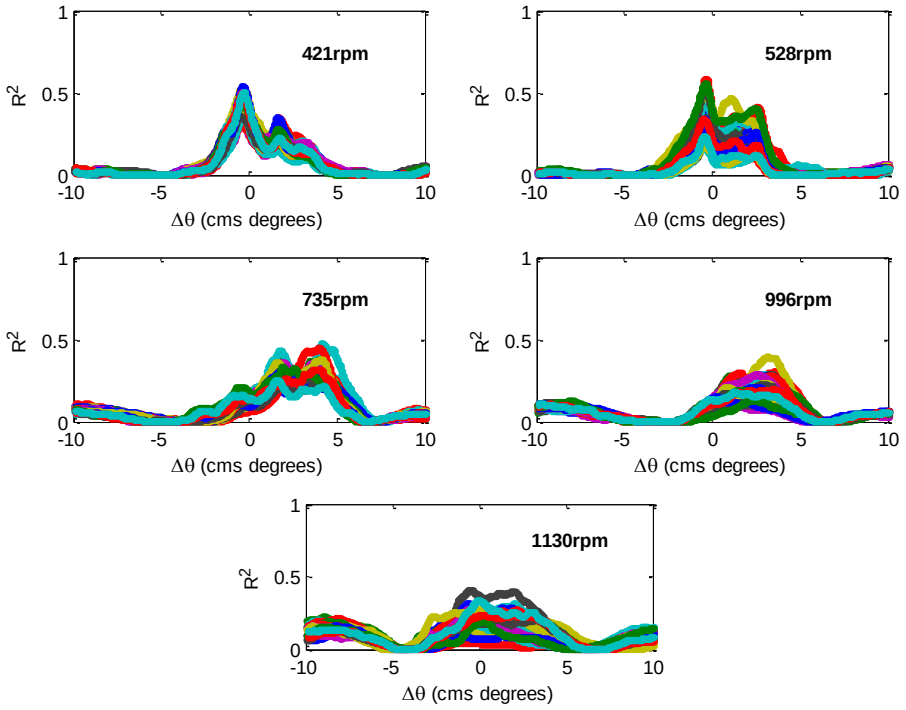

Figure 6.57: Regression coefficients of AES3 vs. AES1 from the canonical correlation of the injection/combustion window for Cylinder 1 (45° camshaft).

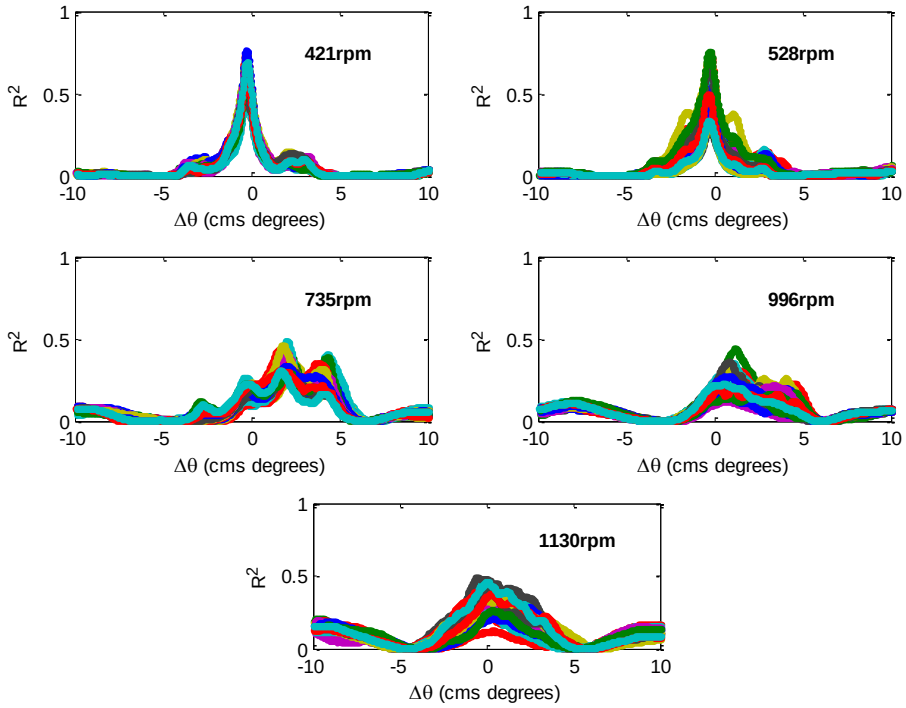

Figure 6.58: Regression coefficients of AES3 vs. AES2 from the canonical correlation of the injection/combustion window for Cylinder 1 (45° camshaft).

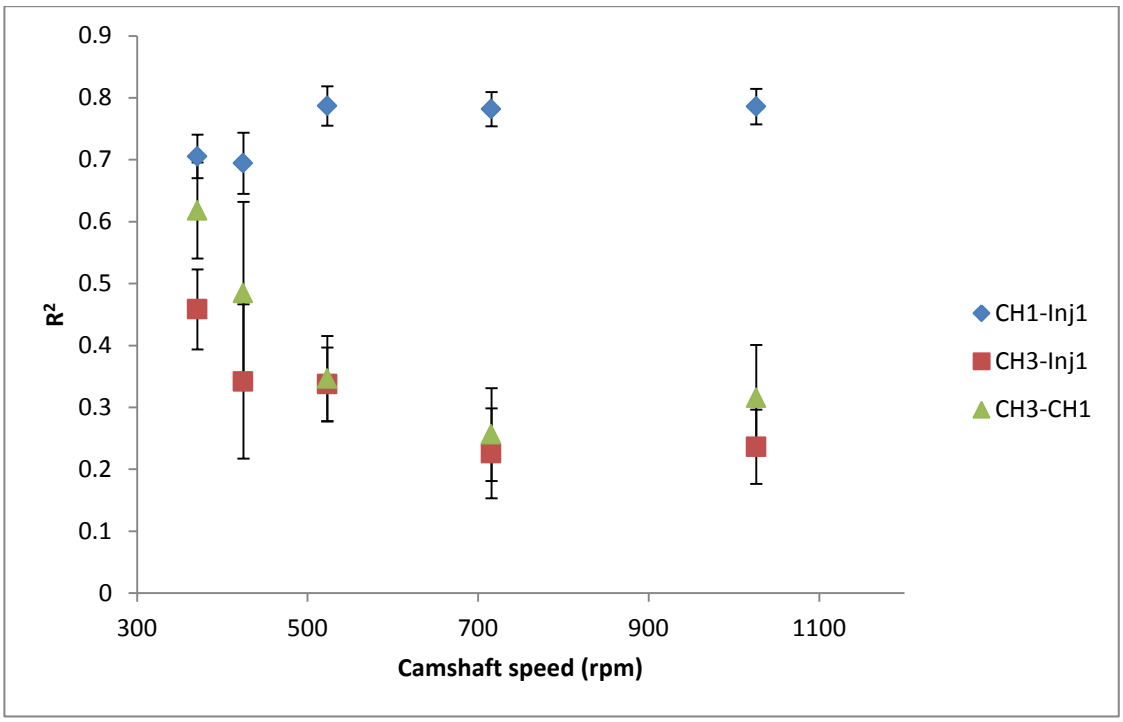

Figure 6.59: Regression coefficients from the canonical correlation of the injection/combustion window for Cylinder 1 (10°cms BTDC1 - 35°cms ATDC1).

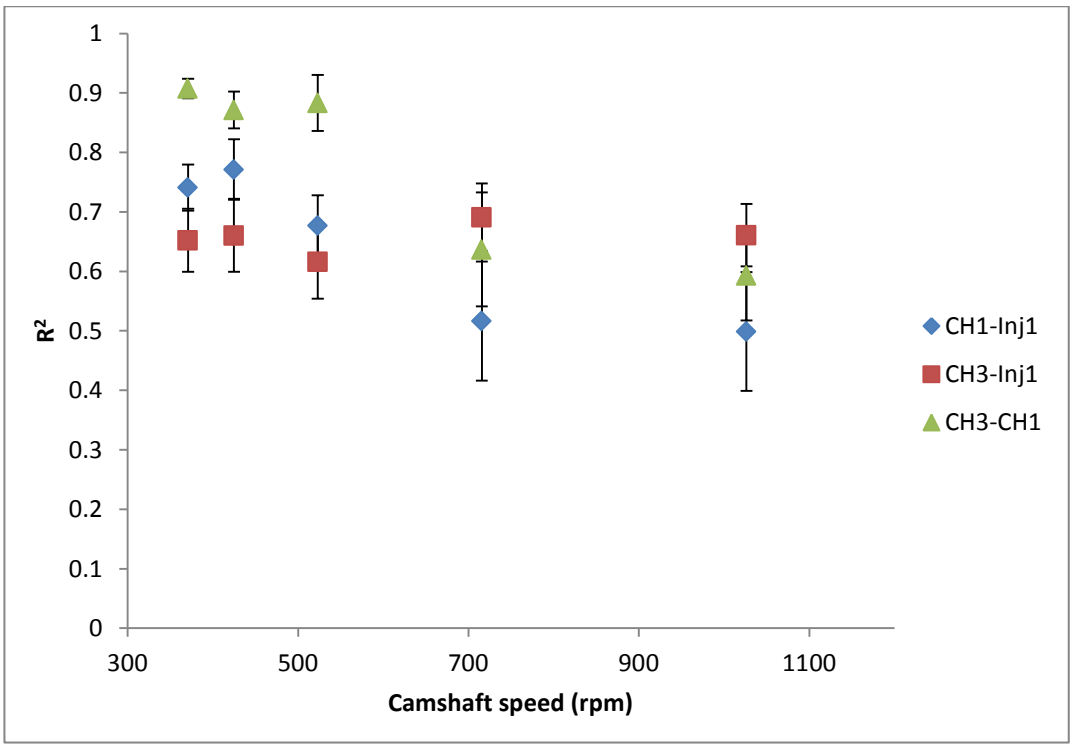

Figure 6.60: Regression coefficients from the canonical correlation of the injection/combustion window for Cylinder 3 (10°cms BTDC1 - 35°cms ATDC1).

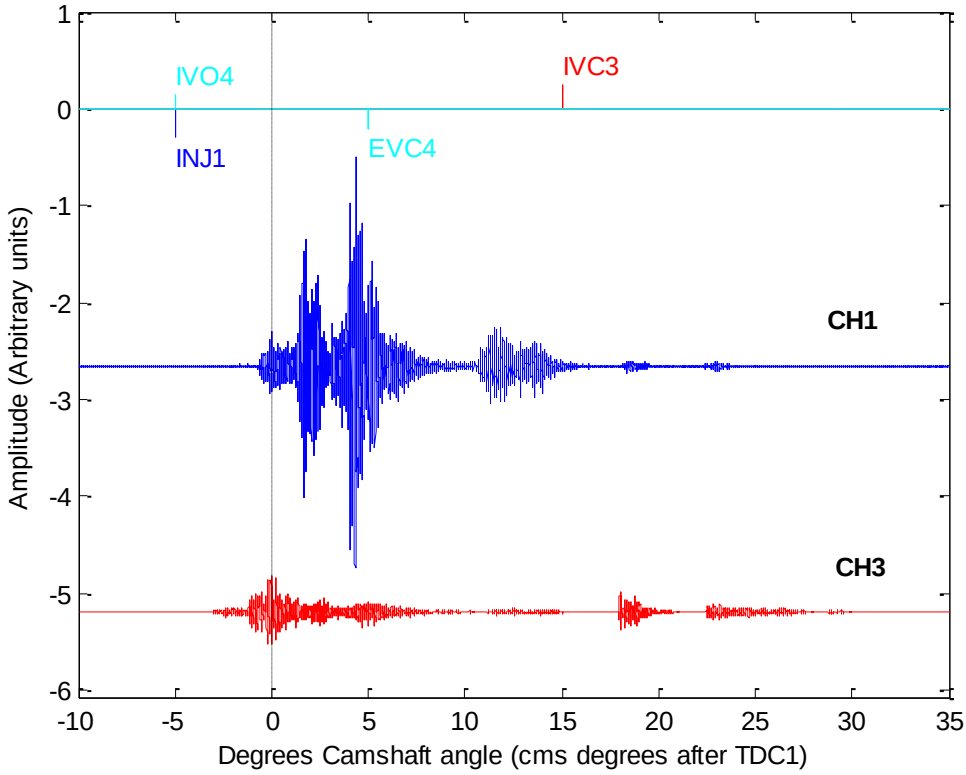

Figure 6.61: Typical raw AE signal from Engine C sensor array2.

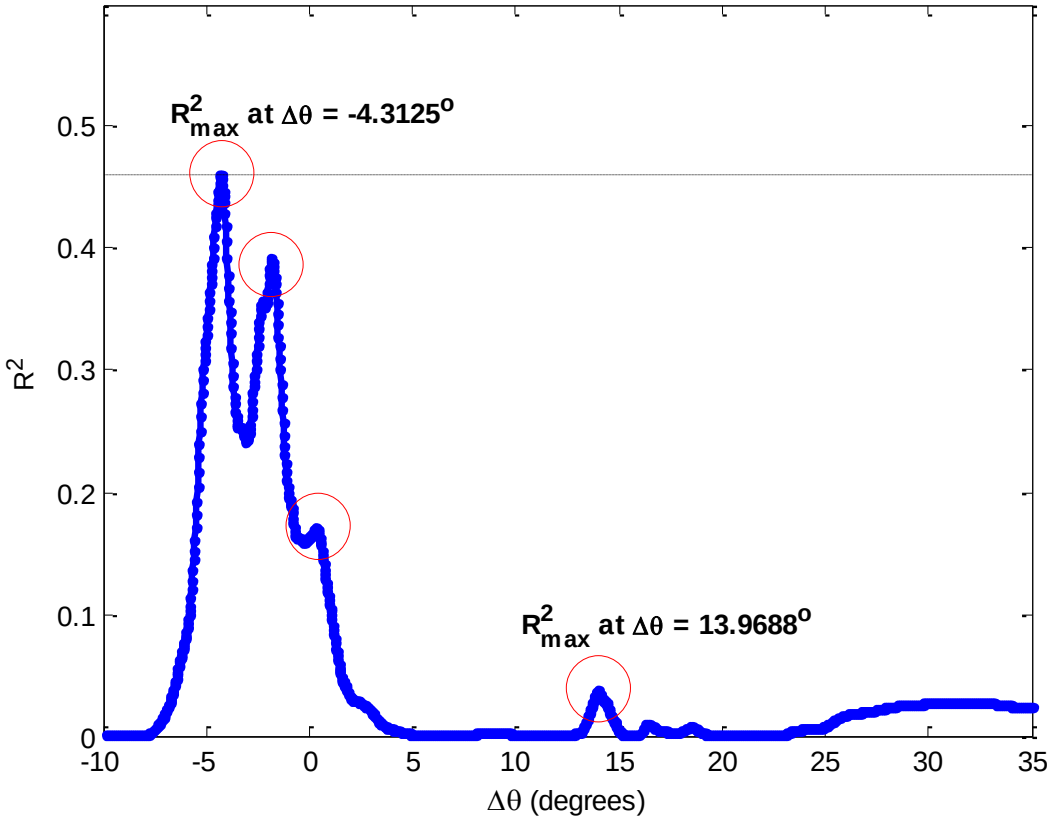

Figure 6.62: Example of the distribution of the regression coefficients over the Cylinder 1 window (15°cms BTDC1 - 45°cms ATDC1) from Engine C, sensor array2.

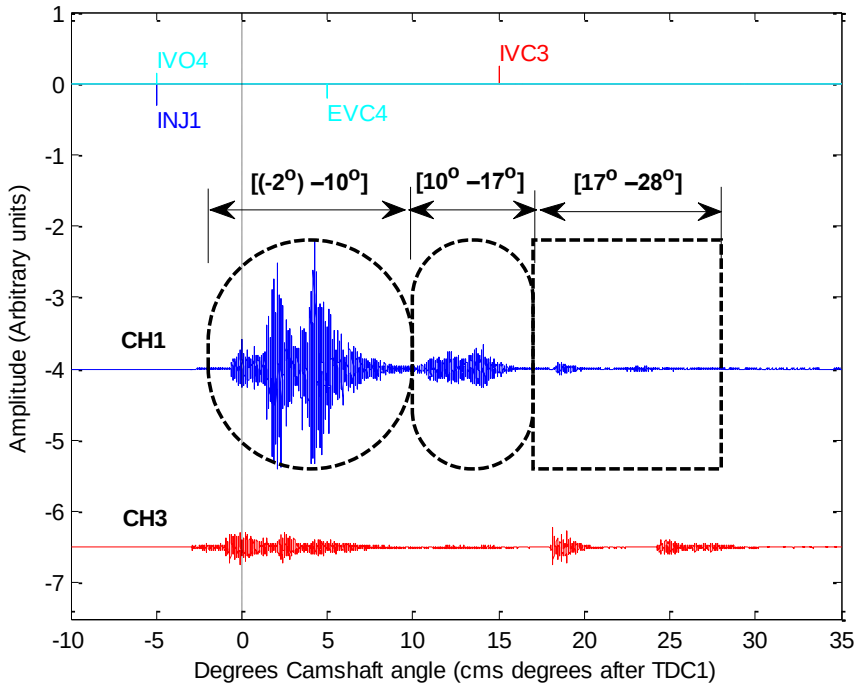

Figure 6.63: Segmentation of AE signal from Engine C, sensor array2 at camshaft speed of 736 rpm.

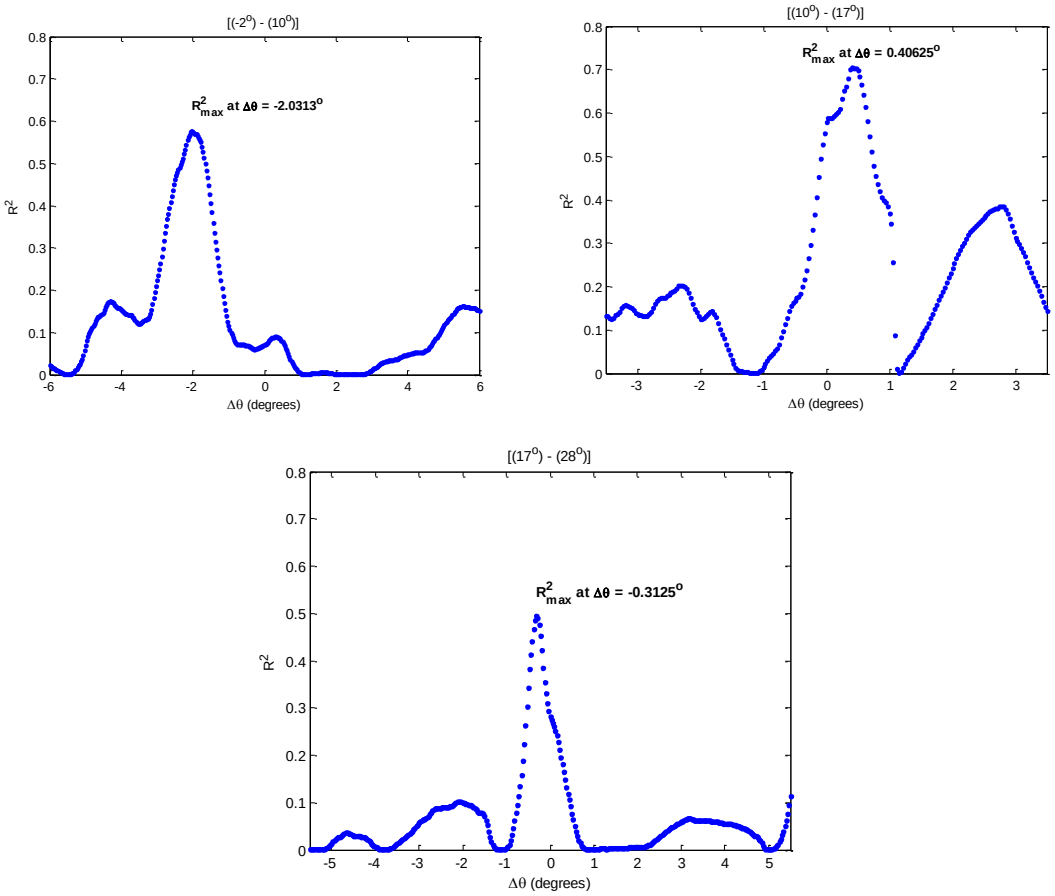

Figure 6.64: Example of the distribution of the regression coefficients for Cylinder 1 window (15°cms BTDC1 - 45°cms ATDC1) from Engine C, sensor array2.

6.3.5 Summary of findings on Engine C (sensor array 2)

This final set of data has exhibited a range of signals from diverse sources recorded at sensors placed in an asymmetrical array. A two-stage process is used here, with CCA being used for the events around TDC of a cylinder to identify if there is sufficient doubt about the best correlation between some or all pairs of sensors to obtain a single angle shift. This signal can then be segmented as many times as are necessary to identify optimally the most likely angle shifts for each sub-event in the time series. It can easily be seen, that combining this with appropriate calibration measurements will allow a fully automated adaptive analysis of multi-source, multi-sensor data in machines.

Chapter 7

Conclusions and Recommendations

7.1 Conclusions

This detailed study of the temporal and spatial structure of the AE during the injection-combustion window of a diesel engine has thrown up a number of new insights into the potential for AE monitoring of machines where multiple sources are involved. These conclusions are summarised in the following:

- The signal transmission in such a complex geometry (i.e. cylinder head) occurs in multiple paths which means that an energy analysis technique is not generally sufficient for signal separation and has to be complemented with other methods to exploit the high temporal resolution offered by AE.

- The transmission paths from the potential sources to a surface mounted sensor array give enough time delay to be separated in a raw, or lightly averaged record, even in small diesel engine.

- The AE energy has a some sensitivity to the surface temperature which may affect the source identification of adjacent (in time and space) engine events (e.g. injection and combustion) especially in small high speed diesel engines.

- The AE record is critically sensitive to the sensor position changing not only in amplitude, but also in temporal structure with quite small changes even within the surface of the cylinder head.

- There is an identifiable AE signature around the time of the injection events in the experimental injection rig which can also be seen in a running diesel engine.

- Taking simple features of the pulses, such as their energy, shows similar trends with crankshaft speed on both the injector rig and on the running engine.

- Detailed analysis of one sensor position has allowed deductions to be made about which parts of the AE time series are associated with injection, combustion and with pressure waves set up in the injector rails.

- The canonical correlation has the capacity to add to more conventional time-based analysis, allowing time (or angle) differences between different parts of a signal recorded at two sensors to be identified automatically for on-line monitoring.

- The ability to have a dynamic measure of phase as well as energy adds considerably to the potential for automated source location in machinery and moves closer to automated spatial location of time-series in mechanically-regulated AE records.

7.2 Future work

This new method (SICCA) of processing multi-source, multi-sensor AE data shows the potential to be implemented more widely in condition monitoring of machines. The next step towards a complete diagnostic kit is to improve SICCA to work in a fully automated way by integrating an ICA algorithm into an advanced version of SICCA (which includes the adaptive threshold and automated peak finder). Also, work is needed on investigating the relationship between the fuel line pressure profile and the structure of the AE in the injector rig. This should help to form a time series model of the injector AE signal which will allow it to be used as a means of metering the fuel entering the engine in each injection cycle. Further work should be focused on the pulsatile structure of the time series in order to account for the pressure wave that are evident in the injector rig, and to better separate injection from combustion (and from other AE-generating events) in the engine. Further development of this technique should consider studying the effect of using alternative fuels in terms of identifying the corresponding features and the significant differences. Finally, SICCA has shown a significant potential to be incorporated to the control system in the automotive engineering which is the most appropriate venue for further development.

References

1. Rao, B., *Handbook of condition monitoring*. 1996: Elsevier.
2. Jardine, A.K.S., D. Lin, and D. Banjevic, *A review on machinery diagnostics and prognostics implementing condition-based maintenance.* Mechanical Systems and Signal Processing, 2006. **20**(7): p. 1483-1510.
3. Mechefske, C.K., *Machine condition monitoring and fault diagnostics.* Vibration And Shock Handbook, 2005.
4. Davies, A., *Handbook of condition monitoring: techniques and methodology*. 1998: Springer.
5. Long, B.R. and K.D. Boutin, *Enhancing the process of diesel engine condition monitoring.* ASME, NEW YORK, NY,(USA). 1996. **27**: p. 61-68.
6. Kim, E.Y., A.C. Tan, and B.-S. Yang, *Acoustic emission for diesel engine monitoring: a review and preliminary analysis*, in *Engineering Asset Management and Infrastructure Sustainability*. 2012, Springer. p. 489-499.
7. GmbH, R.B., *Diesel-Engine Management*. 2004: John Wiley and Sons.
8. Lilly, L., *Diesel Engine Reference Book*. 1984: Butterworth Publishers, Stoneham, MA.
9. Stone, R., *Introduction to internal combustion engines*. 1999: Macmillan Houndmills, Basingstoke, Hampshire.
10. Heisler, *Advanced engine technology* 1995: Edward Arnold.
11. Gu, F., A. Ball, and W. Li, *The condition monitoring of diesel engines using acoustic measurements part 1: acoustic characteristics of the engine and representation of the acoustic signals.* 2000.
12. Gu, F., A. Ball, and W. Li, *The condition monitoring of diesel engines using acoustic measurements-part 2: fault detection and diagnosis.* SAE Technical Papers, 2000.
13. Reuben, R.L., *The Role of Acoustic Emission in Industrial Condition Monitoring.* International Journal of COMADEM, 1998. **1**(4): p. 35-46.
14. Abdou, W., et al., *Monitoring of Diesel Fuel Injection using Acoustic Emission (AE)*, in *Proceedings of the 5th International Conference on Condition Monitoring and Machinery Failure Prevention Technologies*. 2008: Edinburgh, UK. p. 1-11.
15. Pontoppidan, N.H. and R. Douglas, *Event alignment, warping between running speeds*, in *COMADEM 2004 International*. 2004: Cambridge, UK. p. 621–628.

16. Wu, W., A. Tan, and E. Kim, *Enhancing acoustic emission signals from multi-cylinder diesel engine.* 2010.
17. Abdou, W., N. Balodimos, and B. Reuben, *Acoustic emission in diesel engines–towards a time series model for the injection process*, in *Proceedings of 30th European Conference on Acoustic Emission testing and 7th International Conference on Acoustic Emission*. 2012: Granada, Spain. p. 394-406.
18. Albarbar, A., F. Gu, and A.D. Ball, *Diesel engine fuel injection monitoring using acoustic measurements and independent component analysis.* Measurement, 2010. **43**(10): p. 1376-1386.
19. Albarbar, A., et al., *Acoustic monitoring of engine fuel injection based on adaptive filtering techniques.* Applied Acoustics, 2010. **71**(12): p. 1132-1141.
20. Gill, J.D., R.L. Reuben, and J. Steel, *A study of small HSDI diesel engine fuel injection equipment faults using acoustic emission.* Journal of Acoustic Emission(USA), 2001. **18**: p. 211-216.
21. Douglas, R.M., et al., *Acoustic emission as a tool to reveal diesel injector performance*, in *Proceedings of the Condition Monitoring and Diagnostic Engineering Management, COMADEM*. 2004: Cambridge, UK.
22. Gill, J.D., et al., *Detection of Diesel Engine Faults using Acoustic Emission.* Proceedings of the Planned Maintenance, Reliability and Quality, 2nd International Conference, 1998.
23. Fog, T.L., et al. *On condition monitoring of exhaust valves in marine diesel engines*. in *Neural Networks for Signal Processing IX, 1999. Proceedings of the 1999 IEEE Signal Processing Society Workshop.* 1999. IEEE.
24. El-Ghamry, M.H., R.L. Reuben, and J. Steel, *The development of automated pattern recognition and statistical feature isolation techniques for the diagnosis of reciprocating machinery faults using acoustic emission.* Mechanical Systems and Signal Processing, 2003. **17**(4): p. 805-824.
25. Shuster, M., et al., *Piston ring cylinder liner scuffing phenomenon studies using acoustic emission technique.* SAE transactions, 2000. **109**(4): p. 901-913.
26. Douglas, R.M., J.A. Steel, and R.L. Reuben, *A study of the tribological behaviour of piston ring/cylinder liner interaction in diesel engines using acoustic emission.* Tribology international, 2006. **39**(12): p. 1634-1642.
27. Nivesrangsan, P., *Multi-source, multi-sensor approaches to diesel engine monitoring using acoustic emission*. PhD thesis, Heriot-Watt University, Edinburgh, UK, December 2004.

28. Pollock, A.A., *Classical wave theory in practical AE testing.* Progress in Acoustic Emission III. Tokyo, Japan, 1986: p. 21-24.
29. Kolsky, H., *Stress waves in solids*. Vol. 1098. 1963: Courier Dover Publications.
30. Rakopoulos, C.D. and E.G. Giakoumis, *Diesel engine transient operation*. Vol. 5. 2009: Springer.
31. *Four stroke timing diagram*, in *www.splashmaritime.com.au*. n.d.
32. *Two stroke diesel engine*, in *www.automobiletamilan.com*. n.d.
33. *Two stroke timing diagram*, in *www.splashmaritime.com.au*. n.d.
34. Mollenhauer, K. and H. Tschöke, *Handbook of diesel engines.* Handbook of Diesel Engines, Edited by K. Mollenhauer and H. Tschöke. Berlin: Springer, 2010., 2010. **1**.
35. Payri, R., et al., *Influence of injector technology on injection and combustion development - Part 2: Combustion analysis.* Applied Energy, 2011. **88**(4): p. 1130-1139.
36. Payri, R., et al., *Influence of injector technology on injection and combustion development - Part 1: Hydraulic characterization.* Applied Energy, 2011. **88**(4): p. 1068-1074.
37. Chigier, N.A. and J.M. Beer, *Combustion Aerodynamics*. 1972: John Wiley and Sons, Inc., New York, NY.
38. Beer, J., *Combustion Aerodynumics.* Combustion Technology: Some Modern Developments, 2012: p. 61.
39. Foldyna, J., L. Sitek, and V. Habán, *Acoustic wave propagation in high-pressure system.* Ultrasonics, 2006. **44**(0): p. 1457-1460.
40. Heywood, J.B., *Internal combustion engine fundamentals*. 1988.
41. Assanis, D.N., et al., *A predictive ignition delay correlation under steady-state and transient operation of a direct injection diesel engine.* Journal of Engineering for Gas Turbines and Power, 2003. **125**(2): p. 450-457.
42. Pulkrabek, W.W., *Engineering fundamentals of the internal combustion engine*. 2004: Prentice Hall.
43. Murayama, T., et al., *Combustion behaviors under accelerating operation of an IDI diesel engine*. 1980, SAE Technical Paper.
44. Brennen, C.E., *Fundamentals of multiphase flow*. 2005: Cambridge University Press.
45. *Fluid separation in a nozzle hole*, in *www.sensorprod.com*. n.d.

46. Martin, C.S., et al., *Cavitation inception in spool valves.* Journal of fluids Engineering, 1981. **103**(4): p. 564-575.
47. He, X. and D.N. Ku, *Pulsatile flow in the human left coronary artery bifurcation: average conditions.* Journal of biomechanical engineering, 1996. **118**(1): p. 74-82.
48. Ku, D.N., et al., *Pulsatile flow and atherosclerosis in the human carotid bifurcation. Positive correlation between plaque location and low oscillating shear stress.* Arteriosclerosis, Thrombosis, and Vascular Biology, 1985. **5**(3): p. 293-302.
49. Ling, S. and H. Atabek, *A nonlinear analysis of pulsatile flow in arteries.* Journal of Fluid Mechanics, 1972. **55**(03): p. 493-511.
50. Perktold, K., M. Resch, and R.O. Peter, *Three-dimensional numerical analysis of pulsatile flow and wall shear stress in the carotid artery bifurcation.* Journal of biomechanics, 1991. **24**(6): p. 409-420.
51. Greitzer, E.M., C.S. Tan, and M.B. Graf, *Internal Flow*. Internal Flow, by EM Greitzer and CS Tan and MB Graf, pp. 736. ISBN 0521343933. Cambridge, UK: Cambridge University Press, June 2004., 2004. **1**.
52. Zamir, M. and M. Zamir, *The physics of pulsatile flow*. 2000: Springer.
53. Graebel, W., *Engineering fluid mechanics*. 2001: CRC Press.
54. Miller, R.K. and P. McIntire, *Acoustic emission testing Nondestructive testing handbook*. 1987: American Society for Nondestructive Testing.
55. Belchamber, R., *Acoustics—a process analytical tool.* Spectrosc. Eur, 2003. **15**(6): p. 26-27.
56. Vallen, H., *AE Testing Fundamentals, Equipment, Applications.* Journal of Nondestructive Testing(Germany), 2002. **7**(9): p. 1-30.
57. Holroyd, T.J., *The Acoustic Emission & Ultrasonic Monitoring Handbook*. 2000: Coxmoor Publishing Company.
58. Scruby, C.B., *An introduction to acoustic emission.* Journal of Physics E-Scientific Instruments, 1987. **20**: p. 945-953.
59. Atkinson, C.M. and H.K. Kytömaa, *Acoustic wave speed and attenuation in suspensions.* International Journal of Multiphase Flow, 1992. **18**(4): p. 577-592.
60. Scott, I.G., *Basic Acoustic Emission*. 1991: Gordon and Breach Science Publishers New York.

61. *AE Source Location Techniques*, in *https://www.nde-ed.org/EducationResources/CommunityCollege/Other%20Methods/AE/AE_Source%20Location.htm*. n.d.
62. Nivesrangsan, P., J.A. Steel, and R.L. Reuben, *Source location of acoustic emission in diesel engines.* Mechanical Systems and Signal Processing, 2007. **21**(2): p. 1103-1114.
63. Baxter, M.G., et al., *Delta T source location for acoustic emission.* Mechanical Systems and Signal Processing, 2007. **21**(3): p. 1512-1520.
64. Semin, R.A.B. and A.R. Ismail, *Computational Visualization and Simulation of Diesel Engines Valve Lift Performance Using CFD.* American Journal of Applied Sciences, 2008. **5**(5): p. 532-539.
65. Kong, S.-C., Z. Han, and R.D. Reitz, *The development and application of a diesel ignition and combustion model for multidimensional engine simulation*. 1995, SAE Technical Paper.
66. Kao, M. and J.J. Moskwa, *Turbocharged diesel engine modeling for nonlinear engine control and state estimation.* Journal of dynamic systems, measurement, and control, 1995. **117**(1): p. 20-30.
67. Watson, N., A. Pilley, and M. Marzouk, *A combustion correlation for diesel engine simulation*. 1980, SAE Technical Paper.
68. Arrègle, J., et al., *Development of a zero-dimensional diesel combustion model. Part 1: analysis of the quasi-steady diffusion combustion phase.* Applied Thermal Engineering, 2003. **23**(11): p. 1301-1317.
69. Rakopoulos, C., et al., *Analysis of combustion and pollutants formation in a direct injection diesel engine using a multi-zone model.* International journal of energy research, 1995. **19**(1): p. 63-88.
70. Kouremenos, D., C. Rakopoulos, and D. Hountalas, *Multi-zone combustion modelling for the prediction of pollutants emissions and performance of DI diesel engines*. 1997, SAE Technical Paper.
71. Rakopoulos, C.D. and D. Hountalas, *Development and validation of a 3-D multi-zone combustion model for the prediction of DI diesel engines performance and pollutants emissions*. 1998, SAE Technical Paper.
72. Cui, Y., K. Deng, and J. Wu, *A direct injection diesel combustion model for use in transient condition analysis.* Proceedings of the Institution of Mechanical Engineers, Part D: Journal of Automobile Engineering, 2001. **215**(9): p. 995-1004.

73. Jung, D. and D.N. Assanis, *Multi-zone DI diesel spray combustion model for cycle simulation studies of engine performance and emissions*. 2001, SAE technical paper.
74. Hountalas, D.T., et al., *Multi-zone combustion modeling as a tool for DI diesel engine development–Application for the effect of injection pressure*. 2004, SAE Technical Paper.
75. Nishida, K. and H. Hiroyasu, *Simplified three-dimensional modeling of mixture formation and combustion in a DI diesel engine*. 1989, SAE Technical Paper.
76. Reitz, R. and C. Rutland, *Development and testing of diesel engine CFD models.* Progress in Energy and Combustion Science, 1995. **21**(2): p. 173-196.
77. Maghbouli, A., et al., *An advanced combustion model coupled with detailed chemical reaction mechanism for D.I diesel engine simulation.* Applied Energy, 2013. **111**(0): p. 758-770.
78. Weißenborn, E., T. Bossmeyer, and T. Bertram, *Adaptation of a zero-dimensional cylinder pressure model for diesel engines using the crankshaft rotational speed.* Mechanical Systems and Signal Processing, 2011. **25**(6): p. 1887-1910.
79. Jacob, P., F. Gu, and A. Ball, *Non-parametric models in the monitoring of engine performance and condition: Part 1: modelling of non-linear engine processes.* Proceedings of the Institution of Mechanical Engineers, Part D: Journal of Automobile Engineering, 1999. **213**(1): p. 73-81.
80. Matsui, Y., M. Hasegawa, and J. Kawashima, *Analysis of injection rate characteristics of fuel injection systems in IDI diesel engines using an enhanced numerical simulation code.* JSAE Review, 1996. **17**(1): p. 3-9.
81. Schaffnit, J., S. Sinsel, and R. Isermann, *Hardware-in-the-loop simulation for the investigation of truckdiesel injection systems.* American Control Conference, 1998. Proceedings of the 1998, 1998. **1**.
82. Partridge, I. and G. Greeves. *Interpreting diesel combustion with a fuel spray computer model*. in *IMECHE conference transactions*. 1998.
83. Timoney, D.J., *A simple technique for predicting optimum fuel-air mixing conditions in a direct injection Diesel engine with swirl.* Small, 1985. **2011**: p. 02-18.
84. Marcic, M., *Diesel spray liquid phase measuring device.* Sensors and Actuators A: Physical, 2001. **87**(3): p. 124-130.

85. Doudou, A., *Turbulent flow study of an isothermal diesel spray injected by a common rail system.* Fuel, 2005. **84**(2): p. 287-298.
86. Payri, R., et al., *Using spray momentum flux measurements to understand the influence of diesel nozzle geometry on spray characteristics.* Fuel, 2005. **84**(5): p. 551-561.
87. Wang, X., et al., *An experimental investigation on spray, ignition and combustion characteristics of biodiesels.* Proceedings of the Combustion Institute, 2011. **33**(2): p. 2071-2077.
88. Steel, J.A. and R.L. Reuben, *Recent developments in monitoring of engines using acoustic emission.* The Journal of Strain Analysis for Engineering Design, 2005. **40**(1): p. 45-57.
89. El-Ghamry, M., et al., *Indirect measurement of cylinder pressure from diesel engines using acoustic emission.* Mechanical Systems and Signal Processing, 2005. **19**(4): p. 751-765.
90. Jafari, S.M., H. Mehdigholi, and M. Behzad, *Valve fault diagnosis in internal combustion engines using acoustic emission and artificial neural network.* Shock and Vibration, 2014.
91. Nivesrangsan, P., J.A. Steel, and R.L. Reuben, *Acoustic emission mapping of diesel engines for spatially located time series-Part II: Spatial reconstitution.* Mechanical Systems and Signal Processing, 2007. **21**(2): p. 1084-1102.
92. Lim, T., et al. *Predicting AE attenuation in structures by geometric analysis*. in *International Conference on Shape Modeling and Applications, SMI'05, June 13, 2005 - June 17, 2005*. 2005. Cambridge, MA, United states: Inst. of Elec. and Elec. Eng. Computer Society.
93. Robertson, A.I.F., et al., *Source identification using acoustic emission on large bore cylinder liners,* in *26th European Conference on Acoustic Emission Testing*. 2004, EWGAE Berlin.
94. Pontoppidan, N.H., J. Larsen, and T. Fog, *Independent component analysis for detection of condition changes in large diesels* in *COMADEM* 2003. p. p. 493-502.
95. Lee, S.G., et al., *Evaluation of internal leak in valve using acoustic emission method.* Key Engineering Materials, 2006. **326**: p. 661-664.
96. Sharif, M.A. and R.I. Grosvenor, *Internal valve leakage detection using an acoustic emission measurement system.* Transactions of the Institute of Measurement and Control, 1998. **20**(5): p. 233-242.

97. Kaewwaewnoi, W., A. Prateepasen, and P. Kaewtrakulpong, *Investigation of the relationship between internal fluid leakage through a valve and the acoustic emission generated from the leakage.* Measurement, 2010. **43**(2): p. 274-282.
98. Elamin, F., et al., *Diesel engine valve clearance detection using acoustic emission.* Advances in Mechanical Engineering, 2010.
99. Frances, A., et al., *A Study of the Variability of Acoustic Emission Signals from a Medium Size Marine Diesel Engine under Service Conditions.* COMADEM, 2003: p. 503–512.
100. Afzal, H., et al., *Internal flow in diesel injector nozzles: modelling and experiments.* IMechE Seminar Publication on Diesel Injection Systems, 1999. **492**: p. 25-44.
101. Mostafapour, A. and S. Davoudi, *Analysis of leakage in high pressure pipe using acoustic emission method.* Applied Acoustics, 2013. **74**(3): p. 335-342.
102. Neill, G., et al., *Detection of incipient cavitation in pumps using acoustic emission.* Proceedings of the Institution of Mechanical Engineers, Part E: Journal of process mechanical engineering, 1997. **211**(4): p. 267-277.
103. Gu, F., P. Jacob, and A. Ball, *Non-parametric models in the monitoring of engine performance and condition: Part 2: non-intrusive estimation of diesel engine cylinder pressure and its use in fault detection.* Proceedings of the Institution of Mechanical Engineers, Part D: Journal of Automobile Engineering, 1999. **213**(2): p. 135-143.
104. Barelli, L., et al., *Diagnosis of internal combustion engine through vibration and acoustic pressure non-intrusive measurements.* Applied Thermal Engineering, 2009. **29**(8–9): p. 1707-1713.
105. Marcic, M., *A new method for measuring fuel-injection rate.* Flow Measurement and Instrumentation, 1999. **10**(3): p. 159-165.
106. Marčič, M., *New diesel injection nozzle flow measuring device.* Review of Scientific Instruments, 2000. **71**(4): p. 1876-1882.
107. Marcic, M., *Measuring method for diesel multihole injection nozzles.* Sensors & Actuators: A. Physical, 2003. **107**(2): p. 152-158.
108. Carlucci, A.P., F.F. Chiara, and D. Laforgia, *Analysis of the relation between injection parameter variation and block vibration of an internal combustion diesel engine.* Journal of Sound and Vibration, 2006. **295**(1-2): p. 141-164.
109. Gu, F. and A.D. Ball, *Diesel injector dynamic modelling and estimation of injection parameters from impact response. Part I; modelling and analysis of*

injector impacts. Proceedings of the Institution of Mechanical Engineers, Part D: Journal of Automobile Engineering, 1996. **210**(4): p. 293-302.

110. Gu, F., A.D. Ball, and K.K. Rao, *Diesel injector dynamic modelling and estimation of injection parameters from impact response. Part 2: prediction of injection parameters from monitored vibration.* Proceedings of the Institution of Mechanical Engineers, Part D: Journal of Automobile Engineering, 1996. **210**(4): p. 303-312.
111. Elamin, F., F. Gu, and A. Ball, *Diesel Engine Injector Faults Detection Using Acoustic Emissions Technique.* Modern Applied Science, 2010. **4**(9): p. P3.
112. Brown, E.R., et al., *Acoustic emission source discrimination using a piezopolymer based sensor.* Materials Evaluation, 1999. **57**(5): p. 515-520.
113. Luján, J.M., et al., *A methodology for combustion detection in diesel engines through in-cylinder pressure derivative signal.* Mechanical Systems and Signal Processing, 2010. **24**(7): p. 2261-2275.
114. Badawi, B.A., et al., *Identification of diesel engine events from acoustic signals using independent component analysis and time-frequency analysis*, in *SAE 2007 Noise and Vibration Conference and Exhibition*. 2007, SAE International: St. Charles, IL, USA.
115. Li, W., et al., *A study of the noise from diesel engines using the independent component analysis.* Mechanical Systems and Signal Processing, 2001. **15**(6): p. 1165-1184.
116. Pontoppidan, N.H., S. Sigurdsson, and J. Larsen, *Condition monitoring with mean field independent components analysis.* Mechanical Systems and Signal Processing, 2005. **19**(6): p. 1337-1347.
117. Pontoppidan, N.H. and J. Larsen. *Unsupervised condition change detection in large diesel engines*. in *Neural Networks for Signal Processing, 2003. NNSP'03. 2003 IEEE 13th Workshop on*. 2003. IEEE.
118. Pontoppidan, N.H., S. Sigurdsson, and R.P. Plads, *Independent components in acoustic emission energy signals from large diesel engines.* International Journal of COMADEM, 2005.
119. Bizon, K., et al., *Analysis of Diesel engine combustion using imaging and independent component analysis.* Proceedings of the Combustion Institute, 2013. **34**(2): p. 2921-2931.

120. Badawi, B.A., et al., *Identification of Diesel Engine Cycle Events using Measured Surface Vibration*, in *Small Engine Technology Conference & Exposition*. 2006, SAE International: San Antonio, TX, USA.
121. Zheng, G.T. and A.Y.T. Leung, *Internal Combustion Engine Noise Analysis With Time-Frequency Distribution.* Journal of Engineering for Gas Turbines and Power, 2002. **124**: p. 645.
122. Pruvost, L., Q. Leclère, and E. Parizet, *Diesel engine combustion and mechanical noise separation using an improved spectrofilter.* Mechanical Systems and Signal Processing, 2009. **23**(7): p. 2072-2087.
123. Newland, D.E., *An introduction to random vibrations, spectral and wavelet analysis*. 1993: Longman.
124. Tognola, G., et al. *Time-frequency analysis of acoustic emissions: A wavelet approach*. in *Proceedings of the 1995 IEEE Engineering in Medicine and Biology 17th Annual Conference and 21st Canadian Medical and Biological Engineering Conference. Part 2 (of 2), September 20, 1995 - September 23, 1995*. 1995. Montreal, Can.
125. Ding, Y., R.L. Reuben, and J.A. Steel, *A new method for waveform analysis for estimating AE wave arrival times using wavelet decomposition.* NDT & E International, 2004. **37**(4): p. 279-290.
126. Grosse, C.U., et al., *Improvements of AE technique using wavelet algorithms, coherence functions and automatic data analysis.* Construction and Building Materials, 2004. **18**(3): p. 203-213.
127. Peng, Z.K. and F.L. Chu, *Application of the wavelet transform in machine condition monitoring and fault diagnostics: a review with bibliography.* Mechanical Systems and Signal Processing, 2004. **18**(2): p. 199-221.
128. Ranachowski, P. and A. Bejger, *Application of Wavelet Transform for Monitoring of Operation of High-Power Diesel Engine.* Molecular and Quantum Acoustics, 2006. **27**: p. 227-23.
129. Wu, J.-D. and J.-C. Chen, *Continuous wavelet transform technique for fault signal diagnosis of internal combustion engines.* NDT & E International, 2006. **39**(4): p. 304-311.
130. Barelli, L., et al., *Cylinders diagnosis system of a 1 MW internal combustion engine through vibrational signal processing using DWT technique.* Applied Energy, 2012. **92**(0): p. 44-50.

131. Wang, X., et al., *Fault diagnosis of diesel engine based on adaptive wavelet packets and EEMD-fractal dimension.* Mechanical Systems and Signal Processing, 2013. **41**(1–2): p. 581-597.
132. Chandroth, G., A. Sharkey, and N. Sharkey, *Cylinder pressures and vibration in internal combustion engine condition monitoring.* Proceedings of Comadem 99, Sunderland, UK, 1999.
133. Wu, J.-D. and C.-H. Liu, *Investigation of engine fault diagnosis using discrete wavelet transform and neural network.* Expert Systems with Applications, 2008. **35**(3): p. 1200-1213.
134. Wu, J.-D. and C.-H. Liu, *An expert system for fault diagnosis in internal combustion engines using wavelet packet transform and neural network.* Expert Systems with Applications, 2009. **36**(3, Part 1): p. 4278-4286.
135. Li, Y.-O., et al., *Joint blind source separation by multiset canonical correlation analysis.* Signal Processing, IEEE Transactions on, 2009. **57**(10): p. 3918-3929.
136. Chan, M.C., et al. *Integrating principle component analysis and canonical correlation analysis for monitoring water quality in storage reservoir*. in *2nd International Conference on Engineering and Technology Innovation 2012, ICETI 2012, November 2, 2012 - November 6, 2012*. 2013. Kaohsiung, Taiwan: Trans Tech Publications.
137. Speijers, B., D. Dianne, and A. Guzzomi. *Using canonical variate analysis to detect engine misfires*. in *Proceedings: the 7th Australasian Congress on Applied Mechanics (ACAM 7), 9-12 December 2012, the University of Adelaide, North Terrace Campus/National Committee on Applied Mechanics of Engineers Australia*. 2012. Engineers Australia.
138. Lee, C.S. and S.W. Park, *An experimental and numerical study on fuel atomization characteristics of high-pressure diesel injection sprays.* Fuel, 2002. **81**(18): p. 2417-2423.
139. Wang, X., et al., *Experimental and analytical study on biodiesel and diesel spray characteristics under ultra-high injection pressure.* International Journal of Heat and Fluid Flow, 2010. **31**(4): p. 659-666.
140. Payri, F., et al., *The influence of cavitation on the internal flow and the spray characteristics in diesel injection nozzles.* Fuel, 2004. **83**(4–5): p. 419-431.
141. Yeom, J.-K. and H. Fujimoto, *A study on the behavior characteristics of diesel spray by using a high pressure injection system with common rail apparatus.* KSME International Journal, 2003. **17**(9): p. 1371-1379.

142. Gao, Y., et al., *Experimental study of the spray characteristics of biodiesel based on inedible oil*. Biotechnology Advances, 2009. **27**(5): p. 616-624.
143. ASTM, *ASTM E976-98: Standard guide for determining the reproducibility of acoustic emission sensor response*, in *Annual Book of ASTM Standards*. 1999. p. 379-384.
144. El-Shaib, M.N., *Predicting acoustic emission attenuation in solids using ray-tracing within a 3D solid model*. PhD thesis, Heriot-Watt University, Edinburgh, UK, November 2012.
145. Droubi, M.G., *Monitoring particle impact energy using acoustic emission technique*. 2013, Heriot-Watt University.
146. Shehadeh, M., J.A. Steel, and R.L. Reuben, *Acoustic emission source location for steel pipe and pipeline applications: The role of arrival time estimation.* Proceedings of the Institution of Mechanical Engineers, Part E: Journal of Process Mechanical Engineering, 2006. **220**(2): p. 121-133.
147. Noma, H., et al. *High-Temperature Acoustic Emission Sensing Using Aluminum Nitride Sensor*. in *The Sixth International Conference on Acoustic Emission (Acoustic Emission Working Group), South Lake Tahoe (USA)*. 2007.
148. Keprt, J. and P. BENEŠ, *A Comparison of AE Sensor Calibration Methods.* Journal of Acoustic Emission, 2008. **26**: p. 60-70.
149. Theobald, P., B. Zeqiri, and J. Avison, *Couplants and their influence on AE sensor sensitivity.* Journal of Acoustic Emission, 2008. **26**: p. 91-97.
150. Lan, H., et al., *Surface-to-surface calibration of acoustic emission sensors.* Sensors and Actuators A: Physical, 2012. **174**: p. 16-23.
151. Cook, A., et al., *Continuous Monitoring of Powder Size Distribution using High Temperature ATEX Acoustic Emission Sensors*, in *31st Conference of the European Working Group on Acoustic Emission (EWGAE)* 2014: Dresden, Germany.
152. Nivesrangsan, P., J.A. Steel, and R.L. Reuben, *AE mapping of engines for spatially located time series.* Mechanical Systems and Signal Processing, 2005. **19**(5): p. 1034-1054.
153. Beattie, A.G., *Energy analysis in Acoustic Emission.* Materials Evaluation, 1976. **34**(4): p. 73-78.
154. Beattie, A.G. and R.A. Jaramillo, *The measurement of energy in acoustic emission.* Review of Scientific Instruments, 1974. **45**(3): p. 352-357.

155. Duncan, H.A., *Energy processing techniques for straess wave emission signals.* Journal of the Acoustical Society of America, 1979. **65**(6): p. 1556-1561.
156. Munoz, M., et al., *Engine diagnosis method based on vibration and acoustic emission energy*. Insight: Non-Destructive Testing and Condition Monitoring, 2012. **54**(3): p. 149-154.
157. El-Shaib, M., R. Reuben, and T. Lim, *Predicting acoustic emission attenuation in small steel blocks using a ray tracing technique.* Insight-Non-Destructive Testing and Condition Monitoring, 2012. **54**(12): p. 673-680.
158. Smith, S.W., *The scientist and engineer's guide to digital signal processing.* 1997.
159. Smith, S.W., *The Scientist and Engineer's Guide to Digital Signal Processing*. 2009, California Technical Publishing.
160. MacGregor, J. and T. Kourti, *Statistical process control of multivariate processes.* Control Engineering Practice, 1995. **3**(3): p. 403-414.
161. Melzer, T., M. Reiter, and H. Bischof, *Appearance models based on kernel canonical correlation analysis.* Pattern recognition, 2003. **36**(9): p. 1961-1971.
162. Statheropoulos, M., N. Vassiliadis, and A. Pappa, *Principal component and canonical correlation analysis for examining air pollution and meteorological data.* Atmospheric Environment, 1998. **32**(6): p. 1087-1095.
163. H., W., *Canonical Correlation Clarified by Singular Value Decomposition*. 2011, W.H. Press: http://www.nr.com/whp/notes/CanonCorrBySVD.pdf.
164. Kranzowsi, W., *Principles of multivariate analysis: A user's perspective*. 1988, Oxford: University Science Series. Oxford University Press.
165. Thakkar, N., J. Steel, and R. Reuben, *Rail–wheel contact stress assessment using acoustic emission: a laboratory study of the effects of wheel flats.* Proceedings of the Institution of Mechanical Engineers, Part F: Journal of Rail and Rapid Transit, 2012. **226**(1): p. 3-13.
166. *Stuart Diesel Marine Engine manual*. 1970, Stuart Turner Engines Ltd: Henley on Thames, England.
167. Douglas, R.M., et al., *On-line power estimation of large diesel engines using acoustic emission and instantaneous crankshaft angular velocity.* International Journal of Engine Research, 2006. **7**(5): p. 399-410.
168. Orfanidis, S.J., *Optimum signal processing*. 1988: Collier Macmillan.

Appendix A

AE Sensor Calibration Certificates

A1. AE sensor calibration certificate for sensor 99

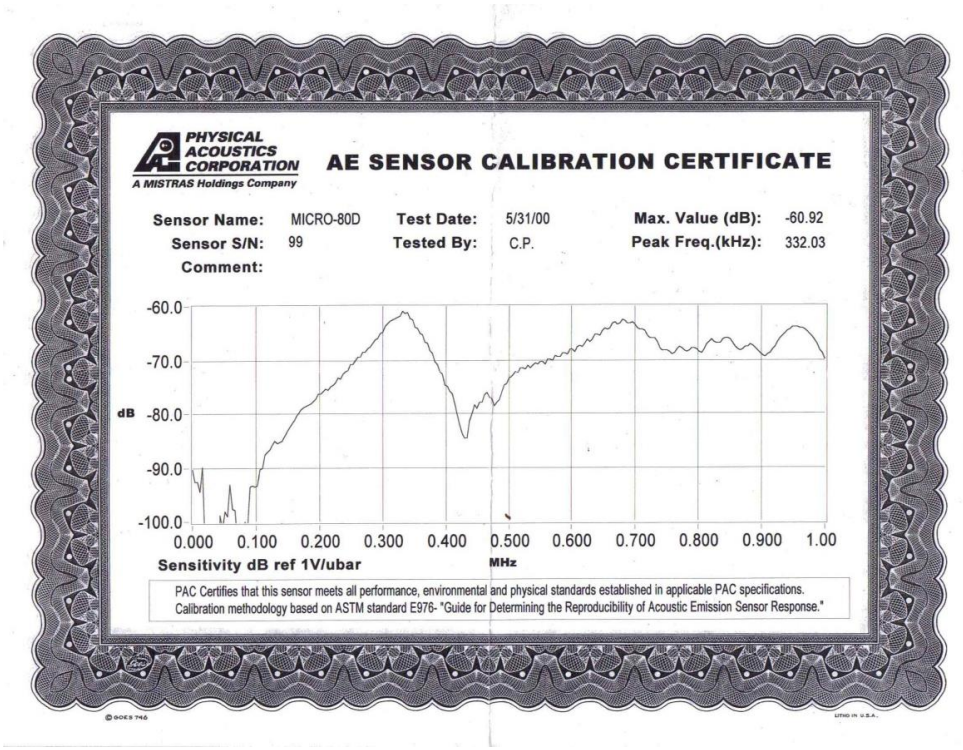

A2. AE sensor calibration certificate for sensor 115

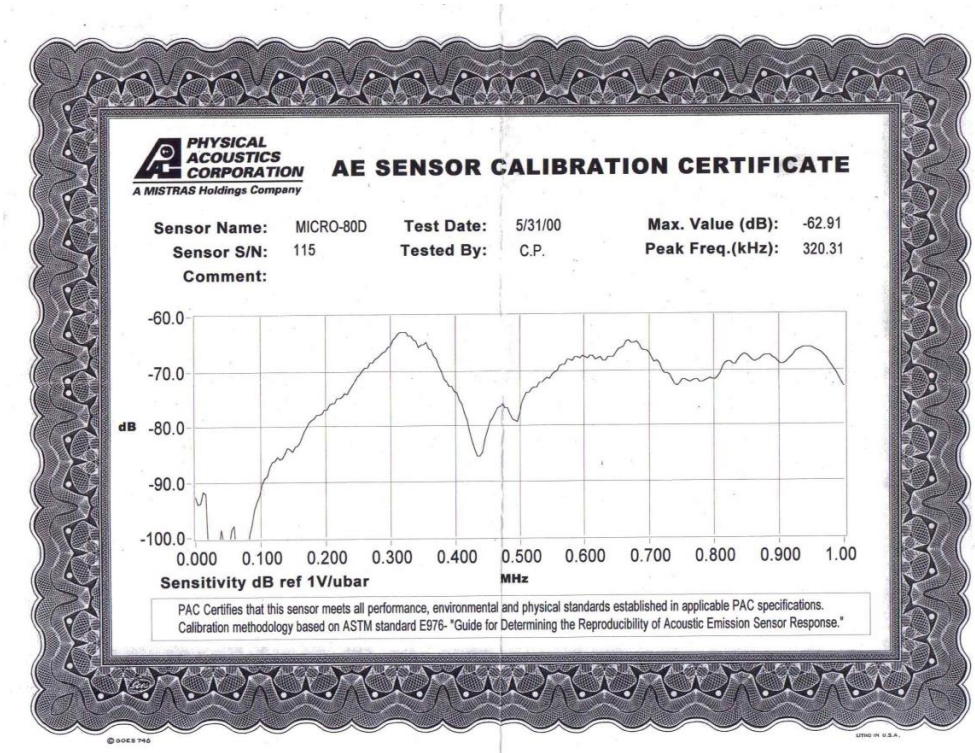

A3. AE sensor calibration certificate for sensor 119

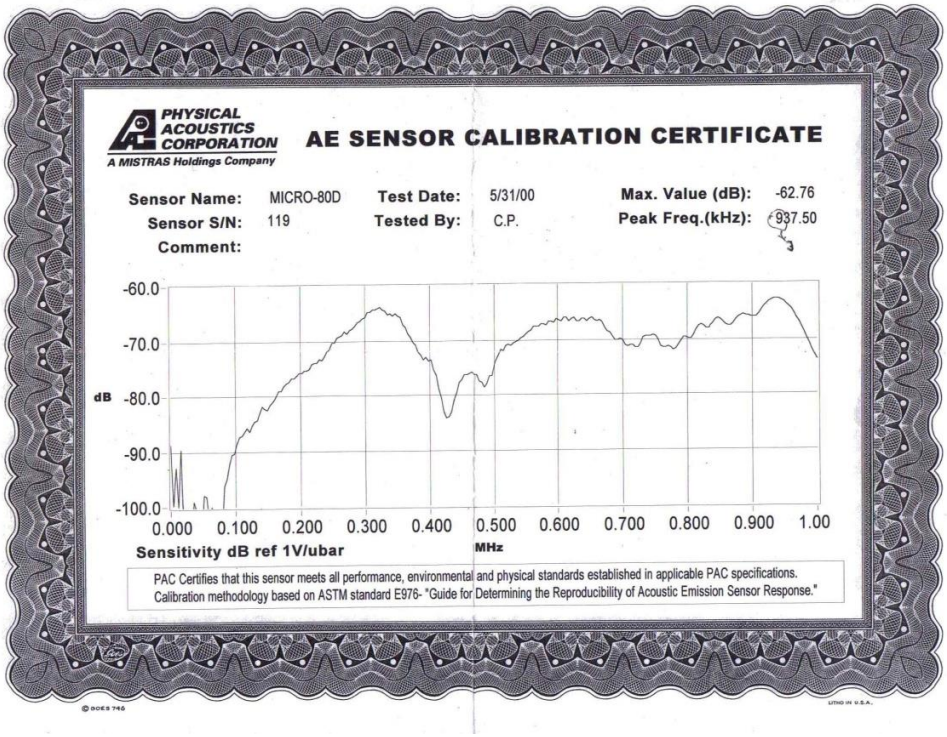

A.4 AE sensor calibration certificate for sensor 127

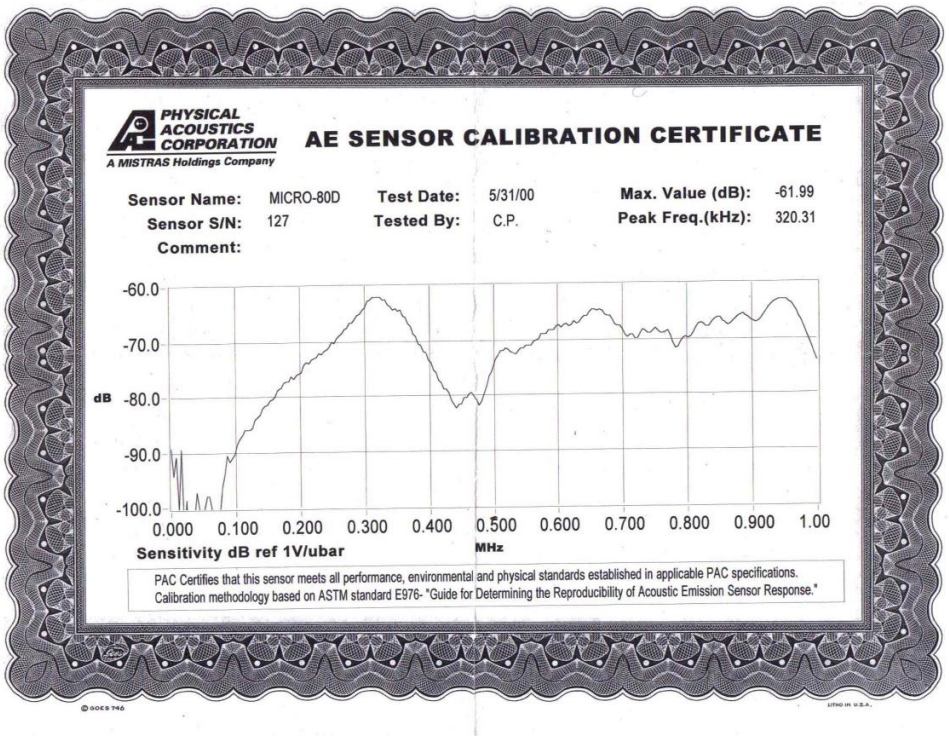

Appendix B

Experimental data Settings

B.1 Calibration of AE sensors

No. of Ch.	No. of Points	Sampling Rate (Hz)	Pre trigger	Trigger level	Pre Amp Gain (dB)	SCU Gain (dB)
3	$5 * 10^5$	$5 * 10^6$	10^3	0.2	40	-12

File Name	Position	Description
A1-A10	1^{ST} mounting Distance between centre and each sensor is 70 mm	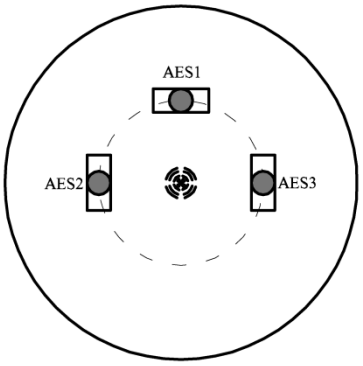
B1-B10	Re-mounting Distance between centre and each sensor is 70 mm	
C1-C10	1^{ST} mounting Distance between centre and each sensor is 70 mm	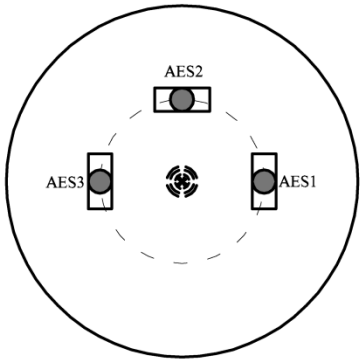
D1-D10	Re-mounting Distance between centre and each sensor is 70 mm	
E1-E10	1^{ST} mounting Distance between centre and each sensor is 70 mm	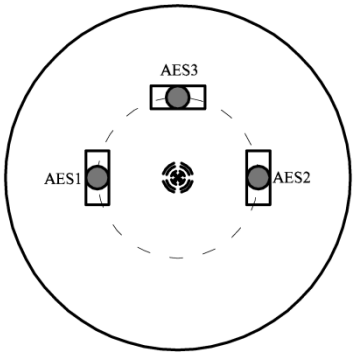
F1-F10	Re-mounting Distance between centre and each sensor is 70 mm	

Table B.1: The settings of three AE sensors calibration experiment.

B.2 Study the behaviour of AE signal through a thin steel plate

File Name	Position	No. of Ch.	No. of Points	Sampling Rate (Hz)	Pre trigger	Trigger level	Pre Amp Gain (dB)	SCU Gain (dB)
A1 - A10	A	2	$5 * 10^4$	$5 * 10^6$	10^3	0.2	40	0
B1 - B10	B	2	$5 * 10^4$	$5 * 10^6$	10^3	0.2	40	0
C1 - C10	C	2	$5 * 10^4$	$5 * 10^6$	10^3	0.2	40	0
D1 - D10	D	2	$5 * 10^4$	$5 * 10^6$	10^3	0.2	40	0
E1 - E10	E	2	$5 * 10^4$	$5 * 10^6$	10^3	0.2	40	0
F1 - F10	F	2	$5 * 10^4$	$5 * 10^6$	10^3	0.2	40	0
G1 - G10	G	2	$5 * 10^4$	$5 * 10^6$	10^3	0.2	40	0

Table B.2: The experimental settings of AE signal behavior through a thin steel plate.

B.3 Attenuation and calibration experiments of engine cylinder head

File Name	Position	No. of Ch.	No. of Points	Sampling Rate (Hz)	Pre trigger	Trigger level	Pre Amp Gain (dB)	SCU Gain (dB)
A1-A5	P1	2	$2.5*10^5$	$2.5*10^6$	10^3	0.2	40	-12
A6-A10	P2	2	$2.5*10^5$	$2.5*10^6$	10^3	0.2	40	-12
A11-A15	P3	2	$2.5*10^5$	$2.5*10^6$	10^3	0.2	40	-12
B1-B5	P4	2	$2.5*10^5$	$2.5*10^6$	10^3	0.2	40	-12
B6-B10	P5	2	$2.5*10^5$	$2.5*10^6$	10^3	0.2	40	-12
B11-B15	P6	2	$2.5*10^5$	$2.5*10^6$	10^3	0.2	40	-12
C1-C5	P7	2	$2.5*10^5$	$2.5*10^6$	10^3	0.2	40	-12
C6-C10	P8	2	$2.5*10^5$	$2.5*10^6$	10^3	0.2	40	-12
C11-A15	P9	2	$2.5*10^5$	$2.5*10^6$	10^3	0.2	40	-12

Table B.3: The experimental settings of AE signal transmission through the cylinder head of Stuart Turner engine (using both Diesel and Bio-diesel fuel experiments).

No. of Ch.	No. of Points	Sampling Rate (Hz)	Pre trigger	Trigger level
3	$2.5*10^5$	$2.5*10^6$	10^3	0.2

File Name	Position	Pre Amp Gain (dB)			SCU Gain (dB)		
		Sensor1	Sensor2	Sensor3	Sensor1	Sensor2	Sensor3
A1-A5	P1	40	60	60	-12	-12	0
B1-B5	P2	40	40	60	-6	6	0
C1-C5	P3	40	40	60	-6	0	-6
D1-D5	P4	40	40	60	0	-12	-12
E1-E5	P5	60	40	60	-12	-12	-12
F1-F5	P6	60	40	40	-12	-12	0
G1-G5	P7	60	40	40	-6	0	-6
H1-H5	P8	60	40	40	0	6	-6
I1-I5	P9	60	60	40	0	-12	-12

Table B.4: The experimental settings of AE signal transmission experiment of sensor array1 on Perkins T1004 (engine C).

No. of Ch.	No. of Points	Sampling Rate (Hz)	Pre trigger	Trigger level
3	$2.5*10^5$	$2.5*10^6$	10^3	0.2

File Name	Position	Pre Amp Gain (dB)			SCU Gain (dB)		
		Sensor1	Sensor2	Sensor3	Sensor1	Sensor2	Sensor3
A1-A5	P1	60	40	60	-12	-6	-6
B1-B5	P2	60	40	60	-6	-12	-6
C1-C5	P3	40	40	60	6	-6	-6
D1-D5	P4	60	40	60	-6	0	-12
E1-E5	P5	20	60	60	0	-6	6
F1-F5	P6	60	60	60	0	-6	6
G1-G5	P7	60	60	60	6	6	0
H1-H5	P8	60	60	60	6	6	6

Table B.5: The experimental settings of AE signal transmission experiment of sensor array2 on Perkins T1004 (engine C).

B.4 Running engine experiments

File Name	Condition	Engine speed (rpm)	Torque (N.m)	Current (Amp)	Voltage (Volts)	T_{exh} (^oC)	T_{amb} (^oC)	Engine oil temp (^oC)	Water in/out temp (^oC)
A1-A5	No load	1494-1500	3.6	0	0	100	20	37	9/13
B1-B5	1 Load	1468-1475	30.3-30.5	11	180	151	20	39	10/13
C1-C5	2 Loads	1435-1436	58.2-59.1	21	180	217	20	40	10/14
D1-D5	3 Loads	1388-1395	86.6-87.5	30	175	283	20	39	10/14
E1-E5	4 Loads	1300-1315	107.7-109.2	38	160	336	20	40	10/15
F1-F5	5 Loads	1200-1204	111.6-113.5	39	150	331	20	41	10/33
G1-G5	6 Loads	1075-1077	108.6-110.9	38	130	303	20	42	10/60
FF1-FF5	5 Loads	1189-1199	109.5-110.5	39	150	319	20	42	10/15
EE1-EE5	4 Loads	1295-1299	107.4-108	37	160	352	20	44	10/37
DD1-DD5	3 Loads	1390-1393	88.3-87.1	30	180	313	21	46	10/16
CC1-CC5	2 Loads	1435-1436	60.2-60.7	21	180	250	21	48	10/38
BB1-BB5	1 Load	1463-1465	31-31.3	10	190	180	21	49	10/46
AA1-AA5	No load	1515-1526	2.5-3.1	0	190	141	21	51	10/14

Table B.6: The experimental settings of Stuart Turner (Engine A) running engine experiment.

No. of Ch.	No. of Points	Sampling Rate (Hz)	Pre trigger	Trigger level
3	$2.5*10^6$	$2.5*10^6$	10^3	0.2

File Name	Engine speed (rpm)	Pre Amp Gain (dB)		SCU Gain (dB)	
		Sensor1	Sensor2	Sensor1	Sensor2
A1-A5	900	40	40	-12	-12
A6-A10	1200	40	40	-12	-12
A11-A15	1500	40	40	-12	-12
A16-A20	1800	40	40	-12	-12
A21-A25	2100	40	40	-12	-12

Table B.7: The experimental settings of Perkins A4.270 (Engine B) running engine experiment.

No. of Ch.	No. of Points	Sampling Rate (Hz)	Pre trigger	Trigger level
4	$2.5*10^6$	$2.5*10^6$	10^3	0.2

File Name	Engine speed (rpm)	Pre Amp Gain (dB)			SCU Gain (dB)		
		Sensor1	Sensor2	Sensor3	Sensor1	Sensor2	Sensor3
A1-A5	728	20	20	20	-6	-6	-6
B1-B5	851	20	20	20	-6	-6	-6
C1-C5	1048	20	20	20	-6	-6	-6
D1-D5	1432	20	20	20	-6	-6	-6
E1-E5	2057	20	20	20	-6	-6	-6
F1-F5	2249	20	20	20	-6	-6	-6
G1-G5	2577	20	20	20	-6	-6	-6
H1-H5	2918	20	20	20	-6	-6	-6
GG1-GG5	2592	20	20	20	-6	-6	-6
FF1-FF5	2237	20	20	20	-6	-6	-6
EE1-EE5	1940	20	20	20	-6	-6	-6
DD1-DD5	1524	20	20	20	-6	-6	-6
CC1-CC5	1068	20	20	20	-6	-6	-6
BB1-BB5	847	20	20	20	-6	-6	-6
AA1-AA5	761	20	20	20	-6	-6	-6

Table B.8: The experimental settings of sensor array 1 in running Perkins T1004 (engine C) experiment.

No. of Ch.	No. of Points	Sampling Rate (Hz)	Pre trigger	Trigger level
4	$2.5*10^6$	$2.5*10^6$	10^3	0.2

File Name	Engine speed (rpm)	Pre Amp Gain (dB)			SCU Gain (dB)		
		Sensor1	Sensor2	Sensor3	Sensor1	Sensor2	Sensor3
A1-A5	837	20	20	20	-6	-6	-6
B1-B5	1057	20	20	20	-12	-6	-6
C1-C5	1473	20	20	20	-12	-6	-6
D1-D5	1990	20	20	20	-12	-6	-6
E1-E5	2262	20	20	20	-12	-6	-6
DD1-DD5	1960	20	20	20	-12	-6	-6
CC1-CC5	1530	20	20	20	-12	-6	-6
BB1-BB5	1068	20	20	20	-12	-6	-6
AA1-AA5	819	20	20	20	-12	-6	-6

Table B.9: The experimental settings of sensor array 2 in running Perkins T1004 (engine C) experiment.

B.5 Injector rig experiments

File Name	position	No. of Ch.	No. of Points	Sampling Rate (Hz)	Pre trigger	Trigger level	Pre Amp Gain (dB)	SCU Gain (dB)
A1-A25	1	1	$2.5*10^6$	$2.5*10^6$	10^2	0.2	40	-12
B1-B25	2	1	$2.5*10^6$	$2.5*10^6$	10^2	0.2	40	-12
C1-C25	3	1	$2.5*10^6$	$2.5*10^6$	10^2	0.2	40	-12
D1-D25	4	1	$2.5*10^6$	$2.5*10^6$	10^2	0.2	40	-12

Table B.10: The experimental settings of AE signal transmission through a diesel injector.

No. of Ch.	No. of Points	Sampling Rate (Hz)	Pre trigger	Trigger level
4	$2.5*10^6$	$2.5*10^6$	10^3	0.2

File Name	Injection pump speed (rpm)	Pre Amp Gain (dB)		SCU Gain (dB)	
		Sensor1	Sensor2	Sensor1	Sensor2
A1-A5	1510	20	20	0	-6
A6-A10	1700	20	20	0	-6
A11-A15	1956	20	20	0	-6
A16-A20	2135	20	20	0	-6
A21-A25	2335	20	20	0	-6
A26-A30	2609	20	20	0	-6

Table B.11: The experimental settings of running injector rig with pressure transducer (Experiment 1).

No. of Ch.	No. of Points	Sampling Rate (Hz)	Pre trigger	Trigger level
3	$2.5*10^6$	$2.5*10^6$	10^3	0.2

File Name	Injection pump speed (rpm)/ throttle position	Pre Amp Gain (dB)		SCU Gain (dB)	
		Sensor1	Sensor2	Sensor1	Sensor2
A1-A5	1523 (Min)	20	20	-12	-12
B1-B5	1455 (Max)	20	20	-12	-12
C1-C5	2207(Min)	20	20	-12	-12
D1-D5	2199 (Max)	20	20	-12	-12

Table B.12: The experimental settings of running injector rig with pressure transducer at different throttle position (Experiment 1).

No. of Ch.	No. of Points	Sampling Rate (Hz)	Pre trigger	Trigger level
3	$2.5*10^6$	$2.5*10^6$	10^3	0.2

File Name	Injection pump speed (rpm)	Pre Amp Gain (dB)		SCU Gain (dB)	
		Sensor1	Sensor2	Sensor1	Sensor2
A1-A5	1020	20	20	-12	+6
A6-A10	1517	20	20	-12	+6
A11-A15	1612	20	20	-12	+6
A16-A20	2110	20	20	-12	+6
A21-A25	1076	20	20	-12	+6
A26-A30	703	20	20	-12	+6

Table B.13: The experimental settings of running injector rig without pressure transducer (Experiment 2).

No. of Ch.	No. of Points	Sampling Rate (Hz)	Pre trigger	Trigger level
3	$2.5*10^6$	$2.5*10^6$	10^3	0.2

File Name	Injection pump speed (rpm)	Pre Amp Gain (dB)		SCU Gain (dB)	
		Sensor1	Sensor2	Sensor1	Sensor2
A1-A5	954	40	40	-12	-12
A6-A10	1272	40	40	-12	-12
A11-A15	1664	40	40	-12	-12
A16-A20	2120	40	40	-12	-12
A21-A25	2438	40	40	-12	-12

Table B.14: The experimental settings of running injector rig without pressure transducer (Experiment 3).